



HAL
open science

Feasibility study of an integrated flat-sheet solar heated membrane distillation module and equipment for autonomous and decentralized seawater desalination: design, modeling and optimization for small communities in remote areas

Qiuming Ma

► To cite this version:

Qiuming Ma. Feasibility study of an integrated flat-sheet solar heated membrane distillation module and equipment for autonomous and decentralized seawater desalination: design, modeling and optimization for small communities in remote areas. Chemical and Process Engineering. INSA de Toulouse, 2019. English. NNT: 2019ISAT0006. tel-03081294

HAL Id: tel-03081294

<https://theses.hal.science/tel-03081294>

Submitted on 18 Dec 2020

HAL is a multi-disciplinary open access archive for the deposit and dissemination of scientific research documents, whether they are published or not. The documents may come from teaching and research institutions in France or abroad, or from public or private research centers.

L'archive ouverte pluridisciplinaire **HAL**, est destinée au dépôt et à la diffusion de documents scientifiques de niveau recherche, publiés ou non, émanant des établissements d'enseignement et de recherche français ou étrangers, des laboratoires publics ou privés.



THÈSE

En vue de l'obtention du

DOCTORAT DE L'UNIVERSITÉ DE TOULOUSE

Délivré par :

Institut National des Sciences Appliquées de Toulouse (INSA de Toulouse)

Présentée et soutenue par :

Qiuming MA

le mercredi 10 avril 2019

Titre :

Étude de faisabilité d'un module plan intégrant distillation membranaire et collecteur solaire pour le dessalement autonome et décentralisé d'eau de mer : conception, modélisation et optimisation pour une application aux petites communautés isolées

École doctorale et discipline ou spécialité :

ED MEGEP : Génie des procédés et de l'Environnement

Unité de recherche :

Laboratoire d'Ingénierie des Systèmes Biologiques et des Procédés (LISBP)

Directeur/trice(s) de Thèse :

Prof. Corinne CABASSUD et Dr. Aras AHMADI

Jury :

Prof. Efrem CURCIO, Rapporteur

Prof. Xavier PY, Rapporteur

Prof. Driss NEHARI, Examineur

Dr. Stéphanie LABORIE, Examinatrice

Prof. Corinne CABASSUD, Directrice de thèse

Dr. Aras AHMADI, Co-directeur de thèse

Dr. Christophe CAMPERI-GINESTET, Invité

THÈSE

En vue de l'obtention du

DOCTORAT DE L'UNIVERSITÉ DE TOULOUSE

Délivré par : Institut National des Sciences Appliquées de Toulouse (INSA de Toulouse)

Spécialité : Génie des Procédés et de l'Environnement

Présentée et soutenue par :

Qiuming MA

Le mercredi 10 avril 2019

Titre :

Etude de faisabilité d'un module plan intégrant distillation membranaire et collecteur solaire pour le dessalement autonome et décentralisé d'eau de mer : conception, modélisation et optimisation pour une application aux petites communautés isolées

Jury :

Prof. Efrem CURCIO (Univ. Calabria, Italie)
Prof. Xavier PY (Univ. Perpignan Via Domitia, France)
Prof. Driss NEHARI (Centre Univ. Aïn Témouchent)
Dr. Stéphanie LABORIE (INSA Toulouse)
Prof. Corinne CABASSUD (INSA Toulouse)
Dr. Aras AHMADI (INSA Toulouse)
Dr. Christophe CAMPERI-GINESTET (Sunwaterlife)

École doctorale :

Mécanique, Énergétique, Génie civil et Procédés (MEGeP)

Unité de recherche :

Laboratoire d'Ingénierie des Systèmes Biologiques et des Procédés (LISBP)

Directeur/trice(s) de thèse :

Prof. Corinne CABASSUD et Dr. Aras AHMADI

Rapporteurs :

Prof. Efrem CURCIO et Prof. Xavier PY

Les petites unités de dessalement au point d'usage sont une alternative pour l'accès à l'eau potable des communautés isolées de zones côtières ou insulaires. La Distillation Membranaire (DM), bénéficie des intérêts potentiels à la fois des technologies thermiques et membranaires. Procédé de distillation, elle permet une excellente qualité de l'eau produite, taux de conversion élevé et c'est un procédé non-pressurisé. Contacteur membranaire, elle permet d'intensifier les procédés (compacité) et une basse température de fonctionnement. Par conséquent, la DM est un procédé de choix pour l'application visée. De plus, les lieux d'implantation ciblés souffrent souvent d'un manque d'accès à l'énergie, mais la plupart d'entre eux sont exposés à des niveaux élevés de radiation solaire. Or, la faible température de fonctionnement de la DM (inférieure à 80°C) permet un couplage possible avec de l'énergie thermique solaire, et des panneaux photovoltaïques (PV) hors réseau peuvent produire l'électricité nécessaire.

Dans cette thèse, la distillation membranaire sous Vide (VMD), qui permet de contrôler la force motrice et la production d'eau en jouant sur la pression de vide utilisé, est la configuration de DM retenue. Afin de réduire davantage les pertes de chaleur du système et d'intensifier le procédé, un module intégrant des membranes planes de DM et un collecteur solaire à plaque plane (FPC) apparaît comme une technologie possible. Cette étude a pour objectifs d'étudier la faisabilité de ce concept et de déterminer les paramètres de l'équipement et les conditions opératoires les plus favorables pour l'application visée en cherchant à réduire la consommation d'électricité (par des panneaux PV) et améliorer simultanément l'efficacité énergétique et la production d'eau dans l'ensemble du module VMD-FPC.

Ce module intégré est conçu et intégralement décrit par différentes couches de modélisation couplées et interconnectées, notamment : (i) le calcul dynamique du rayonnement solaire, pour différents emplacements, conditions ambiantes et propriétés du collecteur; (ii) le modèle de pores de la membrane, décrivant le transfert de chaleur et de matière à proximité et à l'intérieur de la membrane; (iii) le modèle de bulk, représentant les bilans longitudinaux de

chaleur, de matière et de quantité de mouvement; (iv) les dynamiques dans le système de recirculation.

Le développement comporte (i) une stratégie de récupération de chaleur appropriée ramenant la chaleur latente de la vapeur de perméat à basse température au courant de recirculation et (ii) une condensation efficace du perméat avant la pompe à vide qui permet de réduire considérablement la consommation d'électricité par la pompe à vide. Une pompe à chaleur peut atteindre ces objectifs : condenser la vapeur de perméat en évaporant le fluide thermique (évaporateur de pompe à chaleur) et renvoyer la chaleur latente vers le module VMD en condensant cette fois-ci le fluide thermique (condenseur de pompe à chaleur). Par conséquent, une pompe à chaleur avec le fluide thermique approprié est couplée au module VMD-FPC pour augmenter de manière significative l'efficacité du module.

Les analyses de sensibilité et les optimisations multi-objectifs sont ensuite effectuées à partir de séries de simulations. La surface du module, la pression de vide et l'intensité de récupération de chaleur sont les facteurs principaux pour la performance. La productivité quotidienne peut atteindre 96 L pour une surface de module de 3 m². Un coût énergétique quasi-constant de 50 à 60 kWh m⁻³, soit une puissance PV de 4,2 à 5,0 W L⁻¹ sont observés, permettant d'ajuster la capacité du système. Pour une puissance PV limitée à 130 W (installation mobile), plus de 30 L de distillat peuvent être obtenus avec une surface de 0,83 m² par une belle journée d'été à Toulouse, en tenant compte des paramètres de fonctionnement optimisés et des matériaux réels.

Mots-clés : Dessalement d'eau de mer ; Petits systèmes pour régions isolées; Distillation membranaire ; Procédés à énergie solaire ; Optimisation multi-objectifs ; Intensification des procédés

Small-scale desalination at the point of use offers a potential access to drinking water to communities living in remote coastal areas or isolated islands. As an emerging desalination technology, Membrane Distillation (MD) inherits some merits of both the thermal-based and membrane-based technologies: high distillate quality, high water recovery, and non-pressurized process of the former; small footprint due to the high contacting area, filtration of particle-like compounds, and low operating temperature of the latter. Consequently, MD would be a good candidate for the aforementioned application scenario. Moreover, the target places are also often in the lack of stable and centralized heat and power supply, while most of them benefit from high solar radiations. Fortunately, the low MD operating temperature (below 80°C) enables the possible coupling with low-grade solar thermal energy, and off-grid photovoltaic (PV) panels can be used to meet the electric demand.

In this dissertation, Vacuum MD (VMD), which allows to control the mass transfer driving force and water production by the applied vacuum pressure, was selected as MD configuration. In order to further reduce the system heat loss and to intensify the process, the integration in the same module of flat-sheet distillation membranes and direct solar heating by flat-plate collector (FPC) appears as a possible option. This study aims to explore the feasibility of this concept and to determine the more favorable design and operating conditions for the target application. The main task in this regard is to lower electricity consumption (provided by PV panels) and simultaneously improve the energy efficiency and water production throughout the VMD-FPC module. This integrated module is designed and comprehensively modeled through different coupled modeling layers, including: (i) dynamic solar radiation calculation, for different locations, ambient conditions and collector properties; (ii) membrane pore model, describing the heat and mass transfer near and inside the membrane; (iii) feed bulk model, representing the longitudinal heat, mass and momentum balances within the module; (iv) system dynamics in the recirculation system, based on time-varying steady-state phases.

The improvement pathway at this level consists of (i) a proper heat recovery strategy bringing the latent heat of vaporization from low-temperature permeate vapor back to the feed circulation and (ii) an effective permeate condensation before the vacuum pump that allows to significantly reduce the electricity consumption by vacuum pump. A heat pump is capable of achieving these

goals: condensing the permeate vapor by evaporating the thermal fluid (heat pump evaporator), and passing the latent heat back to the feed side of VMD by condensing the thermal fluid (heat pump condenser). Therefore, a heat pump with the appropriate thermal fluid is coupled with the VMD-FPC module to largely increase the efficiency of the desalination module.

The sensitivity analyses and multi-objective optimizations are conducted afterwards based on series of simulations. The module surface area, vacuum pressure and heat recovery intensity are the major factors that decide the performance, and the potential daily productivity of the system can reach up to 96 L for a maximum module surface area of 3 m². A quasi-constant energy cost of 50 - 60 kWh m⁻³ and PV power demand of 4.2 - 5.0 W L⁻¹ are observed, permitting a flexible adjustment of the system capacity according to the demand. Under a limitation of a PV power consumption of 130 W (considering the mobility), more than 30 L of distillate can be obtained by such an equipment with a surface area of 0.83 m² on a sunny summer-day in Toulouse, taking the optimized operating parameters and real-world material properties into account.

Keywords: Seawater desalination; Small-scale systems for remote areas; Membrane distillation; Solar-driven processes; Multi-objective optimization; Process intensification

Scientific productions during thesis

Journal articles

Q. Ma, A. Ahmadi, C. Cabassud, Direct integration of a vacuum membrane distillation module within a solar collector for small-scale units adapted to seawater desalination in remote places: Design, modeling & evaluation of a flat-plate equipment, *Journal of Membrane Science*. 564 (2018) 617–633. doi:10.1016/j.memsci.2018.07.067.

Q. Ma, A. Ahmadi, C. Cabassud, Optimization and design of a novel integrated vacuum membrane distillation - solar flat plate collector module with heat recovery strategy through heat pumps, *Journal of Membrane Science*. (2019). (submitted)

International conference proceedings

Q. Ma, A. Ahmadi, C. Cabassud, Direct integration of solar heating within a VMD module: design, evaluation & optimization, in: *IWA-MTC2017*, Singapore, 2017.

Q. Ma, A. Ahmadi, C. Cabassud, Simulation and optimization of an intensified hybrid system for seawater desalination: vacuum membrane distillation coupled with solar heating, in: *WCCE10*, Barcelona, Spain, 2017.

Q. Ma, A. Ahmadi, C. Cabassud, Simulation and Optimization of a Direct Solar-heating Vacuum Membrane Distillation System, in: *MELPRO2018*, Prague, Czech Republic, 2018.

Q. Ma, A. Ahmadi, C. Cabassud, Towards an Efficient Solar-Heated Vacuum Membrane Distillation Module, in: *IWA-RMTC 2018*, Vadodara, Gujarat, India, 2018.

Acknowledgement

The work in this dissertation for the last three and half years has been funded by China Scholarship Council (CSC) [No. 201504490023], and by the on-going ANR (Agence Nationale de la Recherche) project: LabCom-MOST, created during this thesis. I would like to express my sincere gratitude for their financial and intellectual support.

I would never complete this manuscript without all the help, guidance and valuable suggestions from my supervisors, Dr. Aras Ahmadi and Pr. Corinne Cabassud, in both research and life. They made a perfect team for my thesis study: Aras is an expert in process simulation and optimization, and he unreservedly gave his expertise, creativity and his time to every single stage of my work in last the 3 years. Corinne is an expert in membrane processes and water treatment, and she always provided her vision and experience to guide all the important directions of my thesis, and offered me opportunities for several international conferences. Besides, they helped me with their full support and encouragement to overcome plenty of difficulties not only in work, but also in administrative procedures and in life.

During these years in France, I have also met a lot of nice people inside and outside the lab. From the day when I entered this lab, Paul, Lucas, Allan, Ana, Mathias, Claire, Naïla, Noémie, Angélica, Xie Xiaomin, Yang Lixia, Xu Feishi and everybody, they helped me settle in and we often went to lunch together and always had interesting topics. Then, new faces kept coming and joined the community as well, Deng Hui, Flavie, Mathilde, Alberto, Kritchart, Beatriz, Marine, Dylan, Koji, Mei Mei, Nan Zibin, Fon, Baptiste, Zhang Tianyi, Shenzhou. I just want to say thank you to all of them for their company during my thesis, which rendered my days here with more color. Outside the lab, friends from my French classes, from the Saturday basketball, from the Sunday football and from our lab as well, they have kept me occupied with various funny activities especially during the weekends. So also many thanks to all of them.

I can never have the suitable words to thank my family members, especially my mom, my dad, my grandparents, for their unconditional love and always being supportive.

At last, my deep appreciations again to Prof. Efreem Curcio and Prof. Xavier Py for accepting to be the reviewers of my dissertation, and to Prof. Driss Nehari and Dr. Stéphanie Laborie for attending my defense and being the jury members.

Table of contents

General introduction.....	1
Thesis objectives.....	6
Thesis organization.....	7
I. Background of membrane distillation (MD) and state-of-the-art of coupling MD with solar energy	9
I.1. Membrane distillation	10
I.1.1. Membrane distillation applied to desalination.....	12
I.1.2. Configurations of MD	13
I.1.3. Configurations of MD modules.....	17
I.2. Transfer mechanisms of MD.....	19
I.2.1. Heat transfer	19
I.2.2. Mass transfer.....	22
I.2.3. Profiles along the flow direction	26
I.3. State of the art: MD driven by solar energy	27
I.3.1. Solar thermal collectors	28
I.3.2. Coupling solar thermal collectors with MD	33
I.3.3. Direct integration of solar thermal collectors and MD.....	41
I.3.4. Observations of the literature	46
I.4. Conclusions (in English)	47
I.4. Conclusions (en français).....	49
II. Direct integration of a vacuum membrane distillation module within a solar collector for small-scale units adapted to seawater desalination in remote places: Design, modeling & evaluation of a flat-plate equipment.....	53
II.1. Introduction (in English).....	54
II.1. Introduction (en français).....	55
II.2. Modeling of an integrated VMD-solar module	57
II.2.1. Solar radiation modeling	58
II.2.2. Simultaneous modeling of heat and mass transfer for an integrated VMD-solar module.....	63
II.3. Configuration for a dynamic recycling batch system	69
II.3.1. Temperature-based control strategy for the recycling batch system.....	71

II.3.2. Dynamics for the recycling batch system	72
II.3.3. Solution procedure	73
II.3.4. Performance indicators.....	73
II.4. Results and discussions.....	75
II.4.1. Consistency of the models: solar radiation and VMD	75
II.4.2. General set of parameters for a daily varying operation	77
II.4.3. Performance under temperature-controlled batch regime.....	79
II.4.4. Improved performance under continuous MD operation.....	82
II.5. Conclusions (in English).....	91
II.5. Conclusions (en français).....	91
III. Comparative study of flat-plate DCMD and VMD modules with integrated direct solar heating (DCMD-FPC and VMD-FPC)	93
III.1. Introduction (in English)	94
III.1. Introduction (en français)	95
III.2. Module & system description and modeling.....	96
III.2.1. DCMD module configuration	97
III.2.2. Description of mass and heat transfer in MD modules.....	98
III.2.3. Description of the dynamic system.....	102
III.2.4. Pumping energy consumption.....	105
III.2.5. Model coupling and resolution procedure	107
III.3. Results and discussion	108
III.3.1. Parameter settings and daily operation	108
III.3.2. Influence of parameters.....	113
III.3.3. Discussions on a high potential: Heat recovery & solar concentration	127
III.4. Conclusions (in English)	130
III.4. Conclusions (en français)	131
IV. Optimization and design of a novel integrated vacuum membrane distillation - solar flat plate collector module with heat recovery strategy through heat pumps.....	135
IV.1. Introduction (in English)	136
IV.1. Introduction (en français)	137
IV.2. Process description: coupled solar collector - VMD.....	139
IV.3. Design configuration and modeling of VMD-FPC with integrated heat pump	141
IV.3.1. Coupled solar flat-plate vacuum membrane distillation collector.....	141

IV.3.2. Theoretical study of heat recovery from condensation by heat pump.....	142
IV.3.3. Modeling structure, recirculation and system dynamics	145
IV.4. Performance assessment and analysis	148
IV.4.1. Decision variables, design parameters and main performance indicators.....	148
IV.4.2. Sensitivity analysis via Delta Moment-Independent (DMI) indicator	151
IV.4.3. Fast multi-objective optimization on design and operating conditions.....	152
IV.5. Results and discussions	153
IV.5.1. Sensitivity variation due to heat recovery from permeate condensation.....	153
IV.5.2. Importance of heat recovery level	155
IV.5.3. Global optimization and performance improvement using heat pump	156
IV.5.4. Benchmark optimization of VMD-FPC at fixed heat recovery levels	158
IV.5.5. Pareto-based study of decision variables and key indications on design	162
IV.6. Conclusions (in English)	167
IV.6. Conclusions (en français)	169
V. Practical recommendations on the design of a small MD-FPC system for autonomous and decentralized seawater desalination in remotes areas	171
V.1. Introduction (in English).....	172
V.1. Introduction (en français)	172
V.2. Choice of integrated MD – direct solar heating module and optimal design of recirculation system.....	173
V.2.1. VMD-FPC module materials	175
V.2.2. Operating conditions	177
V.2.3. Collector positions and module dimensions	178
V.3. Seasonal performance of the VMD–FPC based desalination system.....	180
V.4. Dynamic behaviors of the integrated desalination unit	182
V.4.1. Representative daily variations in summer (August 1st)	182
V.4.2. Representative daily variations in winter (February 1st).....	185
V.5. Conclusions (in English).....	186
V.5. Conclusions (en français)	187
General conclusions and perspectives.....	189
Nomenclature	197
Index of figures	203

Index of tables	207
References	209

General introduction

General introduction

The increasing problem of water scarcity is critical. Though our planet earth is covered with liquid water, only 2.5% is freshwater. Moreover, most of the freshwater is inaccessible as it is in the form of ice caps, glaciers or deep underground waters [1]. Only 1.2% of the total freshwater reservoir is surface water, which can be easily used for basic human needs, as well as agricultural and industrial demands after appropriate treatments. According to a recent study in 2016 [2], almost two thirds of the global population (4.0 billion people) suffer from severe water scarcity at least one month in a year, wherein half a billion endure severe water scarcity all year round. Furthermore, a predictive report also in 2016 indicated that these numbers would increase by 40% to 60% by the year of 2050, along with the population growth and economic development [3].

Geographically, arid inland places and some remote coastal areas or isolated islands [4,5] are prone to face the “physical water scarcity” [6] due to limited freshwater resources. For the latter places, the seawater desalination technology could be an alternative pathway to freshwater, given the abundant seawater resource. However, (i) the lack of well commercialized compact desalination facilities for distributed freshwater production adapted to the application in these dispersed communities, (ii) the significant system cost and energy consumption to establish desalination processes, and (iii) the inaccessibility to stable and centralized electricity and heat supply are probably the overwhelming reasons that give rise to another kind of “economic water scarcity” [6]. In order to deal with the critical problem of freshwater provision in these regions, a simple, small-scale, decentralized and even movable desalination system is expected to efficiently fulfill an adequate water productivity of high quality for the drinking need of a family, autonomously without any auxiliary energy source [7]. Under the framework of the common laboratory LabCom MOST [8] associating the LISBP and the company Sunwaterlife, which was created during the thesis, this dissertation aims to develop the knowledge of such a desalination system and to guide its design and operation for a future prototype.

1. Therefore, a first fundamental question is: which desalination technology to apply for remote places?

Generally, a desalination process segregates saline water into a freshwater stream and a concentrated brine stream [9]. Desalination technologies are generally based on two categories of processes, i.e. thermal distillation and membrane separation [10]. Multi-Stage Flash (MSF) and Multi-Effect Distillation (MED) are the earliest generation of desalination technology,

which belong to the category of thermal distillation. The efficient heat reuse between stages (or effects) is already able to cut the energy consumption by about one order of magnitude. However, the multi-stage processes of MSF or MED are not applicable in the case of small and compact system design [11]. The 2nd generation of desalination technology, especially Reverse Osmosis (RO), has witnessed a flourish since 20-30 years ago [12], after huge progresses in fabricating high-flux membranes and the development of energy recovery systems. In 2017, RO is taking up to 65% of the global installed desalination capacity [13]. It avoids the enormous heat demand to heat water up to the boiling point for thermal evaporation and consumes mechanical energy for compression. Besides, the large interfacial area of the membrane makes it possible for a compact design. However, the limited water recovery rate of seawater (only 5% - 15% for household scale, 35% - 50% for larger scale), due to the high sensitivity of osmotic pressure to salt concentration, is one of the main drawbacks of RO. The highest operating pressure of RO is up to 80 bar [12], which corresponds to an osmotic pressure of salt at a concentration below 100 g L^{-1} , limiting the maximal recovery rate and thus inducing the problem of brine disposal and water squander. For instance, half of the pressurized water has to be wasted even at the highest recovery rate (50%) of RO; about 9 m^3 of water has to be rejected to produce only 1 m^3 of potable water if a recovery rate of 10% is assumed for a domestic scale RO, which can potentially cause environmental issues and is not acceptable in areas suffering from water shortage [14].

Finally, 3rd generation of desalination technologies, especially membrane distillation (MD) has emerged to further deal with the above limitations [15]. Possessing characteristics of both thermal distillation and membrane separation, MD has gained its popularity in the domain of brackish or seawater desalination and research interest is continuously growing [15]. Our research group at LISBP has conducted studies on different questions regarding MD since the earlier 90's with the thesis of Nathalie Couffin (2000) [16], David Wirth (2002) [17], Jean-Pierre Méricq (2009) [18], Duong Dao (2013) [19], and Paul Jacob (2018) [20]. In MD, a microporous hydrophobic membrane is used to hold as the physical barrier of the hot feed stream of saline water and the permeate side. Due to the difference in vapor partial pressure between the two sides of the membrane and its hydrophobicity, water evaporates at the membrane pore inlet and gets collected on the other side of the membrane, which behaves as the support for the liquid-water interface and only lets water vapor to pass through its pores. Pure distillate is obtained as a permeate and thus nearly a 100% rejection of salt and other non-volatiles is expected without pressurized process complicating the system operation [21].

General introduction

Furthermore, much higher water recovery rate, even close to the saturation of salt concentration is achievable compared to RO because of no limitation of osmotic pressure [22]. Consequently, the quantity of wasted water can be significantly diminished. Besides, the use of membrane ensures a substantial interfacial area for compact modules, and a working temperature lower than the boiling point. Conclusively, the goal of compactness, simple operation and high production quality can potentially be better accomplished by applying MD technology than other mainstream desalination technologies.

2. Then, the second issue comes up, which specific MD configuration to use?

Four MD configurations have been widely studied in the literature, classified by the type of the permeate side, i.e. Direct Contact MD (DCMD) with low-temperature pure water circulating on the permeate channel where the permeate directly condenses, Air Gap MD (AGMD) with an additional air gap between the membrane and a condenser foil, Vacuum MD (VMD) with a vacuum applied to the permeate side in order to increase the driving force and Sweeping Gas MD (SGMD) with cold inert gas sweeping the distillate in the permeate compartment. Among them, DCMD is the most studied configuration covering nearly half of the literature of MD [13], mainly based on its simplicity in configuration at lab-scale. VMD, which has also received much research attention for the application in desalination mostly because of (i) the controllable driving force by adjusting vacuum pressure, (ii) relatively higher permeate flux compared to other MDs and (iii) the lowest conductive heat loss through the membrane and the lowest mass transfer limitations on permeate side [23].

For an autonomous design, the efficient use of available energy is one of the most important aspect, due to the absence of auxiliary energy resources. Therefore, VMD, who benefits from the lowest heat loss in the process while relatively higher permeate flux, is the preferable choice. Besides, DCMD, who has the simplest configuration, can also be explored to examine the performance, based on the consideration of the operation simplicity and system robustness.

3. Third, what is the energy source to operate the system autonomously?

Fortunately, the relatively low working temperature of MD (below 80°C and even lower in VMD [24]), and the tolerance of fluctuations in operating conditions offer the possibility to equip MD with low-grade renewable energy input [25], such as solar energy, to enhance the

overall thermal energy efficiency. Moreover, the regions that suffer from water scarcity are often exposed to high solar radiation [26]. On the other hand, both thermal utilization and electrical utilization of solar energy are readily available in the market: the former by solar thermal collectors, while the latter by photovoltaic (PV) cells. In conclusion, solar energy is a good candidate as the energy source for the autonomous system, which can provide both heat and electricity by existing technologies.

4. The last question before starting the study is: how to provide solar energy to MD process?

In a previous work in our group, it was proposed in a synthetic way in Figure 1 to represent almost all the coupled MD - solar energy system configurations [27].

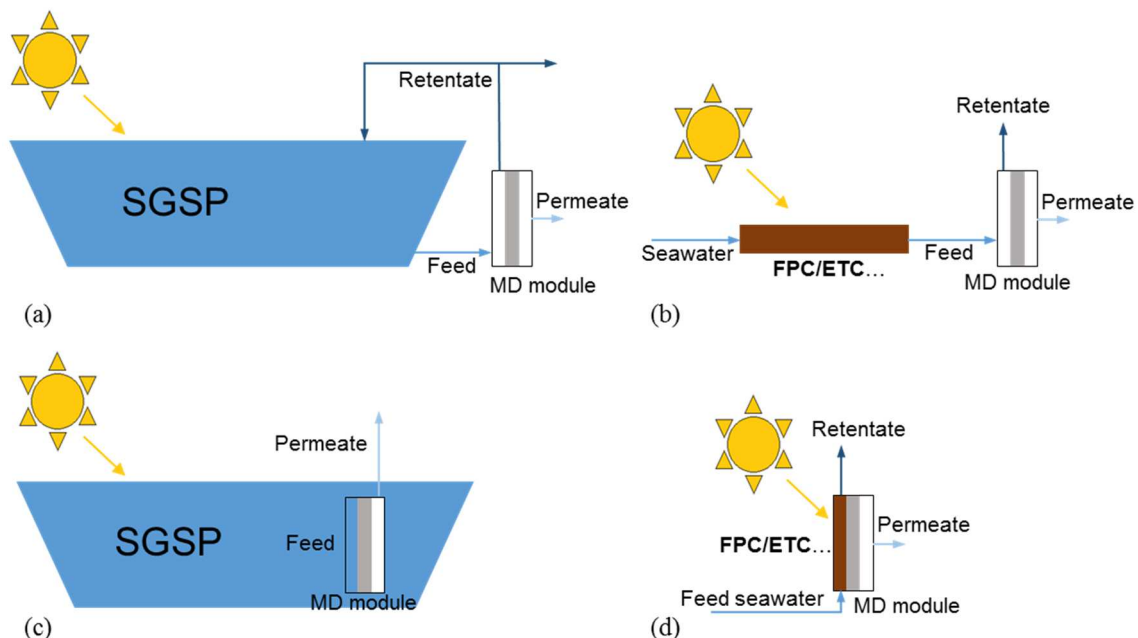


Figure 1: System configurations coupling MD and SC (adapted from Méricq et al. [27])

The upper two configurations have been more studied: (a) feed seawater preheated and fed by a Salinity Gradient Solar Pond (SGSP); (b) feed seawater preheated and fed by Flat-Plate Collectors (FPC) or Evacuated-Tube Collectors (ETC) before being led into MD modules. Moreover, some integrated configurations by combining MD and solar collector (SC) directly into one equipment have been also witnessed, which tackle the issue of heat loss and pressure loss due to piping and connections. The lower two figures in Figure 1 depict the general idea of this integration [27]: (c) MD module directly submerged in an SGSP, where saline water works

General introduction

as the feed; (d) feed seawater directly heated by solar irradiance on the membrane surface inside FPCs or ETCs. They have been relatively less seen, probably because of more difficulty in the study by either experimental or modeling approaches.

Regarding the goal of the expected system, the integrated systems clearly prevails, based on its low thermal loss to efficiently use solar energy, simple configuration to operate, and intensified process for the compact design of the small-scale equipment. Then, SGSP can be eliminated from the choice due to its low solar absorbing efficiency (15 - 25%) and its large applied scale [28]. Consequently, the conception in Figure 1d would be the best system configuration for the current application. However, the proof of this concept and its feasibility for the target application is still to establish and more comprehensive design for this kind of equipment is to yet be proposed.

Thesis objectives

The present manuscript focuses mainly on the design and understanding of a directly-integrated solar-driven MD system targeting the self-supply of drinking water provision for small communities in remote coastal areas or isolated islands. The scientific objectives of the thesis can be summarized as follows:

The first objective consists of a generic design of a hybrid module involving VMD and solar collector in the same integrated equipment and a comprehensive modeling at the scale of the module and at the scale of the whole recirculation system. The feed saline water is recirculated in the system in order not to lose the stored solar energy. Besides, an explicit solar calculation model is necessary to dynamically evaluate the performance and to be easily altered to real solar conditions. Therefore, the modeling is two-folded: the former includes heat and mass transfer inside the hybrid VMD-solar collector module with a detailed modeling of solar energy absorption and utilization using sun-earth geometries, location data, collector properties, etc., while the latter is mainly the dynamic modeling of the recirculation system to illustrate the dynamics throughout a daily operation.

The second objective is the evaluation and analysis of the hybrid VMD-SC system and comparisons with a similar system with a hybrid module using another MD configuration: DCMD. It contains all-day simulations to evaluate the water production and energy consumption, and analysis on the impact of different design and operating parameters to locate

the key factors that determines or restrains the system performance. The comparisons with DCMD would allow a better view of the advantages and disadvantages of applying VMD in a hybrid collector when the same surface area is set for both the solar collector and the membrane module. This study would also allow to explore and compare the potentials of both VMD and DCMD in the hybridization with direct solar heating.

The third objective relates to improving the design and integration of energy-efficient heat recovery devices, i.e. to handle the technological barriers of a coupled solar-powered VMD system. The design and modelling of a VMD-solar module with integrated heat recovery strategy from permeate condensation by heat pump along with effective vapor cooling will be studied. At this level, the aim is to significantly improve energy use and efficiency and to evaluate the influence of production scale on the performance. Optimization and sensitivity analysis studies will then be applied to provide guidelines on design and optimal operating conditions.

Finally, the main indications and conclusions of the analysis and the previous optimizations should lead to the design of an optimal VMD-solar prototype with integrated heat recovery system.

Thesis organization

An extended literature review is presented in Chapter I. The general concept, the advantages, the different configurations and the module design of membrane distillation technology are introduced, followed by the heat and mass transfer mechanisms of the two MD configurations that will be discussed in this dissertation. Moreover, the effort of coupling solar energy to MD systems is comprehensively reviewed and discussed, in order to summarize the literature and to stress on the interest of this study.

In Chapter II, an attempt of coupling a solar flat-plate collector and a flat-sheet vacuum membrane distillation (VMD-FPC) within the same module with similar contact area is made, resulting in a small-scale distributed desalination facility. It consists of the design and modeling of the module with coupled solar energy, dynamic simulations of a recirculation system designed for the module, discussions on the system performance, and analyses on the impacts of several parameters to understand the main drivers and limitations.

General introduction

In order to evaluate the efficiency of VMD when compared to a similar MD-based technology in terms of productivity, energy consumption and hybridization potential with solar energy, a similar FPC is coupled with a flat-sheet DCMD in Chapter III and the obtained DCMD-FPC module is compared with the VMD-FPC module previously introduced in Chapter II. The general conditions applied to both systems are almost the same, for the simulations to be comparative. Furthermore, analyses are conducted on the system potential performance and the influences of parameters for both MD configurations.

Based on the observations made in the first chapters, an original design attempt of equipping the VMD-FPC system with an intensified heat pump is discussed in Chapter IV. The aim in this regard is to simultaneously provide an effective permeate condensation and realize a feasible heat recovery strategy from the permeate condensation, in order to markedly enhance the energy efficiency of the integrated system. Specifically, a heat pump is conceived and coupled with the feed recirculation system and the permeate condensation. All energy-taking aspects of the process including also the cooling demand for the permeate condensation are considered and discussed clearly. Sensitivity analysis and multi-objective optimization are performed in this chapter to guide the design within a multi-criteria context and to indicate the optimal operating conditions for the desired level of production.

Following the study in the previous chapters, finally in the last chapter, a practical recommendation of a small-scale MD-FPC system is discussed in detail under real-world conditions in order to guide the design and fabrication of a future prototype in the laboratory. Its daily operations in both summer and winter is further evaluated, and information on the required capacity of photovoltaic panels, operating parameters and dynamic performance indicators is then provided.

I. Background of membrane distillation (MD) and state-of-the-art of coupling MD with solar energy

I.1. Membrane distillation

Membrane distillation (MD) derives from membrane contactors, which provide non-dispersive contact via microporous membranes with substantial interfacial area for gas/liquid or liquid/liquid contacting operations [29]. For separation processes like absorption, liquid-liquid extraction and distillation, membrane contactors promisingly offer a significant process intensification, as compared to conventional approaches conducted in towers, columns or mixer-settlers [30]. As a specific application of membrane contactors, by definition, MD is a process based on the evaporation of a liquid provoked by a difference in partial pressure between the two sides of a membrane that is used as a support for the liquid/vapor interface, as illustrated in Figure I.1. Water evaporation and transfer through the membrane are driven by the difference between the elevated vapor partial pressure at the membrane surface on the hot feed side, and the relatively lower vapor partial pressure created on the permeate side.

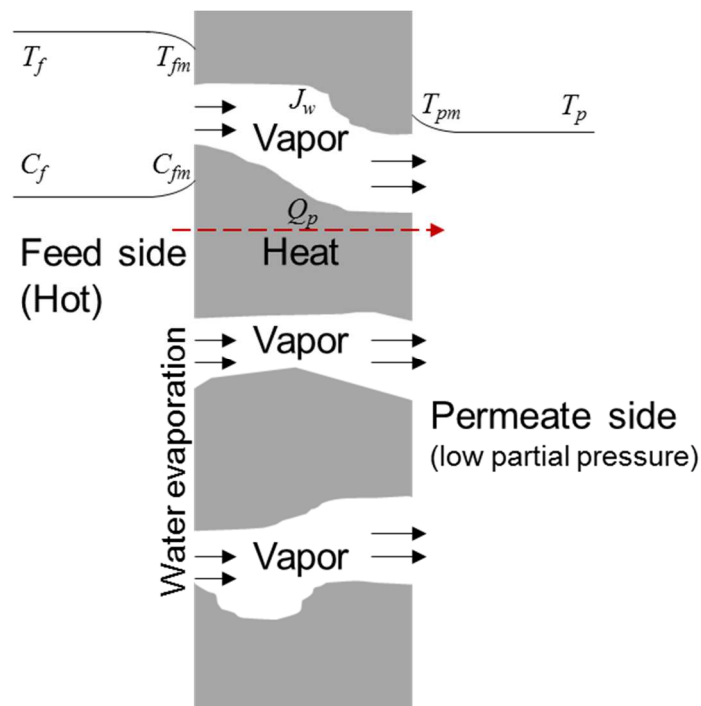


Figure I.1: Schematic of the MD process

In order to generate this driving force, the temperature of the feed stream T_f is typically heated to $30^\circ\text{C} \sim 80^\circ\text{C}$. However, the feed temperature at membrane surface T_{fm} , which actually induces the transmembrane vapor pressure difference, might be lower than T_f due to boundary layer effect when MD is under operation with a certain level of permeate flux. Same occasion may also exist on the permeate side, where the temperature at membrane surface T_{pm} is higher than that in permeate bulk T_p . Consequently, the driving force might be lowered on account of

this temperature polarization phenomenon in MD [31,32], whose significance depends on the operating conditions (membrane material, feed flow, spacers, operating conditions, etc.). Similarly, the feed salt concentration at the membrane surface C_{fm} is higher than the salt concentration at feed bulk C_f , as shown in Figure I.1, inducing the concentration polarization [33]. However, MD has been proven not so sensitive to feed salinity [34], based on its thermal-driven process, in contrast to the widely-applied desalination technology of Reverse Osmosis (RO), which largely depends on the osmotic pressure. Description of temperature and concentration polarization equations will be introduced in the part of this chapter dedicated to heat and mass transfer.

The liquid/vapor interface is often supposed to be located close to the pore inlet. The process requires the use of microporous hydrophobic membranes, whose properties are crucial to ensure a good and sustainable quality of the produced water. Membranes should be porous enough to allow for a good productivity, but a compromise between pore size and hydrophobicity is required to avoid direct liquid transfer by convection through the pores (this phenomenon is called pore wetting [35]) and to only allow vapor passing through the pores to the other side (permeate side) after the evaporation. If no membrane wetting or other failure occurs, theoretically complete rejection of salt and other non-volatiles can be presumed [21]. For that purpose, membranes used for MD commonly have an average pore size from 100nm to 1 μ m [21,31], and are made of polytetrafluoroethylene (PTFE), polyvinylidene fluoride (PVDF) or polypropylene (PP). Along with the water vapor flux J_w through the pores, the heat flux Q_p passes through both the solid membrane material and the pores of the membrane (Figure I.1). Heat transfer is described in more detail in Section I.2.1 of this chapter.

Historically, the concept of MD was firstly patented by Bodell in 1963 as a new approach for producing clean water via evaporation across silicone rubber membranes [36]. Four years later [37], Finley published the very first scientific paper, specifying the MD process in detail and introducing some experimental results. However, an increasing interest for MD developed in the 1980s when highly permeable membranes for MD became available in the market [21]. In the year of 1986, a “Workshop on Membrane Distillation” was held in Rome, Italy, whose major topic was to standardize the terminology for MD process [38], confirming the sprouting research interest in MD. Consequently, a steady increment of the quantity of publications on MD had been witnessed from 1990 to 2010, being described as the “emerging phase” [39]. Finally, based on this research activity, the industrial interest for MD has become significant

when it was demonstrated as a process that could be complementary with reverse osmosis and/or coupled with solar energy or waste heat [22,40,27]. Since then, attempts to upscale both modules and systems have appeared, mainly with a focus for MD's application in the huge developing sector of desalination and for some niche markets. First industrial scale modules have been made and commercialized, tested on site in different places, and some first plants based on MD have been built.

I.1.1. Membrane distillation applied to desalination

In terms of desalination, generally two categories of technology coexist in the global market, i.e. thermal distillation and membrane separation [9]. Within the former, Multi-Stage Flash (MSF) and Multi-Effect Distillation (MED) are the two most applied desalination technologies, which occupy about 21% and 7% of the total capacity of desalination plants according to [13] in 2017. In order to initialize the evaporation, the heating of saline water up to its boiling point at a certain vacuum pressure is needed at the first stage (or effect) in both MSF and MED [41]. Then, the latent heat of condensation is successively reused in the following stages (or effects), where operating temperature and pressure are decreased progressively. Thanks to the heat recovery, the specific thermal energy consumptions (STEC) of MSF and MED per cubic meter of water production are able to be one order of magnitude lower than the latent heat of evaporation of 667 kWh m^{-3} [42], being $53 \sim 78 \text{ kWh m}^{-3}$ and $40 \sim 64 \text{ kWh m}^{-3}$ [13], respectively.

The latter category of membrane separation has flourished since the 60's after the development of the first Reverse Osmosis (RO) membranes and of the adapted process for their use in desalination. Since 2001, the total annual volume of desalinated water produced by RO became higher than that of all thermal plants. Up to the year of 2017, RO takes up to 65% of the total capacity of all kinds of desalination plants, dominating the global market [13]. The growth of RO technology for desalination has been boosted by huge research efforts on developing RO membranes with a good salt retention and a high permeability to water at the same time, and on efficient technical equipment to recover the energy from brines [14]. RO is a barometric process, which means that the driving force is obtained by a pressure difference across a semi-permeable membrane. The applied pressure should be higher than the osmotic pressure of the feed saline water, which linearly depends on its salinity. The requirements for the RO membrane include a high permeability for water, while an extremely low permeability for dissolved salts [43]. Additionally, a physical strength of the membrane is demanded as well, in order to withstand

the fairly high pressure applied on the feed side, which ranges from 55 bar to 80 bars for seawater desalination [12].

MD represents a growing interest in the field of brackish or sea water desalination and significant perspectives are rising [15], which has some characteristics and advantages of both technology categories. The intensified process (module compactness) and the applicability to small-scale systems are the major strengths over the conventional distillations of MSF and MED, added by the relatively lower operating temperature, based on its large interfacial area and feed temperature far below saturation. On the other hand, MD is a non-pressurized process and can replace or be complementary to RO because of its insensitivity to osmotic pressure, which makes possible: (i) to treat some high-salinity feed that cannot be treated by RO and (ii) to push the concentration ratio (and the water recovery rate) to a higher level, while still producing significant fluxes of pure water. In fact, MD can be even applied to the extraction of freshwater from RO brines and to the over-concentration of RO brines [22,40], as discussed in the General Introduction. Additionally, the fact that MD is a thermal process enables the coupling with waste heat and solar energy, and some alternate systems to anticipate the energy transition for fresh water production. Therefore, reduction of water squander and of brine volume without pressurization, as well as possible coupling with thermal solar energy are the major strengths of MD over RO.

I.1.2. Configurations of MD

In the literature, four main MD configurations have been identified and widely studied. They are categorized by the different ways of creating a low partial pressure on the permeate side, i.e. Direct Contact MD (DCMD), Air Gap MD (AGMD), Vacuum MD (VMD) and Sweeping Gas MD (SGMD) [44], as illustrated in Figure I.2. The feed side of all four configurations resembles the hot side of a heat exchanger, as the feed solution is a relatively hot stream that circulates inside one of the compartments of the MD module.

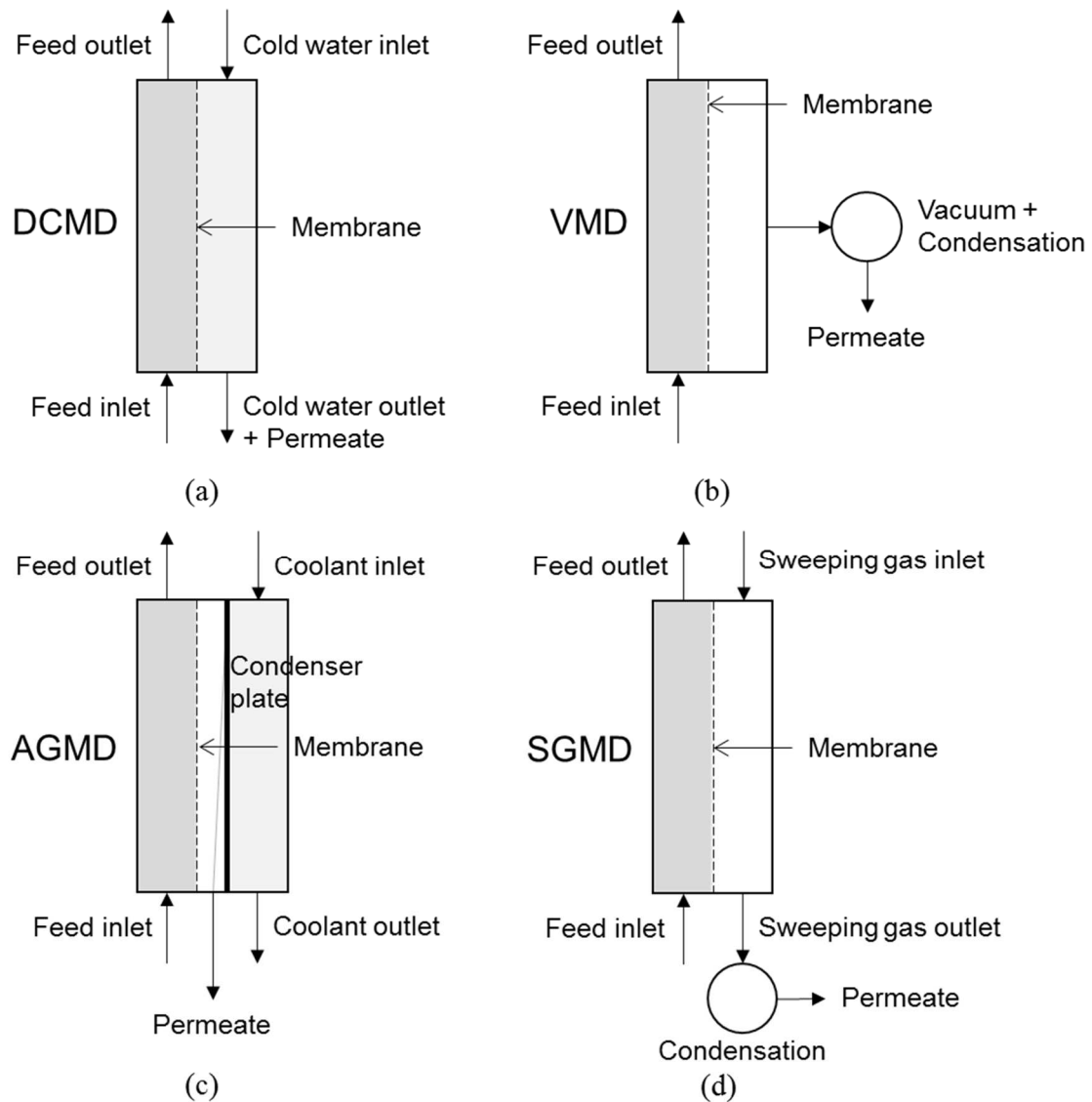


Figure I.2: Basic configurations of membrane distillation: (a) DCMD; (b) VMD; (c) AGMD; (d) SGMD

In DCMD (Figure I.2a), the cold fresh water is in direct contact with the membrane surface on the permeate side, and often in counter-current flow with the hot feed stream. The vapor migrates across the hydrophobic membrane due to the water vapor pressure gradient formed by the temperature difference between the two sides, and then condenses in the cold stream as the permeate production. In this process, the membrane has to support two liquid-vapor interfaces and the vapor only exists inside the pores. It is the simplest type of MD in both the configuration and the operation at lab-scale [39], which gives rise to its popularity. Additionally, heat recovery is possible by preheating the feed with the stream coming out of the permeate side [45]. However, the major drawback is the limited permeate flux due to the strong temperature

polarization phenomenon, which decreases the transmembrane driving force created by the temperature difference between the two sides of the membrane. Moreover, the conductive heat loss is also obvious due to the direct contact of the feed solution, the membrane and the cold distillate water, lowering the thermal efficiency of the DCMD process. Besides, an initial fresh water stream is needed on the permeate side to start the operation, whose temperature has to be maintained low to keep the transmembrane driving force while the permeate flux brings in the enormous latent heat of condensation.

In VMD (Figure I.2b), the permeate side is submitted to an adjustable vacuum at a pressure lower than the vapor saturation pressure on the feed side. A vacuum pump is usually applied to remove the produced vapor and to maintain the vacuum on the permeate side, which allows the vapor to be condensed outside the module to collect the final production. Vacuum pump allows a good control of the driving force and higher permeate flux is expected in VMD process compared to other MD configurations [23], added by the advantage of negligible conductive heat loss through the membrane, and very low thermal polarization on the permeate side [46,47]. Nevertheless, extra condensation facility is needed, reducing the system compactness. Besides, electrical energy consumption is increased by the addition of vacuum pump, though it can be controlled by finding a compromise between the pumping energy and the productivity [17]. As a derivative, a combination of VMD and MED has been successfully developed and commercialized by Memsys [48], being the Vacuum Multi-Effect-Membrane-Distillation (V-MEMD) module.

In order to reduce the conductive heat loss through the membrane, AGMD differentiates from DCMD by applying a stagnant air gap on the permeate side (Figure I.2c). The permeated vapor has to pass through both the membrane and the air gap, and finally condense on a cold surface located inside the module. Consequently, the conductive thermal resistance in AGMD is enhanced and the heat loss is therefore much alleviated compared with DCMD. However, the trade-offs here are a more complex module design and a simultaneously strengthened transfer resistance through the membrane [49], which results in a comparatively lower permeate flux. Another advantage of AGMD lies in the convenient heat recovery by simultaneously condensing the permeate vapor and preheating the feed, when using the feed source to cool the cold condenser surface. Some innovative design based on AGMD has emerged in recent years, such as Permeate Gap MD (PGMD) and Material Gap MD (MGMD), altering the composition of the air gap. The former directly replaces the air in the gap with stagnant permeate [50,51],

yielding higher permeate flux but more heat loss compared to conventional AGMD. The latter diversifies into using either non-conductive material [52] (such as sand or even vacuum in Vacuum Gap MD [50]) or conductive material [51] (such as metal mesh) to fill the gap.

SGMD (Figure I.2d) adopts a blowing cold inert gas on the permeate side, sweeping the water vapor outside of the module and reducing the heat loss. Therefore, mass transfer is enhanced due to the moving gas rather than the stagnant air, and it shares the merit of low conductive heat loss with AGMD. Similarly to VMD, an external condenser is required to collect the distillate from the blowing gas. However, the permeate flux is comparatively lower, and even larger condenser is required due to the big volumetric flow rate of the gas and vapor, adding to the design complexity and system cost [39].

Conclusively, some major strengths and drawbacks of different MD configurations can be summarized in Table I.1 below.

Table I.1: Advantages and disadvantages of different MD configurations [15,53]

Configuration	Advantages	Disadvantages
DCMD	Simple structure	Low permeate flux
	Easy operation at lab-scale	High conductive heat loss
	Possible internal heat recovery	High temperature polarization
		Risk of wetting on 2 membrane sides
VMD	High and controllable permeate flux	Vacuum pump required
	Very low conductive heat loss	External condenser required
	Very low temperature polarization	
AGMD	Low conductive heat loss	Additional transfer resistance by air gap
	Convenient internal heat recovery	More module complexity
		Difficult to control the permeate flux
SGMD	Low conductive heat loss	Large external condenser required
		Sweeping gas might need to be pretreated

As mentioned in the General Introduction, following the previous VMD experimental and simulation study conducted in our team, VMD configuration will be the core of the current study, due to its high and controllable permeate productivity and ignorable conductive heat loss when utilizing solar energy autonomously. Additionally, DCMD will be included in a comparative study as well (Chapter III), mainly due to its simplicity in configuration.

I.1.3. Configurations of MD modules

Compared to the research on energy efficiency, fouling, wetting and new membrane development, studies on MD module design has been less witnessed [54]. Generally, three different configurations have been widely studied in the literature: plate and frame, tubular and spiral wound modules, as shown in Figure I.3.

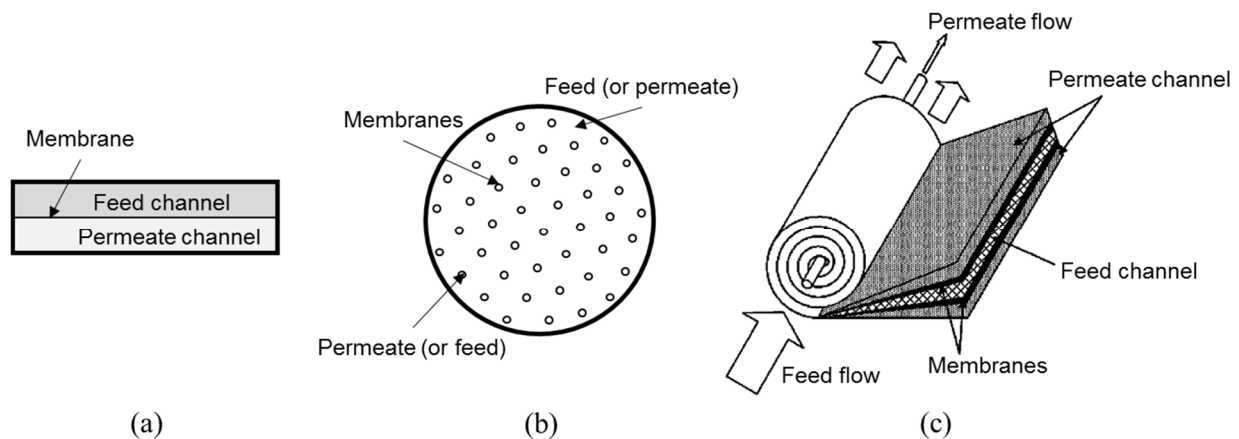


Figure I.3: Configurations of MD modules: (a) plate and frame; (b) tubular; (c) spiral wound (from [55])

Plate and frame modules with flat-sheet membranes are often considered to be the simplest to fabricate, assemble and operate at lab-scale, which are applicable for all four MD configurations [56]. Moreover, membranes can be replaced easily as a consumable. Industrially plat and frame modules have also been seen, all adopting PTFE membranes. The novel concept of merging VMD with MED was applied to the Memsys module [48], which was then installed in the pilot plant Aquaver WTS-40A with a total membrane area of 5.76 m^2 [57], resulting in an STEC of $200 - 400 \text{ kWh m}^{-3}$ and a specific electrical energy consumption (SEEC) of $18 - 20 \text{ kWh m}^{-3}$. Memsys modules of 11-frame-stage and 17-frame-stage have been utilized, with a total membrane area of 1.25 m^2 and 2.5 m^2 , respectively. Also arranged in multi-stage, the Scarab AGMD module, whose configuration is depicted in Figure I.4, contains 10 plastic cassettes with two flat-sheet membranes in each one, yielding a total effective membrane area of 2.8 m^2 [57]. 10 Scarab modules were assembled in five cascades in the pilot plant constructed by Xzero [58], yielding a capacity of daily water production of $0.22 - 0.73 \text{ m}^3$ and a specific heat demand of 700 kWh m^{-3} . Despite the interest in both research and industry, compared to tubular modules, the effective membrane area per unit volume of the module is lower ($400 - 800 \text{ m}^2 \text{ m}^{-3}$ [59])

compared with other module configurations, and spacers are needed to support the membrane and to keep the flow channel in a constant shape.

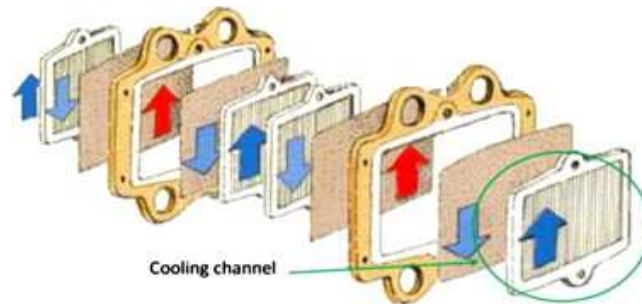


Figure I.4: Scheme of Scarab AGMD module with two adjacent cassettes (shown in yellow) with their corresponding membranes and condensing walls (from [57])

Tubular modules, as presented in Figure I.3b, contain hollow fiber membranes and can be used for DCMD, VMD and SGMD [60]. This configuration resembles a shell-and-tube heat exchanger, and both the shell side and the tube side, or the lumen side, are able to function as the feed side of MD with the other side receiving the permeated vapor. It has been experimentally proven that the inside/out configuration (the feed flows in the lumen side) could result in a higher permeate flux [34]. The effective membrane area of tubular modules with hollow fiber membranes can be much higher per unit volume of module ($2000 - 5000 \text{ m}^2 \text{ m}^{-3}$ [59]) to allow for a smaller footprint. However, the module configuration is more complex than plate and frame modules, and replacing some of the membrane fibers in an operating module can be problematic. Moreover, the permeate flux is reported to be lower than MD modules with flat-sheet membranes [61,62]. Consequently, few industrial applications have been established. A very large scale demonstration plant adopting the tubular modules with PVDF hollow fiber membranes is under operation in South Korea, which has a daily production capacity by DCMD of 400 m^3 [63].

Lastly, the spiral wound module consists of several membrane sheets with spacers keeping them separated. All these sheets are wrapped up around a permeate collection tube in the center, similar to RO membrane modules [55]. According to [59], only AGMD or its alternative, PGMD, has been employed in this module configuration, and an intermediate effective membrane area per unit volume of $800 - 1200 \text{ m}^2 \text{ m}^{-3}$ can be obtained. The pressure drop during the flow is minimized by this configuration, and heat recovery within the module is accessible, reducing heat consumption. However, the fouling tendency remains a problem [59], and such

modules cannot simply be hydraulically cleaned to remove fouling. The Fraunhofer ISE (Institute for Solar Energy Systems) has contributed the most to the research, development and commercialization of spiral wound modules since 2001 [64]. Its spin-off company, Solar Spring, manufactured a PGMD spiral wound module with a total PTFE membrane area of 10 m^2 , and the corresponding system Oryx 150 exhibited a minimum STEC of 210 kWh m^{-3} [57]. Besides, an Aquastill module consists of up to 24 m^2 of membrane made of a special kind of polyethylene (PE) in AGMD configuration [65]. A most recent experimental study on this module revealed a permeate flux in the range of $1.35 - 4.20 \text{ L h}^{-1} \text{ m}^{-2}$, and a STEC in the range of $107 - 296 \text{ kWh m}^{-3}$ could be achieved at a feed temperature of 80°C and a condensing temperature of 20°C [66].

In the current thesis, direction integration of MD modules and solar heating is considered, as discussed in General introduction and will be further introduced in Section I.3.3. As a first attempt, an integrated module based on the plate and frame configuration will be studied in Chapter II, due to its simplicity and relatively large solar absorbing area if no solar concentrator included.

I.2. Transfer mechanisms of MD

Heat and mass transfers happen simultaneously in a MD separation process. Theoretical approaches to describe and model these transfer mechanisms have been important to understand and to analyze the behavior and the performance of MD systems [46]. The widely accepted transfer mechanisms in VMD and DCMD are discussed in this section, assuming normal MD operations without wetting, scaling or fouling that limits or disturbs the process, and a complete salt rejection without liquid or salt entering membrane pores. Consequently, the water evaporation is considered taking place at the membrane surface on the feed side, and the liquid/vapor interface locates at the pore inlet.

I.2.1. Heat transfer

Regarding the heat transfer, the heat flux is firstly transported from the feed bulk at temperature T_f , through the thermal boundary layer, to the membrane surface at temperature T_{fm} on the feed side. The polarization forms up due to the difference between these two temperatures, as shown in Figure I.1. Then, heat passes through the membrane by the latent heat of evaporation and thermal conduction, reaching the membrane surface at temperature T_{pm} on the permeate side. After that, the heat transfer effect differs at permeate side depending on the MD configuration.

In general, the heat transfer process in MD can be described by the analogy between thermal and electrical resistances [21], as in Figure I.5.

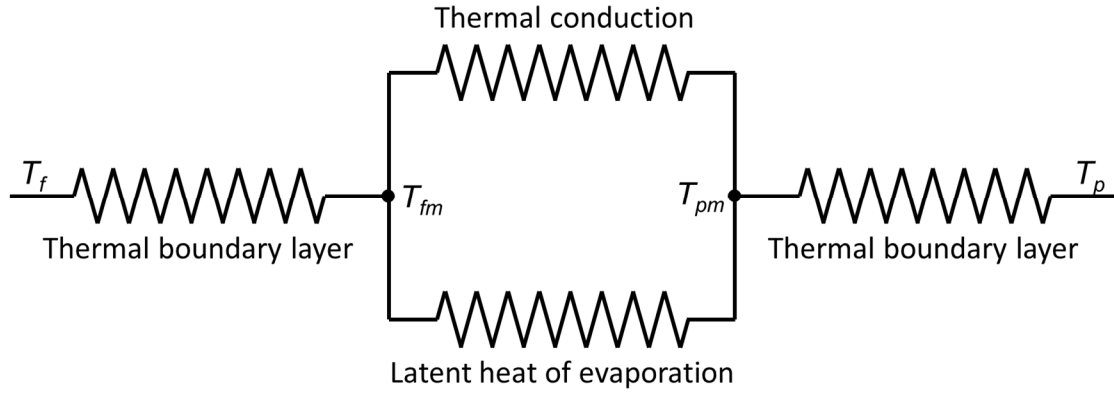


Figure I.5: The arrangement of thermal resistances in MD process

Due to the vacuum environment created on the permeate side, some assumptions can be made on VMD: the heat transfer in the boundary layer on the permeate side (from T_{pm} to T_p) and the heat loss by thermal conduction can be neglected [53,67,68]. Consequently, the total heat flux through the membrane Q_p (W m^{-2}) is formulated below, considering a balance between the amount of heat from the feed bulk to the membrane surface $h_f(T_f - T_{fm})$, and the amount taken away by the latent heat of the permeate flux $J_w \Delta H_v$.

$$Q_p = h_f(T_f - T_{fm}) = J_w \Delta H_v \quad (1)$$

where J_w is the transmembrane permeate flux ($\text{kg m}^{-2} \text{s}^{-1}$), ΔH_v the latent heat of water evaporation (J kg^{-1}), and h_f the heat transfer coefficient ($\text{W m}^{-2} \text{°C}^{-1}$).

In DCMD, on the other hand, all resistances showed in Figure I.5 define the heat transfer process altogether. Thus, the total heat flux through the membrane Q_p is expressed in Eq. 2 [69], consisting of both the thermal energy for water evaporation $J_w \Delta H_v$ and the term for thermal conduction $k_t / \delta_m (T_{fm} - T_{pm})$.

$$Q_p = J_w \Delta H_v + \frac{k_t}{\delta_m} (T_{fm} - T_{pm}) \quad (2)$$

where δ_m is the membrane thickness (m), k_t the thermal conductivity of the membrane layer ($\text{W m}^{-1} \text{ }^\circ\text{C}^{-1}$), which can be predicted via three models, i.e. the Isostrain or parallel model in Eq. 3 [70], the Isostress or series model in Eq. 4 [71], or the flux law model in Eq. 5 [72], all including both the gas inside the pores and the membrane polymer.

$$k_t = \varepsilon k_g + (1 - \varepsilon)k_s \quad (3)$$

$$k_t = \left[\frac{\varepsilon}{k_g} + \frac{(1 - \varepsilon)}{k_s} \right]^{-1} \quad (4)$$

$$k_t = k_g \left[\frac{1 + (1 - \varepsilon)\beta_{s-g}}{1 - (1 - \varepsilon)\beta_{s-g}} \right] \quad (5)$$

$$\text{where } \beta_{s-g} = \frac{k_s/k_g - 1}{k_s/k_g + 2}$$

Besides, the total heat flux Q_p is also transported through the boundary layers on both the feed and the permeate side [73], which gives us the following,

$$Q_p = h_f(T_f - T_{fm}) = h_p(T_{pm} - T_p) \quad (6)$$

where h_f and h_p are the heat transfer coefficients ($\text{W m}^{-2} \text{ }^\circ\text{C}^{-1}$) from the feed bulk to the membrane surface, and from the membrane surface on the permeate side to the permeate bulk, respectively.

A large amount of heat transfer correlations that correlate Nusselt number Nu with Reynolds number Re and Prandtl number Pr can be utilized to estimate the coefficients h_f in both VMD and DCMD, and h_p in DCMD. The definition of dimensionless numbers Nu, Re and Pr is presented in Eq. 7 [74]. Some of the popular correlations are listed in Table I.2.

$$\text{Nu} = \frac{hd_h}{\lambda} \quad \text{Re} = \frac{\rho v d_h}{\mu} \quad \text{Pr} = \frac{\mu c_p}{\lambda} \quad (7)$$

where d_h , λ , μ , c_p , ρ , v are hydraulic diameter (m) of the flow channel, thermal conductivity ($\text{W m}^{-1} \text{ }^\circ\text{C}^{-1}$), dynamic viscosity ($\text{kg m}^{-1} \text{ s}^{-1}$), specific heat capacity ($\text{J kg}^{-1} \text{ }^\circ\text{C}^{-1}$), density (kg L^{-1}) and linear velocity (m s^{-1}) of the fluid, respectively. The heat transfer coefficient h can thus be obtained upon the calculation of Nu.

Table I.2: Some correlations for the calculation of heat transfer coefficients

Flow regime	Correlation	Notes	Ref.
Laminar	$Nu = 1.86 \left(\frac{RePr}{L/d_h} \right)^{\frac{1}{3}} \left(\frac{\mu_f}{\mu_{fm}} \right)^{0.14}$	Re < 2100	[75]
	$Nu = 1.86 Re^{0.96} Pr^{\frac{1}{3}} \left(\frac{d_h}{L} \right)^{\frac{1}{3}}$	Re < 2300; 0.6 < Pr < 5	[76]
	$Nu = 0.097 Re^{0.73} Pr^{0.13}$	1000 < Re < 2100	[77]
	$Nu = 0.298 Re^{0.646} Pr^{0.316}$	150 < Re < 3500	[78]
	$Nu = 4.36 + \frac{0.036 Re Pr \left(\frac{d_h}{L} \right)}{1 + 0.0011 \left(Re Pr \frac{d_h}{L} \right)^{0.8}}$	100 < Re Pr d/L < 1500 For constant heat flux	[70]
	$Nu = 3.66 + \frac{0.0668 Re Pr \left(\frac{d_h}{L} \right)}{1 + 0.045 \left(Re Pr \frac{d_h}{L} \right)^{2/3}}$	100 < Re Pr d/L < 1500 For constant wall temperature	[79]
Transitional	$Nu = 0.116 \left(Re^{\frac{2}{3}} - 125 \right) Pr^{\frac{1}{3}} \left[1 + \left(d_h/L \right)^{\frac{2}{3}} \right]$	2100 < Re < 6000	[80]
Turbulent	$Nu = 0.023 Re^{0.8} Pr^{\frac{1}{3}} \left(\frac{\mu_f}{\mu_{fm}} \right)^{0.14}$	2500 < Re < 1.25×10 ⁵	[21]
	$Nu = 0.023 Re^{0.8} Pr^n$	2500 < Re < 1.25×10 ⁵ n = 0.4 for heating n = 0.3 for cooling	[75]
	$Nu = 0.036 Re^{0.96} Pr^{0.33} \left(\frac{d_h}{L} \right)^{0.055}$	10 < L/d < 400	[76]
	$Nu = \frac{\left(\frac{f}{8} \right) (Re - 1000) Pr}{1 + 12.7 \left(\frac{f}{8} \right)^{\frac{1}{2}} (Pr^{\frac{2}{3}} - 1)} \left[1 + \left(\frac{d_h}{L} \right)^{2/3} \right]$	0.5 < Pr < 200 2300 < Re < 5×10 ⁶ $f = (0.790 \ln Re - 1.64)^{-2}$	[81]

I.2.2. Mass transfer

Similarly to Figure I.5 for the heat transfer, the mass transfer resistances in the MD process can be analogized by electrical resistances [21], as shown in Figure I.6. The mass transfer on the feed side can also be characterized by the concentration boundary layer, from the salt concentration of C_f to a higher value of C_{fm} at membrane surface, as shown in Figure I.1 and Figure I.6. Meanwhile, no concentration profile on the permeate side needs to be considered if MD operates normally without salt penetrating to the permeate.

I.2.2.1 In membrane pores

The pivot of the mass transfer process lies in the vapor diffusion inside the membrane pores, which has been discussed extensively in the literature as a combined effect of Knudsen diffusion,

molecular diffusion, viscous (Poiseuille) flow and surface diffusion [21], known as the famous dusty-gas model. Note that the surface diffusion can be well neglected due to the high hydrophobicity and porosity of the membrane [21], leaving the other three mechanisms inside the pores working together as the mass transfer resistance to the permeate water vapor.

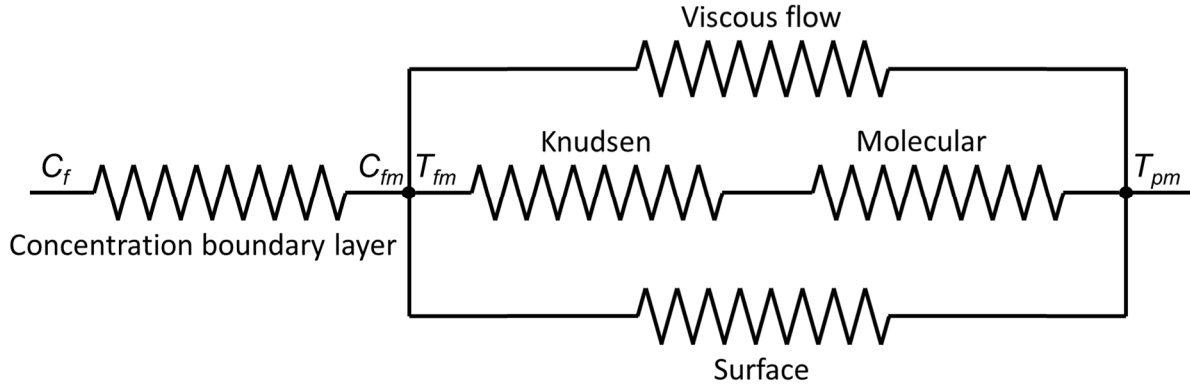


Figure I.6: The arrangement of mass transfer resistances in MD process

Furthermore, more transfer resistances might also be neglected according to the specific situation of a MD process. A dimensionless indicator called Knudsen number (Kn) can inform us the possibility of simplifying the model, defined as [82]

$$\text{Kn} = \frac{l}{2r} \quad (8)$$

where r is the average pore radius (m) and l is the mean free path of the water vapor molecule (m), which is the average traveled distance of the molecules between two collisions, given by [21]

$$l = \frac{k_B T}{\sqrt{2} \pi \bar{P} \sigma^2} \quad (9)$$

where k_B is the Boltzmann constant $1.38 \times 10^{-23} \text{ m}^2 \text{ kg s}^{-2} \text{ K}^{-1}$, T the temperature (in K), σ the collision diameter (water vapor, 2.641 \AA), \bar{P} the mean pressure in membrane pores (Pa).

Collisions between molecules and the pore wall dominate the mass transfer inside the membrane when the pore size is smaller than the vapor mean free path ($\text{Kn} > 1$), which means

the Knudsen diffusion is able to well characterize the vapor transport. Oppositely, when pores are much bigger than the mean free path ($Kn < 0.01$), the molecular diffusion prevails, describing the diffusion of vapor molecules through the stationary air trapped in the pores with a same total pressure level on both sides of the membrane. Therefore, a transitional region with $0.01 < Kn < 1$ is also expected where both diffusion patterns coexist [47,83]. In parallel with these two diffusions, as described in Figure I.6, the viscous flow represents the convective flow driven by the transmembrane pressure gradient, which intervenes when no air existing in the pores and a total pressure difference between the two sides of the membrane presents. It dominates the mass transfer when the pore size is big enough to ignore Knudsen flow ($Kn < 0.01$) [68].

In order to describe the mass transfer inside the pores, Eq. 10 indicates that the water mass flux J_w ($\text{kg m}^{-2} \text{s}^{-1}$) is driven by the vapor pressure difference across the membrane [84],

$$J_w = B_m(P_{fm} - P_{pm}) \quad (10)$$

where B_m represents the overall membrane mass transfer coefficient (s m^{-1}), combining all the diffusion patterns discussed above. P_{fm} and P_{pm} stand for the water partial pressure at the membrane surface on the feed side and the permeate side (Pa), respectively. The former is generated by the feed temperature at membrane surface T_{fm} , and the latter is directly the vacuum pressure P_p in VMD, while in DCMD, P_{pm} is the corresponding saturated pressure of the permeate temperature at membrane surface T_{pm} .

Specifically for VMD, a combined effect of Knudsen diffusion - viscous flow is usually assumed in the description of mass transfer through the membrane [21,85], based on the fact that the mean free path is quite long when vacuum is maintained in membrane pores. Hence, the overall membrane mass transfer coefficient B_m is now composed of B_K for Knudsen diffusion and B_V representing viscous flow, which are calculated as [53],

$$B_K = \frac{2}{3} \frac{\varepsilon r}{\tau \delta_m} \left(\frac{8M_w}{\pi RT_m} \right)^{0.5} \quad (11)$$

$$B_V = \frac{M_w}{8\mu_v} \frac{\varepsilon r^2}{\tau \delta_m} \frac{P}{RT_m} \quad (12)$$

where ε , r , τ , and δ_m are the porosity, the pore radius (m), the tortuosity and the thickness (m) of the membrane, respectively. M_w is the molecular weight of water (kg mol^{-1}), R the gas constant (i.e. $8.314 \text{ J mol}^{-1} \text{ K}^{-1}$), T_m the mean water vapor temperature (K) and P the total pressure inside the pore (Pa), and μ_v the viscosity of the vapor inside the pore (Pa s), which can be calculated from the linearization from the data in [86].

B_m is the sum of these two coefficients,

$$B_m = B_K + B_V \quad (13)$$

It is worth to mention that the viscous flow can be further ignored also because of the rather long mean free path of vapor molecules in vacuum [22], according to Eq. 9, which makes B_K the only dominating effect.

Meanwhile, a combined effect of Knudsen - molecular diffusion is generally assumed to govern the mass transfer through the membrane for the DCMD process [21,87], whereas viscous flow is negligible due to the air existence in the pores and the equal operating pressures on both sides of the membrane. Therefore, B_m can be decomposed into the mass transfer coefficient in Knudsen diffusion B_K and the one in ordinary molecular diffusion B_D , which is calculated as the following [46],

$$B_D = \frac{\varepsilon}{\tau \delta_m} \frac{P D_w}{P_a} \frac{M_w}{R T_m} \quad (14)$$

where P_a is the air partial pressure (Pa) inside the membrane pore, and D_w the water diffusion coefficient ($\text{m}^2 \text{ s}^{-1}$). Then the two mass transfer coefficients are combined in parallel to obtain B_m [45],

$$B_m = (B_K^{-1} + B_D^{-1})^{-1} \quad (15)$$

1.2.2.2 Concentration polarization on the feed side

One the other hand, the profile on the feed side has to be taken into account when modeling the whole MD process, on account that the permeate flux J_w is also determined by the water mass

diffusion from the feed bulk to the membrane surface, which is further decided by the salt concentration polarization [47], yielding

$$J_w = \rho k_m \ln \left(\frac{C_{fm}}{C_f} \right) \quad (16)$$

where k_m is the mass transfer coefficient (m s^{-1}) and C the concentration (g L^{-1}). k_m can also be estimated from the heat transfer correlations listed in Table I.2, simply by replacing Nusselt number Nu and Prandtl number Pr with Sherwood number Sh and Schmidt number Sc [74], respectively. Sh and Sc are defined below in Eq. 17.

$$Sh = \frac{k_m d_h}{D_{s-w}} \quad Sc = \frac{\mu}{\rho D_{s-w}} \quad (17)$$

where D_{s-w} is the diffusion coefficient of the salt in the seawater ($\text{m}^2 \text{s}^{-1}$).

I.2.3. Profiles along the flow direction

The temperatures, flow velocities, pressures (only feed side for VMD, both sides for DCMD) and salt concentration (only feed side) are varying along the flow direction, due to the transmembrane permeate vapor and heat flux along the length of the module. One-dimensional balances can therefore be easily established in connection with J_w and Q_p , which has been the most applied approach when modeling the longitudinal profiles [46], as presented in Eq. 18 - 21 for VMD [46,88].

$$\frac{d(\rho_f c_p v_f T_f)}{dz} = -\frac{Q_p}{\delta_f} \quad (18)$$

$$\frac{d(\rho_f v_f)}{dz} = -\frac{J_w}{\delta_f} \quad (19)$$

$$\frac{dP_f}{dz} = -f \left(\frac{\rho_f v_f^2}{2d_h} \right) \quad (20)$$

$$\frac{d(C_f v_f)}{dz} = 0 \quad (21)$$

where z represents the flow direction, δ_f is the thickness of the feed flow channel (m).

Though being less seen in the literature, two-dimensional modeling of the flow channel has been often accomplished by CFD [89]. The objective of CFD-based studies is mainly the amelioration of the flow channel geometry to improve the heat and mass transfer inside the boundary layer at membrane surface for an existing and designed module, and consequently abate the polarization phenomena on both sides of the membrane.

I.3. State of the art: MD driven by solar energy

As a phase-change process for water treatment, the thermal demand for the latent heat of water evaporation is about 670 kWh m^{-3} , and barely varies with temperature or salinity [42]. Multi-staging could be an effective way to recover the latent heat and reuse it in the following stages, same as the MSF and MED process. This idea has been successfully applied to MD modules, as aforementioned in Section I.1.3, significantly decreasing STEC down to a minimum of a little more than 100 kWh m^{-3} [66]. However, this amount of energy yet needs intensive heat provision, and the multi-staged processes of MSF or MED are not very suitable for small compact system design [11]. Therefore, the energy source for MD operation has become a critical problem.

Traditionally, fossil fuels are still the major energy resource, taking up about 70% of the global energy consumption [90]. However, serious environmental issues occur with the exploitation, transportation and consumption of fossil fuels, such as global warming and air pollution [91]. Furthermore, the depletion of resources and the increasing global demand add to the energy price and the necessity of an alternative. The replacement by renewable energy sources, such as solar energy, geothermal energy, wind energy etc., are potentially capable of exempting us from the above environmental issues cause by fossil fuels. Besides, the replenishing nature of renewable energy can help alleviate the energy crisis and lower the energy cost [92]. Among all kinds of renewable energy, solar energy stands out as one of the most promising choice [93]. Quantitatively, the annual solar radiation that reaches the earth accounts for ten times the amount of all non-renewable energy resources, though the radiation intensity varies all day. Moreover, solar energy can be diversely utilized as heat, electricity and light, which gives it versatility to power different systems [94]. Indeed, solar energy has been applied since ancient time and is widely adopted to various domains, such as industrial and domestic water heating, product drying, space heating, cooling and refrigeration, power generation. Among all these applications, the most common way to capture and thermally utilize solar energy is by Solar

Water Heating (SWH) using solar thermal collectors, especially at a temperature lower than the boiling point [95]. In addition, solar energy can also be directly converted into electrical energy by photovoltaic technology, though still not yet fully cost-competitive with conventional power generation [96].

Based on the above characteristics and applications of solar energy, links could be therefore connected with the energy consumption MD as a thermal-based process, whose operating temperature is relatively low in all types (temperatures usually below 80°C and even lower in VMD [24]), and that fluctuations in operating temperature can be well tolerated. Conclusively, one should consider the possibility of providing the heat demand of MD operation with low temperature SWH system [97]. Moreover, arid regions are often with abundant solar energy resources. Hence, considerable efforts have been made for the coupling of solar energy facilities with MD systems, applying SWH via solar thermal collectors to heat up and maintain the temperature of the feed.

As another important access of solar energy exploitation, photovoltaic (PV) cells, especially crystalline silicon ones, have already been commercialized and are readily available as electricity generators for varying devices, including the components in MD systems (pumps, sensors and etc.), as well practiced in the literature [98–111]. On the other hand, the way that solar thermal collectors are connected to MD systems is more flexible and worth more study, because MD is a thermal process where heat source plays an essential role, and thermal consumption takes up the major part of the total energy consumption [27].

In the following we will successively introduce the common types of solar thermal collectors (Section I.3.1), the studies conducted on coupling them with MD (Section I.3.2), the studies on the direct integration of solar collectors and MD (Section I.3.3), and the observations on the totality of the previous work on the connection of solar energy and MD (Section I.3.4).

I.3.1. Solar thermal collectors

In a SWH system, solar thermal collectors (SC) are the core devices that absorb the incident solar irradiation and convert it into heat stored in water or other kinds of working medium [112]. The aperture area and the positioning of the collector determines the total amount of the solar energy that can be utilized, while the thermal efficiency defines the actual part of stored heat out of the utilizable incoming solar energy. Due to the sparsity of available solar radiation

intensity (usually below 1000 W m^{-2}), the solar thermal collectors can be further categorized by the existence of a concentrator or not, depending on the target temperature of utilization. High-temperature applications (higher than 100°C) generally include steam generation for power generation or driving a Stirling engine [113], which requires solar concentrators to multiply solar incident energy. Low-temperature applications (lower than 100°C) are more widely installed all around the world, aiming mostly domestic water heating without corresponding solar concentrators. The two categories of solar thermal collectors are introduced as follows.

I.3.1.1. Non-concentrating solar collectors

Almost all non-concentrating solar collectors are mounted in stationary, without sun-tracking system [112], which renders great advantages in system simplicity and robustness. Among different types of solar collectors, Flat-Plate Collectors (FPC) and Evacuated-Tube Collectors (ETC) have already been extensively applied in domestic hot water supply and space heating/drying as a rather well-developed technology [114].

The FPC is relatively the simpler one in configuration and in fabrication. A typical FPC is a well-insulated flat-box with a transparent glass or plastic cover (or the glazing) and a dark-colored absorber-plate with selective coating, as shown in Figure I.7. Flow channels are conductively adhered to or directly integrated with the absorber-plate, transferring the absorbed solar energy from the walls of channels to the working fluid flowing inside, and heating it up to 70°C in common applications. It can directly be the water to be heated or a working medium that will pass the thermal energy to water later through heat exchange.

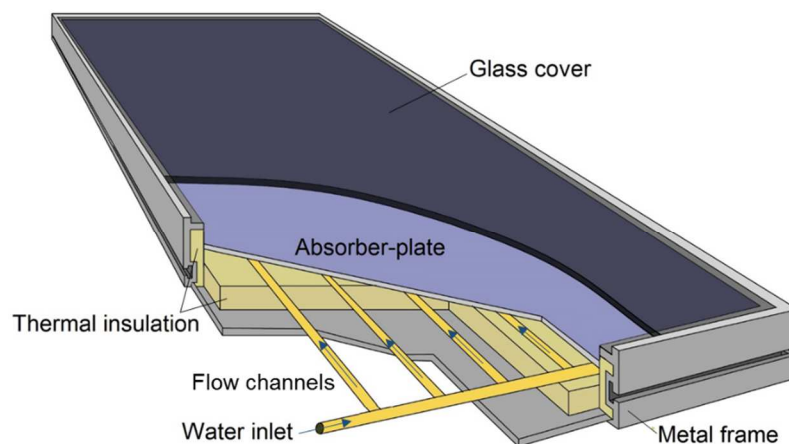


Figure I.7: Configuration of a normal FPC (from [115])

On the other hand, an ETC is capable of reaching higher working temperature than an FPC [116], usually up to 80°C. Generally, two designs of evacuated tubes are utilized in an ETC: water-in-glass type and heat-pipe type [117] (Figure I.8). The former consists of two concentric glass tubes sealed at one end. The surface of the inner tube is coated with selective absorption material and the annular space between the two tubes are evacuated to reduce heat loss. Working fluid, often directly the water to be heated, is in forced or natural flow inside the inner tube. The latter also has an outer glass tube and a vacuum space inside. While instead of an inner glass tube, a metallic tube with fins is sealed together with the outer tube. A working fluid evaporates at the lower end of the metallic tube, then rises up and condenses at the other end, releasing the heat to the water in the storage tank, which is in direct contact. Currently, the water-in-glass evacuated tubes benefit from higher thermal efficiency and lower fabrication costs [116].

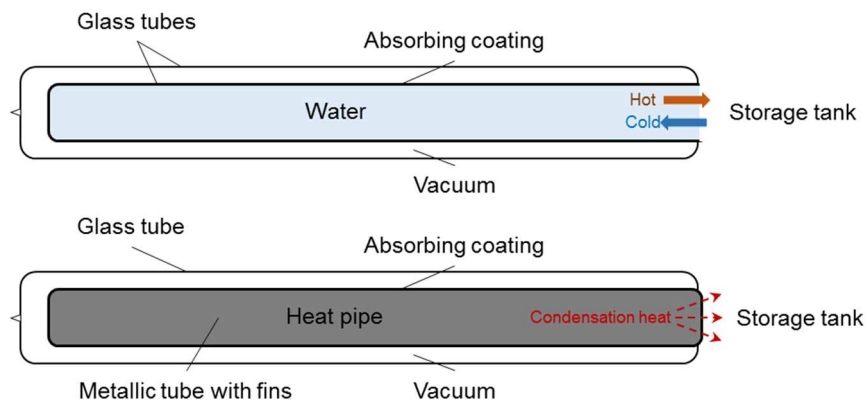


Figure I.8: Configurations of ETCs (from top to bottom): water-in-glass type and heat-pipe type

Adapted for large scale installations and without glazing, a solar pond is an artificially constructed pond where significant temperature rises in its lower region are kept from convection [28]. The most common type of a solar pond is the Salinity-Gradient Solar Pond (SGSP), where a gradient of salt concentration is created along the depth of the pond. The warm brine with the highest salt concentration is conserved at the bottom of the pond due to density difference, whose heat can be then extracted by heat exchangers [118]. Thus, the feature that an SGSP stores thermal energy inside saline water enables a perfect combination with desalination. The retentate of the desalination process can be directly adopted as the salt source of an SGSP, reducing the system cost as well as relieving the environmental impact of the rejected brine [28][119].

Generally, an SGSP comprises of three layers [118]: the upper convective zone (UCZ), the non-convective zone (NCZ), and the lower convective zone (LCZ), as denoted in Figure I.9. The UCZ is a relatively thin layer with cold and low salinity water at a temperature close to the ambient. A continuous water flushing is necessary to prevent the augmenting salt concentration by the salt diffusion from lower layers, and to compensate the evaporation on the top surface [120]. Below the UCZ, both a temperature gradient and a salinity gradient exist in the NCZ, keeping the water with less salt concentration and lower temperature always on top due to density difference [118]. Consequently, the natural convection is suppressed to prevent the heat from escaping the LCZ at the bottom, where the temperature and salinity are nearly uniform and the absorbed solar energy is stored in long-term as sensible heat of saline water.

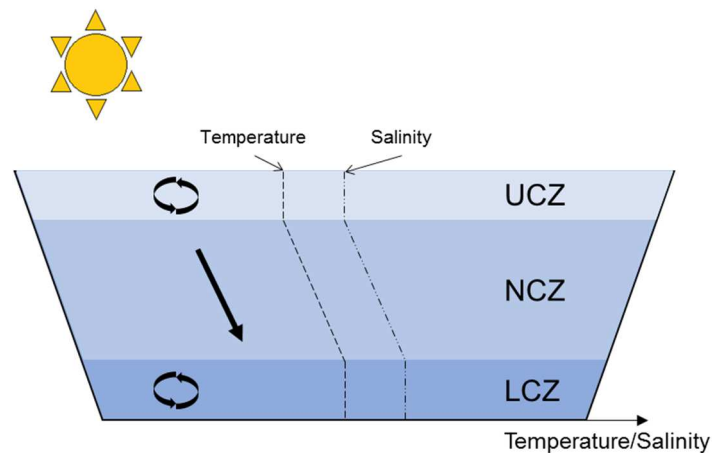


Figure I.9: Different layers of an SGSP

I.3.1.2. Concentrating solar thermal collectors

Based on the type of the concentrator, two groups of collectors have been studied extensively in the literature: line-focus and point-focus. The former uses cylindrical reflectors or refractors to focus beam radiation on a “line” or a rectangular surface, while the latter applies circular optical components to focus on a “point” [112]. Compound Parabolic Collectors (CPC), Parabolic Trough Collectors (PTC) and the collectors with Linear Fresnel Reflectors (LFR) belong to the former group, as illustrated in Figure I.10, while Parabolic Dish Collectors (PDC) and a solar tower with a heliostat field are the common example of the latter group, as illustrated in Figure I.11.

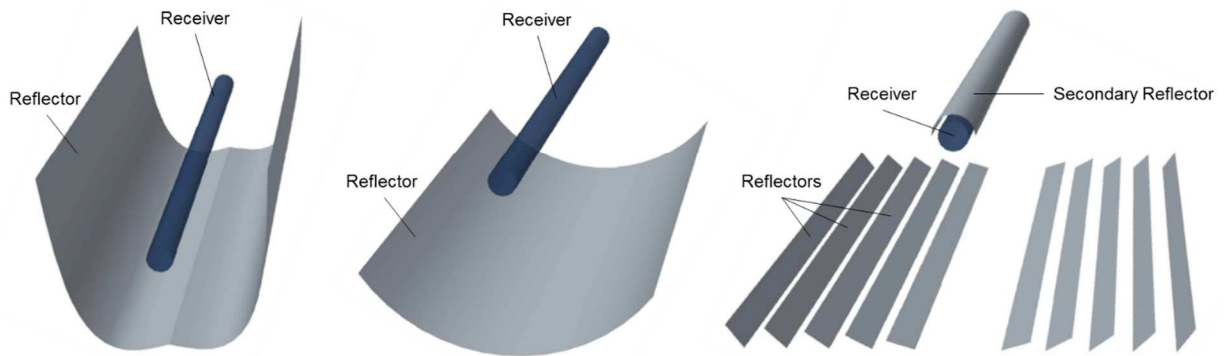


Figure I.10: Line-focusing concentrating solar collectors (from left to right): CPC, PTC, and LFR

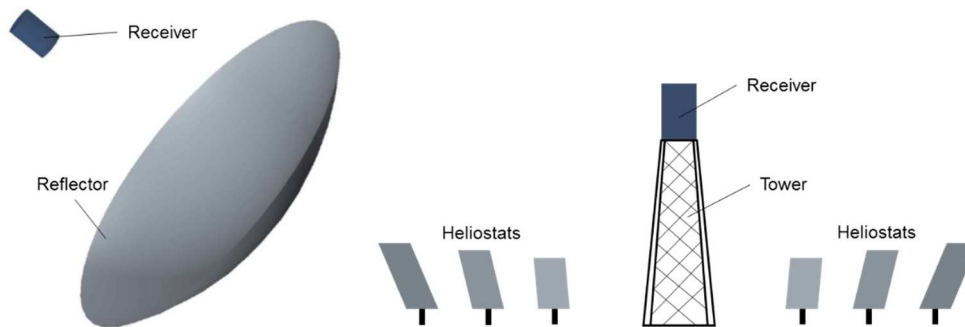


Figure I.11: Point-focusing concentrating solar collectors (from left to right): PDC and solar tower

Line-focusing collectors are often installed with one-axis solar tracking [113]. The CPC often consists of multiple different parabolic parts, concentrating solar irradiance onto a flat or tubular receiver. The concentration ratio of a CPC is relatively low, usually from 2 to 10 [121], thus CPCs are not frequently applied to Concentrating Solar Power (CSP) systems for steam generation, and instead, they work well with concentrating photovoltaic power generation. Contrarily, PTCs and LFR collectors are capable of reaching higher concentration ratios and raising the operating temperature up to 400 ~ 500°C [122]. The PTC is the most utilized type of concentrator in CSP systems with evacuated tube receivers, occupying more than 80% of the installed capacity [123]. Being much less utilized by CSP and less seen in applications, the LFR is composed of a set of flat or curved mirror strips, which reflects the incident irradiance onto an evacuated tube with a secondary reflector installed above the mirrors [124].

Point-focusing collectors are able to achieve even higher concentration ratios (over 100), occupying a large solar field. Therefore, an even higher temperature can be attained, being $700^{\circ}\text{C} \sim 750^{\circ}\text{C}$, and CSP systems are often the target application. However, two-axis tracking is necessary to follow the sunray in two dimensions. In this group, various receivers are applicable, such as cylindrical, spherical, conical and spiral absorbers [91]. Moreover, the receiver moves together with the concentrator in a PDC, while it stands still as the collecting tower with the turning heliostats.

Conclusively, the common working temperatures and thermal efficiencies of the discussed solar thermal collectors are listed in Table I.3. Concerning the applications of heat provision for MD, the working temperature of the non-concentrating collectors are more suited. Moreover, the complexity, market availability and cost of the non-concentrating collectors also prevail. Furthermore, SGSP exhibits a much lower efficiency than FPC and ETC, and it prefers larger scale to be cost competitive [28]. Therefore, the widely commercialized domestic FPCs and ETCs are obviously the better choice to couple with small-scale MD systems. FPC is a little bit lower in efficiency than ETC, but simpler in configuration, lower in system cost and more robust in terms of maintenance [125].

Table I.3: Characteristics of different solar thermal collectors [118,123,125,126]

Collector type		Working temperature	Thermal efficiency
Non concentrating	FPC	$< 100^{\circ}\text{C}$	65 ~ 75%
	ETC	$< 100^{\circ}\text{C}$	70 ~ 80%
	SGSP	$< 100^{\circ}\text{C}$	15 ~ 25%
Concentrating	CPC	$50^{\circ}\text{C} \sim 250^{\circ}\text{C}$	50 ~ 60%
	PTC	$150 \sim 350^{\circ}\text{C}$	30 ~ 40%
	LFR	up to 400°C	Not enough information
	PDC	$250 \sim 700^{\circ}\text{C}$	30 ~ 40%
	Solar tower	$500 \sim 1000^{\circ}\text{C}$	30 ~ 40%

I.3.2. Coupling solar thermal collectors with MD

Overall in the literature, non-concentrating solar thermal collectors have been more favored in driving MD systems because the scope of operating temperature matches more with MD process (40°C to 80°C), and no complexity by sun-tracking installations is necessary, confirming the discussions in the last section I.3.1. Nevertheless, MD systems can also work with concentrating ones to produce freshwater as a supplementary to a CSP plant with PTCs,

LFRs or a solar power tower [127–129], simply by applying seawater as the cooling medium for the CSP and reusing the heated seawater for MD process. Furthermore, among the non-concentrating solar thermal collectors, FPCs and ETCs are preferred over SGSP based on their higher efficiency in solar energy absorption and better market availability [88]. Besides, solar collectors with low concentration ratios have also been applied, such as CPC [11,130]. On the other hand, it is worth to mention that all the concerned studies utilized a variety of materials of membranes and other components, which might also be influential to their results, but the discussion on materials is out of the thesis scope.

I.3.2.1. Simulation-based studies

Theoretical modeling and simulations on solar-driven MD systems have been an important approach to evaluate the feasibility and possible performance. Most of these works have not been further developed into experimental systems. Hogan et al. were among the very first practitioners of feeding MD systems with solar heated saline water [131]. A hollow fiber DCMD module was coupled with solar FPCs with heat recovery in the system loop. Simulations by TRNSYS solar simulation program [132] showed an FPC area of 3 m², a membrane area of 1.8 m² and a heat exchange area of 0.7 m² for heat recovery were needed for the target productivity of 50kg per day, which is a good production capacity for domestic fresh water demand. Theoretical approach was also carried out for flat-sheet DCMD modules [133] with the assumption of constant feed and permeate flow rate and a controlled working temperature, pointing out that the heat recovery is the only way to improve productivity and thermal efficiency when the amount of thermal energy brought in by solar energy was limited by a certain solar collector area. More recently, a simulation study, also with the help of TRNSYS software, on a small-scale FPC-driven DCMD system (as shown in Figure I.12) exhibited a daily production rate of 19.7 kg per m² of membrane or 6.3 kg per m² of FPCs [69]. A surprising decrease in permeate flux and thermal efficiency was observed with increasing feed flow rate, which contradicts the results from conventional DCMD systems. The authors explained that the increasing flow velocities shortened the residence time of the feed within the thermal collector, which led to a decrease in feed inlet temperature. Other than DCMD modules, an explicit dynamic modeling and simulation work of a spiral-wound AGMD module with internal heat recovery was reported [134], using Aspen Custom Modeler [135], and optimizations under different solar irradiation profiles were performed to provide suggestions for the system configuration. Same for the AGMD module with internal heat recovery, a designed control system for the coupling of solar collectors in a tiny scale was modeled and optimized [136], a

maximum water production of 0.25 kg in a sunny day was attained with a solar collector area of 0.07 m² and a flat-sheet membrane area of 0.05 m².

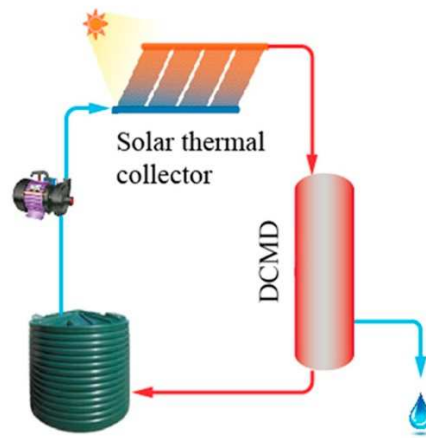


Figure I.12: Schematic diagram of the solar thermal DCMD process in [69]

An optimized scale-up of the previous system was further investigated, aiming a productivity of 2000 kg h⁻¹ [137]. The proposed membrane area and solar collector area were respectively 1622 and 1722m², and the recorded daily distillate production reached 29.37 m³ in summertime. An even larger solar collector (ETC) area of 1983 - 3360 m² was applied to 50 hollow fiber DCMD module with a calculated total membrane area of 56.5 m², yielding a production capacity of 31 m³ per day and a STEC of 436 kWh m⁻³ with heat recovery, which was 43% lower than the value without heat recovery [138]. It was also stated that bigger solar collector area could significantly decrease the consumption of auxiliary heating. Relatively large-scale system simulations with 350 - 550 m² of ETCs for DCMD were also seen in [139], coupling the solar system with the MD system via a controlled temperature level, and providing more than 1 m³ in a daily operation under the meteorological data of Busan, South Korea. Being rarely seen, an SGSD desalination system was coupled with solar collectors and PV panels, and a comprehensive process modeling and economic optimization was performed on such a system [111]. Solar energy was rigorously modeled and applied to the FPC and the PV panels in the system. Optimized results indicated an FPC area of 27 m² and a PV area of 4 m² are required for the target productivity of 240 L per day.

I.3.2.2. Experimental studies

Experimental efforts in both small-scale (solar collector area ≤ 10 m²) and large-scale (solar collector area > 10 m²) are available in the literature as well. As depicted in Figure I.13, the

former is often referred to as “compact” systems with solar heating and MD in one loop, while the latter often consists of separated solar-collecting loop and an MD loop, which are in contact via heat exchangers.

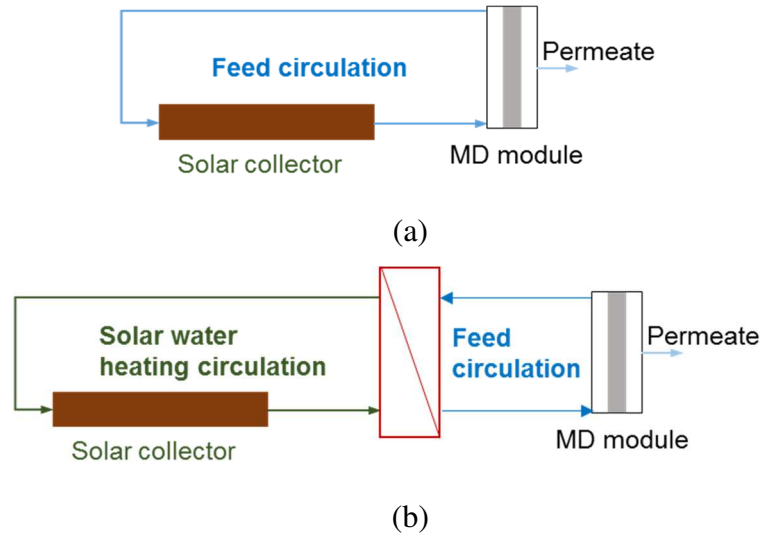


Figure I.13: Schematics of solar driven MD: (a) One-loop compact systems; (b) Two-loop large systems

A small-scale stand-alone membrane distillation unit driven by solar energy was designed, manufactured and tested in Irbid, Jordan under the project “SMADES” [98]. The adopted solar FPCs possessed an area of 5.73 m², heating the feed circulation directly for a spiral-wound AGMD module with a membrane area of 10 m². Daily water production reached 19 L per m² of the aperture area of the FPCs, and the STEC was in the range of 200 - 300 kWh m⁻³ with condensation heat recovery inside the module. Under the same project “SMADES”, another small-scale autonomous solar-driven MD system with the same type of AGMD module and the same aperture area of solar FPCs was tested in Alexandria, Egypt [100]. A productivity of 11.2 L per day per m² aperture area was recorded, and a STEC of around 647 kWh m⁻³ can be calculated from the data provided. As a modification of AGMD, a PGMD module of 8.5 m² with internal heat recovery was connected to a small FPC field of 6.96 m² for seawater desalination operations from 2005 to 2010 in Pozo Izquierdo-Gran Canary Island, Spain [102]. In sunny days, the productivity varied between 59 - 117 L day⁻¹ with a STEC from 140 to 350 kWh m⁻³, and a varying SEEC of 2.1 to 51.2 kWh m⁻³. Small-scale systems were also established for VMD process. A hollow-fiber VMD module of 0.09 m² effective membrane area for underground water desalination was fed by solar collectors of 8 m² [140], and the system flowsheet is shown in Figure I.14. A daily cumulated production of 173.5 kg was

obtained with a calculated STEC of 7858 kWh m^{-3} and an SEEC of 317 kWh m^{-3} in October in Hangzhou, China. A flat-sheet VMD module of 0.25 m^2 for seawater desalination was later installed in Xiamen, China, in heat-exchange with ETCs of 2.16 m^2 aperture area [141]. NaCl solution was utilized to test the system, yielding an average productivity of $4 \text{ kg m}^{-2} \text{ h}^{-1}$ (membrane area based), which was much lower than the value ($14.4 \text{ kg m}^{-2} \text{ h}^{-1}$) of the same VMD module with steady heat supply, and a STEC of 750 kWh m^{-3} , which was almost the same as the aforementioned VMD study in China. A most recent work on small-scale experiments was conducted on a solar-driven DCMD system [142]. A packed bed evaporative heat exchanger with cross water/air cooler was applied on the permeate circulation to enhance the driving force for MD process, and ETCs of 2.61 m^2 in total was utilized to power the process and a maximum daily productivity of 33.55 L was observed. The use of the cooling exchanger improved the production by a factor of 1.25.

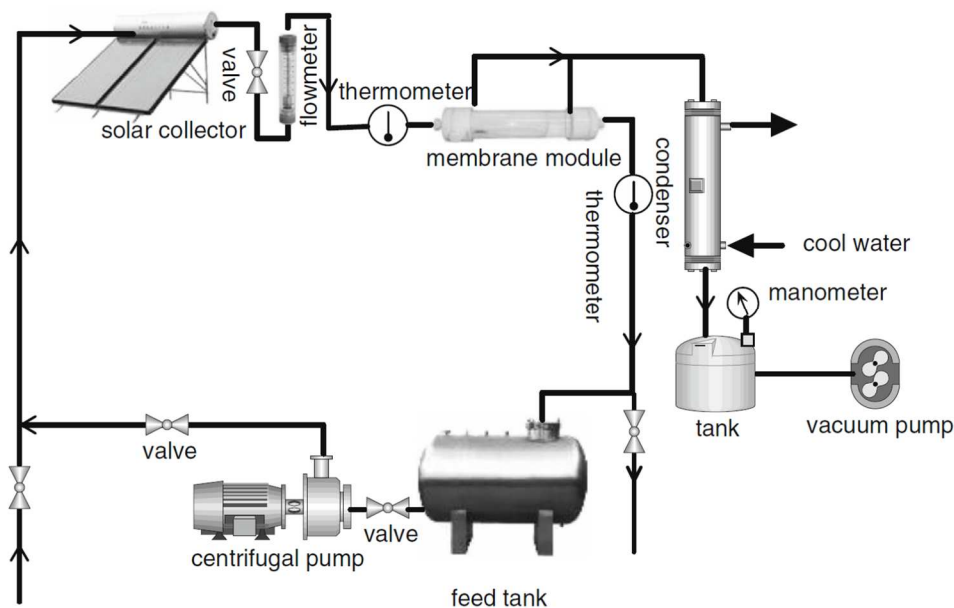


Figure I.14: Flowsheet of the solar-heated MD system in [140]

For relatively large-scale systems, a two-loop system with a FPC field of 72 m^2 (solar loop) and a set of AGMD modules with internal heat recovery of 40 m^2 (desalination loop) was constructed and studied in Aquba, Jordan under the project “SMADES” [99], as presented in Figure I.15. The two loops were connected by a heat exchanger, and the desalination loop was able to produce $2 - 11 \text{ L}$ of freshwater per m^2 of solar collector with a specific energy consumption (SEC) in the range of $200 - 300 \text{ kWh m}^{-3}$. A photovoltaic field of 1440 W_p was installed to provide the electricity demand. Pilot-scale pre-commercial AGMD modules of 2.8

m^2 and 9 m^2 were connected via heat exchangers to a solar-collecting field of CPCs of 500 m^2 in Almería, Spain [11,143]. A dispersed value of STEC was reported, being from 294 to 2200 kWh m^{-3} , and a permeate flux up to $7 \text{ L h}^{-1} \text{ m}^{-2}$ was recorded. Furthermore, the authors claimed that heat recovery plays an essential role in augmenting the system thermal efficiency and hence the performance, and multi-staging might be a good candidate for heat recovery if a compact system is not targeted. Fraunhofer ISE established 3 full-scale demonstration MD plants, two of which were solar energy driven, installed in Amarika (Namibia) and Gran Canary (Spain), and one was powered by waste heat from Diesel engine, installed in Pantelleria (Italy) [144]. The plant in Amarika consisted of a solar FPC field of 232 m^2 and 12 AGMD modules with a total membrane area of 168 m^2 , producing 2.08 m^3 of fresh water per day at a STEC of 171 kWh m^{-3} . Similarly, the one in Gran Canary was composed of a solar loop of 186 m^2 of FPCs, an AGMD loop of 120 m^2 in total and a photovoltaic field of 1920 W_p , being reported to yield 1.4 m^3 of daily productivity and 271 kWh m^{-3} of STEC. Detailed thermal energy flows in all plants were presented as well, only 28% and 30% of the whole solar irradiation went into the desalination loops in Namibia plant and in Gran Canary plant, respectively. Besides, it was noted that both the SECs were a bit higher than the figures obtained in lab-scale studies. Apart from the systems with AGMD module, one solar-driven autonomous system with DCMD modules of a total area of 3.39 m^2 was built and tested in Jeddah, Saudi Arabia [109]. Solar FPCs of 20 m^2 were utilized as the thermal energy source, while photovoltaic panels of a peak power of 1.48 kW were installed to meet the electricity demand of the whole system. The configuration without heat recovery was able to produce a daily average flux of 3.31 L h^{-1} at a STEC of 2342 kWh m^{-3} , while the one with heat recovery showed a daily average flux of 4.59 L h^{-1} at a STEC of 1609 kWh m^{-3} , via arranging heat exchange between the permeate and the feed circulation before entering the feed storage tank. Finally, a recent study of estimating the necessary solar collector area to power a hollow-fiber VMD module was presented, aiming a distillate production of 10 m^3 per day [145]. The experiment and simulation resulted in a solar collector area of 1450 m^2 with an efficiency assumption of 50% for the solar collectors, and a STEC of 580 kWh m^{-3} .

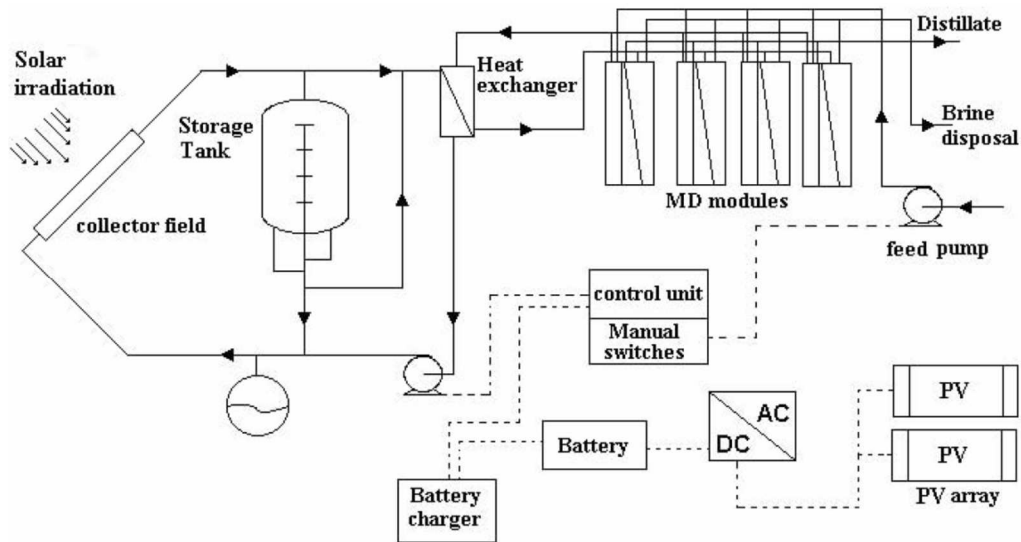


Figure I.15: Flowsheet of the large “SMADES” MD system in Aquba, Jordan (from [99])

Based on all the research reviewed above, those major contributions on the performance evaluation of solar-driven MD systems are chronologically summarized in Table I.4 below in order to have a holistic view of the work conducted previously, with the information on MD configuration, SC type, the existence of heat recovery, daily freshwater production, areas of membrane and SC, SEC in terms of the volume of the freshwater produced.

Table I.4: Data from the literature on the coupling of solar collectors and MD systems

MD study	SC Type	Latent heat recovery	SC area (m ²)	Membrane area (m ²)	Daily production (L)	SEC (kWh m ⁻³)	Year
DCMD Simulation	FPC/ETC	External HE	3	1.8	50	42.7 - 556* (thermal)	1991 [131]
AGMD Experiment	FPC/ETC	Internal condensation	5.9	8	63 - 161	117 (thermal)	2003 [146]
DCMD Simulation	ETC	Internal & External HE	32	3.2	50 - 280	N/A	2005 [133]
AGMD Experiment	FPC	Internal condensation	5.73	10	120	200 - 300 (thermal)	2007 [98]
AGMD Experiment	FPC	Internal condensation	72	40	144 - 792*	200 - 300 (thermal)	2007 [99]
AGMD Experiment	FPC	Internal condensation	5.73	N/A	64	647* (thermal)	2008 [100]
VMD Experiment	N/A	-	8	0.09	15.6*	8176* (thermal + electrical)	2009 [140]

Chapter I: State of the art

AGMD Simulation	FPC	Internal condensation	72	10	578.8 - 706.5	343* (thermal)	2010 [134]
AGMD Experiment	CPC	Internal condensation	500	2.8	N/A	810 - 2200 (thermal)	2011 [11]
AGMD Experiment	CPC	Internal condensation	500	9	No HR: 60* HR: 95*	No HR: 1805 HR: 294 (thermal)	2012 [143]
AGMD PGMD[147] VGMD[50] Simulation	ETC	Internal condensation	11	2.28	105	369* (thermal)	2012 [50]
AGMD Experiment+ Simulation	N/A	Internal condensation	0.07*	0.05	0.2 – 0.25	N/A	2012 [136]
PGMD Experiment	FPC	Internal condensation	6.96	8.5 - 10	5 - 120	140 – 350 (thermal)	2012 [102]
AGMD Simulation	ETC	Internal condensation	1722	1628	15890 - 29370	N/A	2012 [137]
AGMD Experiment	FPC	Internal condensation	232	168	2080	171 (thermal)	2013 [144]
AGMD Experiment	FPC	Internal condensation	185.6	120	1400	271 (thermal)	2013 [144]
DCMD Simulation	ETC	External HE	3360	56.5*	31000	No HR: 771 HR: 436 (thermal)	2013 [138]
VMD Simulation	FPC	-	N/A	0.15	38	N/A	2013 [103,106]
VMD Experiment	ETC	-	2.16	0.25	3	750 (thermal)	2014 [141]
AGMD Experiment+ Simulation	FPC	Internal condensation	11.9	0.2	16	804 (thermal)	2015 [148]
DCMD Experiment	SGSP	-	2	0.1	2.32*	2029* (thermal + electrical)	2015 [149]
DCMD Experiment	FPC	External HE	20	3.39	No HR: 18.4* HR: 25.2*	No HR: 2342 HR: 1609 (thermal)	2015 [109]
DCMD Simulation	N/A	-	4.7	0.13	N/A	896 - 1433 (thermal)	2015 [150]

VMD Experiment+ Simulation	N/A	External condensation	1450	53	10000	580 (thermal)	2016 [130]
DCMD Simulation	SGSP	-	N/A	0.1	2.5 (per m ² of SGSP)	800 - 980 (thermal)	2016 [151]
DCMD Experiment	ETC	-	2.61*	1	26.76 - 33.55	N/A	2017 [142]
DCMD Simulation	FPC	-	22.6	7.2	140	N/A	2017 [69]
SGMD Simulation	FPC	-	27 + 4 (PV)	1.03	240	N/A	2018 [111]
MS-DCMD Simulation	ETC	External HE	350 - 550	2.4*	400 - 1170	N/A	2018 [139]

N/A: Not available in the paper

HE: Heat exchanger

*: Calculated or estimated from data or figures in the corresponding paper

I.3.3. Direct integration of solar thermal collectors and MD

As discussed on Figure 1 in General introduction, the direction integration of solar thermal collectors can be another approach to couple solar heating with MD process, aiming less heat and pressure loss in the piping and connections. Besides, the intensified process of the integrated module is more adaptive to small-scale compact systems. However, it should be noted that the integration of solar heating and MD in the same module is less flexible in modularity and the surface area of the solar collecting is fixed when given a certain area of membrane. Hence, some potential advantages and limitations of both the “separated” (Figure 1a, 1b) and “integrated” (Figure 1c, 1d) modules are listed in Table I.5.

Table I.5: Potential Advantages and limitations of the direct integration of MD and SC

System type	Advantages	Limitations
Separated solar-driven MD module	Easy to scale up Controllable operating temperature Multi-usage of solar energy	Extra heat exchanging & piping Additional heat & pressure loss
Integrated solar-MD module	Low heat & pressure loss Simple configuration & easy to operate Intensified process	Fixed Solar collecting area Less modularized

Various designs of the direct integration of MD and SC have been proposed in the literature. It is worth to mention that all integrated modules reviewed below were inlaid into a “one-loop” system as in Figure I.13a because of the integrality of the module. A hybrid solar distillatory, combining flat-sheet AGMD with a conventional basin still [152], was one of the earliest practice of this idea. Experiments as well as numerical simulations revealed that the daily distillate productivity was only $2.18 \text{ kg m}^{-2} \text{ day}^{-1}$, and the calculated specific solar energy consumption was as high as 2880 kWh m^{-3} . Also by the same research group, an innovative module equipped with both flat sheet AGMD and solar photovoltaic cells was designed and studied [105], as in Figure I.16, adopting the photovoltaic/thermal (PV/T) concept, which combines solar cells with thermal collecting unit adhered beneath [121]. The results showed an even lower distillate production of $1.22 \text{ kg m}^{-2} \text{ day}^{-1}$, while with a higher energy saving ratio because of the electricity produced by the PV cells.

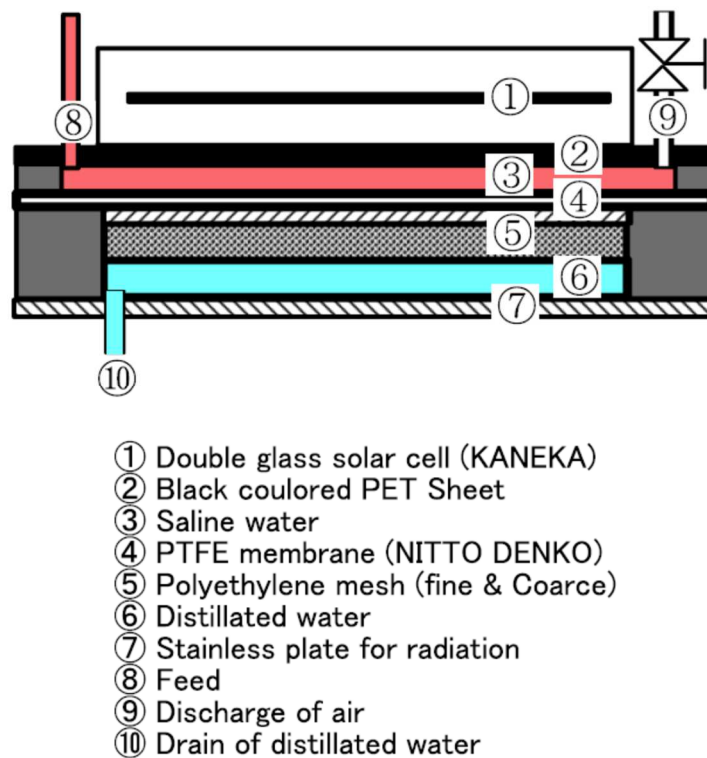


Figure I.16: The schema of the hybrid solar distillator in [105]

Then, both experimental and modeling work was conducted by Chen and Ho for DCMD [153] and Ho et al. [154] for AGMD. The space for water circulation under the absorber-plate functioned as the MD module with feed side heated by the absorber-plate of the solar collector, as illustrated in Figure I.17. However, the dynamic performance with varying solar condition and accumulated water production was not studied, and the performance increment with

integrated solar energy was only evaluated globally by means of some operating parameters in conventional MD process such as vapor permeate flux, inlet feed temperature and flow velocity at the membrane surface.

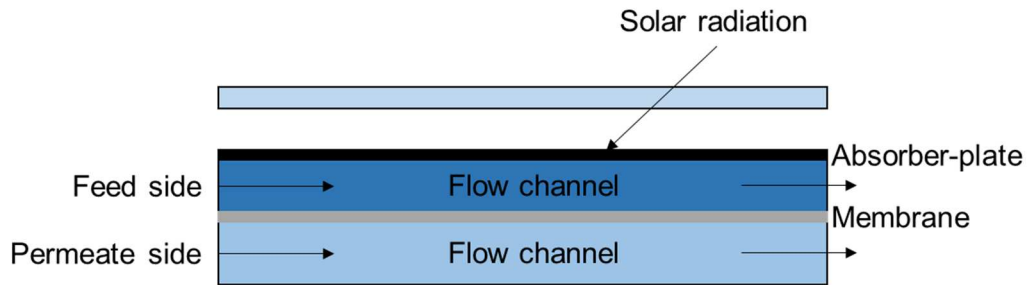


Figure I.17: Schematic of the directly integrated DCMD module in [153]

Besides, Mericq et al. [27] conducted a series of indicative simulations on the integrated solar-VMD module and the separated VMD module with solar collecting unit, providing some general conclusions on freshwater production, while a pathway towards the design of coupled VMD - solar collector modules would require the dynamic evaluation and the detailed design and description of the solar absorption in VMD. A solar-integrated simultaneous heat and mass transfer model would therefore offer the possibility of evaluating different intensified design configurations under reasonable assumptions. Recently, an innovative 2-level water harvesting device of solar thermal membrane distillation was designed and tested [155], including the heat recovery between levels, as displayed in Figure I.18. Results exhibited a production of $3.67 \text{ kg m}^{-2} \text{ day}^{-1}$ and a solar efficiency of 72%. However, the productivity remained limited.

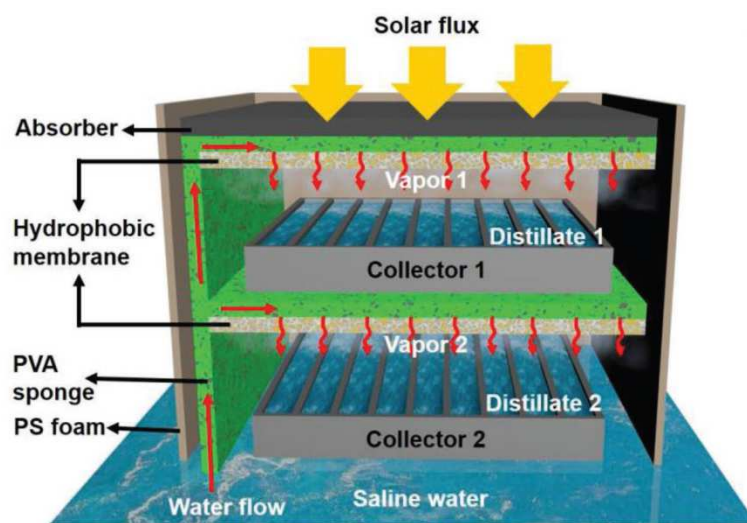


Figure I.18: Schema of high-efficient solar-thermal membrane distillation module in [155]

Other than flat-sheet type modules, hollow fiber VMD modules were also studied with this integration idea by being inserted into the cylindrical absorber of CPC solar collectors (Figure I.19) [156], which offers possibility of directly absorbing intensified radiation for freshwater production to overcome the sparsity of solar energy. Alternatively, hollow fiber membranes were submerged straightaway into an SGSP to minimize the heat loss before the VMD process [157]. However, in the before-mentioned studies, the detailed and dynamic solar energy modeling is still lacking. Besides, the comparison of the permeate flux between the integrated module and the non-integrated might be biased because the temperature of the solar collector of the integrated module was modeled independently from the VMD process, possibly without considering the influence of the heat taken away by evaporation.

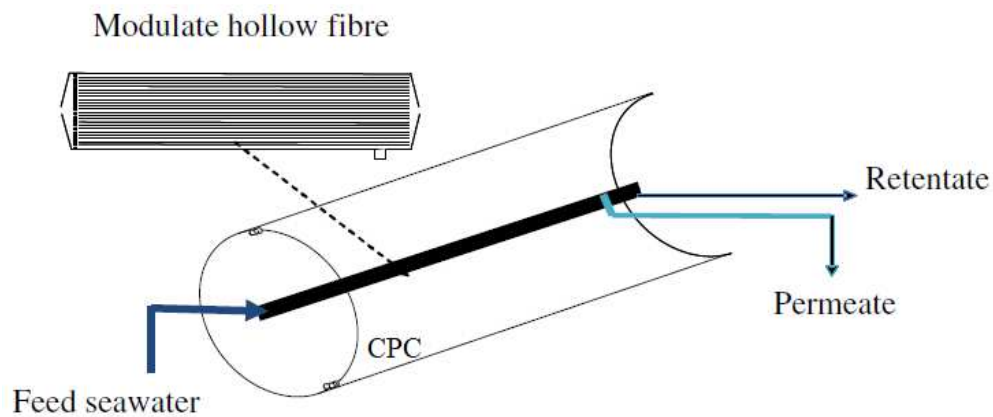


Figure I.19: Hollow fiber membranes integrated inside the absorber of a CPC (from [156])

Most recently, a delicately fabricated VMD-ETC module was studied via both simulations and experiments [158]. Hollow fibers membranes of 0.2 m^2 were inserted into the ETC tubes with a total solar absorbing area of 1.6 m^2 (module configuration shown in Figure I.20), and the module was designed to be able to produce fresh water and provide domestic hot water simultaneously. $3.2 \sim 4.8 \text{ L}$ of drinking water and a certain amount of bath water at 45°C could be produced on a daily basis, at a cost of 1 kWh electricity consumption and $4.7 - 9.6 \text{ kWh}$ solar exposure, which corresponds to an SEEC of $208 \sim 313 \text{ kWh m}^{-3}$ and a STEC of more than 1000 kWh m^{-3} to produce fresh water. Therefore, such a design still needs improvement in both productivity and energy consumption.

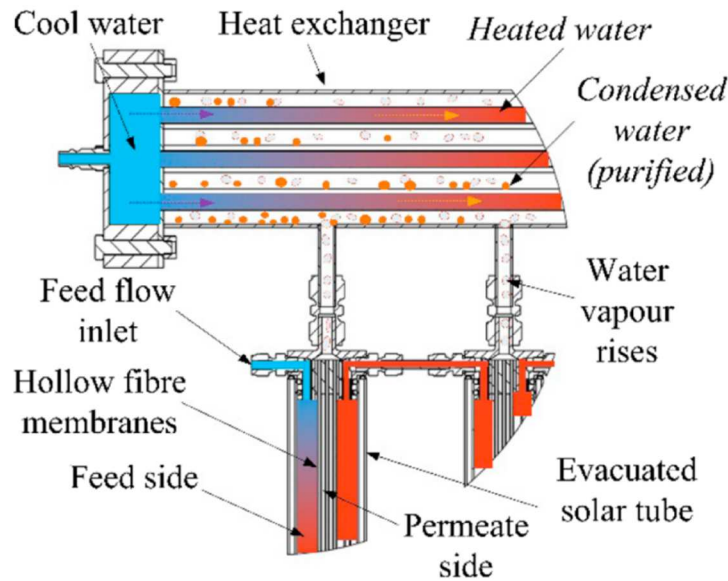


Figure I.20: Configuration of the VMD-ETC module in [158]

Another approach of directly integrating MD process with solar collectors is by fabricating new composite membrane with high solar energy absorptivity, which can simultaneously act as the absorber-plate of the solar collector, as well as the membrane that separates the vapor from the feed solution [159–162], as illustrated in Figure I.21. Studies were carried out for AGMD [159,160], VMD [161] and DCMD [162] with both simulations and experiments. It is proven that the temperature polarization effect, which deters the MD process from reaching the maximum permeate flux, can be alleviated or even fully eradicated by this configuration, along with the common merits of integrated modules such as less thermal and pressure loss and more compact modules. However, the amount of solar thermal energy that can be utilized is fixed by a certain aperture area, which directly determines the final water production in case of solar energy being the only heat source. Therefore, it is the solar absorptivity of the whole module that matters most, and in that sense, a normal coated absorber-plate with glass covers probably still has a better overall absorptance (up to 0.98 [163]) than the fabricated composite membrane (maximum absorptance a little lower than 0.9 [160]), which is still in R&D phase and might be hard to acquire in the market for now.

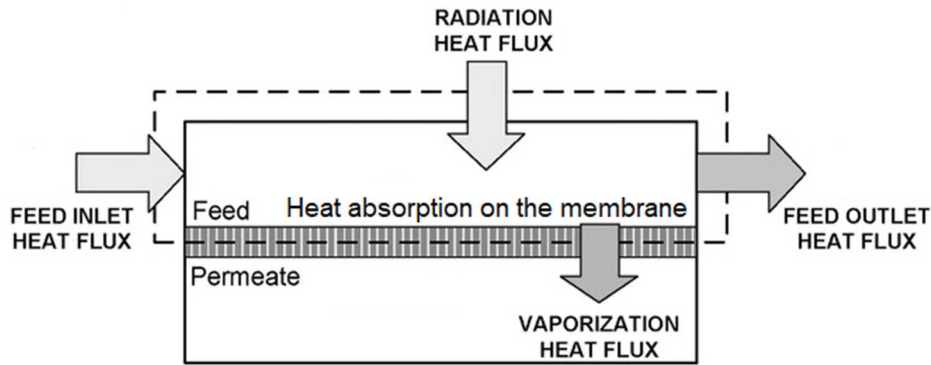


Figure I.21: The direct radiation absorption on the surface of a composite membrane in [161]

I.3.4. Observations of the literature

It is difficult to compare all the reviewed results in I.3.2 and I.3.3 among themselves, because of their difference in MD configuration, module configuration, module size and membrane properties etc. Nevertheless, from an energy point of view, all the daily distillate productions reviewed above were below 30 L per m² solar collecting surface area, and the value was even below 10 if heat recovery was excluded. Considering the surface area of the entire apparatus, the productivity was relatively low compared to conventional MD systems with continuous auxiliary heating source ($\sim 10 \text{ L m}^{-2} \text{ h}^{-1}$, defined in terms of the membrane area). Hence, an idea of integrating the MD with SC systems into one equipment has been practiced to reduce the energy loss in compact small-scale use, but few studies are available and no clear evidence on performance elevation has been shown yet. On the other hand, the SEC in previous studies scattered to a wide range from 100 to more than 2000 kWh m⁻³, which is still more costly than other thermal desalination processes such as MSF and MED. Furthermore, much higher consumption was encountered if heat recovery was not considered, on account that the demand of latent heat for water evaporation is around 667 kWh m⁻³ [42]. Conclusively, an efficient latent heat recovery regime is of great interest to surmount the obstacle of the restricted solar energy supply, in order to achieve significant improvements in both water productivity and thermal energy consumption [164]. This aspect demands more in-depth study especially in the case of small-scale distributed system where multi-staging is hardly applicable [11], and in the flat-plate design of the integrated modules under normal solar insolation where the surface areas of the membrane and the solar collecting unit are identical [105,153,154,159,160]. Besides, little work has been seen towards the latent heat recovery design in VMD research, even though VMD possesses the merits of low thermal loss and high productivity. The reason is probably

due to the low temperature of condensing water vapor in vacuum environment, which induces great difficulty of reusing the latent heat of condensation.

Another overall observation in the literature is, in spite of all of the effort on coupling solar energy with MD processes, most of them were focused on the thermal energy consumption of the solar-driven MD system without specifying the electricity expense during the process, which is more important to be evaluated based on the fact that heat consumption is mostly or entirely provided by the low-grade solar thermal energy taken from nature at no extra cost. Moreover, nearly no study on the energy consumption has included the discussion of cooling energy consumption on permeate condensation, which could be significant in VMD if the condenser is placed outside the vacuum, and in DCMD if a cold permeate side is desired to induce higher permeate flux. A total consideration of energy consumption was reported by A. Criscuoli et al. [165] through experiments, including data for heating, cooling and vacuum pumping consumptions. The results showed that the minimum energy requirement for DCMD with the consideration of cooling cost was 3550 kWh m^{-3} , while the value for VMD was 1100 kWh m^{-3} . Nevertheless, results reported in this work were most likely provided without considering the consumption for vapor condensation in the cold trap in VMD. Therefore, an in-depth evaluation of innovative solar driven MD systems is yet to be fully developed, taking into account all energy aspects including the heating, pumping and cooling stages.

I.4. Conclusions (in English)

As a relatively new generation of water treatment technology, membrane distillation (MD) has proven its potential for seawater desalination. Thus, research on different configurations and modules has been very active since about one decade, based on both modeling and experimental approaches. Some first industrial scale modules and plants have already been built. Upon understanding the transfer mechanisms of MD, certain drawbacks are inevitable, such as high thermal energy consumption for evaporation. Fortunately, the facts that MD is a thermal process that requires low operating temperature and has a high tolerance for fluctuated heat provision enable the possible coupling with solar thermal energy, which is often abundant in arid regions. Therefore, numerous efforts have been reported in the literature towards the solar-driven MD modules and systems, mainly adopting the non-concentrating solar collectors such as flat-plate collectors (FPC), evacuated-tube collectors (ETC) and salinity-gradient solar ponds (SGSP).

Throughout an explicit review of the solar-driven MD configurations studied in the literature, from a perspective of both water production and energy efficiency, the following observations would be made: (i) the water productivity is directly proportional to the amount of solar energy available and utilized; (ii) improved design to enhance the thermal efficiency is essential to an autonomous system; (iii) the reported energy consumptions of solar driven MD systems can still be lowered, and should emphasize more on electric consumption; (iv) the inclusion of heat recovery is able to enhance productivity and reduce thermal consumption, but more work is yet to develop especially for compact and integrated modules and for VMD; (v) direct integration of solar heating and MD in one module has been proposed but without enough studies. It might be a good candidate for decentralized fresh water production at domestic scale, but still needs more exploration to ameliorate the performance to be adapted to the target application in this thesis; (vi) complete evaluations of all energy aspects including the cooling energy required for permeate condensation have seldom been provided.

Based on these observations in the literature, potential targets of the current thesis study can be envisioned, aiming an autonomous decentralized solar driven desalination system for a domestic utilization of small production capacity (a family in small communities). A module integrating MD and solar collector can contribute to a simple and compact system design, which will be the stepping-stone to address on the efficient use of the sparse solar energy. Direct utilization of the absorbed solar energy for the MD process is one of the biggest advantages of this configuration. The surface of the membrane, where the absorbed heat is utilized for evaporation, would be nearer to the place of solar absorption. Thus, the heat and pressure loss in piping and joints can be reduced and the process can be intensified.

Moreover, it should be noted that, for a conventional MD module (without an integrated system design of solar heating): (i) the VMD configuration benefits from the highest productivity per unit membrane surface and the least conductive heat loss across the membrane, while the DCMD configuration prevails in simplicity at lab-scale and has been more utilized; (ii) FPCs and ETCs both have the suitable working temperature, market popularity, and relatively high efficiency in solar absorption, and the former is simpler in configuration. Therefore, the exploration of the possible design and evaluation of VMD or DCMD modules integrated with FPC constitutes the premier task of the thesis. The choice of VMD or DCMD cannot be easily decided at the beginning of this thesis, due to the lack of comprehensive comparisons on the systems integrated with solar energy. VMD is a better choice in terms of the potential

performance of the process, therefore a module integrating VMD and FPC (VMD-FPC) will be the first trial in this thesis (Chapter II), and then a similar module of DCMD-FPC will be comparatively studied (Chapter III).

Then, a practical heat reuse for the designed system will be one big leap further to the competitiveness in the application. In order to tackle this issue, multi-staging is no more a good choice because of the objective of small-scale domestic system, though it has already been proven effective not only in conventional MSF and MED but also in MD. Hence, upon the selection of the module design, an adapted feasible heat recovery strategy for the target application awaits conception and evaluation to massively promote the overall system performance. The first trial of utilizing a heat pump to recover latent heat of vaporization will be studied in Chapter IV, following the integrated systems studied in Chapter II and III.

Finally, a comprehensive evaluation and optimization on the water productivity and energy consumption is required in order to produce the eventual guidance and prediction for the operation of the designed integrated module and system. To accomplish this final mission, all aspects of energy consumption, including the cooling energy for permeate condensation, have to be all included in the design and holistically appraised, as will be presented in Chapter IV. Additionally, examples with real-world parameters and optimized adjustable conditions should be provided in detail (as will be discussed in Chapter V), to give clear information and suggestions for a first prototype and an ultimate outlook for the application, which will be among the following work of LabCom MOST.

I.4. Conclusions (en français)

Technologie émergente de traitement d'eau, la distillation membranaire (MD) a un grand potentiel de développement pour le dessalement d'eau de mer. Ainsi, depuis les années 2010 les travaux de recherche se multiplient sur différentes configurations et modules, avec des approches à la fois de modélisation et expérimentales. De premiers modules et installations industriels ont vu le jour. La connaissance des mécanismes de transfert en MD, conduit à penser que certains de ses inconvénients sont inévitables, tels que la consommation élevée d'énergie thermique pour l'évaporation. Mais la MD présente également les avantages d'être un procédé nécessitant principalement de l'énergie thermique, avec une relativement basse température de fonctionnement (<80°C) et une tolérance à des variations de chaleurs, ce qui permet un couplage avec l'énergie solaire thermique, souvent abondante dans les régions arides. Ceci

explique que récemment de nombreux efforts de recherche concernent les modules et systèmes MD assistés par l'énergie solaire, principalement avec des collecteurs solaires sans concentration, tels que les collecteurs plans (FPC), les collecteurs à tube sous vide (ETC) et les étangs solaires à gradient de salinité (SGSP).

Une revue littéraire des configurations de MD conventionnelles assistées par l'énergie solaire, permet de faire les observations suivantes sur la production d'eau et l'efficacité énergétique :

- (i) la productivité d'eau est directement proportionnelle à la quantité d'énergie solaire disponible et utilisée;
- (ii) une amélioration de l'efficacité thermique est essentielle pour concevoir un système autonome;
- (iii) les consommations d'énergie des systèmes MD à énergie solaire peuvent encore être abaissés, et devraient mettre davantage l'accent sur la consommation électrique;
- (iv) la mise en place d'une récupération de chaleur est capable d'améliorer la productivité et de réduire la consommation thermique, mais plus de travail reste à développer, notamment pour les modules compacts et intégrés et pour la VMD;
- (v) l'intégration directe dans un même module du solaire et de la MD a été proposée et a fait l'objet de très peu d'études. Elle présente un potentiel pour la production décentralisée d'eau douce à l'échelle domestique, mais des travaux sont à réaliser pour améliorer les performances et s'adapter aux objectifs d'application de cette thèse;
- (vi) des évaluations complètes de tous les aspects énergétiques, y compris l'énergie de refroidissement requise pour la condensation du perméat, ont rarement été fournies.

Sur la base des observations issues de l'état de l'art, les objectifs initiaux de cette thèse étudient peuvent être vraiment envisagés et précisés avec en point de mire la conception d'un système de dessalement décentralisé autonome pour une utilisation domestique de petite capacité de production (une famille à une petite collectivité). Un module intégrant MD et collecteur solaire thermique peut constituer un système simple d'utilisation et compact propice à une utilisation efficace de l'énergie solaire clairsemée. Un des arguments majeurs en faveur de cette configuration est que l'intégration du chauffage solaire et de la séparation MD dans un même équipement utiliserait directement l'énergie solaire absorbée pour la MD. Cette absorption aurait au plus proche de son point d'utilisation pour la vaporisation de l'eau, localisée à la surface de la membrane, ce qui limiterait la perte de chaleur et de pression dans les tuyauteries et les joints et intensifierait le procédé.

De plus, on note que, pour un module conventionnel de MD (module n'intégrant pas d'énergie solaire et sans prendre en compte l'ensemble du système) : (i) la configuration VMD est connue pour bénéficier à la fois la plus grande production d'eau par unité de surface de membrane et de la plus faible perte de chaleur de conduction à travers la membrane, tandis que la configuration DCMD est souvent plus utilisée car plus simple d'utilisation à l'échelle du laboratoire; (ii) les collecteurs thermique de type FPC et ETC, qui ont une température de fonctionnement appropriée pour la MD, sont disponibles facilement sur marché et présentent un rendement d'absorption solaire relativement élevé. Le FPC a une configuration plus simple que l'autre. Par conséquent, les travaux exploratoires de cette thèse vont être principalement centrés sur l'exploration de la conception et l'évaluation de modules intégrant la MD et un collecteur de type FPC. La question du choix entre VMD et DCMD ne peut pas totalement tranchée au début de la thèse sur la base de la littérature, ces systèmes n'ayant pas été comparés globalement à l'échelle du système et pas couplés à un collecteur solaire. L'intérêt potentiel de la VMD étant plus grand en termes de performances du procédé, nos travaux vont dans un premier temps s'intéresser à un module intégrant VMD et FPC (Chapitre II), puis nous comparerons un module VMD-FPC et un module DCMD-FPC (Chapitre III).

Puis, il apparaît clairement à ce stade que la récupération/réutilisation de la chaleur latente est un élément clé de la compétitivité du système. A cet effet, la MD multi-étages est une alternative dont l'efficacité a été prouvée pour la MSF et la MED classiques (sans membranes), mais aussi pour la MD. Toutefois, elle n'apparaît pas comme une option réaliste pour un système domestique de petite capacité de production. Des premières tentatives de couplage d'un module MD conventionnel avec une pompe à chaleur montrent l'intérêt de cette alternative, dont nous étudierons au chapitre IV l'intérêt potentiel pour son couplage avec le module intégré MD-FPC, qui sera retenu à l'issue du chapitre II et III. En effet, il apparaît essentiel de coupler la conception du module avec une stratégie de récupération de chaleur réaliste et adaptée à l'application visée. Cette stratégie doit être élaborée de manière à améliorer les performances de l'ensemble du système.

Il apparaît enfin qu'il faudra faire dans cette étude évaluation et une optimisation complètes de la productivité d'eau et de la consommation d'énergie avant de proposer des recommandations pour la conception du module intégré et pour le fonctionnement de l'ensemble du système. Pour bien accomplir cette mission finale, tous les aspects de la consommation d'énergie, y compris l'énergie de refroidissement nécessaire à la condensation du perméat, doivent être inclus et

Chapter I: State of the art

évalués globalement. Ce travail fera l'objet du chapitre IV. De plus, des exemples avec des paramètres réels et des conditions ajustables optimisées doivent être fournis en détail, de manière à donner au chapitre V des informations et consignes claires en vue de la réalisation d'un premier prototype, qui pourrait être réalisé par le LabCom MOST dans la suite de ces travaux.

II. Direct integration of a vacuum membrane distillation module within a solar collector for small-scale units adapted to seawater desalination in remote places: Design, modeling & evaluation of a flat-plate equipment

This chapter is extracted from a published paper:

Q. Ma, A. Ahmadi, C. Cabassud, Direct integration of a vacuum membrane distillation module within a solar collector for small-scale units adapted to seawater desalination in remote places: Design, modeling & evaluation of a flat-plate equipment, *Journal of Membrane Science*. 564 (2018) 617–633. doi:10.1016/j.memsci.2018.07.067.

II.1. Introduction (in English)

As mentioned in Chapter I (Section I.3.3), some attempts have already been made in the literature to directly integrate solar heating into varying MD configurations (DCMD, VMD, AGMD). For instance, flat-sheet membranes were inserted into the space under the absorber-plate of a normal Flat-Plate Collector (FPC) [153,154], and the feed was heated directly by the solar energy absorbed by the collector. However, process dynamics driven by the dynamic nature of the solar radiation has not been taken into consideration, and the performance increment with integrated solar energy was only globally evaluated on the permeate flux by means of some key operating parameters in conventional MD process. Hollow-fiber membranes could also be integrated with cylindrical solar absorbers for VMD process [156], but the detailed and dynamic solar energy modeling was still lacking, and the result evaluations might be biased because the absorber temperature of the integrated module was modeled independently from the MD process without considering the influence of the heat taken away by evaporation. One promising new approach is by composite membranes which can absorb solar radiation and separate vapor from feed solution simultaneously [161], however up to now, this concept are still being studied, for example, under the framework of the project Extrasea, which involves the LISBP (thesis of Tianyi Zhang), as stated in Section I.3.3.

Aiming to design a small-scale compact seawater desalination unit for remote coastal areas or islands, an integrated module coupling vacuum membrane distillation (VMD) and a solar flat-plate collector (FPC) is presented, modeled and studied in this first chapter, with an extensive description of simultaneous mass and heat transfer for the hybrid solar-VMD module.

The conceived hybrid VMD-FPC module generally consists of a glass cover, an absorber-plate, a hydrophobic microporous membrane, and feed and vapor compartments on opposite sides of the membrane, functioning under different recycling and control strategies. The feed channel is beneath and in direct contact with the absorber-plate, so that the solar energy absorbed can be efficiently transferred to the seawater to be used for VMD process. The research approach is grounded in an extensive description of simultaneous mass and heat transfer of the VMD process with a coupled solar radiation modeling, for a comprehensive analysis of the design and sensitivities of the intensified VMD-FPC system. The solar energy calculations involve the estimation of solar radiation on the ground based on isotropic sky modeling, while the transmission, reflection, and absorption of solar radiation are further integrated and referred to as functions of incoming radiations and main properties of the solar FPC. The VMD model is

built both at the scale of the membrane (membrane pore model) and at the scale of the module (feed bulk longitudinal model), and is then coupled with the above-mentioned solar energy model.

Thus, several design and operating parameters under the influence of process dynamics are investigated at a small domestic scale to provide common-sense indications on performance and feasibility when a thermally autonomous configuration is targeted. The effects of varying solar and VMD parameters on daily water production, energy consumption and gained output ratio (GOR) are analyzed through several series of simulations. Additional aspects including performance sensitivities to (i) feed temperature levels, (ii) recycling system configuration (temperature-controlled batch regime vs. continuous MD operation) and (iii) heat recovery from condensation are also discussed and elucidated at the end.

II.1. Introduction (en français)

Comme décrit au chapitre I (Section I.3.3), on trouve dans la littérature quelques tentatives d'intégration d'apport d'énergie solaire thermique dans diverses configurations de distillation membranaire (DCMD, VMD, AGMD). Par exemple, des membranes planes ont été insérées dans l'espace situé sous la plaque d'absorption en d'un collecteur plan conventionnel (FPC) [153,154], et le liquide d'alimentation est ainsi chauffé directement par l'énergie solaire absorbée par le collecteur. Cependant, la dynamique des procédés liée à la variation temporelle du rayonnement solaire n'est pas prise en compte, et l'augmentation des performances par intégration de l'énergie solaire n'a été évaluée globalement qu'en s'intéressant au flux de perméat et ceci en considérant seulement certains paramètres clés de fonctionnement dans un procédé MD conventionnel. L'intégration de membranes à fibres creuses dans des absorbeurs solaires cylindriques pour le procédé VMD a également été proposée [156], mais l'approche proposée ne prend là-ici pas en compte une modélisation détaillée et dynamique de l'énergie solaire. De plus, la température de l'absorbeur du module intégré a été modélisée indépendamment du procédé de MD, sans prendre en compte la perte de chaleur par évaporation, ce qui peut biaiser les résultats. Une nouvelle orientation prometteuse consiste à utiliser des membranes composites capables à la fois d'absorber le rayonnement solaire, pour augmenter la température localement et de jouer leur rôle de contacteur membranaire, support de l'interface liquide/vapeur [161]. Cependant, ce type de concept imaginé dans les années 2010 est en cours d'étude et développement, par exemple dans le cadre du projet Extrasea, dont le LISBP est partenaire (thèse de Tianyi Zhang, en cours), comme indiqué à la Section I.3.3.

Dans le but de concevoir une unité compacte de dessalement d'eau de mer destinée à des zones côtières ou insulaires isolées, un module intégré couplant distillation membranaire sous vide (VMD) et un collecteur solaire plan (FPC) est présenté, modélisé et étudié dans ce chapitre, avec une description détaillée du transfert simultané de matière et de chaleur pour le module hybride solaire-VMD.

Le module proposé VMD-FPC hybride comporte globalement un couvercle en verre, une plaque d'absorption de la chaleur, une membrane microporeuse hydrophobe et un compartiment dans lequel circule le liquide d'alimentation et un compartiment recueillant la vapeur d'eau, de part et d'autre de la membrane compartiments. L'ensemble peut fonctionner avec des différentes stratégies de recyclage et de contrôle. Le compartiment d'alimentation est en dessous et en contact direct avec la plaque captant, pour que l'énergie solaire absorbée puisse être efficacement transférée dans l'eau de mer à traiter par VMD. L'approche scientifique repose sur une description détaillée du transfert simultané de matière et de chaleur du procédé VMD avec une modélisation couplée du rayonnement solaire, en vue d'une analyse complète de la conception du système intensifié VMD-FPC et de la sensibilité de ses grandeurs caractéristiques et de ses paramètres opératoires. Les calculs d'énergie solaire prennent en compte le rayonnement solaire au sol estimé par une modélisation du ciel isotrope, ainsi que la transmission, la réflexion et l'absorption du rayonnement solaire sont pris en compte et considérés comme fonctions des rayonnements entrants et des propriétés principales du FPC solaire. Le modèle VMD est construit à la fois à l'échelle de la membrane (modèle des pores de la membrane) et à celle du module (modèle longitudinal de l'alimentation), puis est couplé avec le modèle d'énergie solaire mentionné ci-dessus.

Ainsi, plusieurs paramètres de conception et de fonctionnement influencés par la dynamique du procédé sont étudiés pour l'application à un petit équipement (échelle d'une famille ou d'une petite communauté) pour fournir des indications raisonnables sur les performances et la faisabilité quand l'objectif visé est celui d'une configuration thermiquement autonome. Les effets de divers paramètres solaires et de la VMD sur la production d'eau journalière, la consommation d'énergie et le « gained output ratio » (GOR) sont analysés par plusieurs séries de simulations. En complément sont également discutés à la fin de ce chapitre notamment la sensibilité des performances aux (i) niveaux de température de l'alimentation, (ii) à la

configuration du système de recyclage (régime discontinu avec contrôle de température versus fonctionnement en continu) et (iii) à la récupération de chaleur de condensation.

II.2. Modeling of an integrated VMD-solar module

The configuration of an integrated solar - VMD module is shown in Figure II.1. The flat-box space for water channel under the absorber plate in a normal domestic solar FPC functions as the feed side of flat-sheet type VMD. Solar radiation penetrates the glazing cover, which is used to diminish the heat loss, and then gets absorbed by the absorber-plate. The feed side of VMD can therefore benefit from solar energy by the direct contact with the solar-heated absorber-plate. The whole collector is insulated by thermal insulation material and packaged as a normal FPC.

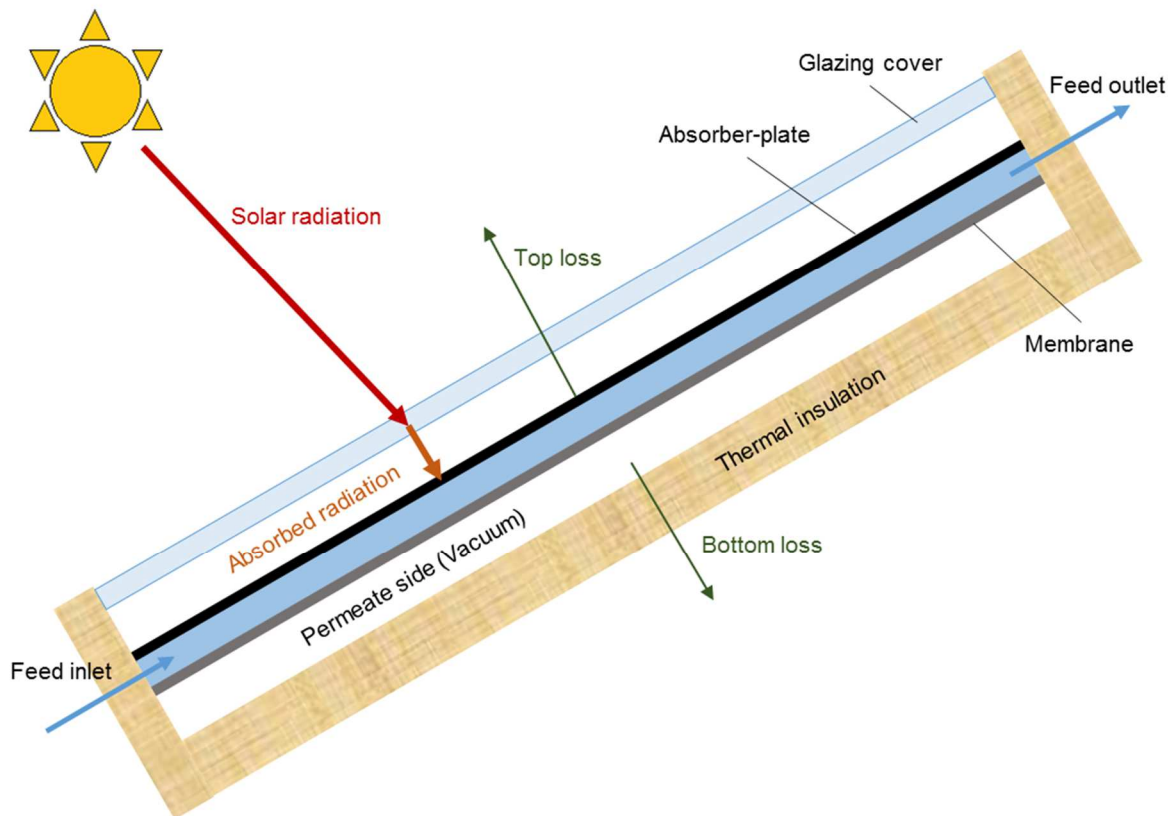


Figure II.1: Cross-sectional view of the proposed integrated VMD-FPC module

The dimensions, i.e. the length L , the thickness δ_f and the width W of the feed side channel, in such a rectangular box module are among the design parameters. Other design parameters are either solar absorption or VMD related. The former includes collector position (slope β and azimuth angle γ), properties of the glazing cover (refractive index n_c , extinction coefficient K ,

thickness δ_c and emittance ε_c), and properties of the absorber-plate (absorptance α_n and emittance ε_{ap}). The latter generally consists of vacuum pressure p_p , membrane Knudsen permeability coefficient K_m , feed flow Reynolds number and feed temperature T_f .

With all these parameters as the input conditions, the modeling of the whole module can be divided into three main parts: (i) solar radiation model, which calculates the final solar energy amount utilized by the module; (ii) membrane pore model, which describes the local permeate flux and polarization; (iii) feed bulk longitudinal model, which gives the profile along the flow direction. Globally, the modeling process of these three parts and the interconnections between them follow the flowchart in Figure II.2 below. Detailed modeling will be discussed in Section II.2.1 for the solar radiation model and II.2.2 for the membrane pore and feed longitudinal model.

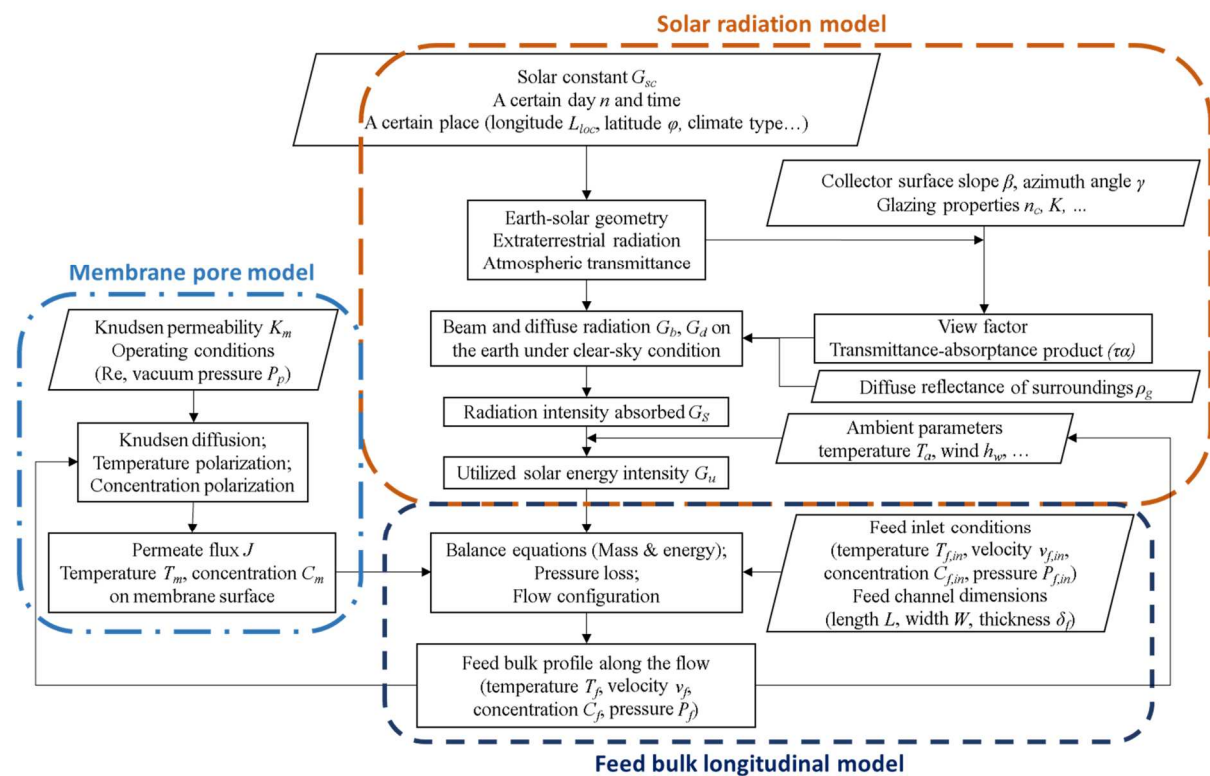


Figure II.2: Schematic of the modeling process of VMD-FPC module

II.2.1. Solar radiation modeling

II.2.1.1. Solar energy received

The World Radiation Center (WRC) has adopted 1367 W m^{-2} as the ‘‘Solar Constant’’ G_{sc} , which is the solar energy intensity received on a surface normal to the propagation of the

radiation, based on terrestrial solar radiation measurements [112]. Variations of G_{SC} exists because of the fluctuation of sun-earth distance. A simple equation to predict the extraterrestrial radiation incident on the plane normal to the radiation G_{on} on the n th day of the year [166] is given as,

$$G_{on} = G_{SC}(c_1 + c_2 \cos B + c_3 \sin B + c_4 \cos(2B) + c_5 \sin(2B)) \quad (1)$$

With $c_1 = 1.000110$, $c_2 = 0.034221$, $c_3 = 0.001280$, $c_4 = 0.000719$, $c_5 = 0.000077$, and where B is given by [112] on the n th day of the year,

$$B = (n - 1) \frac{360}{365} \quad (2)$$

Moreover, as illustrated in Figure II.3, it is necessary to determine the incidence of beam radiation on a surface, referred to as the included angle θ , representing the angle between the collector having a slope β and a surface azimuth angle γ , and the normal direction to G_{on} , given by Eq. 3 [112] as follows,

$$\cos \theta = \sin d \sin \varphi \cos \beta - \sin d \cos \varphi \sin \beta \cos \gamma + \cos d \cos \varphi \cos \beta \cos \omega + \cos d \sin \varphi \sin \beta \cos \gamma \cos \omega + \cos d \sin \beta \sin \gamma \sin \omega \quad (3)$$

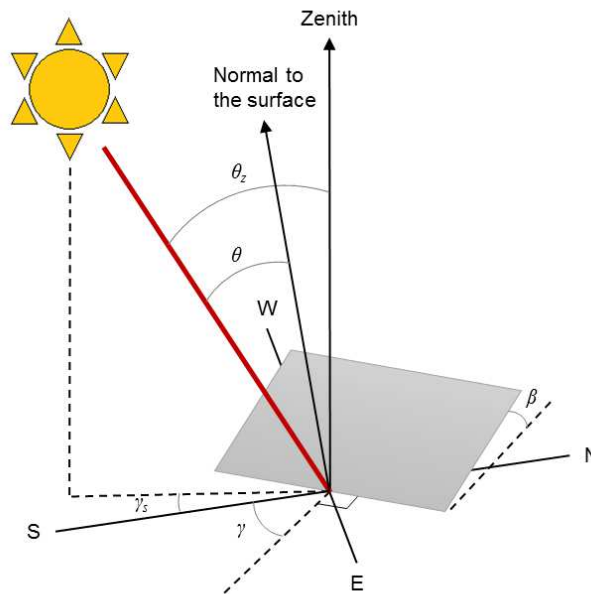


Figure II.3: Zenith angle, slope, azimuth angle, and solar azimuth angle for a tilted surface [112]

Where φ is the local latitude, ω is the hour angle rotating 15° per hour, and declination d represents the angular position of the sun at solar noon with respect to the plane of the equator [167]:

$$d = 23.45 \sin\left(360 \frac{284 + n}{365}\right) \quad (4)$$

After the extraterrestrial radiation being scattered and absorbed by the atmosphere, beam (τ_b) and diffuse (τ_d) radiation must be treated separately to obtain the final amount that reaches the ground. Assuming a standard cloudless “clear-sky”, the atmospheric transmittance for beam radiation τ_b is given as the ratio between G_{bn} and G_{on} [168]:

$$\tau_b = \frac{G_{bn}}{G_{on}} = a_0 + a_1 \exp\left(\frac{-k}{\cos\theta_z}\right) \quad (5)$$

Where G_{bn} stands for the beam radiation received on a surface that normal to the direction of the radiation. θ_z is the zenith angle (Figure II.3), which is the included angle between the vertical and the line to the sun, and can be calculated using Eq. 3 by assuming $\beta = 0^\circ$. The constants a_0 , a_1 and k for the standard atmosphere with 23 km visibility are found via correction factors from a_0^* , a_1^* and k^* that are applicable for altitudes less than 2.5 km through Eq. 6 [168].

$$\begin{cases} a_0^* = 0.4237 - 0.00821(6.0 - Al)^2 \\ a_1^* = 0.5055 - 0.00595(6.5 - Al)^2 \\ k^* = 0.2711 - 0.01858(6.5 - Al)^2 \end{cases} \quad (6)$$

Where Al is the altitude of the observer in kilometers, with correction factors as shown in Table II.1 below: $r_0 = a_0/a_0^*$, $r_1 = a_1/a_1^*$, $r_k = k/k^*$.

Table II.1: Correction factors for climate types [168]

Climate Type	r_0	r_1	r_k
Tropical	0.95	0.98	1.02
Midlatitude summer	0.97	0.99	1.02
Subarctic summer	0.99	0.99	1.01
Midlatitude winter	1.03	1.01	1.00

Hence, the clear-sky horizontal beam radiation can be obtained by,

$$G_b = G_{on}\tau_b\cos\theta_z \quad (7)$$

With regards to the diffuse radiation (τ_d), an empirical relationship between the transmission coefficients for beam and diffuse radiation for clear days was given by Liu and Jordan [169]:

$$\tau_d = \frac{G_d}{G_{on}\cos\theta_z} = 0.271 - 0.2939 \tau_b \quad (8)$$

Where G_d is the diffuse radiation on the horizontal surface.

Consequently, the total amount of solar radiation on the ground surface is the sum of G_b and G_d . In reality, the surface of the solar collector is often tilted to acquire more radiation. In order to take the inclination into consideration, the isotropic diffuse model can be assumed [170]: three components, i.e. beam, isotropic diffuse, and solar radiation diffusely reflected by the ground are included, while all diffuse radiation is considered isotropic. The surface of the collector has a view factor to the sky $F_{c-s} = (1+\cos\beta)/2$ and a view factor to the ground $F_{c-g} = (1-\cos\beta)/2$.

Assuming the surroundings to have a uniform diffuse reflectance of ρ_g for the total solar radiation, together with the geometric factor R_b representing the ratio of beam radiation on the tilted surface to that on a horizontal surface at any time, expressed as $\cos\theta/\cos\theta_z$, the whole radiation intensity received on the collector surface (W m^{-2}) can be expressed as,

$$G_T = G_b R_b + G_d F_{c-s} + (G_b + G_d)\rho_g F_{c-g} \quad (9)$$

II.2.1.2. Solar energy absorbed

Given their significant impact on solar collector performance, the transmission, reflection, and absorption of solar radiation were integrated and referred to as functions of the incoming radiation and the main characteristics of the solar collector, i.e. the thickness, refractive index, and extinction coefficient of the cover material, etc.

Transmittance of the cover τ and angular absorptance of the absorber plate α are essential for the calculation of absorbed radiation. For simplicity, a global value $(\tau\alpha)$ is used. The value of $(\tau\alpha)$ is very nearly equal to 1.01 times of the product of τ and α , which is a good approximation in most cases [112]. However, beam radiation, diffuse radiation and ground-reflected radiation (g) must be separately completed with different transmittance-absorptance corrections $(\tau\alpha)$. Hence, based on Eq. 9, the total solar energy absorbed can be expressed as,

$$G_s = G_b R_b (\tau\alpha)_b + G_d (\tau\alpha)_d \left(\frac{1 + \cos\beta}{2} \right) + (G_b + G_d) \rho_g (\tau\alpha)_g \left(\frac{1 - \cos\beta}{2} \right) \quad (10)$$

To determine the contribution of transmittance-absorptance into the beam radiation, referred as to $(\tau\alpha)_b$, first the value of α has to be estimated by a polynomial fit with respect to the absorptance α_n of the absorber-plate at normal direction. As formulated in Eq. 11, the transmittance τ of single-cover collectors can be resumed to a product of two transmittance situations: (i) only with reflection losses (τ_r in Eq. 12) [112] and (ii) only with absorption losses (τ_a in Eq. 14) [171].

$$\tau \cong \tau_a \tau_r \quad (11)$$

$$\tau_r = \frac{1}{2} \left(\frac{1 - r_{\parallel}}{1 + r_{\parallel}} + \frac{1 - r_{\perp}}{1 + r_{\perp}} \right) \quad (12)$$

$$r_{\perp} = \frac{\sin^2(\theta_2 - \theta_1)}{\sin^2(\theta_2 + \theta_1)}, \quad r_{\parallel} = \frac{\tan^2(\theta_2 - \theta_1)}{\tan^2(\theta_2 + \theta_1)} \quad (13)$$

$$\tau_a = \exp\left(\frac{-K\delta_c}{\cos\theta_2}\right) \quad (14)$$

Here r_{\perp} and r_{\parallel} are the perpendicular and parallel reflection of the incident radiation; θ_1 and θ_2 the angles of incidence and refraction with the refractive indexes of the medium n_1 and n_2 , respectively (Figure II.4); δ_c the thickness of the cover; and K the extinction coefficient of the cover material. r_{\perp} and r_{\parallel} were derived for smooth surfaces and are components of a radiation passing from medium 1 with a refractive index n_1 to medium 2 with a refractive index n_2 .

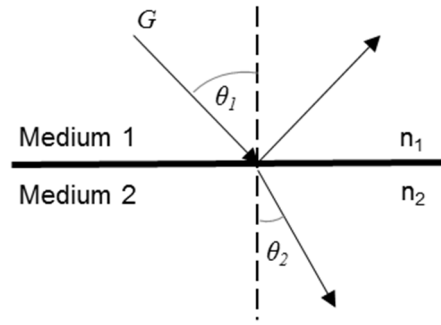


Figure II.4: Incidence and refraction angles in the interface of two media

Finally, $(\tau\alpha)_d$ for diffuse radiation is determined through a simplification by defining an equivalent angle for beam radiation that gives the same transmittance as for diffuse radiation [172]. The similar approach is applied to $(\tau\alpha)_g$ of the ground-reflected radiation. They can be formulated as follows,

$$\theta_{e,g} = 90 - 0.5788 \beta + 0.002693 \beta^2 \quad (15)$$

$$\theta_{e,d} = 59.7 - 0.1388 \beta + 0.001497 \beta^2 \quad (16)$$

II.2.2. Simultaneous modeling of heat and mass transfer for an integrated VMD-solar module

For an integrated module, the model is given at two interconnected levels (Figure II.5): (i) near the membrane surface and inside the pores, namely, “membrane pore model”, (ii) along the membrane surface on the shell side of VMD module where the feed solution is flowing, namely, “feed bulk longitudinal model”.

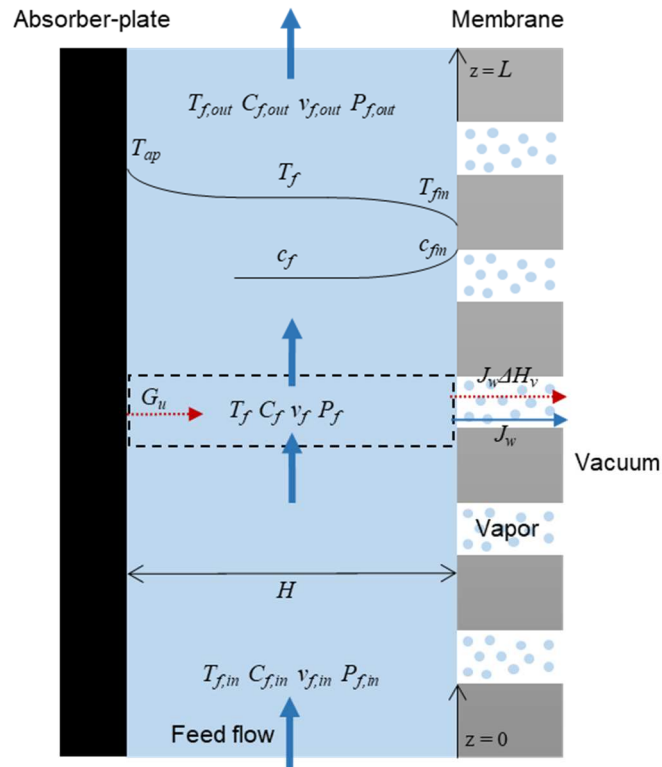


Figure II.5: Schematic of VMD modeling

II.2.2.1. Membrane pore model

At the scale of membrane pores, membrane pore model has previously been experimentally validated for a large range of operating conditions [22] and allows the description of the permeate flux as well as temperature and concentration polarization (temperature and concentration change near the membrane surface on the feed side). The originality in such an approach is to handle genuinely the solutions based on even high salt concentrations. The assumptions and considerations in this regard are: (i) no wetting, crystallization or biofouling on the membrane; (ii) vaporization occurring only at pore inlet where the liquid-vapor interface holds; (iii) mass transfer through the membrane due only to Knudsen diffusion of the water vapor inside membrane pores (collision of molecules with the pore wall) [80]; (iv) disregarding heat loss through the membrane and boundary layer on the permeate side due to the vacuum [40]; (v) considering heat transfer through the membrane due only to water vaporization; (vi) calculation of seawater properties based on its water molar fraction x_w and its activity coefficient γ_w obtained by the PHREEQC software (version 2.13.1, US Geological Survey) [18].

At this level, the consideration of “membrane pore model” consists of a local resolution of a system of three non-linear algebraic equations, i.e. Knudsen diffusion through the membrane

(Eq. 17), concentration polarization (mass balance at the membrane surface) (Eq. 18) and temperature polarization (heat balance at the membrane surface) (Eq. 19) [40]. The heat loss due to the permeation phenomenon through the membrane is principally characterized by the heat transferred through the boundary of the feed side, i.e. $h_f(T_f - T_{fm})$, which at steady state conditions, might be considered as equal to the amount of heat flux across the membrane ($J_w \Delta H_v$); thus, determined by the loss of latent heat of vaporization (Eq. 19).

As shown in Figure II.5, by providing the main feed side properties (T_f, C_f, v_f) at a given length of the module, the resolution of the “membrane pore model” allows for a local resolution of permeate vapor flux through the membrane (J_w), the concentration and temperature polarizations alongside the membrane, i.e. the temperature and concentration at the membrane surface (T_{fm}, C_{fm}).

$$J_w = \sqrt{M_w} K_m (\gamma_w x_w P_{T_{fm}}^0 - P_p) \quad (17)$$

$$J_w = \rho_f k_m \ln \left(\frac{C_{fm}}{C_f} \right) \quad (18)$$

$$J_w \Delta H_v = h_f (T_f - T_{fm}) \quad (19)$$

Where h_f is the convective heat transfer coefficient for the heat transfer from feed bulk to the membrane surface, which affects markedly the water flux through the membrane and is often estimated from Nusselt number correlations. The following correlations for the feed-side heat transfer coefficient in the rectangular channels are used (Eq. 20) for laminar regime [173] and transitional or turbulent regime [81]. On the other hand, the mass transfer coefficient k_m on feed side can also be estimated from these semi-empirical correlations given in Eq. 20 by replacing Nusselt number Nu and Prandtl number Pr in the equations into Sherwood number Sh and Schmidt number Sc [74], respectively defined in Eq. 21.

$$\text{Nu} = 1.86 \left(\frac{\text{RePr}d_h}{L} \right)^{0.33} \left(\frac{\mu_f}{\mu_m} \right)^{0.14} \text{ for } \text{Re} < 2300$$

$$\text{Nu} = \frac{\left(\frac{f}{8} \right) (\text{Re} - 1000) \text{Pr}}{1 + 12.7 \left(\frac{f}{8} \right)^{\frac{1}{2}} (\text{Pr}^{\frac{2}{3}} - 1)} \left[1 + \left(\frac{d_h}{L} \right)^{2/3} \right] (\text{Pr}_f / \text{Pr}_m)^{0.11} \text{ for } \text{Re} \geq 2300 \quad (20)$$

$$\text{With } f = (0.790 \ln \text{Re} - 1.64)^{-2}$$

$$\text{Nu} = \frac{h_f d_h}{\lambda} \quad \text{Pr} = \frac{c_p \mu}{\lambda} \quad \text{Sh} = \frac{k_m d_h}{D_{s-w}} \quad \text{Sc} = \frac{\mu}{\rho D_{s-w}} \quad (21)$$

Where d_h is the hydraulic diameter and L is the total length of the flow channel; μ , c_p , ρ and λ are the dynamic viscosity, heat capacity, density and thermal conductivity of the feed seawater, respectively. These seawater properties of the feed bulk and at the membrane surface are taken from the regressions in [18] obtained by physical property database. The regressions for the calculation of viscosity μ (Eq. 22), density ρ (Eq. 23), and thermal conductivity λ (Eq. 24) [18] are as follows, where all temperatures are in °C.

$$\mu = aT^2 + bT + c, \text{ for } 25^\circ\text{C} < T < 90^\circ\text{C} \quad (22)$$

With a, b, c indicated in Table II.2.

Table II.2: Coefficients a, b, c in Eq. 22 for the calculation of viscosity [18]

Concentration range (g L ⁻¹)	a (×10 ⁷ Pa s °C ⁻²)	b (×10 ⁵ Pa s °C ⁻¹)	c (×10 ³ Pa s)
0 ~ 30	1.16	-2.18	1.37
30 ~ 90	1.30	-2.51	1.57
90 ~ 165	1.49	-2.87	1.78
165 ~ 255	1.82	-3.49	2.15
255 ~ 300	2.19	-4.20	2.56

$$\rho = n_1 + n_2T + n_3T^2 + n_4T^3 + n_5T^4, \text{ for } 0^\circ\text{C} < T < 300^\circ\text{C} \quad (23)$$

With $n_i = a + bw + cw^2 + dw^3 + ew^4$ and a, b, c, d, e indicated in Table II.3.

Table II.3: Coefficients a, b, c, d, e in Eq. 23 for the calculation of density [18]

n_i	a	b	c	d	e
n_1 (kg m ⁻³)	1.001×10 ³	0.7666×10 ³	-0.0149×10 ³	0.2663×10 ³	0.8845×10 ³
n_2 (kg m ⁻³ °C ⁻¹)	-0.0214	-3.496	10.02	-6.56	-31.37
n_3 (kg m ⁻³ °C ⁻²)	-5.263×10 ⁻³	39.87×10 ⁻³	-176.2×10 ⁻³	363.5×10 ⁻³	-7.784×10 ⁻³
n_4 (kg m ⁻³ °C ⁻³)	15.42×10 ⁻⁶	-167.0×10 ⁻⁶	980.7×10 ⁻⁶	-2573×10 ⁻⁶	876.6×10 ⁻⁶
n_5 (kg m ⁻³ °C ⁻⁴)	-0.0276×10 ⁻⁶	0.2978×10 ⁻⁶	-2.017×10 ⁻⁶	6.345×10 ⁻⁶	-3.914×10 ⁻⁶

$$\lambda = aT^2 + bT + c, \text{ for } 25^\circ\text{C} < T < 90^\circ\text{C} \quad (24)$$

With a, b, c indicated in Table II.4.

Table II.4: Coefficients a, b, c in Eq. 24 for the calculation of thermal conductivity [18]

Concentration (g L ⁻¹)	a (×10 ⁶ W m ⁻¹ °C ⁻³)	b (×10 ⁵ W m ⁻¹ °C ⁻²)	c (×10 W m ⁻¹ °C ⁻¹)
0 ~ 30	-6.23	1.71	5.67
30 ~ 90	-6.15	1.69	5.76
90 ~ 165	-6.06	1.66	5.85
165 ~ 255	-5.94	1.62	5.96
255 ~ 300	-5.82	1.59	6.07

Besides, heat capacity c_p of the seawater is taken from the correlation in [174], as in Eq. 25. S is the salinity in g/kg, which equals 1000× w . Here T is in Kelvin instead.

$$c_p = (a_1 + a_2S + a_3S^2) + (b_1 + b_2S + b_3S^2)T + (c_1 + c_2S + c_3S^2)T^2 + (d_1 + d_2S + d_3S^2)T^3 \quad (25)$$

With all the coefficients indicated in Table II.5.

Table II.5: Coefficients in Eq. 25 for the calculation of heat capacity [174]

Subscript	a (kJ kg ⁻¹ K ⁻¹)	b (kJ kg ⁻¹ K ⁻²)	c (kJ kg ⁻¹ K ⁻³)	d (kJ kg ⁻¹ K ⁻⁴)
1	5.328	-6.913×10 ⁻³	9.6×10 ⁻⁶	2.5×10 ⁻⁹
2	-9.76×10 ⁻²	7.351×10 ⁻⁴	-1.927×10 ⁻⁶	1.666×10 ⁻⁹
3	4.04×10 ⁻⁴	3.15×10 ⁻⁶	8.23×10 ⁻⁹	-7.125×10 ⁻¹²

At last, D_{s-w} is the diffusion coefficient of the salt in the seawater (m² s⁻¹), which is estimated by the correlation in Eq. 26 with salt being assimilated as NaCl and pure water at 25°C being taken as the reference, adapted from Stokes-Einstein equation [175]. Here T is also in Kelvin.

$$D_{s-w} = 1.68 \times 10^{-9} \times \frac{T}{298.15} \times \frac{8.90 \times 10^{-4}}{\mu} \quad (26)$$

II.2.2.2. Feed bulk longitudinal model

Further, in order to establish longitudinal profiles in the module, i.e. the bulk flow in the feed side (Figure II.5), “feed bulk longitudinal model” is applied. It consists of a system of ordinary differential equations to predict the spatial variation of hydraulic pressure, temperature, flow

velocity and salt concentration along the flow direction (z), given for a flat-sheet type VMD. These equations are given below (Eq. 27-30), under steady-state conditions, representing mass balances, energy balance and momentum equation for the solution of the flow through the feed side, respectively.

$$\frac{d(\rho_f v_f)}{dz} = \left(\frac{-J_w}{\delta_f} \right) \quad (27)$$

$$\frac{d(C_f v_f)}{dz} = 0 \quad (28)$$

$$\frac{d(\rho_f c_p v_f T_f)}{dz} = \frac{G_u - J_w \Delta H_v}{\delta_f} \quad (29)$$

$$\frac{dP_f}{dz} = -f \left(\frac{\rho_f v_f^2}{2d_h} \right) - \rho_f g \sin \beta \quad (30)$$

Where δ_f is the thickness of the feed channel (m) and v_f , C_f , and T_f represent velocity, concentration and temperature ($^{\circ}\text{C}$) of the feed bulk, respectively. ΔH_v is the latent heat of water vaporization, f the Darcy friction factor, and d_h the hydraulic diameter in feed flow channel taken as $2(W\delta_f)/(W+\delta_f)$ for a flat-sheet type VMD module.

The description of heat transfer in VMD in Eq. 29 includes two phenomena: (i) permeation-related heat loss, (ii) the solar heating of feed. The heat loss due to the permeation phenomenon through the membrane is characterized by the latent heat of vaporization. This is to say that the decrease in the feed temperature or the sensible heat loss by the water permeate flux ($-J_w c_p T_{fm}$) can be neglected, compared to the amount of latent heat loss. Regarding the solar heating in the feed side, the final utilized solar energy G_u is determined as shown in Eq. 31, based on the amount of total solar energy absorbed G_S , given previously through Eq. 10.

$$G_u = G_S - U_t(\bar{T}_{ap} - T_a) - U_{bo}(T_p - T_a) \quad (31)$$

Where, U_t and U_{bo} are the heat loss coefficients through the top and bottom (edge loss neglected), \bar{T}_{ap} is the mean temperature of the absorber-plate, T_a is the ambient temperature, and T_p is the permeate temperature, which is assumed to be the same as T_{fm} [18]. T_{ap} can be estimated from heat transfer coefficient h_{ap} using the heat transfer correlations for rectangular

channels, together with the feed bulk temperature T_f and the total solar energy absorbed G_s , disregarding the heat capacity of the thin metallic absorber plate.

$$h_{ap}(T_{ap} - T_f) = G_s \quad (32)$$

U_{bo} can be calculated directly from the properties of thermal insulation material, referred to as the ratio between the insulation thermal conductivity λ_i and thickness δ_{bo} (Eq. 33). Regarding U_t , an empirical equation was proposed [176], formulated in Eq. 34, which fits for mean plate temperatures between the ambient and 200°C to within $\pm 0.3 \text{ W m}^{-2} \text{ K}^{-1}$.

$$U_{bo} = \left(\frac{\lambda_i}{\delta_{bo}} \right) \quad (33)$$

$$U_t = \left[\frac{N}{\frac{C}{\bar{T}_{ap}} \left[\frac{\bar{T}_{ap} - T_a}{N + F} \right]^e + \frac{1}{h_{wi}}} \right]^{-1} \quad (34)$$

$$+ \left[\frac{\sigma(\bar{T}_{ap} + T_a)(\bar{T}_{ap}^2 + T_a^2)}{\left(\frac{1}{\varepsilon_{ap} + 0.00591N h_{wi}} \right) + \left(\frac{2N + F - 1 + 0.133 \varepsilon_{ap}}{\varepsilon_c} \right) - N} \right]$$

With,

$$F = (1 + 0.089 h_{wi} - 0.1166 h_{wi} \varepsilon_{ap})(1 + 0.07866 N)$$

$$C = 520 (1 - 0.000051 \beta^2) \text{ for } 0^\circ < \beta < 70^\circ; C = 520 (1 - 0.000051 \times 70^2) \text{ for } 70^\circ < \beta < 90^\circ$$

$$e = 0.430 \left(1 - \frac{100}{\bar{T}_{ap}} \right)$$

Where, N is the number of covers (1-cover module in this thesis), ε_c and ε_{ap} are the emittance of the cover and the absorber plate, and h_{wi} is the heat transfer coefficient of wind.

II.3. Configuration for a dynamic recycling batch system

A first configuration was considered (Figure II.6), which consists of a direct recycling loop over the module with a temperature-based control to operate the VMD process at a certain temperature level, or simply let the temperature of the feed side in the module be naturally determined by the interaction between the amount of solar radiation absorbed and the amount of heat loss due to the vaporization on the membrane surface.

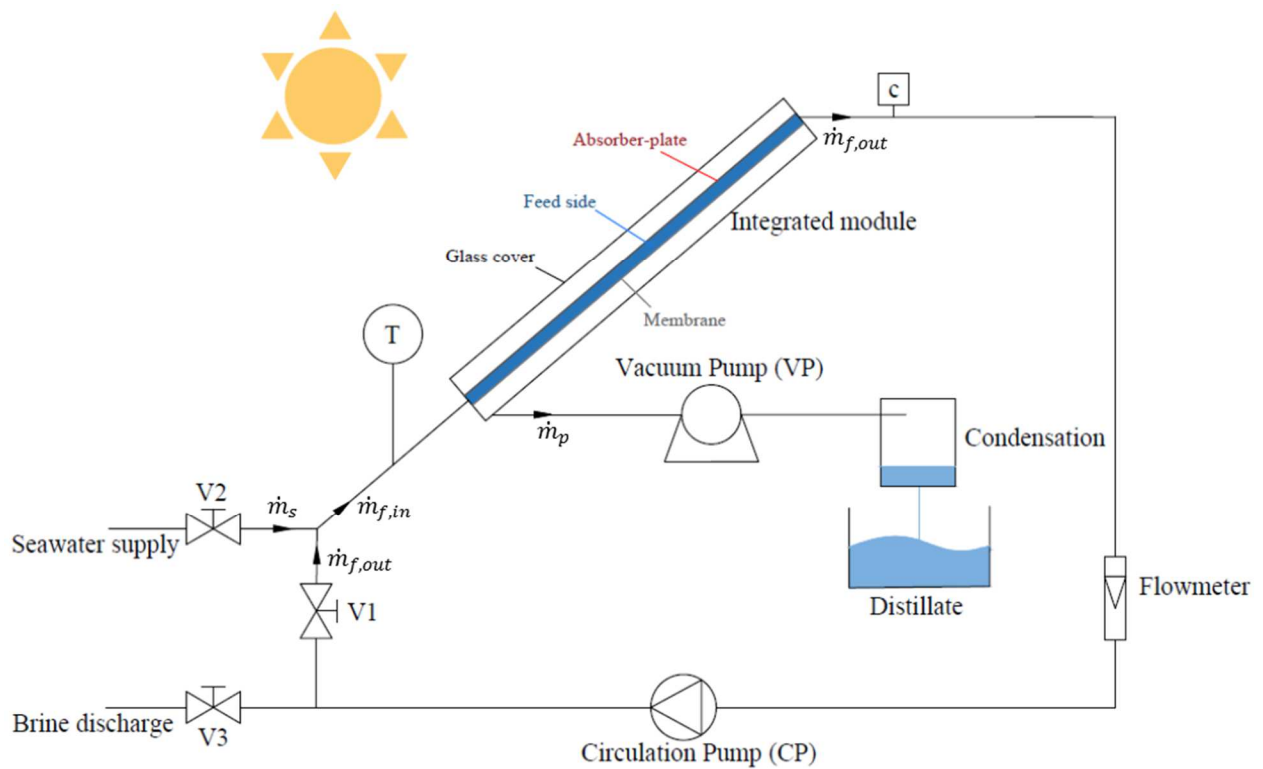


Figure II.6: Configurations for the recycling batch system

As shown in Figure II.6, the feed side of the module is filled by the seawater source via valve V2; while the circulation pump (CP) conducts the feed through valve V1 during the recirculation phase, i.e. no brine discharge (valve V3 closed). In this fashion, the feed in the collector is circulated under the absorber-plate which is heated by solar radiation through the glazing cover, forming the same configuration as a normal FPC. The water vapor is then sucked out from membrane pores by the vacuum pump (VP), where a reasonable vacuum pressure is maintained on the permeate side.

Since the seawater source is introduced to compensate the loss of mass flow rate exiting the module due to the vaporization and permeation of pure water via V2, the salt concentration is continuously increasing, when no brine discharge is taken place. Therefore, when the salt concentration reaches a certain preset level, the brine has to be evacuated through V3 and compensated equally in mass by new feed seawater inlet via V2. On the permeate side, it is worth to note that, unlike certain recycle configurations reported in the literature where the permeate goes first to a condenser or a cold trap [40,177,178], here the permeate flux is directly pumped out by the vacuum pump and gets collected. This is because in our experimental

practice, it was found that adding a condensing device before the vacuum pump introduces more joints and valves in the vacuum, which leads to more probability of leakage and other problems. Moreover, an effective condensation of the water vapor within a cold trap before the vacuum pump is costly due to the low water saturation temperature under vacuum pressure, and requires expensive equipment and consumables such as liquid nitrogen, which is not much accessible in remote places.

II.3.1. Temperature-based control strategy for the recycling batch system

As described earlier, firstly, the recycling configuration (Figure II.6) was undertaken to control reasonably the temperature level on the feed side and to establish its influence on the quality of separation, as seen in separated solar-powered MD system [133].

Theoretical approximations reveal that the heat loss due to the latent heat of vaporization, when operating under normal continuous MD permeate flux ($\sim 10 \text{ kg m}^{-2} \text{ h}^{-1}$) with no supplementary supply heat, is far greater than the amount of solar energy that can be utilized for a same surface of collector even under optimal solar conditions. Accordingly, the intermittent VMD operation following a designed control strategy was modeled and tested.

The control strategy is illustrated in Figure II.7 and can be described as follows. After filling the whole module with seawater, if the sensor temperature of the feed inlet (T in Figure II.6) is not higher than a preset value T_{max} , all the pumps are turned off, enabling the collector to function under solar absorption stand-alone, i.e. the free convection regime. Feed temperature thus rises while no permeate flux occurs. Meanwhile, if it is already over a preset system stop time t_{ss} , the whole system stops operating until a preset start time t_{sr} in the next morning and then restarts. When T becomes higher than T_{max} during the free convection regime, both pumps (CP and VP) are turned on and vacuum is created on the permeate side with the feed seawater circulating in the collector, water vaporizes and is transferred through the membrane pores as vapor. In the meantime, if the salt concentration is above a certain limit value C_{limit} , the feed is evacuated (brine discharge) and then gets refilled by seawater source with the temperature T_s and the concentration C_s . As discussed before, the feed temperature normally drops while running VMD because of the insufficiency of solar thermal energy, thus when T is lower than a certain minimum value T_{min} , all pumps are shut off and the system goes back to free convection driven by solar utilization, in order to raise, once again, the feed temperature.

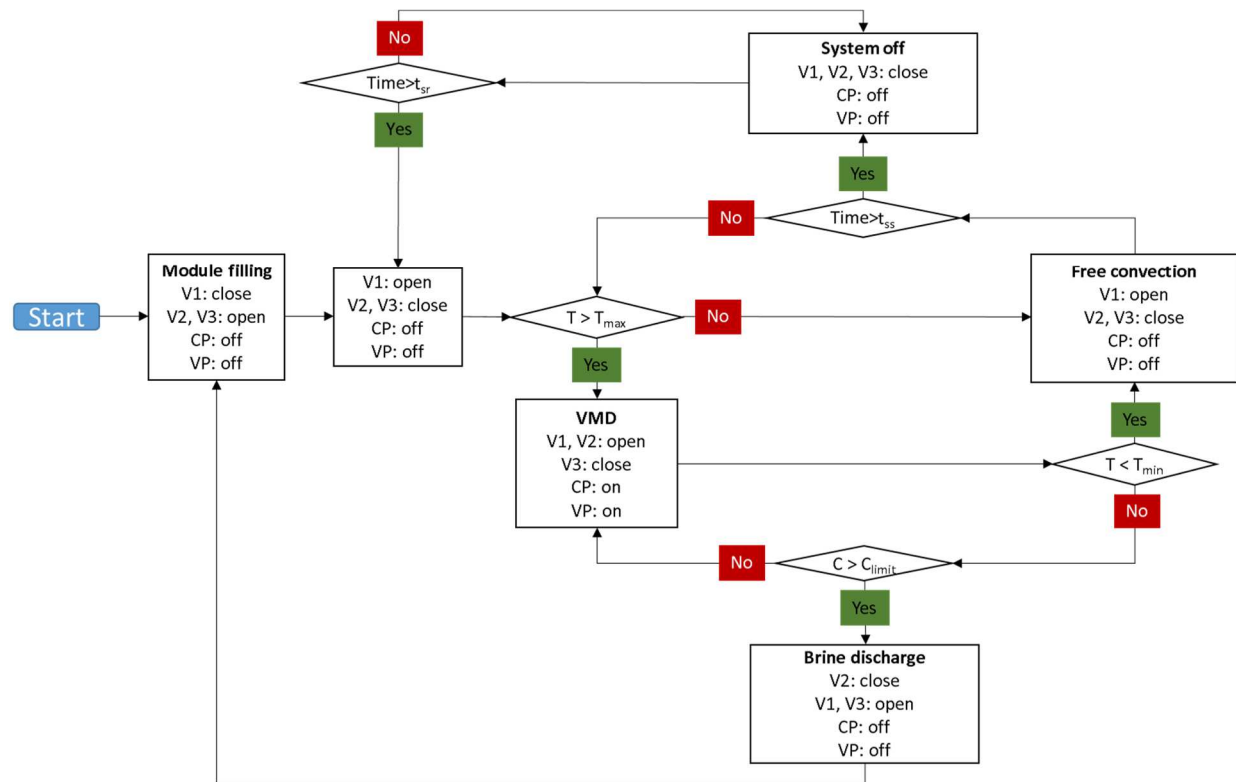


Figure II.7: Control strategy for the recycling batch system

II.3.2. Dynamics for the recycling batch system

The process dynamics was studied for time-varying steady-state phases. Hence, a set of differential equations was established that describes temporal variations related to the recycle system in order to determine the time-dependent boundary conditions of the VMD-solar module (Table II.6). Such an approach is relevant, because it allows not only for the study of process performance over a wide range of operating conditions, but also for the study of process design including the recycling strategy, and this comes with reasonable complexity in terms of numerical resolution.

Overall, the temporal terms in Table II.6 describe the accumulation of the recycling system in total mass (m), the energy balance and the partial mass balance of salt, respectively. For a direct recycling loop over the module, no mass accumulation is globally observed. This is due to a continuous compensation for water loss throughout the permeation (\dot{m}_p) with an equal mass of supply seawater (\dot{m}_s) through V2 in Figure II.6 ($\dot{m}_s = \dot{m}_p = J_w A_C$). The overall change in energy content of the recycle system is likewise time-dependent, due to the overall amount of solar energy utilized, sensible and vaporization heat loss along the module by permeation, and due to the introduction of supply seawater as well. Given the constancy of flow rate across the

module due to the permanent compensation of water permeation by supply seawater, the time-dependent increase in salt concentration is described by the amount of the supply seawater newly introduced into the system with a constant concentration of C_s .

Table II.6: Dynamics of the recycling batch system

$$\frac{dm}{dt} = \dot{m}_s - \dot{m}_p = 0 \quad (35)$$

$$\frac{d(c_p m T)}{dt} = G_u A_C + c_p \dot{m}_s T_s - J_w A_C (c_p T_{fm} + \Delta H_v) \quad (36)$$

$$\frac{dC}{dt} = \left(\frac{C_s}{\rho_s}\right) \left(\frac{J_w}{\delta_f}\right) \quad (37)$$

II.3.3. Solution procedure

All models were programmed under Python (version 2.7). To handle the time-varying steady-state phases, first, a system of differential-algebraic equations (DAEs) was solved over the module's length. This includes a set of ordinary differential equations (ODEs) for the feed side, namely the feed bulk longitudinal model (Eq. 27-30), that was discretized over the module's length via finite differences and solved in conjunction with the set of algebraic equations describing the membrane pore model (Eq. 17-19). Second, to account for dynamics relative to the recycling systems, Scipy ODE package under Python using the Real-valued Variable-coefficient Ordinary Differential Equation solver (Isoda) [179] was used to handle the dynamic balance equations presented in Table II.6. The integration through Isoda package for the dynamic recycle systems was chosen to automatically readjust time step-sizes with relevant consistency according to a space discretized over the module's length. Furthermore, the package provides an automatic method switching between the implicit Adams method for non-stiff problems and another method based on backward differentiation formulas (BDF) for stiff problems.

II.3.4. Performance indicators

Assuming cloudless weather during a one-day operation (Aug 1st, 8h00 to 20h00), two indicators were initially utilized to evaluate the system performance: Daily freshwater productivity D_p (kg m⁻²) and specific pumping energy consumption SEEC (kWh m⁻³), which is the ratio of electrical energy supplied for pumping to the total volume of freshwater produced.

Specifically for VMD, it consists of the consumption of both the circulation pump (CP) and the vacuum pump (VP).

The energy requirement for CP in Figure II.6 was determined from the total pressure loss ΔP between the inlet and outlet of the collector, as formulated below.

$$\dot{P}_{cp} = \frac{F_V \Delta P}{\eta_{cp}} \quad (38)$$

Where F_V is the volumetric flow rate on the feed side ($\text{m}^3 \text{s}^{-1}$), and η_{cp} the efficiency of CP which is taken as 0.7, and \dot{P}_{cp} is the circulation power (W).

Assuming a well-sealed system, the energy requirement for VP is proportional to the amount of permeated water vapor flux (J_w). Assuming an adiabatic compression from the vacuum pressure P_p to the atmosphere pressure P_{atm} , the following equation has been derived in the literature [180]. Here, the permeate temperature T_p is supposed to be the same as the temperature at the membrane surface on the feed side (T_{fm}) by the assumption of no conductive heat loss through the membrane.

$$\dot{P}_{vp} = \frac{J_w A_C}{M_w \eta_{vp}} R T_p \left(\frac{\gamma}{\gamma - 1} \right) \left[\left(\frac{P_{atm}}{P_p} \right)^{1-1/\gamma} - 1 \right] \quad (39)$$

Where A_C is the membrane area as well as the collector area (m^2), M_w the molecular weight of water (kg mol^{-1}), R is the ideal gas constant ($8.3145 \text{ J mol}^{-1} \text{ K}^{-1}$), γ is the adiabatic index, and \dot{P}_{vp} is the vacuum pump power (W). Vacuum pump efficiency η_{vp} is taken as 0.75.

Besides, two additional performance parameters, namely gained output ratio (GOR [164], Eq. 40) and water recovery rate RR (Eq. 41), were indeed included to enrich further discussions on the interest of solar autonomous devices and of VMD for seawater desalination. The value of GOR is formulated by the ratio of energy utilized to produce freshwater (latent heat for vaporization) and all the energy input [164], including both absorbed solar energy and pumping energy. It is worth to note that the electricity consumption by pumping was not always taken into the calculation of GOR in the literature [181–183], while in the author's opinion, all the energy consumption should be considered as the energy input to enable the GOR to fairly

represent the energy efficiency of MD processes, especially for VMD when vacuum pumps are installed. For the recycling batch system, RR is defined as the total volume of water produced against the total volume of seawater supplied between two brine discharges. Aiming a thermally autonomous system, no auxiliary heating device was considered in the current design.

Consequently, GOR is obtained from:

$$GOR = \frac{D_p A_c \Delta H_v}{\int (\dot{P}_{cp} + \dot{P}_{vp} + G_s) dt} \quad (40)$$

While RR is calculated as:

$$RR = \frac{V_{D,total}}{V_{s,total}} \times 100\% \quad (41)$$

Where $V_{D,total}$ and $V_{s,total}$ are the total volume of produced distillate and supplied seawater during the whole operation between two brine discharges (m^3).

In this chapter, the value of RR is fixed for all occasions because of the total recirculation of the feed and brine discharge only happens when the set value of C_{limit} is attained, given as,

$$RR = 1 - \frac{C_s}{C_{limit}} \quad (42)$$

II.4. Results and discussions

II.4.1. Consistency of the models: solar radiation and VMD

The solar radiation model in this paper enables the acquirement of solar energy reaching the absorber in sunny days at any time anywhere in the world. It was compared with the daily solar radiation calculation of the online available Photovoltaic Geographical Information System 5 (PVGIS 5) [184]. The solar radiation received by a collector facing south (azimuth angle is 0°) with an inclination of 25° in August at Toulouse was taken from PVGIS 5 as well as calculated by the current model on the average day of month (Aug 16th) [112], which is shown in Figure II.8. Here solar time is defined as the time based on the apparent angular motion of the sun across the sky with solar noon being the time the sun crosses the meridian of the observer [112].

As illustrated in Figure II.8, the solar radiation model in this thesis was proved to be consistent to describe the daily variation of solar radiation received when compared with the actual data from PVGIS 5 (average relative deviation of 7.3%).

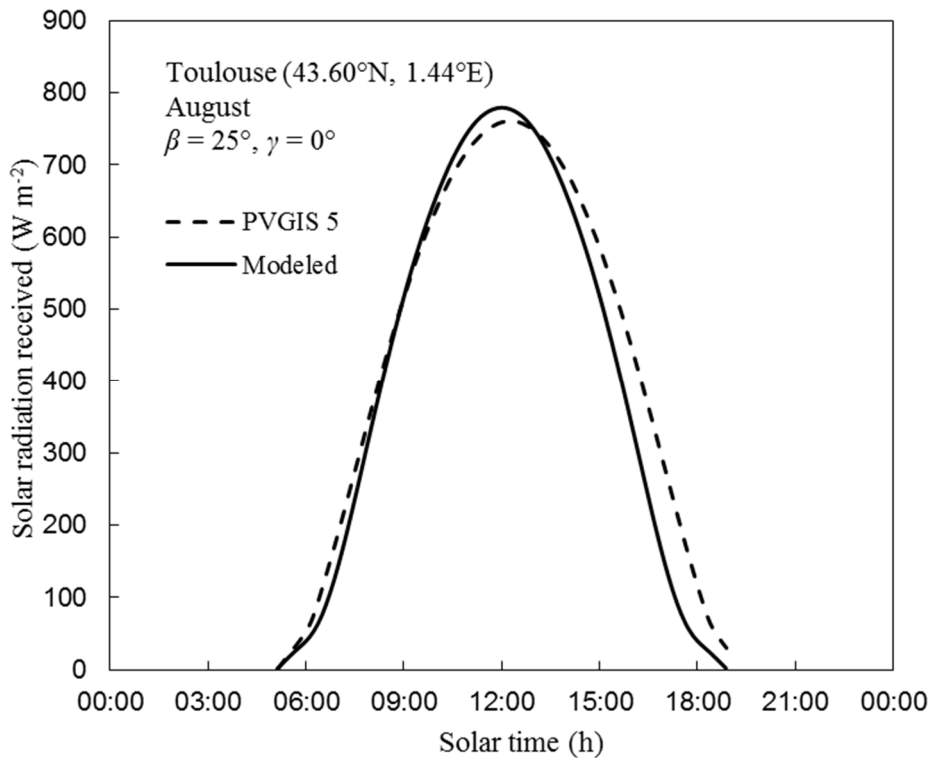


Figure II.8: Comparison between the theoretical modeling of solar radiation on a fixed absorber with the data provided by the Photovoltaic Geographical Information System 5 (PVGIS 5)

Although the VMD model coupling heat & mass transfer at the boundary layer of the membrane on the feed side has already been validated before in a large range of operating conditions [22], it was again compared with results provided by a newly-built experimental VMD device at lab-scale ($K_m = 3.61 \times 10^{-6} \text{ s mol}^{1/2} \text{ m}^{-1} \text{ kg}^{-1/2}$). The predicted permeate flux was compared to experimental results using Temperature Variation (TV) method [185] at the steady-state phase from 38°C to 52°C, as shown in Figure II.9. Simulation results showed a good coherence between the predicted and the experimental data (average relative deviation of 6.6%). However, the deviation became more significant for lower permeate flux, below $5 \text{ kg m}^{-2} \text{ h}^{-1}$. This can be explained by the fact that lower water vapor flux at lower feed temperatures might induce larger measurement relative error, because other disturbance became relatively more significant compared to that under higher permeate flux at higher feed inlet temperatures.

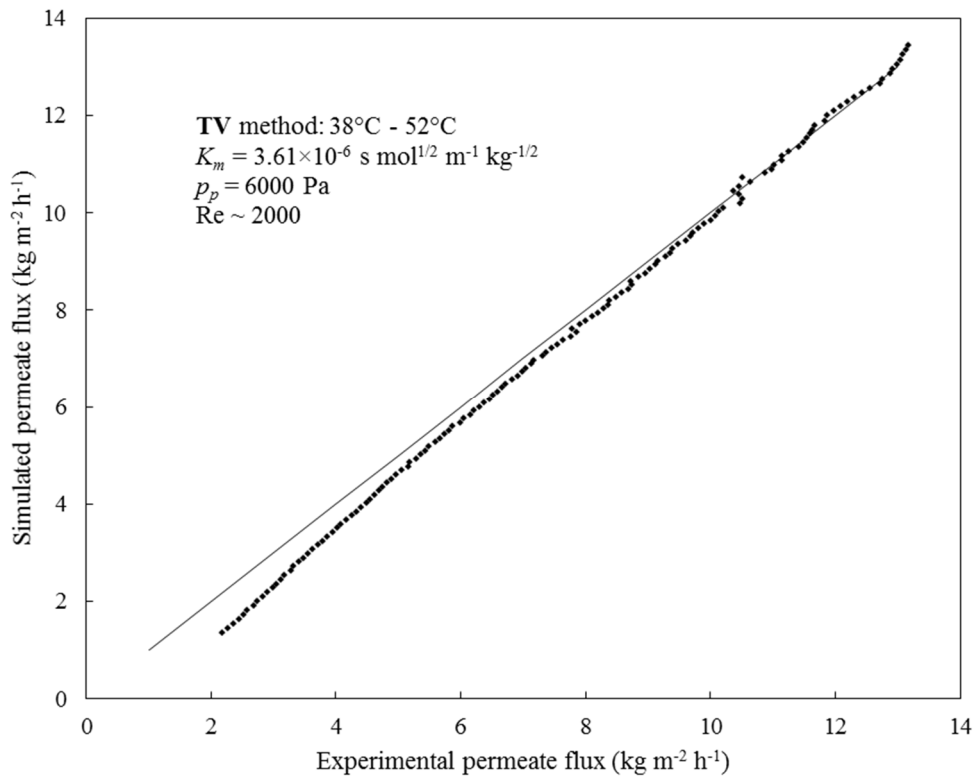


Figure II.9: Comparison between experimental and predicted permeate flux from VMD model

II.4.2. General set of parameters for a daily varying operation

Table II.7 provides an exhaustive list of parameters considered in this chapter, with all the parameters firstly set to common values to observe the general performance of the system. Given these reference values, further analyzes on parameters will be presented afterwards.

As described earlier, Toulouse in France was chosen as the location together with all corresponding local parameters (Table II.7). Ambient temperature was assumed to have a sinusoidal variation with the maximum 35°C at solar noon and the minimum 20°C at solar midnight on the 1st August. A glass cover with the thickness of 2 mm was considered for the integrated module, whose optical properties are 1.5 for refractive index, 0.88 for emittance and 16 m⁻¹ for extinction coefficient. The heat conduction inside the absorber-plate was assumed to be negligible because it is often a thin plate made from metal with good heat conductivity. The absorptance at normal direction was set to be 0.93 with the consideration of coating on the absorber-plate which is the case in the fabrication of solar collectors. Heat loss through the insulation was assumed to be 0.9 W m⁻² K⁻¹. It should also be mentioned that the insulation covers the side and the bottom of the whole integrated module with the surface area of 0.5 m × 0.7 m and the inclination of 25° facing south.

Table II.7: Parameters of the integrated VMD-solar module

Parameters	Values	Description	
Location (Toulouse)	L_{loc}	358.56°	Longitude in degrees west, $0^\circ < L < 360^\circ$
	φ	43.60°	Latitude, north positive, $-90^\circ < \varphi < 90^\circ$
	Al	150.0 m	Altitude of the location
	h_{wi}	10 W m ⁻² °C ⁻¹	Heat transfer coefficient of the wind
	r_0, r_1, r_k	0.97, 0.99, 1.02	Correction factors for midlatitude summer
	ρ_g	0.2	Diffuse reflectance of the surroundings
	T_{amax}	35°C	Highest ambient temperature
	T_{amin}	20°C	Lowest ambient temperature
Collector properties	n_c	1.5	Refractive index of the cover
	K	16 m ⁻¹	Extinction coefficient of the cover
	δ_c	0.002 m	Thickness of the transparent cover
	ε_c	0.88	Emittance of the cover
	α_n	0.93	Absorptance in normal direction
	ε_{ap}	0.1	Emittance of the absorber-plate
	U_{bo}	0.9 W m ⁻² °C ⁻¹	Heat loss coefficient of the insulation
Collector positions & dimensions	β	25.0°	Slope of the solar collector
	γ	0.0°	Azimuth angle of the solar collector
	W	0.5 m	Width of the collector
	δ_f	0.005 m	Thickness of the feed channel
	L	0.7 m	Length of the collector
Membrane properties	K_{mref}	3.7×10 ⁻⁶ s mol ^{1/2} m ⁻¹ kg ^{-1/2}	Knudsen permeability coefficient at 20°C
	P_p	5.0×10 ³ Pa	Permeate pressure (Vacuum pressure)
System operation parameters	C_s	35 g L ⁻¹	Salt concentration of the seawater supply
	T_s	25°C	Temperature of the seawater supply
	T_{min}	40°C	Low switching temperature
	$T_{interval}$	10°C	$T_{max} - T_{min}$, operating temperature interval
	C_{limit}	300 g L ⁻¹	The highest operating salt concentration
	Re (40°C)	600	Circulation Reynolds number when at 40°C

For the VMD operation parameters, the Knudsen permeability coefficient of the adopted membrane was taken as a common value of 3.7×10⁻⁶ s mol^{1/2} m⁻¹ kg^{-1/2} [22] inside a feed channel with a thickness of 5 mm, while vacuum pressure on the permeate side was initially set to 5000 Pa. Circulation flow rate was initially fixed to a relatively low value which equals a Reynolds number of 600 at 40°C, due to the conclusion of the preference of lower flow rate

from other works on solar-powered MD systems [69,160]. Based on the control strategy described in Section II.3.1, switching temperatures T_{min} and T_{max} for the control strategy were initially set to 40-50°C with an operation interval of 10°C. Considering the ability of VMD to further concentrate the brine to a relatively high level [40], C_{limit} is set to be 300 g L⁻¹, giving a water recovery rate RR equal to 88.3%.

II.4.3. Performance under temperature-controlled batch regime

For a VMD-solar module under temperature controlled regime, daily variations of the system (from 8 am to 8 pm), including feed side temperature T_f , concentration C_f , permeate flux J_w , and solar radiation falls on the surface of the module G_T and further absorbed by the module G_S , are shown in Figure II.10.

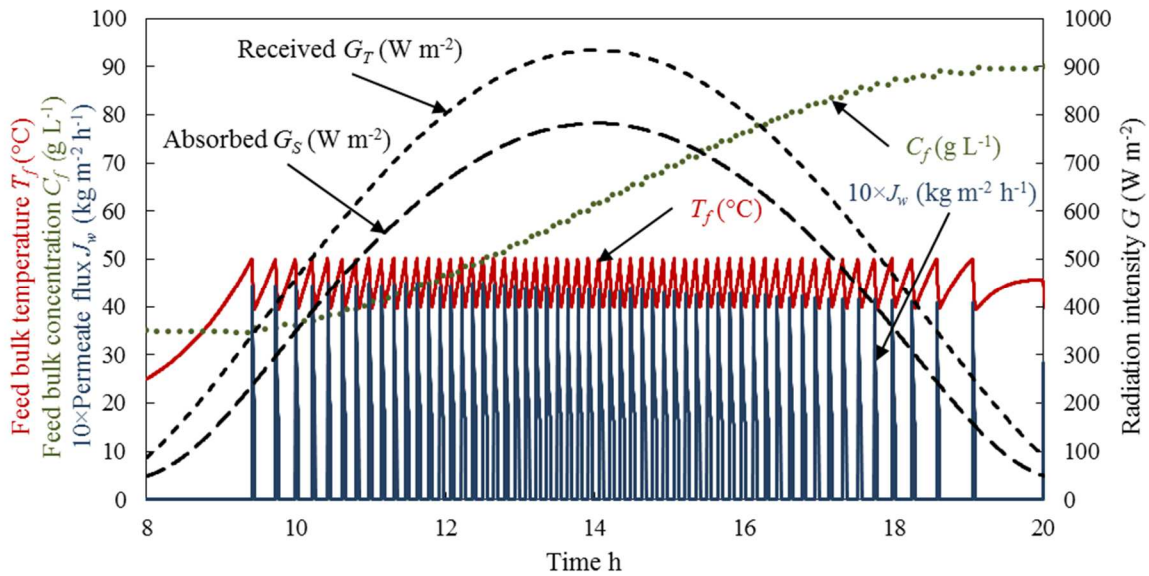


Figure II.10: Daily variation of solar radiation, feed temperature, feed concentration and permeate flux when operating under controlled temperature (Toulouse, Aug 1st; $\beta = 25^\circ$; $K_m = 3.7 \times 10^{-6} \text{ s mol}^{1/2} \text{ m}^{-1} \text{ kg}^{-1/2}$; $P_p = 5000 \text{ Pa}$; $Re(40^\circ\text{C}) = 600$)

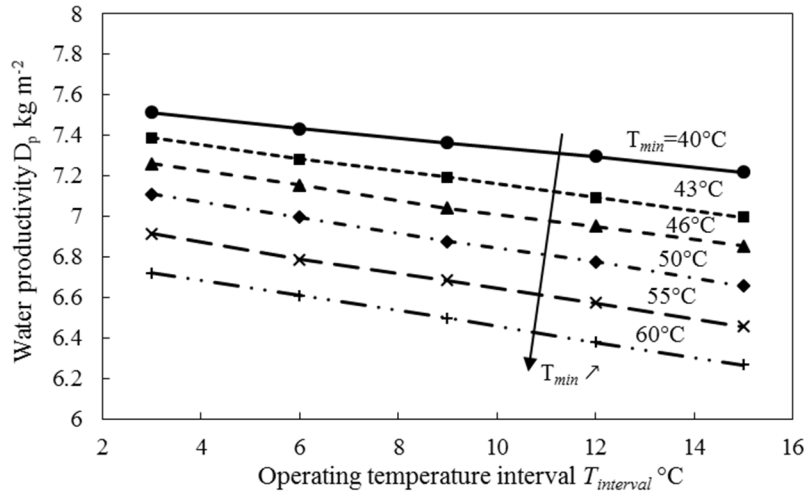
Feed temperature T_f varied between T_{min} (40°C) and T_{max} (50°C) with the switching of the pumps, and concentration C_f accumulated intermittently as water only vaporized to the permeate side when the system operated with VMD process. The permeate flux J_w only occurred when the pumps were switched on with T_f at T_{max} . The switching frequency became higher near noon time on account of the shorter time to raise the feed temperature to T_{max} with stronger G_T and G_S . Furthermore, we can see that solar energy is never enough to sustain the

thermal need of the VMD process at the given operating conditions, as T_f was always falling to T_{min} after pumps were turned on. Finally, the daily productivity D_p of this simulation recorded $7.36 \text{ kg}\cdot\text{m}^{-2}$ while the specific pump energy consumption being 237.9 kWh m^{-3} . GOR value of this single-stage system without heat recovery was 0.673. No “brine discharge” process happened during the 1-day operation because the salinity C_f reached to 90 g L^{-1} at the end of the operation, far from C_{limit} .

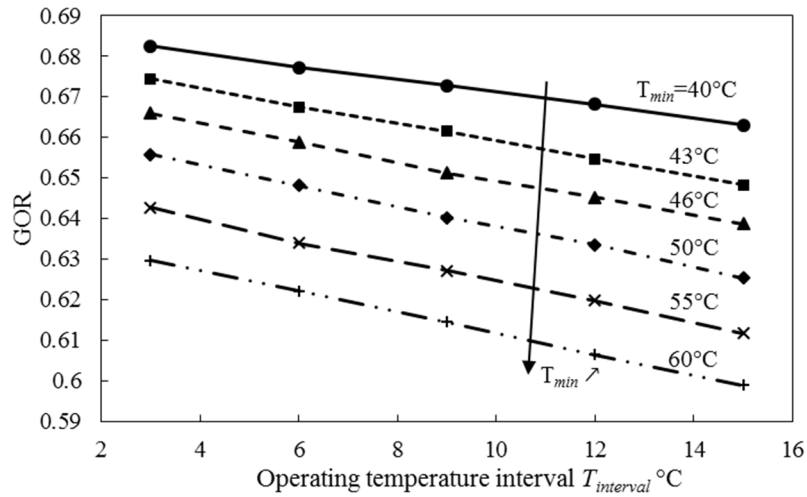
Throughout the control strategy, as shown in Figure II.7, the average operating temperature on the feed side was maintained between two limit temperatures T_{min} and T_{max} . As explained in Section II.3.1, both vacuum and circulation pumps start functioning when the feed temperature reaches T_{max} . Contrarily, when the temperature drops to magnitudes lower than T_{min} , both pumps stop functioning in order to provide the free convection stand-alone regime without permeation. Therefore, those switching temperatures become essential factors that influence system performance.

Several simulations were carried out to correlate the global performance of the membrane distillation process to the temperature level along the module, which is determined by T_{min} and $T_{interval}$ ($T_{max} = T_{min} + T_{interval}$). Results are shown in Figure II.11, other parameters remained the same as listed in Table II.7.

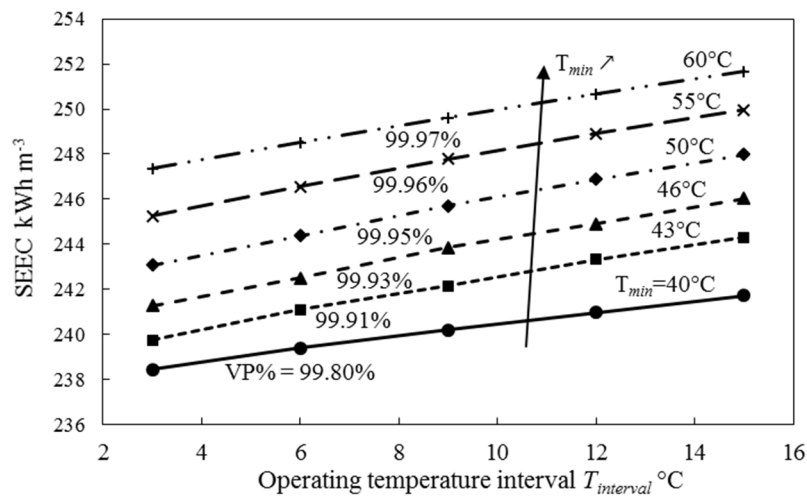
Surprisingly, better performance with higher D and GOR was achieved for lower temperature levels i.e. lower T_{min} and lower $T_{interval}$ (Figure II.11 (a) and (b)). When decreasing T_{min} from 60°C to 40°C , D_p and GOR would increase by 13.4% and 9.5%, on average. Similarly, in Figure II.11 (c) a slight performance improvement with 3.8% smaller SEEC was observed when operating at lower temperature levels. Hence, lower working temperatures were identified to be more favorable, as opposed to conventional MD systems with no use of direct solar heating. Such a surprising preference for low working temperatures is due to higher overall heat loss when operating under relatively elevated temperatures. The latter results in a decrease of the utilized solar energy and an increase in the specific volume of the water vapor at membrane surface temperature (the temperature at the gas-liquid interface on the feed side is taken equal to the temperature on the permeate side), that induces, in its turn, more energy requirements to provide the vacuum. In addition, a major consumption of vacuum pump was observed for the current configuration presented in Section II.3 (Figure II.11 (c)).



(a)



(b)



(c)

Figure II.11: Influence of operating temperature levels on the module performance of (a) water productivity D_p ; (b) GOR; (c) SEEC

II.4.4. Improved performance under continuous MD operation

After the analysis provided in Section II.4.3, it was revealed that as long as enough pressure driving force is provided, lower feed temperature yielded better performance. Such an observation brought the idea of a possible performance improvement under continuous running without temperature-based control strategy, which is a particular specificity of an integrated direct solar-VMD module. In order to obtain the lower feed temperature the possible, pumps were let run continuously. In this fashion, feed temperatures were stabilized nearly above the bubble temperature that corresponds to the vacuum pressure on the permeate side, yielding a relatively low permeate flux. That is to say, the vacuum pressure determined, to some extent, the feed temperature.

Daily variation of the system is illustrated in Figure II.12. All parameters remained the same as listed in Table II.7, except the switching temperatures being excluded. Different from the variation under controlled temperature, the module under continuous regime yielded low permeate flux J_w which tended slowly to increase with the gradual increment in the amount of solar radiation. Feed temperature T_f faced a small accordance with the solar radiation variation; however, its value stayed more or less stable during the day. Feed concentration was indeed accumulating during the whole day with almost the same trend as in Figure II.10. In this continuous regime, the final water productivity D_p and GOR achieved was 7.98 kg m^{-2} and 0.712, which were higher by 8.4 % and 5.8 %, respectively, when compared with the recycling batch operation. On the other hand, the specific pump energy consumption showed no clear difference. Based on the assumption of no system leakage, the consumption of vacuum pump was determined according to the amount of water flux obtained across the membrane. Additionally, a continuous functioning regime added extra energy requirement for the circulation pump, which, however, was much smaller than that of the vacuum pump, as described before. Therefore, a greater overall efficiency together with higher water productivity with nearly no significant extra energy consumption was observed when operating under continuous functioning of pumps.

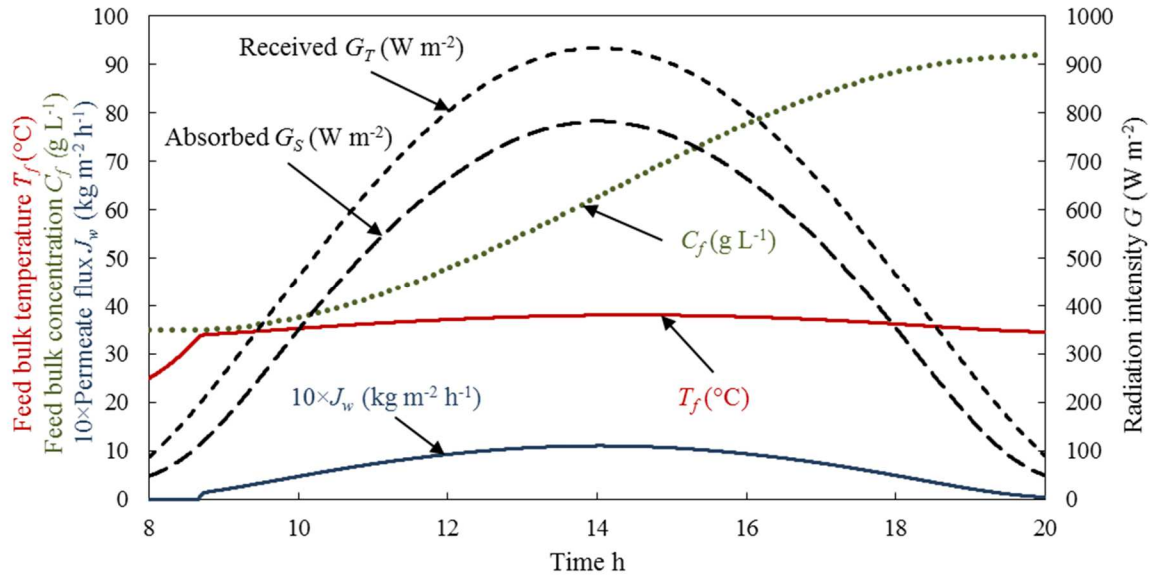
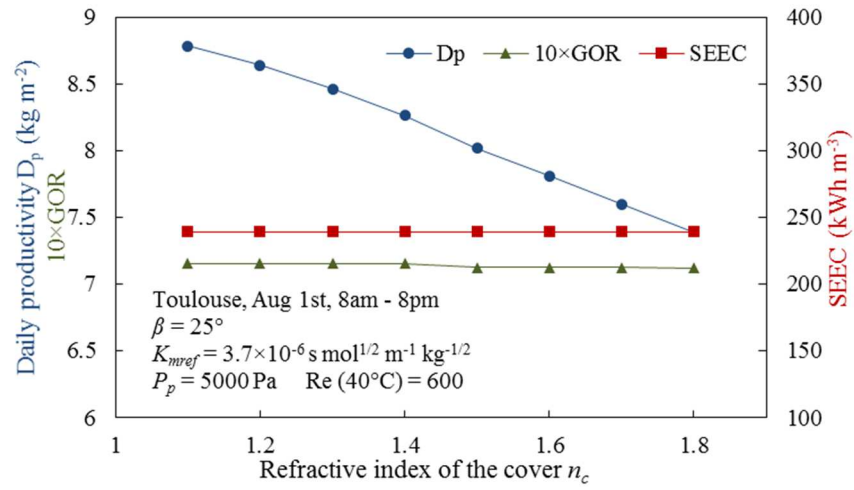


Figure II.12: Daily variation of solar radiation, feed temperature, feed concentration and permeate flux when operating under continuous pumping regime (Toulouse, Aug 1st; $\beta = 25^{\circ}$; $K_m = 3.7 \times 10^{-6} \text{ s mol}^{1/2} \text{ m}^{-1} \text{ kg}^{-1/2}$; $P_p = 5000 \text{ Pa}$; $Re (40^{\circ}C) = 600$)

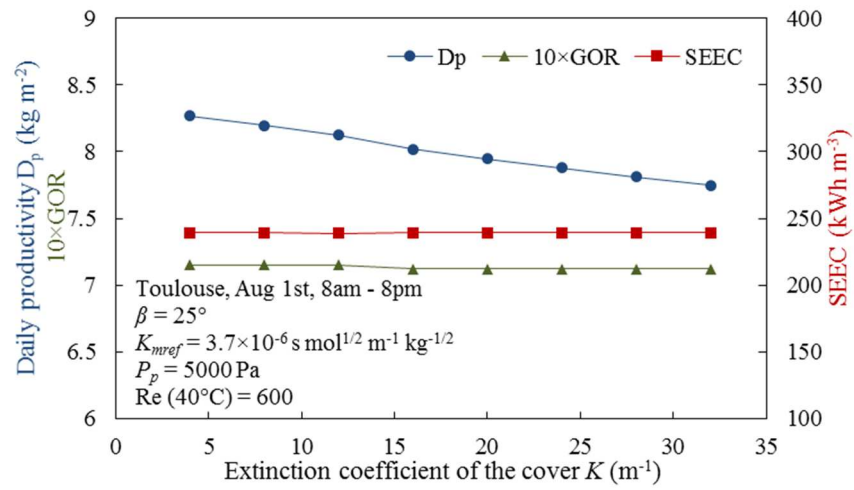
Subsequently, several parameter analyses were performed based on a continuous regime to examine the impact of different parameters on the system performance. For the analysis of each parameter, only the parameter itself varied while all the others were kept the same as their reference values listed in Table II.7.

II.4.4.1. Solar concerned design parameters

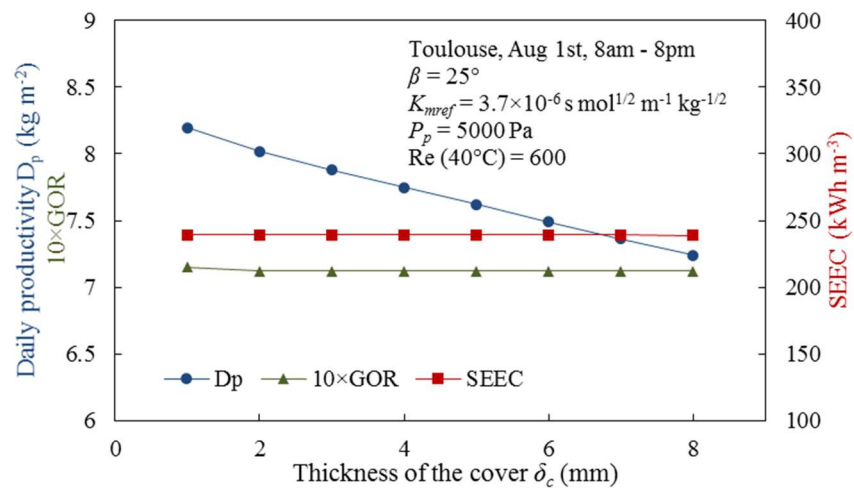
The influence of main solar oriented parameters, i.e. properties of the glazing cover (refractive index n_c , extinction coefficient K and thickness δ_c), solar absorptance for the absorber plate in normal direction (α_n) and collector slope (β), on the overall efficiency of module was studied through Figure II.13-15, respectively.



(a)



(b)



(c)

Figure II.13: System performance at varying glazing cover properties: (a) refractive index n_c , (b) extinction coefficient K , (c) thickness δ_c

These parameters intervened chiefly in the characterization of the thermal energy captured from the solar segment to provide heat for the water production of the VMD process. Hence, their direct incidence was on the total amount of water produced. However, given that the pumping power requirement is mainly related to the maintenance of vacuum pressure, the total amount of specific pumping energy consumption for the following three cases remained almost the same despite the variations of solar concerned parameters and the water productivity (Figure II.13-15). In addition, the value of GOR was found to be almost constant in these figures, too. The explanation lay in the proportionality of the water production $D_p A_C$ with solar energy absorbed, and with VP consumption as well. Thus, only CP consumption in the denominator of GOR (Eq. 40) was not proportional to water production $D_p A_C$, which was too small to make a difference when compared to VP consumption. Consequently, not much variation was observed on GOR either.

The glazing cover of the collector is the first layer that receives solar energy. The results showed, in Figure II.13, that the performance was similarly influenced by varying each of these 3 parameters. A monotonic negative effect of all the three cover-concerned parameters on water productivity D_p for the 12-hour operation on 1st Aug in Toulouse was observed, while specific energy requirements for pumping remained almost the same (SEEC being around 239 kWh m^{-3}). The global GOR showed only a slight decrease with the increment of these parameters, from 0.715 to 0.712 for all the 3 variations. These cover properties represent in fact a technological limitation regarding the efficiency of heat transfer in the module. For certain commercial cover materials, n_c usually can be found to be as low as about 1.3, K can be as low as 4 m^{-1} [186], and δ_c cannot be too thin considering the mechanical strength of the cover.

As shown in Figure II.14, the water productivity D_p increases almost linearly with the increment of α_n , i.e. the solar absorptance for the absorber plate in normal direction. The behavior is easy to comprehend because the solar energy utilized, as the only heat input to the system, is directly linked to the energy absorbed by the absorber-plate. Similarly as shown in Figure II.13, specific pumping energy stayed at about 239 kWh m^{-3} , regardless of this variation, and GOR rose slightly from 0.712 to 0.715 when increasing α_n from 0.8 to 0.98. In practice, α_n is often enhanced by coating the absorber-plate with selective surfaces such as black chrome to maximize the radiation absorption. In the latter case, the value can reach as high as 0.96 [112].

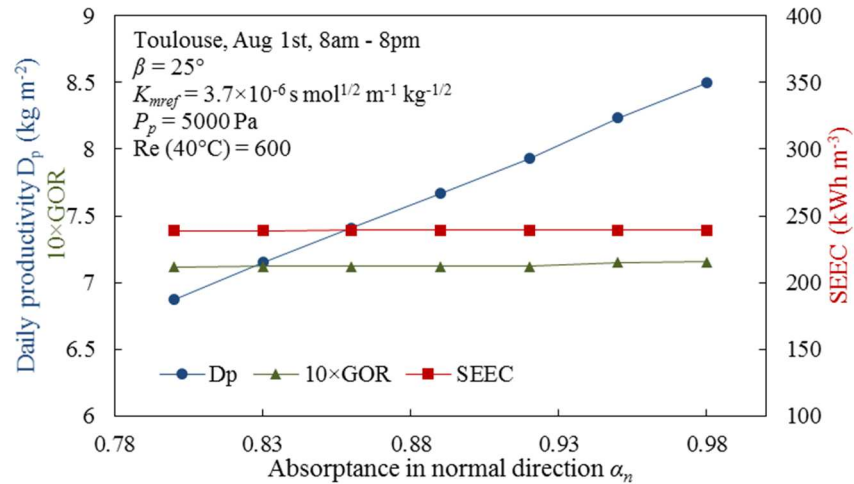


Figure II.14: System performance at varying solar absorptances in normal direction (α_n)

Varying the collector slope β in Figure II.15, the water production revealed a maximum for β at 20° . Nevertheless, the optimal slope 20°C is not necessarily the same all year around. In winter days rather than August, for instance, the optimum inclination will be higher because the solar altitude becomes lower. On the other hand, the pumping power needed for the recirculation actually augmented markedly with the increment of the slope because of the increasing pressure compensation of the vertical height difference between the inlet and the outlet with more tilted collectors. However, due to the slightness of CP consumption compared to that of VP, still no sensitive variation in the total pumping power was observed in such a situation. Consequently, GOR showed no clear variation.

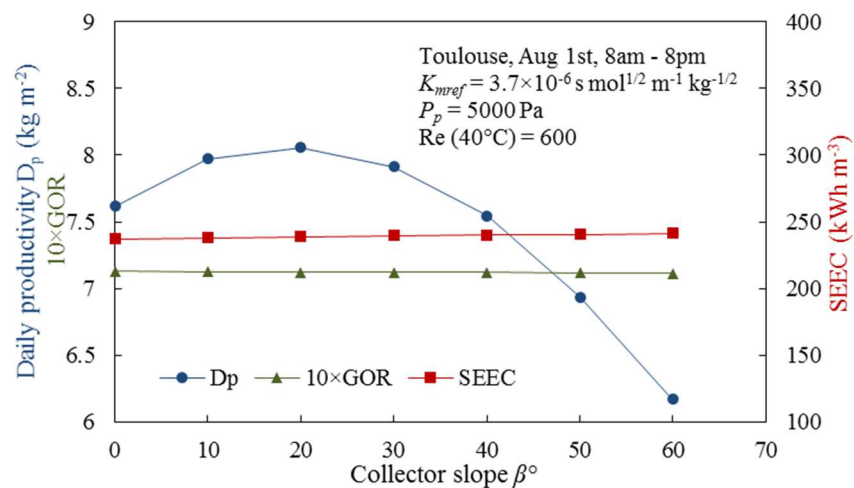


Figure II.15: System performance at varying collector slopes β

II.4.4.2. Membrane permeability and VMD parameters

Surprisingly as shown in Figure II.16, for this specific integrated VMD-solar system, both water productivity D_p and specific pumping energy SEEC were not markedly influenced by the membrane permeability coefficient (K_{mref}) especially for K_{mref} greater than $3 \times 10^{-6} \text{ s mol}^{1/2} \text{ m}^{-1} \text{ kg}^{-1/2}$. It should be noted that theoretically when the feed temperature is fixed, (and obtained after independent heating) the membrane permeability coefficient (K_{mref}) is identified as the key parameter for the determination of permeate flux in membrane distillation processes [187]. The explanation for this observation is that the heat consumption behaved to be almost proportional to the amount of water flux permeated (and previously vaporized). This is because the vaporization stood as the main source of energy exchange throughout the vacuum distillation, and given that the latent heat of vaporization is much greater than the sensible heat (under normal conditions, the latent heat is more than 5 times greater than the sensible heat for temperatures from 0°C to 100°C). The solar energy as the only heating source became indeed the main limitation, as it should compensate the proportional heat loss due to the mass transfer, regardless of the membrane permeability. On the other hand, when K_{mref} is too small, i.e. below $2 \times 10^{-6} \text{ s mol}^{1/2} \text{ m}^{-1} \text{ kg}^{-1/2}$, less water is permeated with lower GOR and higher specific pump consumption. The latter indicates that for very small K_{mref} values, the membrane permeability can also become a limitation.

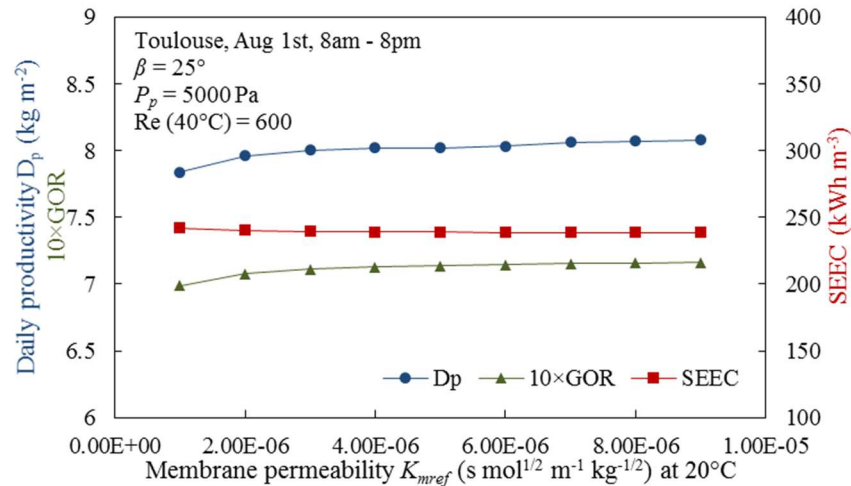


Figure II.16: System performance at varying membrane permeability coefficients (K_{mref})

As expected, because of its direct effect on the driving force, a key parameter in VMD process, the vacuum pressure P_p on the permeate side greatly affected the three performance criteria of the system, as illustrated in Figure II.17. Water productivity D_p decreased from 8.77 kg m^{-2} at

1500 Pa as vacuum pressure to 6.75 kg m⁻² at 15000 Pa as vacuum pressure; meanwhile, specific pumping energy decreased drastically with the increment of vacuum pressure, from 375 kWh m⁻³ to 121 kWh m⁻³. In other words, the price of producing water can be lowered by 2/3 if sacrificing only less than 1/4 of daily water production. A significant indication should be given in this regard, that contrary to conventional VMD devices with supplied heat, for an integrated solar-VMD module (thermally autonomous) the application of strong vacuum pressures is no more relevant. Indeed an interesting optimal range of GOR was found at P_p level from 4500 Pa to 7500 Pa, balancing the water production and energy consumption and allowing a daily water productivity of about 7-7.5 kg m⁻². It can be inferred that lower P_p than this range incurred much higher energy consumption but relatively limited increase in water production, while higher P_p than this range jeopardized the water production more than the benefit of cutting down energy consumption. However, the specific consumption stayed rather important even at low vacuum level, which was mostly taken up by the VP consumption, as discussed earlier. This emphasizes the necessary amelioration to be made on the use and the placement of VP.

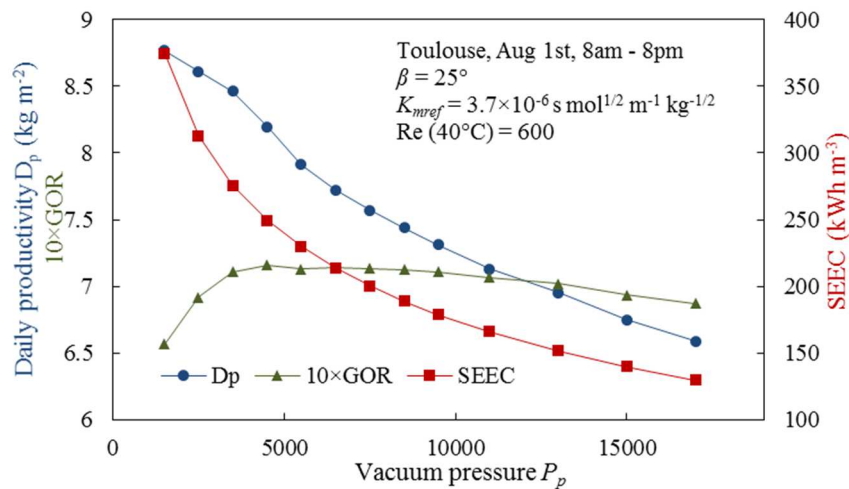


Figure II.17: System performance at varying vacuum pressures (P_p)

Theoretically, even if MD is less affected by concentration polarization when compared to RO, higher Reynolds number might diminish the temperature and concentration polarization by lowering boundary layer effect and enhancing simultaneously heat and mass transfer, which improves the permeate flux [188]. However, for our given set of parameters in Table II.7 and the salt concentration ranging from 35 to 90 g L⁻¹ (in Figure II.12) in the 12-hour operation, the results in Figure II.18 indicated that variations in Reynolds number had almost no influence on water productivity D_p . In this module configuration, the Reynolds number affected both the

heat transfer from the absorber-plate to feed bulk and the heat delivery from feed bulk to the boundary layer on the membrane surface. The former was limited by the available solar energy while the latter directly provided the latent heat for water production. Furthermore, the amount of these two phenomena had to be finally equal because of no other heat exchange existing for the feed recirculation with the assumption of no conductive heat loss by the membrane or piping. Therefore, the latent heat for water production shared the constraint from the amount of solar energy brought in, which then limited the water production from growing with increasing Reynolds number. However, the pumping energy faced an increase with higher Re, which is due to the higher orders of magnitude of pumping energy utilized by CP when operating at higher circulation flow rates (from 1 kWh m⁻³ to 135 kWh m⁻³ when Re was from 300 to 5800). This increment of SEEC consequently induced a decrease in GOR. Therefore, it seems that lower Re is preferred to reduce the pumping energy consumption without diminishing water production. However, it is now necessary to remind that our modeling did not take into account the possible occurrence of membrane scaling and fouling, which may occur at the liquid/vapor interface or pore inlets especially at high salt concentrations, low temperatures, and low feed flow rates [189]. Therefore, an interconnected design of C_{limit} and Re for system operation with further consideration of scaling and fouling in the model as well as experimental examinations will be needed to conclude on the choice of Re.

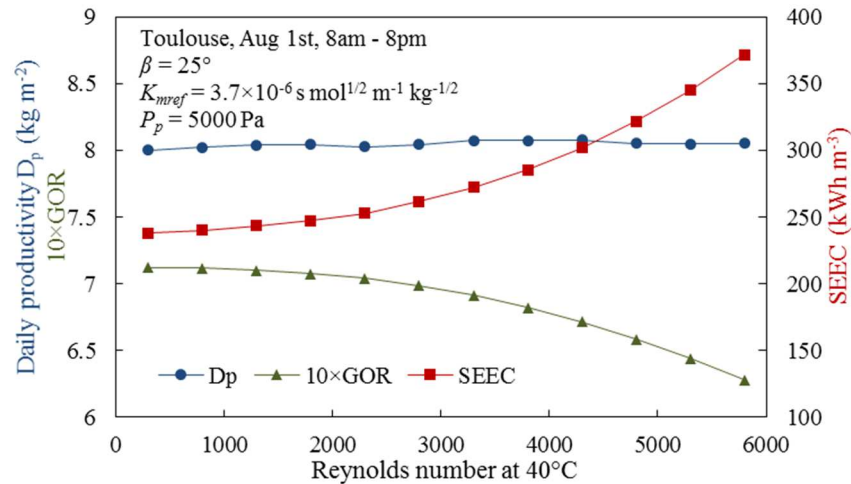


Figure II.18: System performance at varying Reynolds numbers

II.4.4.3. Preliminary potential exploration: Heat recovery ratio

As discussed above, the water productivity was always limited around 8 kg m⁻² due to the sparsity of solar energy and the relatively huge amount of thermal demand for water liquid-

vapor phase change ($\sim 667 \text{ kWh m}^{-3}$) [42]. However, the current system configuration was initially studied without considering energy recovery from permeate condensation, because of the technical difficulty in recuperating the condensation heat in common VMD process [53,190], and all the results presented before were based on the solar energy as the sole heating source. Meanwhile, heat recovery has been proven to be able to substantially enhance the MD process and frequently applied in a variety of ways. For example in DCMD, the feed stream can be preheated by heat exchanging with the permeate stream before receiving auxiliary heating. While in AGMD, the feed stream can serve as the cooling fluid for condensing the permeate and absorbing the condensation heat [42].

Therefore, as a preliminary step, a simple value of heat recovery ratio, which is defined as the proportion of the permeate condensed before the VP with its latent heat recuperated to the feed recirculation, was assumed and studied to demonstrate the sensitivity of overall performances to the quality of heat transfer and heat economy. As shown in Figure II.19, the heat recovery from condensation markedly improves the overall performance because of the boost in supplied thermal energy and the reduction of the permeate vapor created before the VP. With a moderate heat recovery ratio of 0.5, for example, the water productivity reached 15.44 kg m^{-2} . When a better heat recovery ratio of 0.9 was reached, nearly 40 kg m^{-2} of water could be attained with a GOR of almost 4. It should also be noted that GOR was observed to be over unity for heat recovery ratios above 0.3.

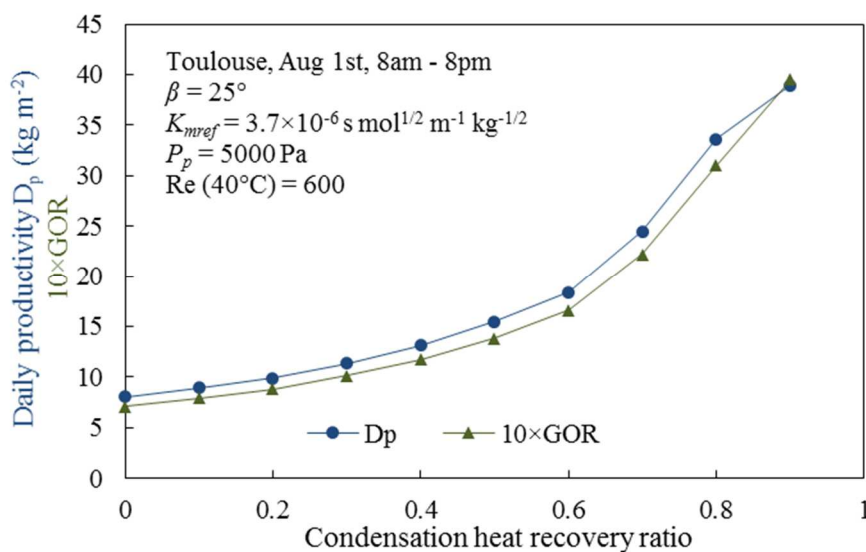


Figure II.19: System performance at varying heat recovery ratios

II.5. Conclusions (in English)

A direct integration of solar FPC and VMD in the same module was extensively modeled and dynamically studied in this chapter to examine the feasibility and the performance of freshwater production at small-scale in compact systems, aiming domestic drinking water in remote coastal area or isolated islands with no auxiliary heat provision.

Initially, the directly integrated module was inlaid with a temperature-based control strategy in order to operate on a certain level of feed temperature, compensating periodically the heat loss due to permeation via stand-alone solar heating. This first study showed that, as opposed to the common observation of MD systems, low working temperatures were favored (40°C instead of 60°C); even though the mean transient permeate flux would remain low.

Therefore, a series of simulations without temperature control and under a continuous run of pumps was conducted, where the feed temperature was relatively low, nearly above the dew point at the vacuum pressure. Accordingly, the daily water productivity reached 8 kg m⁻² where GOR attained above 0.71 without the heat recovery from condensation during a 12-hour operation. Analysis on the parameters suggested that water production was naturally shaped by the level of vacuum pressure, but GOR seemed to have an optimal value at P_p within 4500-7500 Pa. Instead, the membrane permeability coefficient and the Reynolds number of the feed flow showed a relatively smaller impact on the water production. On the other hand, solar oriented parameters were found to exert a greater influence on water production, and it has been globally observed that the solar energy, as the only heating source, became indeed the main performance limitation, regardless of the quality of mass transfer. This result highlighted the importance of further improvements concerning the heat transfer in integrated solar-VMD modules. Furthermore, potentials were shown that the heat recovery from condensation improves markedly the system performance, without developing the detailed approach and considering the additional consumption to realize this heat recuperation. At a moderate recovery ratio of 0.5, more than 15 kg m⁻² of water could be produced. Chapter IV will discuss a detailed implementation of a heat pump for heat recovery in this hybrid module.

II.5. Conclusions (en français)

L'intégration d'un collecteur plan solaire (FPC) solaire et de distillation membranaire sous vide (VMD) dans le même module a été modélisée, et la dynamique d'un système intégrant ce

module a été simulée dans ce chapitre afin d'examiner sa faisabilité et ses performances pour la production d'eau potable à petite échelle dans des systèmes compacts, destinés aux communautés isolées de zones côtières ou insulaires sans accès à la centrale.

Dans un premier temps le fonctionnement du module intégré a été simulé dans le cas d'une stratégie de contrôle de la température d'alimentation dans le module grâce à un recyclage du concentrat destiné à compenser la perte de chaleur due au perméat via l'apport d'énergie solaire thermique dans le module. Un cycle de fonctionnement de type batch est proposé qui comporte une étape de décharge quand la concentration dans la boucle de circulation devient trop élevée et pénalise la production d'eau. Cette étude a montré que, contrairement à ce qui est couramment observé dans les publications relatives à la MD, une température d'alimentation basse (40°C plutôt que 60°C) est préférable, même si le flux de perméat transitoire resterait relativement faible.

Ensuite, le fonctionnement continu du système a été simulé sans contrôle de la température, dans le cas d'une température d'alimentation relativement basse, légèrement supérieure au point de rosée à la pression de vide. En conséquence, la production de l'eau par jour atteint 8 kg m^{-2} lorsque le « gained output ratio » (GOR) est supérieur à 0,71 sans récupération de la chaleur de condensation au cours d'un fonctionnement pendant 12 heures. L'analyse des paramètres suggère que la production d'eau est principalement fonction du niveau de vide, mais le GOR semble avoir une valeur optimale pour une P_p comprise entre 4500 et 7500 Pa. Par contre, la perméabilité de la membrane et le nombre de Reynolds en entrée de module ont impact plus modéré sur la production d'eau. D'autre part, il a été constaté que les paramètres relatifs à l'énergie solaire ont une influence plus forte sur la production d'eau. Il a également été observé que l'énergie solaire, en tant que seule source thermique, devient effectivement la principale limitation des performances, quelle que soit la qualité du transfert de matière. Ce résultat montre l'intérêt de continuer à améliorer transfert de chaleur dans les modules intégrant captage d'énergie solaire thermique et VMD. De plus, la récupération de la chaleur de condensation peut améliorer considérablement les performances du système, si on ne prend pas en compte la consommation supplémentaire nécessaire pour réaliser cette récupération de chaleur. Avec un taux de récupération modéré de 50%, plus de 15 kg m^{-2} d'eau pourraient être produits par jour. Le chapitre IV permettra de prendre en compte une stratégie de mise en œuvre réaliste d'une pompe à chaleur pour la récupération de chaleur.

III. Comparative study of flat-plate DCMD and VMD modules with integrated direct solar heating (DCMD-FPC and VMD-FPC)

III.1. Introduction (in English)

In the previous chapter, a flat-plate equipment directly integrating VMD and solar energy has been proposed, modeled and evaluated explicitly in order to demonstrate the contribution of (i) the membrane distillation under vacuum (VMD) and (ii) the integrated design of solar-MD module for efficient desalination using a limited amount of solar energy absorbed. Regarding the VMD process, it has been observed that the location of the permeate condenser has a marked influence on the electrical power required by the vacuum pump, and a permeate condensation in the vacuum before the vacuum pump is preferable. Indeed, if the permeate vapor is pumped out directly without pre-condensation under vacuum, the power consumption is increased considerably, knowing that for such autonomous systems, the electricity is generally provided by photovoltaic panels on site. On the other hand, the feasibility, efficiency and practicability of such a subcooled condensation before the vacuum pump have been either partially described or not discussed in the literature.

Before a thorough optimization and an improvement of the design of the VMD-solar module proposed in the second chapter, it is interesting in this chapter to compare the VMD-FPC system with a similar integrated module (MD-solar) using the well-known DCMD. The motivation for such a comparison is mainly related to the substantial difference between these two MD configurations. DCMD actually represents the diametrical opposite of VMD from the point of view of water production and electricity consumption. A DCMD-based module is often considered as implying the lowest power consumption possible because of its simplicity and its basic configuration which only includes the work of liquid recirculation pumps, while admitting a very low permeate flux as opposed to a VMD-based module. However the conclusion on the energy consumption are often made without taking into account the whole system in DCMD, and notably the required energy to maintain a cold temperature on the permeate side.

In the present chapter, the comparative study between VMD-FPC and DCMD-FPC is performed through simulations for the same size and the same concept of the integrated module. The recycling system in DCMD-FPC is also similar to the one described in Chapter II. Evaluations are therefore presented in order to observe and to compare the energy consumption and the production of the two systems, when considered at a global scale accounting required energy inputs. In addition, detailed analyses on the impact of different parameters are carried out in order to identify the main factors contributing to the improvement of both systems and to discuss their different hybridization perspectives within a solar-MD desalination module.

III.1. Introduction (en français)

Dans le chapitre précédent, un équipement plan intégrant VMD et apport direct d'énergie solaire thermique a été proposé, modélisé et évalué explicitement afin de d'évaluer les contributions (i) de la distillation membranaire sous vide (VMD) et (ii) de la conception du module intégré énergie solaire-MD à l'efficacité du dessalement en utilisant une quantité limitée d'énergie solaire absorbée. En ce qui concerne la VMD, il a été observé que l'emplacement du condenseur de vapeur d'eau (le perméat) a une très grande influence sur la puissance électrique requise par la pompe à vide, et qu'il est préférable de placer le condenseur avant la pompe à vide. En effet, si le perméat sous forme de vapeur est pompé sous vide directement après le module, sans pré-condensation, la consommation d'énergie est considérablement plus élevée, sachant que l'électricité est généralement fournie par des panneaux photovoltaïques sur site pour des systèmes autonomes. D'autre part, la faisabilité et l'efficacité d'une telle condensation sous-refroidie avant la pompe à vide ont été partiellement décrites ou n'ont pas été discutées dans la littérature.

Avant une optimisation approfondie et une amélioration de la conception du module VMD-solaire proposé dans le deuxième chapitre (et qui feront l'objet du chapitre IV), il est intéressant de comparer dans ce chapitre le système VMD-FPC à un système basé sur un module plan intégré similaire mais utilisant la DCMD, qui est très connue. Cette comparaison est principalement motivée par la différence substantielle entre ces deux configurations de La MD. La DCMD est diamétralement opposée à la VMD du point de vue de la production et de la consommation d'électricité. Un module de DCMD est souvent considéré comme le plus sobre énergétiquement en raison de sa simplicité et de son principe qui ne nécessite que le travail des pompes de recirculation des liquides. Par contre, il produit un flux de perméat très faible par rapport à un module de VMD. Il est important de noter que cette conclusion sur la consommation énergétique est établie sans prendre en compte le système global et notamment l'apport énergétique pour maintenir froid le liquide condenseur côté perméat.

Dans ce chapitre, le VMD-FPC et DCMD-FPC sont comparés au moyen de simulations réalisées en prenant en compte un module intégré de même taille et de même configuration que celle présentée au chapitre II. Le système de recyclage dans le module DCMD-FPC est également similaire à celui décrit au chapitre II pour le module VMD-FPC. Les deux systèmes sont ensuite évalués et comparés en termes de consommation d'électricité et de production d'eau,

en prenant en compte chaque système dans sa globalité et en considérant les besoins énergétiques. De plus, l'impact de différents paramètres est analysé afin d'identifier les facteurs principaux qui contribuent à l'amélioration de chaque système et de discuter de leurs différentes perspectives d'hybridation dans un module de dessalement MD-solaire.

III.2. Module & system description and modeling

Comparisons made in the literature between DCMD and VMD [165,191–195] have already pointed out that VMD is advantageous in terms of the permeate flux and thermal energy efficiency due to the negligible conductive heat loss, while DCMD is simpler in system layout and operation. However, most of these comparisons are based on fixed feed conditions, especially fixed feed temperature levels, which is not the case in the recycling-batch system described in Chapter II and in the following of this chapter. Moreover, the evaluation of energy consumption in the above-mentioned comparisons was either totally absent [191–193], or provided partially without considering the intensive cooling demand for permeate vapor condensation under the vacuum in a conventional VMD [165,194,195].

In this chapter, a simple cooling approach for the distillate recirculation has been considered in the case of DCMD-solar desalination module, which serves to maintain the transmembrane vapor pressure difference by a constant source seawater flow in direct heat exchange with the permeate side. To provide a fair comparison, a very close system description has been applied here for VMD-FPC and DCMD-FPC. However, certain necessary readjustments have been additionally involved: (i) a slight change of module configuration in DMCD-based module should be made, as later described in Section III.2.1, which implies that the permeate side of the DCMD-FPC module becomes the cold circulating distillate; (ii) the diffusion mechanism inside the membrane pores for DCMD and VMD is not the same because of the difference in pore pressure (cf. Section I.2), a different description of membrane permeability has to be adapted for DCMD and will be further described in Section III.2.2, instead of a using the coefficient for Knudsen diffusion in Chapter II as proposed for VMD; (iii) the recirculation of the cold distillate on the permeate side has to be considered and added to system dynamics, together with a simple cooling cycle for the permeate side to keep the transmembrane vapor pressure difference. Detailed descriptions and system dynamics in this regard will also be provided in Section III.2.3.

III.2.1. DCMD module configuration

The configuration of the considered DCMD-FPC module is shown in Figure III.1.

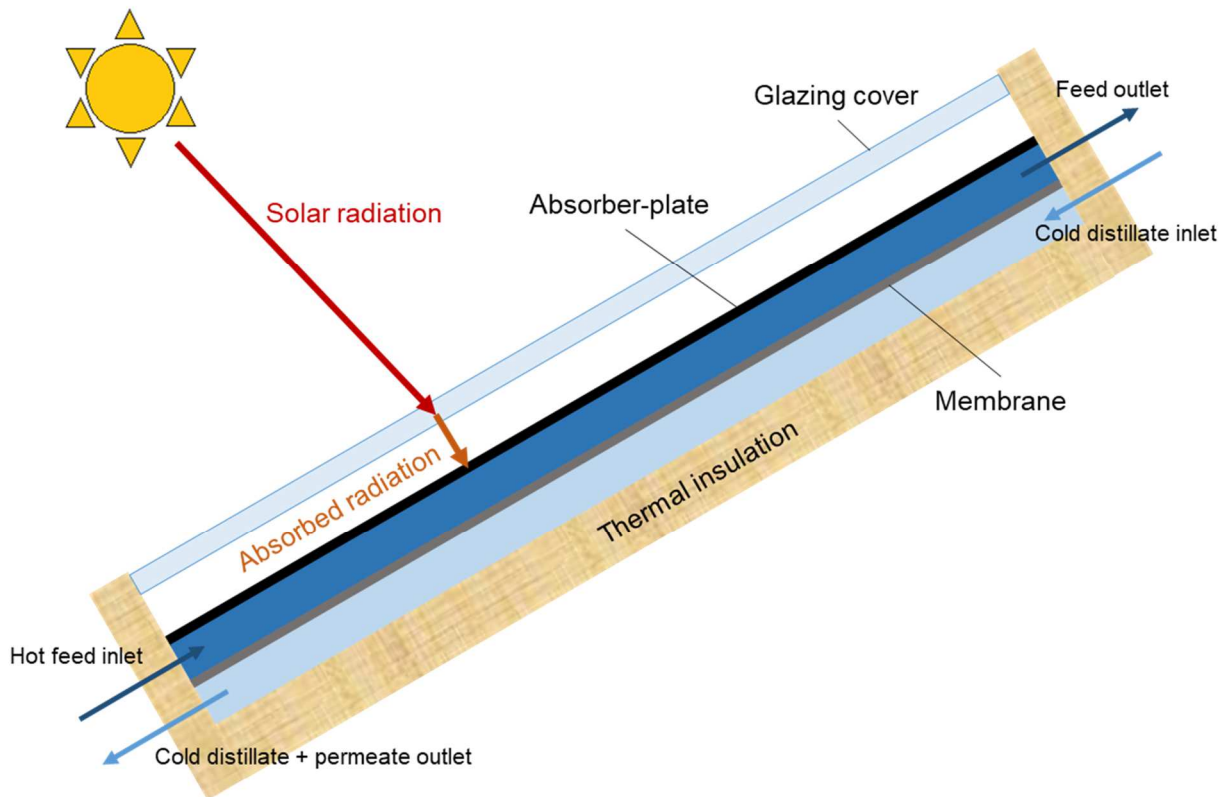


Figure III.1: Configuration for an integrated DCMD-FPC module

Solar radiation passes through the glass cover and get absorbed by the absorber-plate of a solar Flat-Plate Collector (FPC), heating the DCMD feed side by direct contact. The feed side and permeate side are both beneath the absorber-plate, separated by the membrane with saline water and distillate water circulating counter-currently. A temperature difference is created between these two sides by the heating on the feed side from the absorber-plate and a cooling cycle for the permeate side outside of the module, which constitutes the driving force instead of the vapor pressure difference created by the applied controllable vacuum in the VMD-FPC module in Chapter II. In this chapter, the cold distillate is used to be circulating on permeate side, as a conventional DCMD configuration. The entire module is thermally insulated, same as a common FPC, to reduce heat loss to the environment. On the other hand, the solar radiation model in Section II.2.1 was directly taken into the current study without any modification, obtaining the received solar irradiance G_T , absorbed solar irradiance G_S (W m^{-2}). Coupled with the MD model, the final utilized solar energy G_u (W m^{-2}) can be acquired by deducting the top loss through the over and the bottom loss from the thermal insulation.

III.2.2. Description of mass and heat transfer in MD modules

The governing equations consider the permeate vapor flux through the membrane, the heat transfer in the membrane, on the feed side and on the permeate side (temperature polarizations) and the salt diffusion on the permeate side (concentration polarization). The following main assumptions were applied in this study.

- (i) a combined effect of Knudsen - molecular diffusion governing the mass transfer through the membrane in DCMD [21,87]; while a combined effect of Knudsen diffusion - viscous flow governing the mass transfer through the membrane in VMD [21,85], same as explained in Section I.2;
- (ii) steady state;
- (iii) no wetting, crystallization or biofouling on the membrane;
- (iv) a 100% salt rejection, thus no salinity on the permeate side;
- (v) vaporization occurring only at pore inlet where the liquid-vapor interface holds;
- (vi) thermal conduction through the membrane and boundary layer on the permeate side in VMD negligible due to the vacuum and no liquid existing on the vacuum side [22].

Based on Assumption (i), the diffusion coefficient used in Chapter II for VMD, which only considered Knudsen permeability K_m , is no longer applied to this chapter, and the contribution of viscous flow will be added and discussed. Furthermore, coefficients of the permeability for DCMD and VMD has to be respectively modeled based on membrane properties according to the above-cited mechanisms, which will be introduced in this section.

III.2.2.1. Transfer equations in DCMD

a) Heat transfer

Total heat flux through the membrane Q_p ($W m^{-2}$) is formulated as [69], consisting of both the thermal energy for water evaporation taken away by the permeate flux J_w ($kg m^{-2} s^{-1}$), and the thermal conduction.

$$Q_p = J_w \Delta H_v + \frac{k_t}{\delta_m} (T_{fm} - T_{pm}) \quad (1)$$

where ΔH_v is the latent heat of water vaporization (J kg^{-1}), T_{fm} and T_{pm} the membrane surface temperature of the feed and the permeate side, δ_m the thickness of the membrane (m). k_t is the thermal conductivity of the membrane layer ($\text{W m}^{-1} \text{ }^\circ\text{C}^{-1}$), which can be expressed by Eq. 2, applying the Isostress model [71].

$$k_t = \left(\frac{\varepsilon}{k_g} + \frac{1 - \varepsilon}{k_s} \right)^{-1} \quad (2)$$

where ε represents the porosity of the membrane. k_s is the conductivity of the membrane solid part, while the gas (air and water vapor) trapped in the pore k_g can be estimated by the following correlation [196],

$$k_g = 2.72 \times 10^{-3} + 7.77 \times 10^{-5} T_m \quad (3)$$

On the other hand, the total heat flux Q_p is also transported through the boundary layers of the feed and the permeate side [73], which gives us the following,

$$Q_p = h_f(T_f - T_{fm}) = h_p(T_{pm} - T_p) \quad (4)$$

where T_f and T_p are bulk temperatures. Due to temperature polarization, the former is higher than T_{fm} while the latter is lower than T_{pm} . h_f and h_p are heat transfer coefficients ($\text{W m}^{-2} \text{ }^\circ\text{C}^{-1}$) of the feed and the permeate side, respectively.

Correlations that correlate Nusselt number with Reynolds number Re and Prandtl number Pr are applied to the calculation of heat transfer coefficients. The ones proposed in Chapter II is adopted, which are as follows,

$$Nu = 1.86 \left(\frac{Re Pr d_h}{L} \right)^{0.33} \left(\frac{\mu_f}{\mu_m} \right)^{0.14} \quad \text{for } Re < 2300 \quad (5)$$

$$Nu = \frac{\left(\frac{f}{8} \right) (Re - 1000) Pr}{1 + 12.7 \left(\frac{f}{8} \right)^{\frac{1}{2}} (Pr^{\frac{2}{3}} - 1)} \left[1 + \left(\frac{d_h}{L} \right)^{\frac{2}{3}} \right] \left(\frac{Pr_f}{Pr_m} \right)^{0.11} \quad \text{for } Re \geq 2300 \quad (6)$$

$$\text{With } f = (0.790 \ln Re - 1.64)^{-2}$$

where d_h is the hydraulic diameter (m) and L is the length (m) of the flow channel. Dynamic viscosity μ (Pa s), density ρ (kg m⁻³), thermal conductivity λ (W m⁻¹ °C⁻¹) and heat capacity c_p (J kg⁻¹ °C⁻¹) of both saline water and distilled water are calculated by the regressions in [18].

b) Mass transfer

The water mass flux J_w (kg m⁻² s⁻¹) is driven by the vapor pressure difference across the membrane due to the temperature difference [84],

$$J_w = B_m(P_{fm} - P_{pm}) \quad (7)$$

where B_m represents the overall membrane mass transfer coefficient (s m⁻¹), and P_{fm} and P_{pm} stand for the water partial pressure at the membrane surface on the feed side and the permeate side (Pa), respectively.

As described in the assumptions, B_m can be decomposed into the mass transfer coefficient in Knudsen diffusion B_K and the one in ordinary molecular diffusion B_D , which are calculated as follows,

$$B_K = \frac{2}{3} \frac{\varepsilon r}{\tau \delta_m} \left(\frac{8M_w}{\pi R T_m} \right)^{0.5} \quad (8)$$

$$B_D = \frac{\varepsilon}{\tau \delta_m} \frac{P D_w M_w}{P_a R T_m} \quad (9)$$

where ε , r , τ , and δ_m are the porosity, the pore radius (m), the tortuosity and the thickness of the membrane (m), respectively. M_w is the molecular weight of water (kg mol⁻¹), and R is the gas constant (i.e. 8.3145 J mol⁻¹ K⁻¹). T_m is the mean water vapor temperature (K) inside the membrane pore, P and P_a are the total pressure and the air partial pressure (Pa) inside the membrane pore, and D_w is the water diffusion coefficient (m² s⁻¹). It is worth to mention that the Knudsen permeability K_m utilized in Chapter II equals $B_K/\sqrt{M_w}$.

Then the two mass transfer coefficients are combined to obtain B_m [45],

$$B_m = (B_K^{-1} + B_D^{-1})^{-1} \quad (10)$$

Empirically, the product of the total pressure P and the water diffusion coefficient D_w can be calculated as a function of the temperature [69],

$$PD_w = 1.895 \times 10^{-5} T_m^{2.072} \quad (11)$$

Antoine equation is adopted for the calculation of pure water vapor pressure on each side of the membrane with the corresponding temperature at the membrane surface [21],

$$P^0 = \exp\left(23.1964 - \frac{3816.44}{T - 46.13}\right) \quad (12)$$

Then, the water vapor partial pressure on both side of the membrane has to take salt existence into consideration [21],

$$P = x_w \gamma_w P^0 \quad (13)$$

where x_w is the water molar fraction and γ_w is the water activity coefficient, which can be obtained by the correlation proposed in [18].

On the other hand, the permeate flux J_w is also determined by the water mass diffusion from the feed bulk to the membrane surface, which is further decided by the salt concentration polarization [47], yielding

$$J_w = \rho k_m \ln\left(\frac{C_{fm}}{C_f}\right) \quad (14)$$

where k_m is mass transfer coefficient (m s^{-1}) on the feed side, and C is the concentration (g L^{-1}). k_m can also be estimated from the correlations given in Eqs. 5 and 6 by replacing Nusselt number Nu and Prandtl number Pr by Sherwood number Sh and Schmidt number Sc [74].

III.2.2.2. Modification of transfer equations in VMD

When compared with the VMD modeling at the scale of the module in Section II.2.2.1, the only difference here lies in the diffusion mechanism inside the membrane pores, which is now the

combination of Knudsen diffusion and viscous flow, instead of the assumption of solely Knudsen diffusion for the diffusion in VMD. The impact of this modification will be checked in Section III.3.1.

Moreover, the diffusion coefficients need to be modeled from the material properties of the membrane, in order to be comparable with the DCMD model described above. Compared with Section III.2.2.1, the modeling of VMD process takes 2 modifications into account. Firstly, the overall membrane mass transfer coefficient B_m is now composed of Knudsen diffusion B_K and the one in representing viscous flow B_V , which is calculated as [53],

$$B_V = \frac{M_w \varepsilon r^2 P_m}{8\mu_v \tau \delta_m RT_m} \quad (15)$$

where μ_v is the viscosity of the vapor inside the pore, which can be calculated from the linearization from the data in [86].

B_m is the sum of these two coefficients,

$$B_m = B_K + B_V \quad (16)$$

The effect on the production of considering viscous flow will be discussed later to confirm the negligibility of B_V in VMD, as in Chapter II. Secondly, there is no more need to model the thermal conductivity of the membrane and the boundary layer on the permeate side, as explained in the assumptions. Therefore, the heat transfer becomes simply the heat transfer from the feed bulk to the membrane surface and the heat loss through membrane by vapor permeating, expressed as,

$$Q_p = h_f(T_f - T_{fm}) = J_w \Delta H_v \quad (17)$$

III.2.3. Description of the dynamic system

A recycling system was considered, same as in Chapter II, to not only fully store and exploit the solar energy absorbed by the module, but also to raise the water recovery rate to reduce the brine discharge of the system. For the VMD-FPC module, the VMD system design and dynamic modeling were already explicitly introduced and explained in Section II.3, which included a

recycling system on the feed side as well, and a vacuum pump directly connected to the permeate side. Therefore, Section 2.3 is dedicated to the description of the DCMD system for the DCMD-FPC module.

III.2.3.1. System configuration for DCMD-FPC module

Similar to the recycling batch system for the VMD-FPC module, the configuration of the system designed for the DCMD-FPC module is shown in Figure III.2.

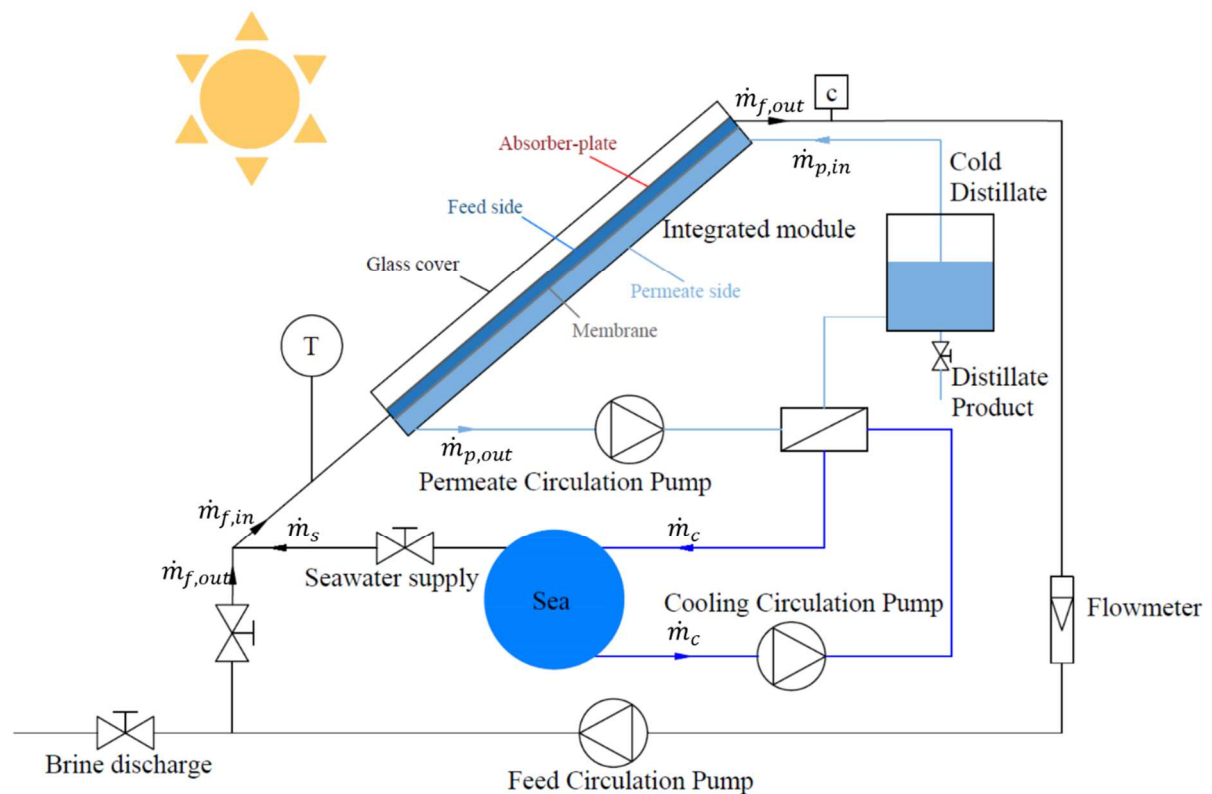


Figure III.2: Flowsheet of recirculation system for DCMD-FPC module

Three water circulation loops function simultaneously, i.e. the feed recirculation, the cold distillate recirculation and the cooling seawater circulation. The feed stream absorbs thermal energy from the absorber-plate and induces higher vapor partial pressure, which generates vapor flux passing through the membrane pores when inside the module. The mass loss by permeate flux in the feed recirculation is compensated directly by the seawater supply instantaneously, while the whole feed side is evacuated by the discharge when the salt concentration gets too high and detected by the concentration meter at the outlet of the module. Counter-currently, the cold distillate on the permeate side gains the mass from the direct condensation of the vapor that passing through the membrane. However, thermal energy is also

transferred to the circulation on the permeate side due to heat conduction through the membrane and permeate vapor condensation. Therefore, a cooling strategy for the cold distillate circulation is needed in order to substantially remove the additional heat delivered to the permeate side. Thus, the temperature of the distillate can be maintained lower than the feed, so that the transmembrane vapor pressure difference can be kept and the vapor inside the pores can be continuously condensed in the cold distillate due to its higher pressure than the saturation point at the temperature of the permeate side. In the current configuration, the cooling of the permeate stream is realized by heat exchanging with the cooling seawater circulation, which constantly draws seawater at environment temperature from the sea.

III.2.3.2. System dynamics

The process dynamics was studied for time-varying steady-state phases [88]. Heat and mass balances were applied to both the feed side and the permeate channel, and salt mass conservation was used to track the accumulation of salt concentration.

Dynamics of the feed side are described by Eqs. 18 - 20. As aforementioned, mass loss to the permeate ($J_w A_m$) was made even by the seawater supply \dot{m}_s (kg s^{-1}), which gives us Eq. 18. Then, temperature change on the feed side was determined by the solar energy utilized G_u , supplied seawater and total heat loss through the membrane Q_p , yielding Eq. 19. Finally, salt mass kept augmenting during the process due to the no-salt-passing assumption and the salt introduction constantly from the seawater supply with a concentration of C_s (g L^{-1}), as presented in Eq. 20.

$$\frac{dm_f}{dt} = \dot{m}_s - J_w A_m = 0 \quad (18)$$

$$\frac{d(c_p m_f T_f)}{dt} = G_u A_m + c_p \dot{m}_s T_s - Q_p A_m \quad (19)$$

$$\frac{d(C_f V_f)}{dt} = \frac{C_s \dot{m}_s}{\rho_s} \quad (20)$$

where m_f is the total mass in the feed channel (kg), A_m is the surface area of the membrane, same as the collector A_C (m^2) and V_f is the total volume of the feed channel (m^3).

On the other hand, the rate of mass gain in the distillate tank was all from the permeate ($J_w A_m$), and the temperature change was decided by the total heat transferred from the feed side Q_p and the heat taken away by the cooling circulation, as listed in Eqs. 21 and 22. A uniform temperature at any time was assumed for the fresh water inside the distillate tank T_d and the permeate side T_p of the module ($T_d = T_p$).

$$\frac{dm_d}{dt} = J_w A_m \quad (21)$$

$$\frac{d(c_p m_d T_d + c_p m_p T_p)}{dt} = Q_p A_m - Q_c A_c \quad (22)$$

where m_d and m_p are the total mass in the distillate tank and the permeate channel (kg), respectively. A_c and Q_c are the heat exchanging surface (m^2) and the heat flux taken away by the cooling ($W m^{-2}$), which was solved by the “ht.lx” library in Python [197] for a counter-current heat exchanger.

III.2.4. Pumping energy consumption

The power consumption taken into consideration contains the consumption by circulation pumps in both DCMD-FPC and VMD-FPC systems and the additional consumption by the vacuum pump in the case of VMD-FPC. Due to the autonomous design of the system, thermal energy is entirely supplied by the available solar radiation on the surface of the MD-FPC module, which is more or less fixed with a given module at given location and time. While on the other hand, the power consumption for the system operation cannot be fulfilled by the module or the system itself, instead it requires external power supply from the grid, which is not often accessible in the targeted remote places and should be provided by on-site photovoltaic panels. Consequently, it is worth to correlate the electricity demand to the production capacity of the desalination system.

III.2.4.1 Circulation pump

The electricity consumption of the circulation pumps is proportional to the pressure loss ΔP during the flow in the module, which consists of the friction loss and the gravitational loss due to the slope β of the module, neglecting the pressure loss in piping and joints. Therefore, the pressure loss in this study can be expressed as [74],

$$\Delta P = fL \frac{\rho v^2}{2d_h} + \rho gL \sin\beta \quad (23)$$

where L is the length of the module (m), v is the flow velocity (m s^{-1}), and g is the gravitational acceleration (9.81 m s^{-2}). f is the Darcy friction factor, being calculated by the correlations below [198,81].

$$f = \frac{96}{\text{Re}} \quad \text{for } \text{Re} < 2300 \quad (24)$$

$$f = (0.790 \ln \text{Re} - 1.64)^{-2} \quad \text{for } \text{Re} \geq 2300 \quad (25)$$

Finally, the power consumption \dot{P}_{cp} (W) of a circulation pump is [88]

$$\dot{P}_{cp} = \frac{F_V \Delta P}{\eta_{cp}} \quad (26)$$

where F_V is the volumetric flow rate ($\text{m}^3 \text{ s}^{-1}$), and η_{cp} is the efficiency of the pump, which is taken as 0.7. In the system for the DCMD-FPC module, both the feed and the permeate circulation pumps were included in the calculation, while only feed circulation pump presented in the one for the VMD-FPC because of no permeate circulation existed.

III.2.4.2. Vacuum pump in VMD system

A well-sealed system was assumed in this study, and thus the energy consumption by the vacuum pump is proportional to the amount of permeate vapor flux, according to the system configuration in Chapter II and in Section III.2, where all the vapor is pumped out by the vacuum pump. Rather than an adiabatic compression from the vacuum pressure P_p to the atmospheric pressure P_{atm} adopted in Chapter II, here an isothermal compression is deemed more accurate to describe the process because of the relatively low permeate flow rate [180]. Accordingly, the power consumption \dot{P}_{vp} (W) is

$$\dot{P}_{vp} = \left(\frac{J_w A_m}{M_w \eta_{vp}} \right) RT_p \ln \left(\frac{P_{\text{atm}}}{P_p} \right) \quad (27)$$

where R is the ideal gas constant ($8.31446 \text{ J mol}^{-1} \text{ K}^{-1}$), and the efficiency η_{vp} equals 0.75 throughout the study. Here, the permeate temperature T_p is supposed to be the same as the temperature at the membrane surface on the feed side T_{fm} by the assumption of no conductive heat loss through the membrane.

III.2.5. Model coupling and resolution procedure

The system dynamics interacts with both the MD models and the solar radiation model, as shown in Figure III.3. Operating conditions from the description of system dynamics (bulk temperatures, feed bulk concentration, flow rates) provided input parameters for MD model (Section III.2.2) and Solar radiation model (Section II.2.1), while the results from both MD model and Solar radiation model imposed variations on operating conditions. During the simulation, the correlations for the calculation of mass & heat transfer coefficients and seawater properties were invoked by all these models.

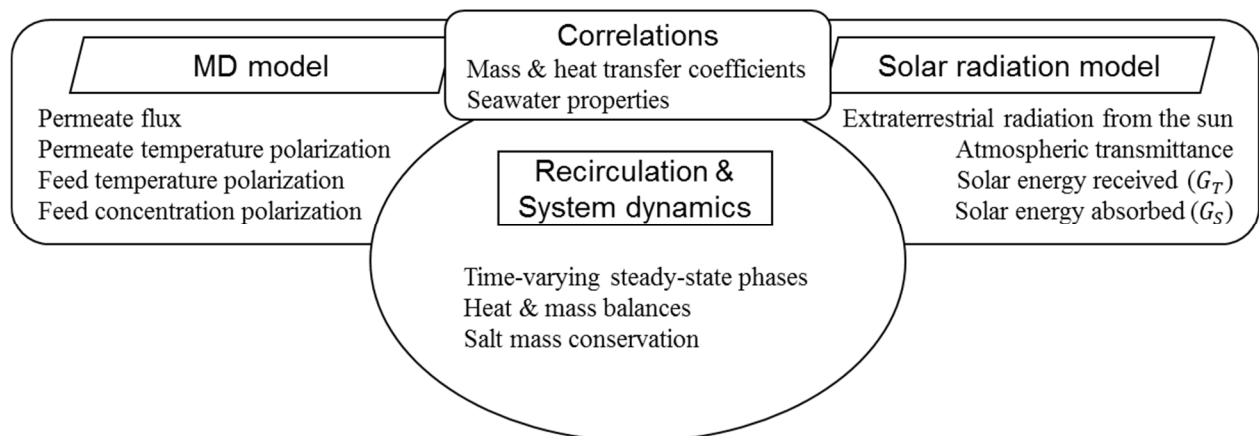


Figure III.3: Schematic of interconnected modeling structure: MD model, solar radiation model and system dynamics

All models were programmed under Python (version 2.7). The integration for system dynamics (Eqs. 18 - 22) was realized by the Real-valued Variable-coefficient Ordinary Differential Equation solver (Isoda) in Scipy ODE package [179], in conjunction with the resolution of MD model (Section 2.2) and Solar radiation model by the Scipy fsolve package [199]. Automatic readjustments of time step-sizes and switches between the implicit Adams method for non-stiff problems and another method based on backward differentiation formulas (BDF) for stiff problems are provided by the Isoda package, in order to smoothly handle the integration.

III.3. Results and discussion

III.3.1. Parameter settings and daily operation

Concerning such a DCMD-FPC module, different categories of parameters, i.e. location, material properties, positions & dimensions, and operating conditions, were included in the simulation. Table III.1 presents an exhaustive list of all the parameters that intervened in the simulation.

Table III.1: Parameter settings of integrated module and system operation for both DCMD-FPC and VMD-FPC

Parameters	Values	Description	
L_{loc}	358.56°	Longitude in degrees west, $0^\circ < L < 360^\circ$	
φ	43.60°	Latitude, north positive, $-90^\circ < \varphi < 90^\circ$	
Al	150.0 m	Altitude of the location	
h_{wi}	10 W m ⁻² °C ⁻¹	Heat transfer coefficient of the wind	
Location & time	Date	Aug 1st	
	time	8 am - 8 pm	
	r_0, r_1, r_k	0.97, 0.99, 1.02	Correction factors for mid-latitude summer
	ρ_g	0.2	Diffuse reflectance of the surroundings
	T_{amax}	35°C	Highest ambient temperature
	T_{amin}	20°C	Lowest ambient temperature
	Material properties	n_c	1.5
$K\delta_c$		0.032	Product of extinction coefficient and thickness
ε_c		0.88	Emittance of the cover
α_n		0.93	Absorptance in normal direction
ε_{ap}		0.1	Emittance of the absorber-plate
ε		0.713	Porosity of the membrane
τ		5	Tortuosity of the membrane
r_m		0.22 μm	Pore size of the membrane
δ_m		117.7 μm	Thickness of the membrane
k_p		0.15 W m ⁻¹ °C ⁻¹	Thermal conductivity of the membrane polymer
U_{bo}	0.9 W m ⁻² °C ⁻¹	Heat loss coefficient of the insulation	
Positions & dimensions	β	25.0°	Slope of the solar collector
	γ	0.0°	Azimuth angle of the solar collector
	W	0.5 m	Width of the collector
	L	0.7 m	Module length
	δ_f	5 mm	Thickness of the feed side
δ_p	5 mm	Thickness of the cold distillate side (only DCMD)	

	C_s	35 g L ⁻¹	Salt concentration of the seawater supply
	T_s	25°C	Temperature of the seawater supply
	C_{limit}	300 g·L ⁻¹	The highest operating salt concentration
	\dot{m}_f	100 kg h ⁻¹	Feed circulation flow rate
Operating conditions	\dot{m}_p	100 kg h ⁻¹	Permeate circulation flow rate (only DCMD)
	\dot{m}_c	150 kg h ⁻¹	Cooling circulation flow rate (only DCMD)
	m_d	5 kg	Initial mass in the distillate tank (only DCMD)
	U_c	1000 W m ⁻² °C ⁻¹	Cooling heat exchange coefficient (only DCMD)
	A_c	0.1 m ²	Cooling heat exchange surface (only DCMD)
	P_p	5000 Pa	Permeate pressure (only VMD)

The longitude, latitude and average altitude of Toulouse, France were chosen as an example for system operation and to give indications on the future experiments here in the laboratory. A 12-hour operation, from 8am to 8pm on Aug 1st was assumed, along with the daily ambient temperature varying from 20°C to 35°C and other parameters that affects the solar irradiance.

The properties of the glass cover, the absorber-plate, the membrane and the insulation were all taken into account as the 11 parameters in this category shown in Table III.1. The first 5 parameters in material properties generally determine the amount of the solar energy absorbed from the received irradiance, and the other 6 parameters influenced how the module utilizes the energy input. The material properties other than the membrane were kept the same as listed in Table II.7, while for the newly inserted membrane properties, the given data of the PVDF membrane Durapore™ by Millipore was applied [20]. It is worth to note here that the tortuosity was set to a rather high value of 5 because of two reasons: (i) this value is much more difficult to evaluate compared to other membrane properties and is not given by the membrane manufacturer; (ii) more importantly, a tortuosity of 5 together with other membrane properties listed in the table corresponds to a Knudsen permeability of $5.74 \times 10^{-6} \text{ s mol}^{1/2} \text{ m}^{-1} \text{ kg}^{-1/2}$, which is at the same scope of the real values given by the experiments done in our laboratory [35]. Nevertheless, lower tortuosity values will be included in Section 3.2.2 by the discussion on the influence of membrane properties.

It is worth noting that in the positioning angles and the dimensions of the flat-plate module, the collector area ($W \times L = 0.5\text{m} \times 0.7\text{m}$) of both DCMD-FPC and VMD-FPC modules was considered the same as the membrane area A_m , because they shared the same surface in the integrated design, neglecting edges and margins. Besides, in VMD the thickness and the the

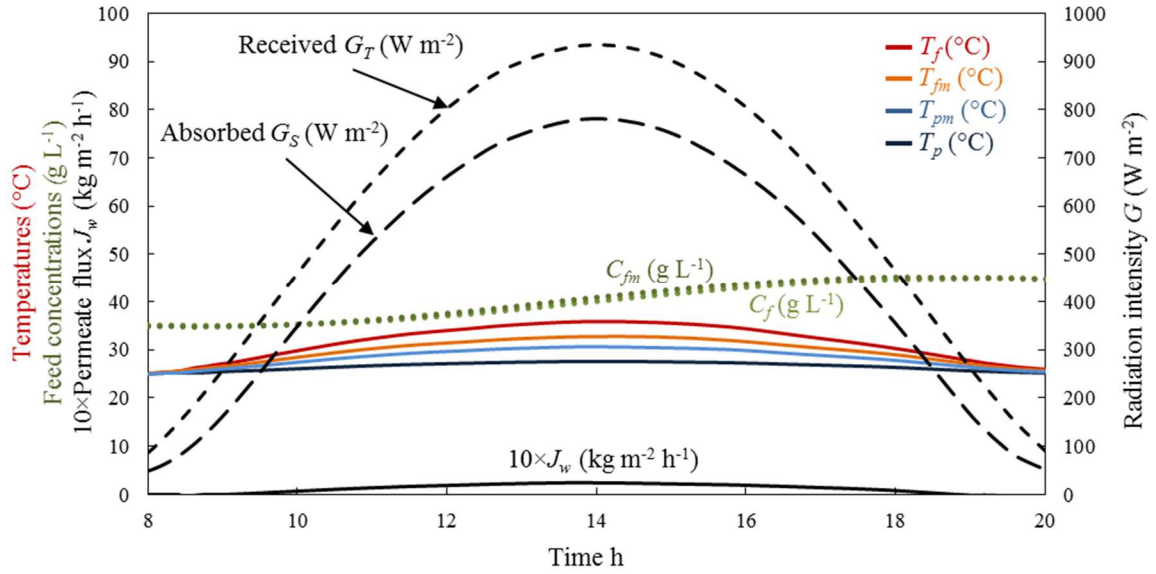
flow rate of permeate side were excluded due to the total vapor phase inside the vacuum on the permeate side, which was assumed to be a uniform vacuum pressure at 5000 Pa. Contrarily for the DCMD-based system, the same thickness and flow rate as the feed side for the permeate side was taken. Rather low flow rates at 100 kg h^{-1} (corresponds to a Re of around 130) were initially taken based on the conclusion that lower flow rate is beneficial to the performance of solar-driven DCMD [69]. Nevertheless, the flow rates will be later varied in a large range to see their impact on the system performance. A distillate mass of 5 L was assumed to be already in the cold distillate circulation before the daily operation, to initiate the permeate circulation.

The considered seawater source had a constant concentration of 35 g L^{-1} and a constant temperature of 25°C . The limit of salt concentration before discharge in the module was set to be a higher value of 300 g L^{-1} , giving a maximal water recovery rate of 88.3%, same as explained in Chapter II. Specifically for the DCMD-FPC, a small heat exchanger of 0.1 m^2 for cooling the permeate was set, whose overall heat transfer coefficient was $1000 \text{ W m}^{-2} \text{ K}^{-1}$, as a normal liquid-liquid plate heat exchanger [200]. The cooling seawater circulated at a flow rate of 150 kg h^{-1} , more than the flow rate of the cold distillate in order to ensure a good cooling effect. All the above settings for the cooling cycle would be later varied as well to discuss their influences.

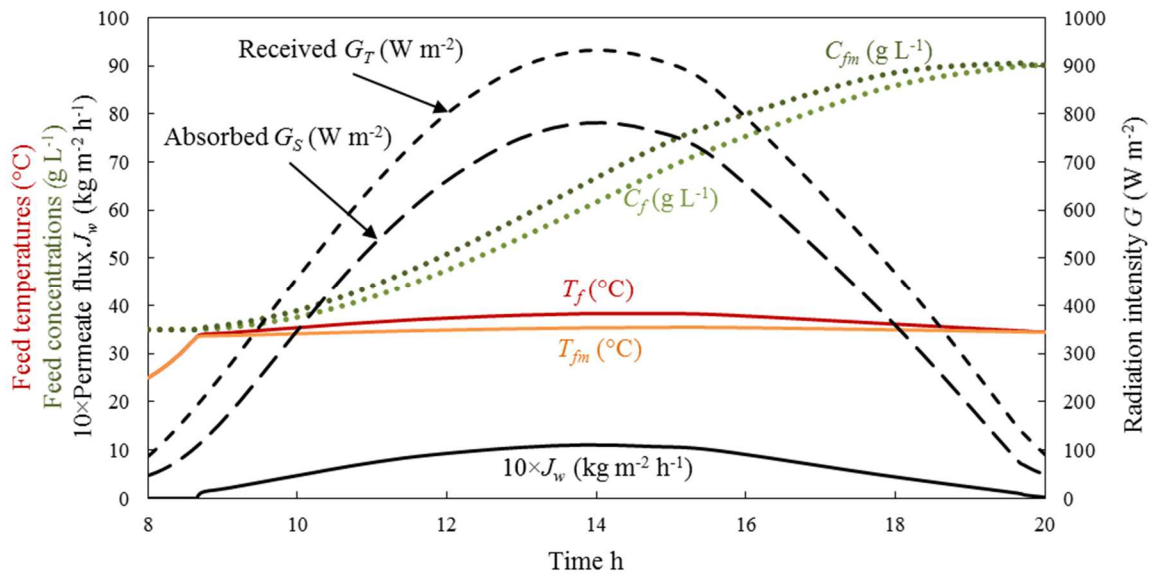
Under the settings of all the parameters listed in Table III.1, simulations for the DCMD-FPC system and the VMD-FPC system were performed, resulting in daily variations of solar irradiance, temperatures, concentrations and permeate fluxes as shown in Figure III.4.

Similarity between Figure III.4a and 4b was observed for all the variations. Received solar irradiance G_T is exactly the same in both of the figures because of the same date and location chosen, and the absorbed irradiance G_S also seems to be nearly the same. The operating temperatures and permeate fluxes all rise a bit with the increment of solar irradiation and all go down with the decreasing solar condition in the afternoon. Besides, both of the concentrations kept accumulating as shown in Figure III.4, and the slope is bigger when near noon because of relatively higher permeate flux under stronger solar radiation. At the same time, temperature polarizations (differences between T_{fm} and T_f , and the difference between T_{pm} and T_p for DCMD-FPC) and concentration polarizations (differences between C_{fm} and C_f) of both systems are more obvious with higher permeate flux at noon. Specifically for the DCMD-based system, the temperature of the bulk on the permeate side T_p did not react too much to other variations

due to the cooling effect impeding it from augmenting. As for the VMD-based system, the feed temperature started at the original 25°C in the beginning of the day and then was raised to a certain point before being more or less stabilized, when the water vapor pressure on the feed side reached the level of the vacuum pressure and permeate flux began to appear.



(a)



(b)

Figure III.4: Daily variation of solar irradiance, feed and permeate temperature, feed concentration and permeate flux of (a) DCMD-FPC system; (b) VMD-FPC system

Despite the similar variations, the difference on the production was obvious. After the day, the VMD system can produce 8.08 kg m^{-2} of distillate water (2.83 L), while the DCMD-FPC module will produce only 1.46 kg m^{-2} (0.51 L). Therefore, the permeate flux in Figure III.4b is much higher than that in 4a, even though it is already rather low. Even though the temperature polarizations ($T_{fm} < T_f$) on the feed side seem to be in the same range for both DCMD-FPC and VMD-FPC, the extra temperature polarization on the permeate side ($T_{pm} > T_p$) for DCMD-FPC significantly reduced the transmembrane vapor pressure difference (between T_{fm} and T_{pm} , as shown in Figure III.4a) and the permeate flux, while the pressure on the permeate side in VMD process is kept constant by the vacuum pump. As a result, the salt concentration C_f of the VMD-FPC system accumulated much more than the DCMD-based system because of more water permeated, and its concentration polarization phenomenon is stronger compared to the nearly-invisible difference between C_f and C_{fm} in Figure III.4a. However, the difference in power consumption for these two systems was even more significant. The DCMD-FPC system produced the distillate at an expense of only 2.76×10^{-3} kWh (average PV power consumption 0.23W, corresponding SEEC 5.42 kWh m^{-3}), while the value for the VMD-FPC system was 0.45 kWh (average PV power consumption 37.5W, corresponding SEEC 158.4 kWh m^{-3}), most of which was consumed by the vacuum pump, because of the configuration of the VMD system where vacuum pump was used to compress all the produced water vapor. This important consumption is inevitable, and can be seen as the replacement of the huge expense on maintaining an extremely low temperature in “cold traps”, which is usually installed before the vacuum pump to condense vapor in vacuum. On the other hand, the total absorbed solar energy for both systems recorded about 2 kWh during the 12-hour operation. Considering a latent heat of vaporization of 2260 kJ kg^{-1} [201], the DCMD-based system only utilized 0.32 kWh out of the 2 kWh (16% thermal efficiency) for water production, while the VMD-based system transferred as much as 1.78 kWh into the final distillate (89% thermal efficiency). In conclusion, significantly higher electricity consumption and solar energy utilization efficiency both existed for the VMD-FPC, compared to the DCMD-FPC.

Besides, the assumptions of mass transfer mechanisms inside the membrane pore are revisited here by some extra simulations. For DCMD, the daily production would be 106.9% higher if only considering Knudsen diffusion instead of a combined effect of Knudsen-molecular diffusion; while it would be 18.3% higher if only molecular diffusion is considered. Therefore, this combined Knudsen-molecular diffusion is necessary for better prediction of the permeation, without the need of including viscous flow due to the existence of air. For VMD, molecular

diffusion does not exist due to the vacuum and no air. The daily production would only be 0.06% lower if viscous flow is further excluded and only Knudsen diffusion is assumed to govern the transfer inside the pores. Therefore, it confirms the assumption in Chapter II that solely Knudsen diffusion is already enough to describe the transfer mechanism of VMD.

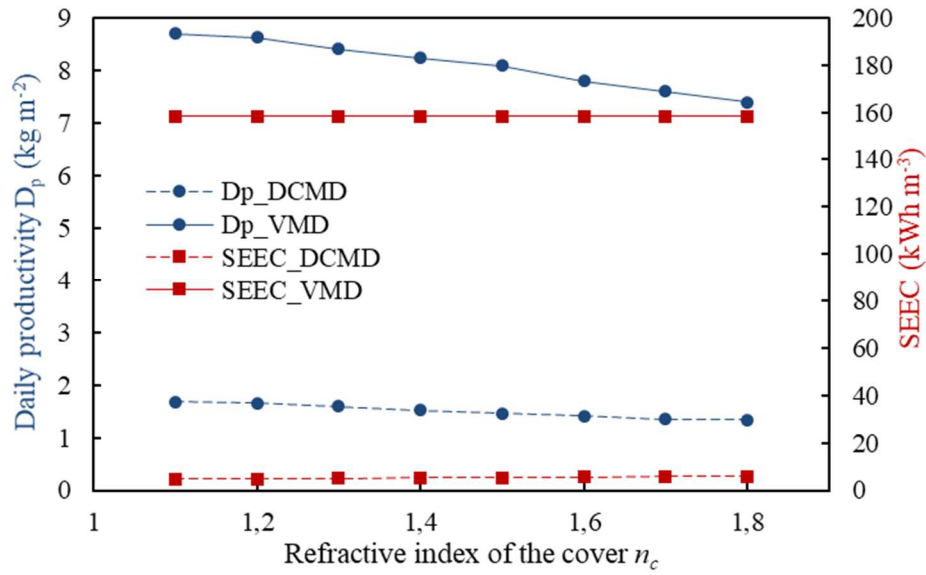
III.3.2. Influence of parameters

In order to examine the individual influence of some parameters on the performance, the value of each parameter was varied one-at-a-time (OAT, same as the approach applied in Chapter II) while keeping all the other parameters the same as listed in Table III.1 as a module of $0.5 \times 0.7 \text{ m}^2$. In addition, in order to be comparable with the discussions in Section II.4.4, the performance observations are based on the same daily productivity D_p and SEEC. The studied parameters include the material properties of solar absorption and the membrane, the operating conditions, and the module position and dimensions, which are presented and discussed as follows.

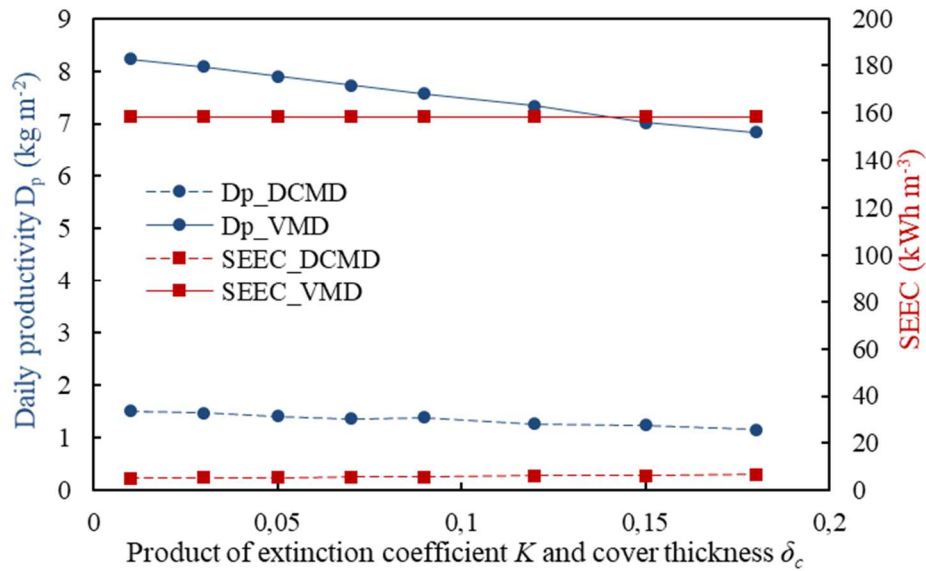
III.3.2.1. Solar oriented material properties ($A_m = A_c = 0.5 \times 0.7 \text{ m}^2$)

The main solar oriented material properties that exert influence on system operation include the properties of the glass cover (n_c and $K\delta_c$) and the absorptance α_n in normal direction of the absorber-plate. These parameters characterized the solar energy absorption of the module, being the only thermal energy source of the system.

The first layer of the integrated module is the glass cover. As expected and shown in Figure III.5, increasing the values of the concerned properties had bigger negative impact on the daily distillate productivity D_p for the VMD-based system than the DCMD one. The VMD-FPC system was much more productive than the DCMD-FPC, with specific consumption unaffected by the properties of the glass cover, same reason as explained in Section II.4.4. However, the SEEC of the DCMD-based system varied a little bit with different values of these properties, though not clear in these figures because of much smaller value compared to the value of VMD. It increased from 4.7 to 5.9 kWh m^{-3} with n_c from 1.1 to 1.8, and from 5.2 to 6.8 kWh m^{-3} with $K\delta_c$ being from 0.01 to 0.18. The circulation flow rates are fixed in these calculations and thus the total pumping consumption remained the same while the productivity D_p decreased with the increments of these properties. As a result, the specific consumption of the DCMD-based system raised when bigger n_c or $K\delta_c$ were imposed.



(a)



(b)

Figure III.5: Daily distillate productivity and specific electrical energy consumption for DCMD-FPC and VMD-FPC systems at varying glass cover properties: (a) refractive index n_c ; (b) product of extinction coefficient K and thickness δ_c

Similar observations of the absorptance α_n of the absorber-plate is shown in Figure III.6. However, the absorptance α_n had a positive impact on the productivity D_p for both MD configurations, based on the fact that higher absorptance directly enabled greater amount of the solar energy absorbed. On the other hand, D of the DCMD-FPC system stayed limited at 1.60 kg m⁻² even with the highest absorptance, while SEEC ranged from 6.75 kWh m⁻³ with α_n at 0.8 to 4.95 kWh m⁻³ with α_n at 0.98, whose variation was also limited. Compared to the positive

impact of α_n on the productivity of the VMD-FPC, the strong conductive heat loss through the membrane in DCMD-FPC might severely diminished the benefit from higher solar absorption.

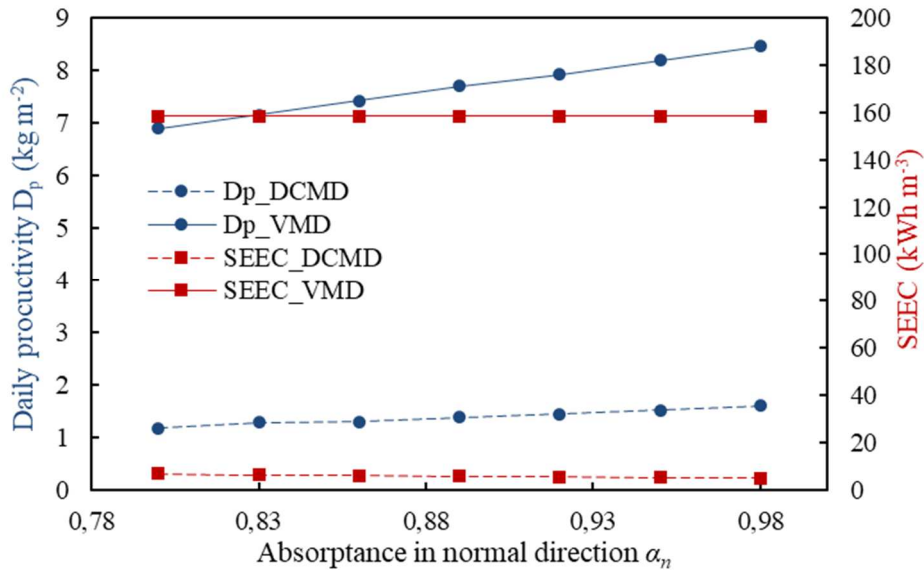
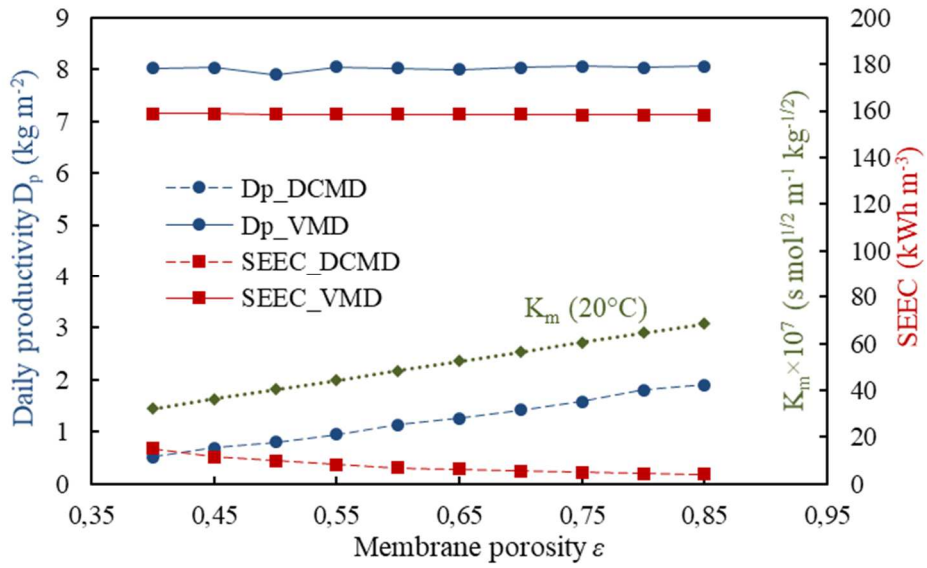


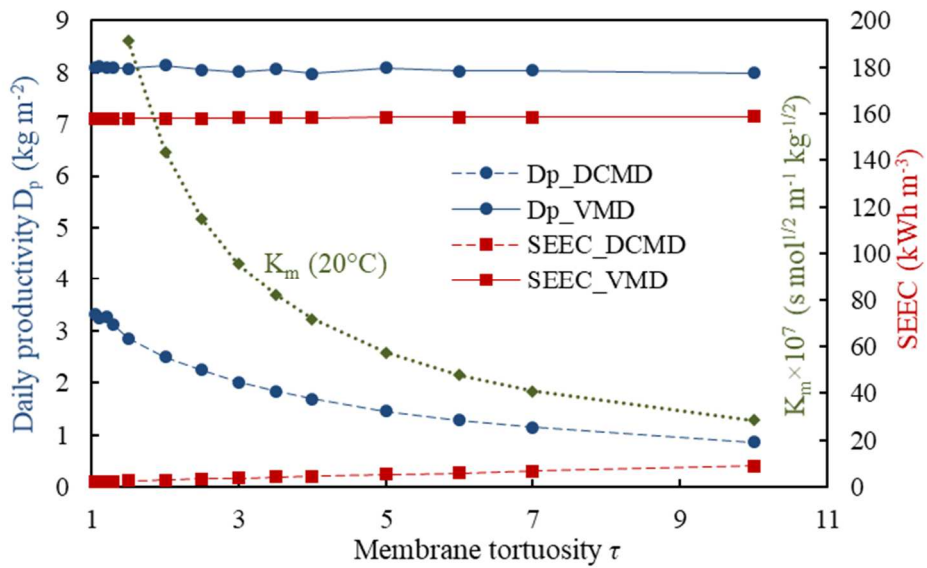
Figure III.6: Daily distillate productivity and specific electrical energy consumption for DCMD-FPC and VMD-FPC systems at varying absorptance α_n in normal direction of absorber-plate

III.3.2.2. Membrane properties ($A_m = A_c = 0.5 \times 0.7 \text{ m}^2$)

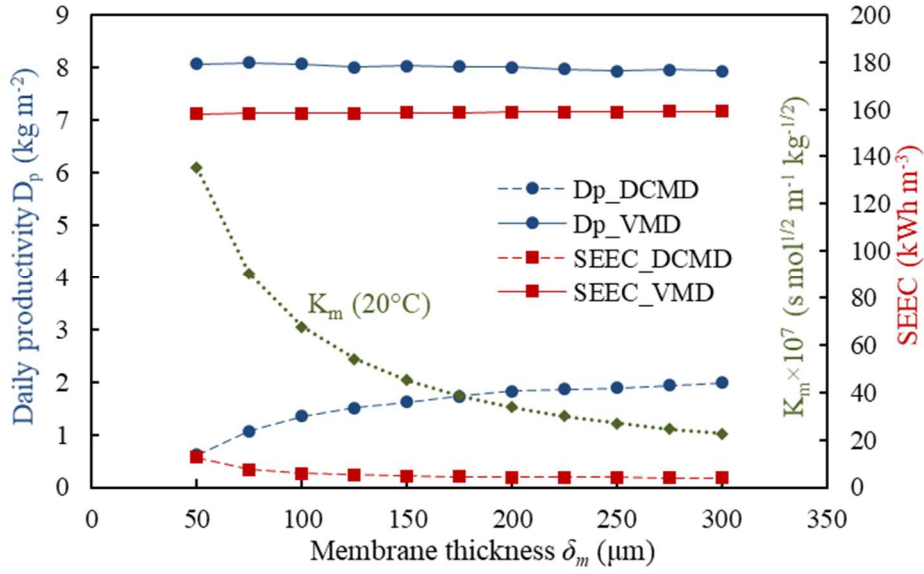
For both DCMD-based and VMD-based desalination systems, four characteristic membrane properties were considered, that is to say porosity ε , tortuosity τ , thickness δ_m and pore size r , as they characterize the membrane permeability and decide the mass transfer quality of the separation process. Influence of these properties on the performance of both modules are summarized in Figure III.7a-d, together with the corresponding Knudsen permeability of the membrane.



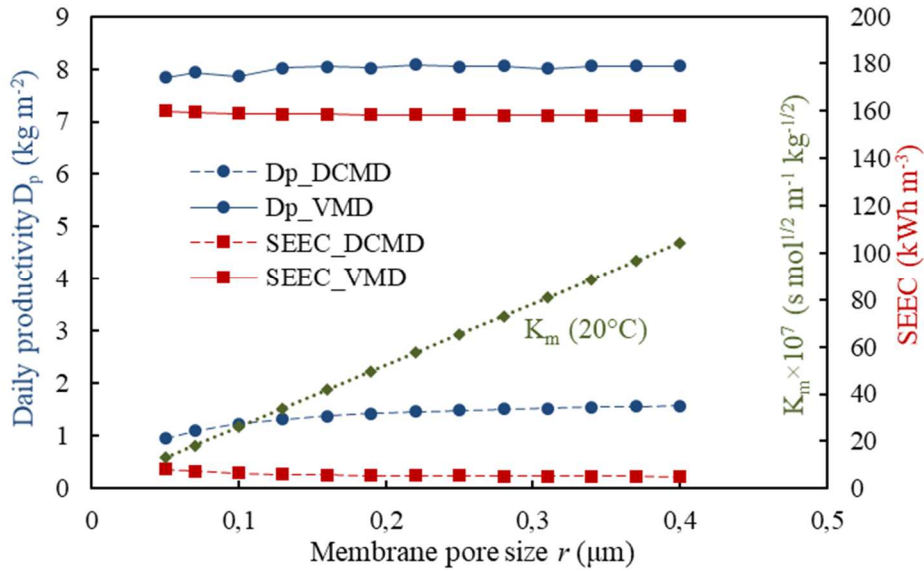
(a)



(b)



(c)



(d)

Figure III.7: Daily distillate productivity and specific electrical energy consumption for DCMD-FPC and VMD-FPC systems at varying membrane properties: (a) porosity ε , (b) tortuosity τ , (c) thickness δ_m , (d) pore size r

Clearly, these permeability-oriented parameters had very small influence (almost no influence) on the water production and pumping consumption of the VMD-based system, the same as previously discussed for the Knudsen permeability K_m of the membrane due to the restraining from limited solar energy income in Chapter II. Oppositely, both the D_p and the SEEC of the DCMD-based system acted sensitively to membrane properties, which indicates that the sparse solar radiation is not the only constraint in DCMD-FPC. Higher porosity and lower tortuosity

seemingly benefited the system a lot with greater production and less pumping consumption, because of the enhanced permeability of the membrane, as the K_m shown in Figure III.7a and 7b, which increases linearly with higher porosity and exponentially with lower tortuosity. A low tortuosity of 1.2 could push the productivity D_p up to 3.3 kg m^{-2} , which however seemed to be the limit for even lower tortuosity (same D_p of 3.3 kg m^{-2} with a τ of 1.05). Similarly, the larger pore size was able to do the same job of boosting the production, but only to a limited extent. Larger than an average pore size of $0.3 \text{ }\mu\text{m}$, no clear improvement on the system performance is visible at an increasing pore size even though the Knudsen permeability keeps rising linearly, and the risk of membrane wetting would be significantly increased. Lastly, thicker membranes in the case of DCMD-FPC were found to be of interest to both D_p and SEEC, even it induced lower membrane permeability. The reason is that by increasing the membrane thickness, another important factor, the conductive thermal loss, came into play. The thicker the membrane, the bigger thermal resistance of this layer. Therefore, this observation proved that reducing transmembrane conductive heat loss and increasing the thermal efficiency in the DCMD-FPC system are more important than enhancing membrane permeability.

Having in mind that the conduction thermal loss of the membrane might be essential to the DCMD-based system, the thermal conductivity of the membrane polymer k_p is therefore analyzed here in Figure III.8. The VMD-based system was not taken into consideration because of the neglected conductive loss through the membrane.

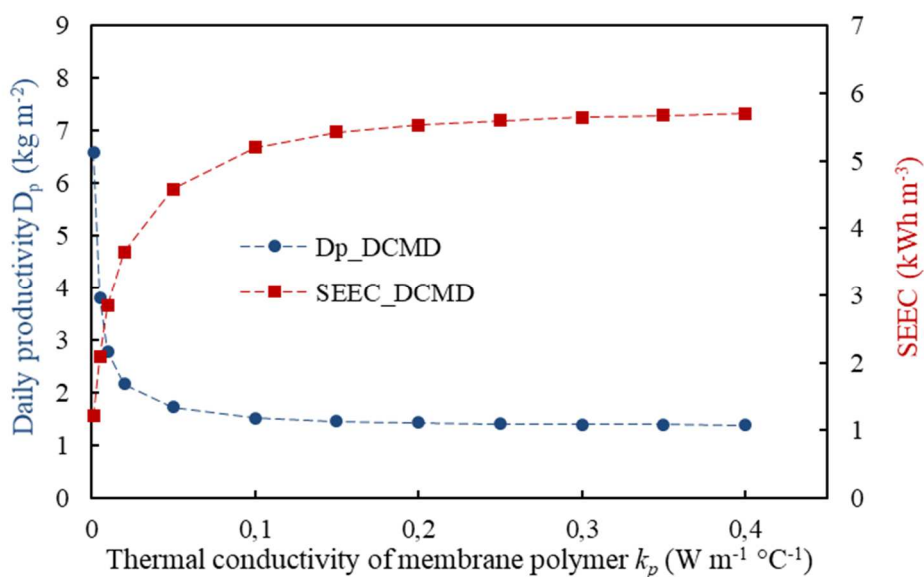


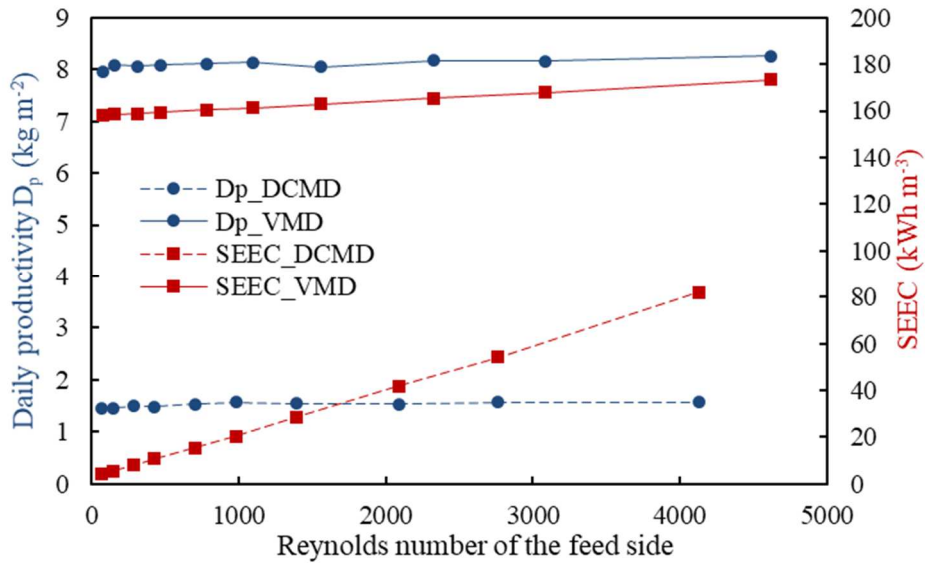
Figure III.8: Daily distillate productivity and specific electrical energy consumption for the DCMD-FPC system at varying thermal conductivities k_p of membrane polymer

As expected and discussed above, the production of DCMD-FPC responded a lot to this parameter, which could even reach up nearly to the D_p of the VMD system with extremely low thermal conductivity. Therefore, the conductive heat loss can be identified as the dominant factor that caused the large productivity difference between DCMD-based and VMD-based system. Besides, SEEC exhibits an inverse trend compared to the trend of D_p , because of the invariability of the total pumping consumption at fixed flow rates of the feed and the distillate, which is the product of SEEC and total water produced. However in reality, the thermal conductivity of the membrane is still in the range from 0.15 to 0.30 W m⁻¹ K⁻¹ (0.17 for PP, 0.19 for PVDF and 0.25 for PTFE) [202], where there seemed no significant influence on system performance from Figure III.8.

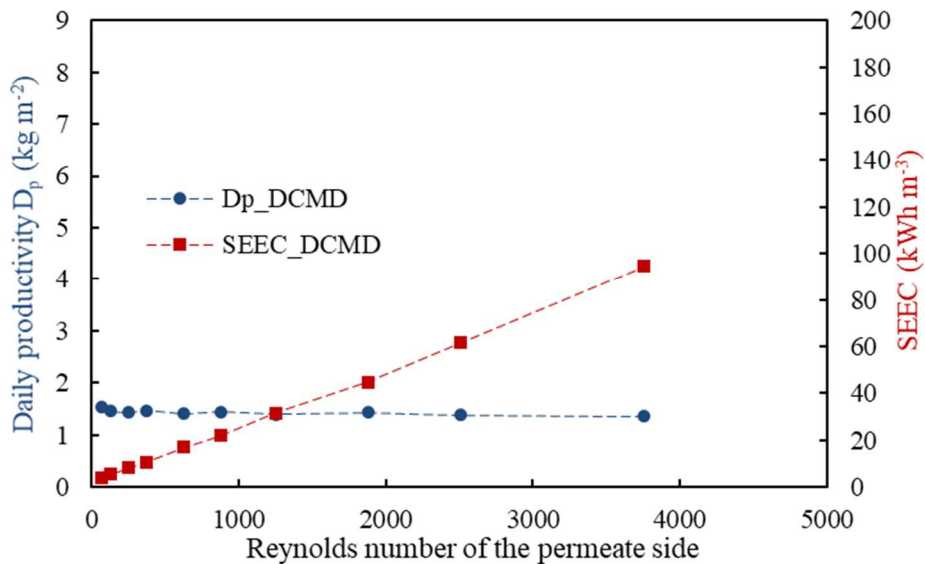
III.3.2.3. Operating conditions ($A_m = A_c = 0.5 \times 0.7 \text{ m}^2$)

Firstly, the permeate pressure P_p was again identified to be the major factor determining the performance of a VMD-FPC system, same as reported previously in Figure II.17. Then, the flow rate of the feed recirculation \dot{m}_f for both DCMD-FPC and VMD-FPC systems and the flow rate of the cold distillate recirculation \dot{m}_p for the DCMD-FPC system are discussed as follows. In order to be more interpretable, instead of flow rates, the corresponding average Reynolds number were illustrated in Figure III.9.

For the VMD-based system, higher Reynolds number of the feed did not end up with higher production due to the limited available solar energy, only adding slightly to the energy consumption of pumping, as already discussed in Chapter II. From Figure III.9, similar behaviors can be observed for DCMD-based system, where an almost constant D_p is observed in spite of the varying Reynolds numbers of the feed or the permeate side. Apart from the same limitation by the incoming solar energy as for VMD-based system, here the conductive heat loss accounts for another important constraint, as discussed in Section III.3.2.2.



(a)



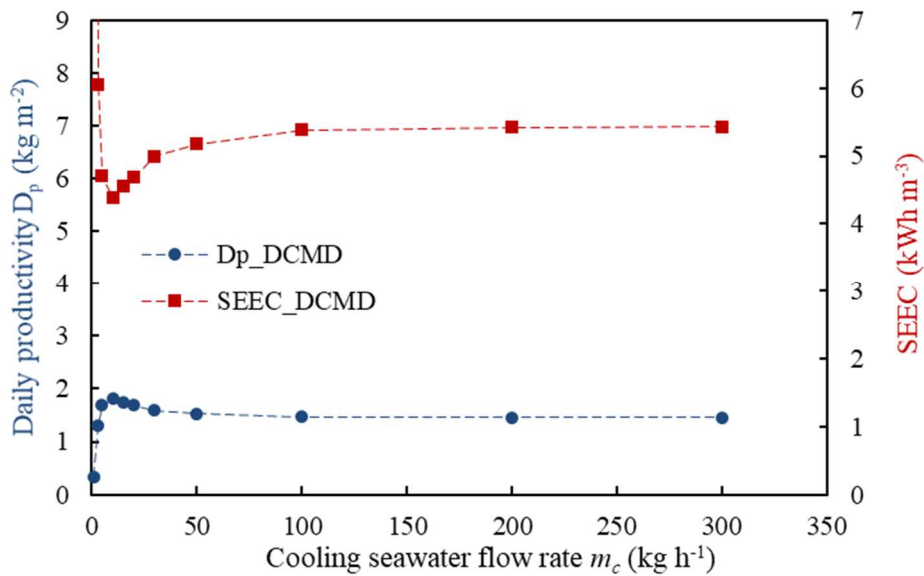
(b)

Figure III.9: Daily distillate productivity and specific electrical energy consumption at varying Reynolds numbers: (a) feed side for both DCMD-FPC and VMD-FPC modules; (b) permeate side for DCMD-FPC module only

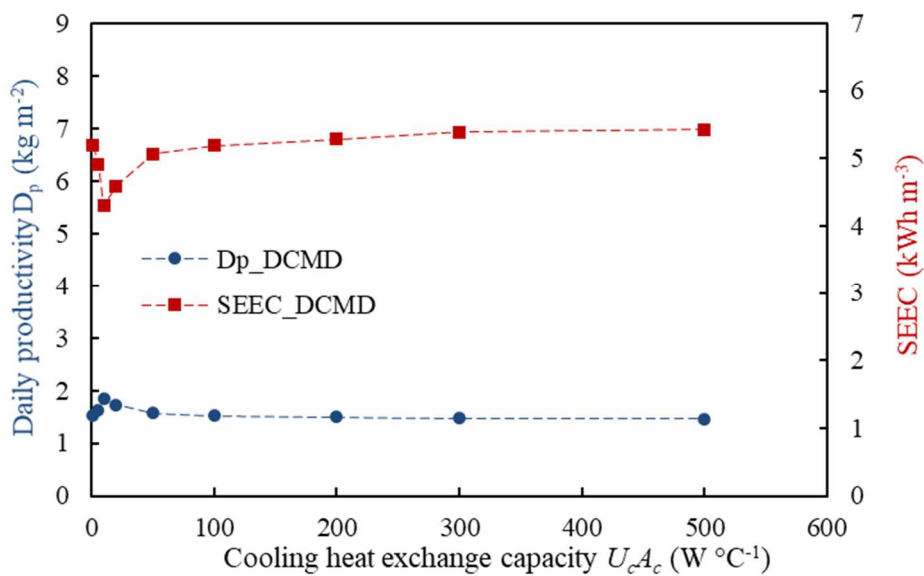
On the other hand, the pumping consumption of DCMD-FPC were nearly proportional to the Reynolds number (from 2 Wh at an Re around 70 to 45 Wh at an Re around 4000) because of the linear relation between the power consumption of CP and the flow rate, as expressed in Eq. 26, and no other electricity consumptions taken into account. Then, due to the unchanged D_p , SEECs of the DCMD-FPC in Figure III.9 also increases linearly with Re of either the feed flow or the cold distillate circulation. While for VMD-FPC, the majority of the pumping

consumption was taken up by the consumption of the vacuum pump. At a low Re of the feed flow ($Re < 500$), over 99% of the total consumption was found out to be spent on VP. Even when the feed flow was at the highest Re of 4600 in Figure III.9a and the consumption by CP would be at its maximum, 0.46 kWh was consumed by VP, out of the total consumption of 0.50 kWh, leaving only 44 Wh consumed by the CP of the feed circulation. Then, the power consumption of VP is proportional to the amount of permeate vapor and not influenced by the feed flow rate, according to Eq.27. Therefore, the major part of the SEEC of VMD-FPC in Figure III.9a that belongs to the vacuum pump stayed constant due to the constant D_p . For the left that consumed by CP in VMD-based system, its total amount increased with the Re at the same pace as the DCMD-based system. However, the total SEEC (by VP and CP) of VMD-FPC in Figure III.9a ascends more slowly with the increasing feed Re than the ascending pace of the SEECs of DCMD-FPC, which is because of the greater production in VMD-FPC incurring lower specific consumption by the CP and thus smaller slope of the total SEEC of the VMD-based system. Regarding the water productivity D_p for DCMD-FPC, in fact, it increased slightly from 1.45 to 1.58 kg m^{-2} with feed Re from below 100 to about 4000, while it decreased from 1.55 to 1.37 kg m^{-2} with permeate Re from below 100 to nearly 4000. This observation further backs up the important impact of transmembrane conductive thermal loss in DCMD. Higher feed Re can help to enhance the heat transfer from the feed bulk to the boundary layer to provide for water evaporation and heat conduction through the membrane. However, higher permeate Re helped to improve the reception of not only water condensation heat but also conductive heat loss by enhancing heat transfer from the permeate boundary layer to the bulk. In consequence, the higher permeate Re permitted larger overall heat loss from the limited solar energy input and caused the production declination. Conclusively, higher Re of both the feed and the permeate side contributes to higher pumping consumption without enhancing the productivity of the DCMD-FPC, therefore lower Re is more favorable for this simple recirculation system, same as concluded for VMD-FPC in Chapter II in case no heat recovery strategy was implemented.

Beside the feed and permeate recirculation, a cooling cycle is involved also in the system as illustrated in Figure III.2, where seawater source is circulating and cooling the permeate recirculation. The concerned parameters are the cooling flow rate \dot{m}_c , the heat exchange coefficient U_c and the heat exchange surface A_c , and the latter two intervene the model by their product $U_c A_c$. Figure III.10 presents their impact on the system performance of DCMD-FPC module.



(a)



(b)

Figure III.10: Daily distillate productivity and specific electrical energy consumption at varying: (a) cooling circulation flow rate, (b) cooling heat exchange capacity $U_e A_c$

Both very low values of m_c and $U_e A_c$ were preferred by the DCMD-based system, being around 10 kg h^{-1} and $10 \text{ W } ^\circ\text{C}^{-1}$. However, the possible improvement by adjusting the cooling condition was still very limited compared to altering membrane properties as discussed in Section III.3.2.2. Furthermore, this preference again confirms the strong influence of heat conduction through the membrane. Better cooling effect can ensure a lower temperature of the cold distillate on the permeate side, which strengthens the driving force and thus the permeate flux. On the other

hand, such lower temperature can induce bigger transmembrane conductive heat loss. Therefore, the low values of the optimal choice indicated that, for the same module configuration, more emphasis should be put on reducing heat conduction in DCMD instead of enhancing the productivity. Besides, the variations of SEECs in Figure III.10 are due to the variations of the production, while the total consumption, taken the CPs on the feed and the permeate was not affected at all by the cooling condition.

III.3.2.4. Module position and dimensions

Firstly, the module position was fixed by the slope β and the azimuth angle γ . The latter is usually set to 0, facing sharply south, for non-tracking non-concentrating solar collectors to maximize the received energy on the surface. Hence, the position parameter in question is the inclination of the module. The productivity D_p of both systems exhibited a same favorite slope at around 20° , as shown in Figure III.11. However, the pumping consumption behaved differently. Theoretically, bigger slope added to the burden of circulation pumps to overcome greater pressure difference between the bottom and the top of the module due to the elevated module height. Thus, both of the feed pump and the permeate pump had to consume more at bigger inclination in the DCMD-FPC system, while the improvement of water production from 0° to 20° was limited. The specific consumption of the VMD-FPC system, on the other hand, seldom reacted to the variation of the slope because the majority of the consumption was taken up by the vacuum pump, as discussed in Section II.4.4.

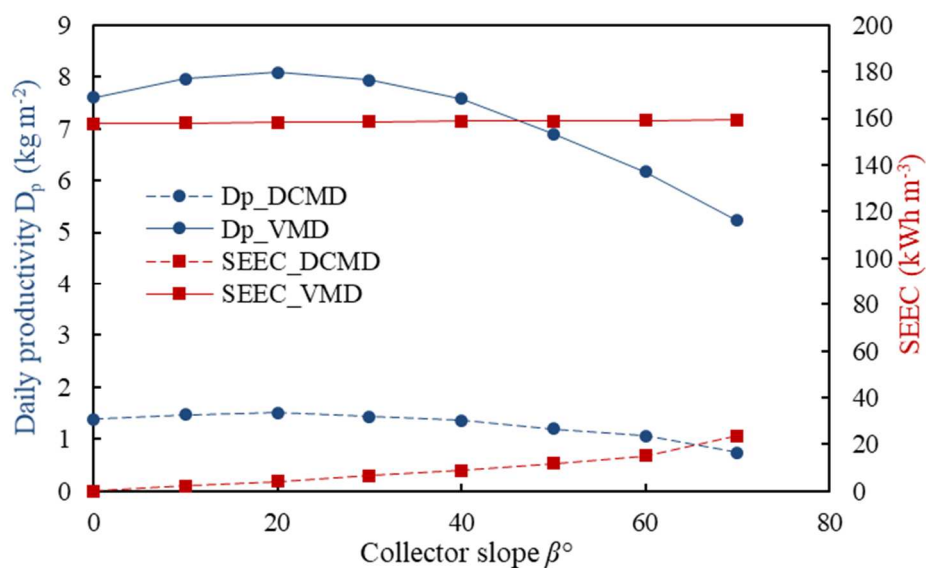
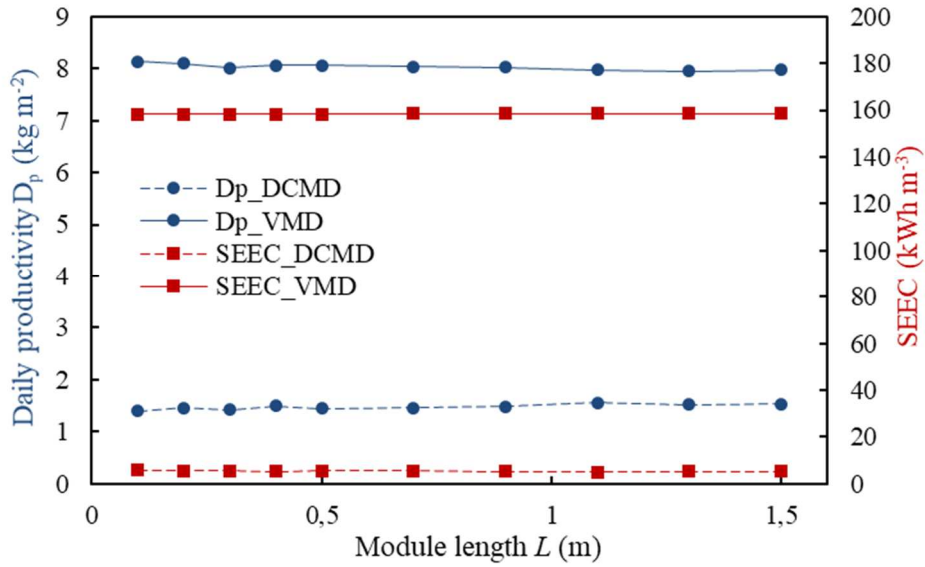
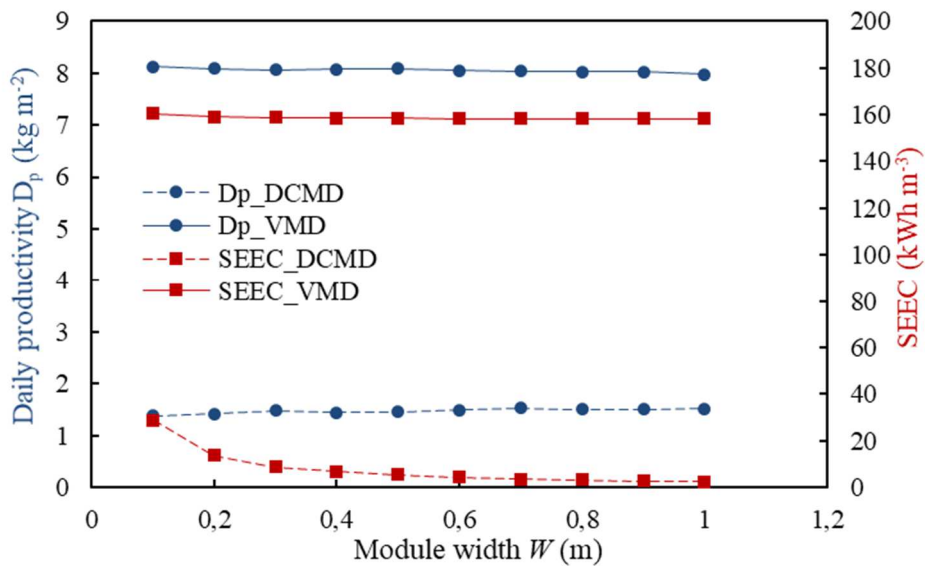


Figure III.11: Daily distillate productivity and specific electrical energy consumption at varying slope β

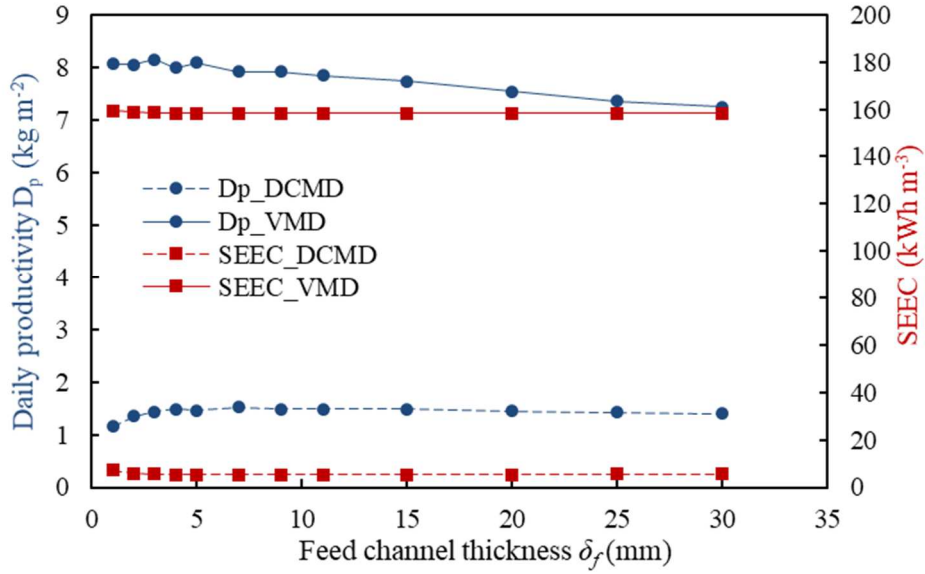
Secondly, the dimensions of the MD module consisted of the module length L , the module width W and the thicknesses of feed δ_f and permeate δ_p . In the VMD-based module, there would be no discussion on the thickness of the permeate side because of the assumption of a uniform vacuum space without water circulation. The influences of the dimensions on the performance of both DCMD-FPC and VMD-FPC are illustrated in Figure III.12.



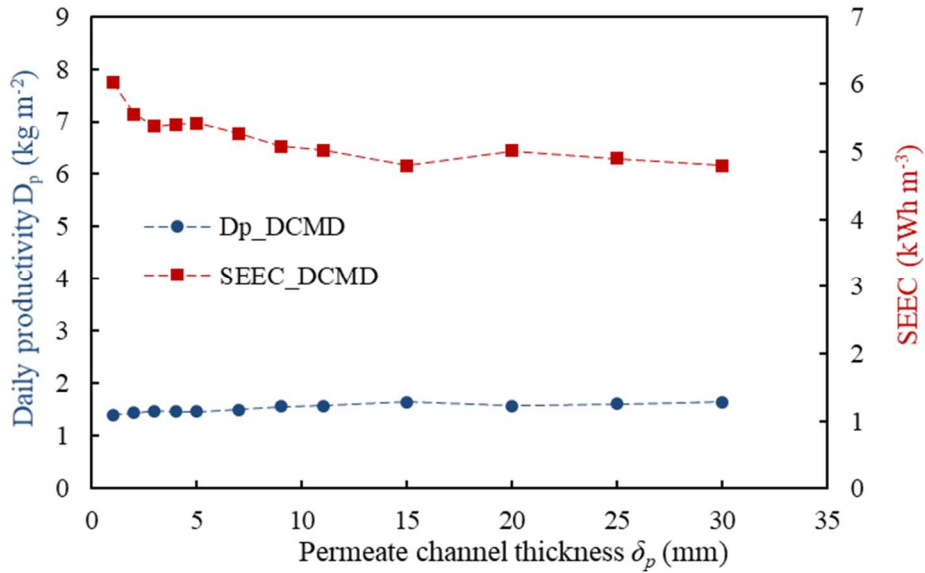
(a)



(b)



(c)



(d)

Figure III.12: Daily distillate productivity and specific electrical energy consumption at varying module dimensions for DCMD-FPC and VMD-FPC systems: (a) length L , (b) width W , (c) thickness of feed channel δ_f ($W \times L = 0.5 \times 0.7$ m²), (d) thickness of permeate channel δ_p ($W \times L = 0.5 \times 0.7$ m²)

The length of the module hardly altered the performance of both systems. With very limited thermal energy input from the absorber-plate, the total water volume and the heat and mass transfer inside the channel, which were connected with the length, did not seem to be influential. Similarly, no clear influence of the module's width was observed except for the SEEC of the DCMD-based module. This observation was due to the augmenting flow velocities and

Reynolds numbers on both sides of the membrane, when decreasing the module width under fixed flow rates. Thus, higher pressure loss was induced and consequently higher CP power was demanded, according to Eq. 23 and 26. Furthermore, it was found by simulations that if fixing the flow velocities by scaling the flow rates proportionally to the width, a constant SEEC of DCMD-based module could also be attained. Conclusively, the surface dimensions (width W and length L) do not influence sensibly the productivity and specific consumption, thus the scale-up of the module can be achieved simply by bigger module surface or several modules in parallel.

The thickness of the channels had a smaller impact on the flow Reynolds number based on its slightness compared to the width W . The hydraulic diameter of the flow channel was thus nearly double the value of the thickness ($d_h = 2W\delta/(W + \delta) \approx 2\delta$), combined by the flow velocity which was in inverse proportion with the thickness at given flow rates ($v = F_V/(W\delta)$), the effect of the thickness on Re calculation was therefore almost eliminated. From Figure III.12c, different trends of the productivities for the VMD-based and DCMD-based systems emerged. When the feed channel thickness was smaller than 5 mm, the D of the VMD-based system held steady while the D of the DCMD-based system slowly went up. After the value of 5 mm, the former slowly went down while the latter also went down. A thinner layer of feed channel helps to enhance heat convection and alleviate temperature polarization for higher permeate flux [203], that is why the D_p of VMD-based module kept on decreasing with higher δ_f . However, the overall heat input from solar absorption limited the production to a certain level even the feed channel was thinner than 5 mm. On the other hand, a thinner feed channel of DCMD also reinforced the heat transfer and brought the temperatures at the bulk and at the membrane surface closer. However, larger transmembrane temperature difference was created simultaneously, admitting greater conductive heat loss and thus reducing the overall accumulated water production, which was already addressed as the one of the major factors in determining the production capacity of the DCMD-FPC system. After a certain thickness, the heat transfer condition inside the feed channel started to take part in the water production, and a rather slight decrease from 1.53 to 1.39 kg m⁻² at a feed channel thickness from 7 mm to 30 mm was discovered. Besides, the pressure loss by friction along the flow channel was consequently in inverse proportion with δ^3 according to the first term on the right in Eq. 23. As a result, thinner channels induced higher circulation pump consumption, especially when at extremely small value, as observed in the Figure III.12c and 12d, though not really outstanding compared to the huge overall electric consumption of the VMD-based module mostly consumed

by vacuum pump. At last, the variation of D_p with varying permeate channel thickness δ_p in Figure III.12d might probably be explained also by the more important heat loss with thinner flow channels, as explained for δ_f of the feed channel.

III.3.3. Discussions on a high potential: Heat recovery & solar concentration

Both solar-integrated MD systems studied in this chapter have relatively low water productions due to the enormous heat consumption by feed evaporation and the limited thermal energy source provided only by direct solar absorption. This highlights clearly the importance of enhancing the thermal energy income for the feed circulation in case an increase in permeate flux and water production is desired. Generally, two approaches can be conceived in the current application: Heat recovery from the permeate side back to the feed circulation, and solar concentration to multiply the absorbed heat by the module.

III.3.3.1 Heat recovery ($A_m = A_c = 0.5 \times 0.7 \text{ m}^2$)

For the DCMD-FPC module, the heat recovery is usually carried out by recuperating the thermal energy from the cold distillate or the cooling water. In the current system, the cooling was carried out by direct heat exchanging between the distillate and the circulating seawater. Therefore, a fixed Heat Recovery Ratio (HRR) of all the heat exchanged by cooling was deemed as a relevant way to study the influence of heat recovery on system performance. On the other hand for the VMD-FPC module, a certain ratio of the permeate vapor was presumed to be condensed by a certain facility before the vacuum pump, whose heat was redirected to the feed circulation, same as discussed in Section II.4.4.3. Thus, this ratio in VMD equals to a fixed HRR of all the condensation heat of the permeate. However, the discussion was incapable of evaluating the corresponding amount of supplementary electricity needed for both heat recovery approaches.

Figure III.13 demonstrates a substantial increase in water productivity for both systems if heat recovery strategies are implemented. The D_p of the DCMD system was markedly improved from around 1.5 kg m^{-2} without heat recovery to nearly 30 kg m^{-2} with 0.9 of the heat gained by the cooling stream putting back to the feed. Regarding the VMD system, the increment of D_p was from around 8 kg m^{-2} to even more than 50 kg m^{-2} .

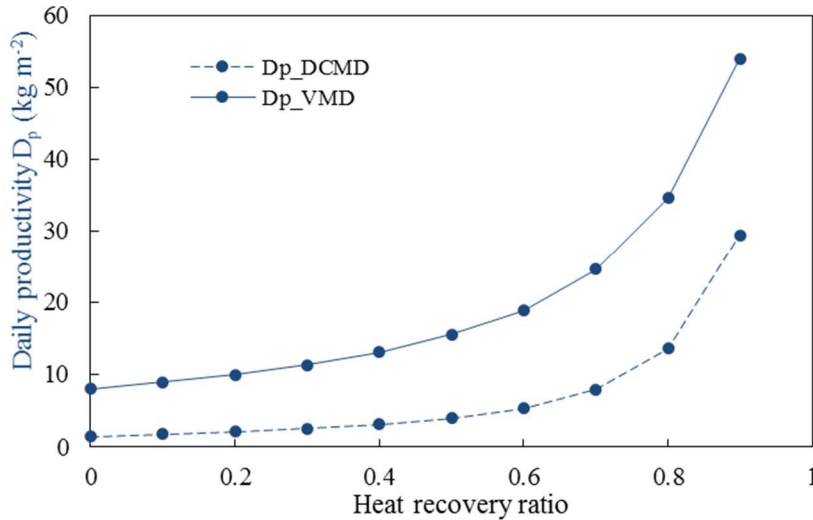


Figure III.13: Daily distillate productivity D_p for DCMD-FPC and VMD-FPC systems at varying heat recovery ratios (HRR)

In reality, a high HRR is not easy to attain. For DCMD, the vapor condensation directly takes place inside the cold distillate, whose temperature has to be low enough to maintain the driving force for vapor transfer, thus the latent heat of the permeate vapor is then stored in the cold distillate in liquid phase. Therefore, this heat is hard to be directly recovered back to a liquid feed at higher temperature. For VMD, the temperature of the permeate side is even lower in the vacuum, thus the same difficulty exists for heat recovery. However, the latent heat is still stored in vapor phase on the permeate side, which might be recaptured through condensation elsewhere. Considering such difficulty in heat recovery, high HRRs are not quite realistic and feasible, especially for the DCMD-FPC system. If applying an intermediate HRR (0.3 to 0.7) to a small module of 1 m^2 , the potential production of the DCMD-FPC system would still be much too low (2.5 to 7.9 kg) compared to the VMD-FPC system (11.3 to 24.6 kg) even on Aug 1st, when the solar condition might be the best on the northern hemisphere. This production of DCMD-FPC can hardly fulfill the drinking demand (2 L per day per person [204]) of a small family. Added by the above discussion on the heat recovery possibilities on both systems, VMD-FPC is therefore reckoned to be the one that is worth further study. It is however needed to check the existence and the feasibility of an innovative approach for heat recovery in the VMD-FPC system and further to evaluate its relevance in terms of extra energy requirements.

III.3.3.2. Solar concentration ($A_m = A_c = 0.5 \times 0.7 \text{ m}^2$)

A solar Concentration Ratio (CR) is defined as the solar aperture area to absorber area, which can be approximated by the factor of the increment of the absorbed solar energy on the absorber-

plate [112]. As introduced in Chapter I, only low concentration ratio can be applied to MD applications. Indeed, it was found that a concentration ratio over 7 could lead to a feed temperature over 100°C in the afternoon for both DCMD and VMD-based systems, which was then rejected by the simulation. Consequently, Figure III.14 illustrated the water productivities of DCMD-FPC and VMD-FPC with varying concentration ratios up to 7. Similar to the discussion on the heat recovery, the extra energy consumption by solar tracking systems for the concentrator and other supplementary facilities could not be evaluated at current stage.

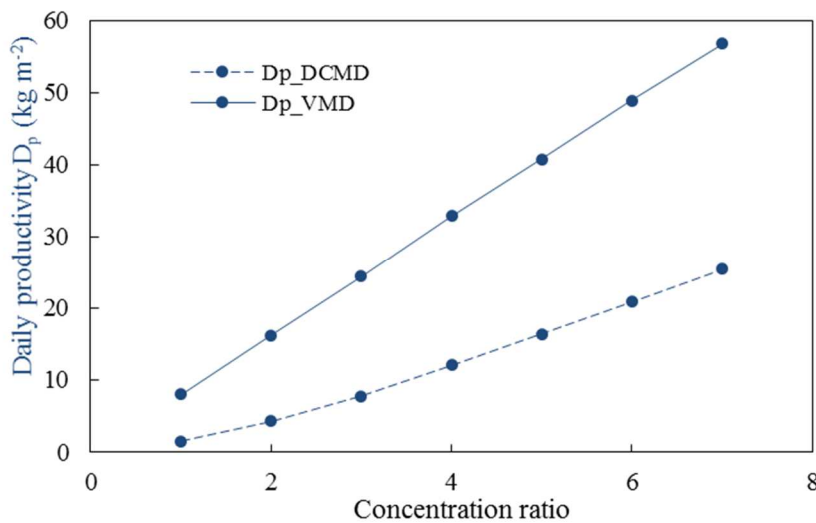


Figure III.14: Daily distillate productivity D_p for DCMD-FPC and VMD-FPC systems at varying concentration ratios (CR)

Unlike Figure III.13, the productivity linearly responded to the increasing CR due to the linear increments in the heat supply by the absorbed solar energy. The production capacity difference between DCMD and VMD-based systems is still obvious, same as the discussion on HRR. At a moderate CR of 3, the D_p of VMD-FPC could reach up to 24.5 kg m^{-2} while that of DCMD-FPC was only able to yield a productivity of 7.8 kg m^{-2} , even lower than the VMD-FPC without heat recovery or solar concentration. The D_p of DCMD-FPC became also interesting when the CR was over 5 ($> 16 \text{ kg m}^{-2}$) in terms of the domestic drinking water provision. However, larger CR would leave larger footprint, decreasing the compactness and the mobility of the system. For example, CR = 5 means a concentrator of an aperture area of more than 5 m^2 needs to be installed for a module of 1 m^2 . Furthermore, the complexity in concentrator design and solar-tracking when increasing CR adds to the problem of applicability in remote communities. At last, the design of solar concentrator is also part of module design, which demands further study.

III.4. Conclusions (in English)

Based on a previous design of an integrated module coupling direct solar heating with VMD process (VMD-FPC system), a similar DCMD-based desalination system was studied in order to contrast the two diametrically opposite MD technologies in terms of water production and power consumption and to compare their hybridization potentials when coupled with direct solar heating scenarios. To provide a fair comparison between the original VMD-FPC module and the DCMD-FPC, a similar dynamic recycling system was indeed defined. However, additional readjustments in terms of diffusion mechanism and recirculation system have been made, as the description of membrane permeability is different in DCMD, and knowing that in case of DCMD a permeate recirculation has to be included together with a simple cooling cycle for the permeate side to keep the transmembrane vapor pressure difference.

Simulations for daily 12-hour operations revealed that the water production of the DCMD-FPC system (0.51 L for the 0.35 m² module) was much lower than that of the VMD-FPC system (2.83 L for the same 0.35 m² module) under the same parameters and operating conditions, which indicated a huge difference in the thermal efficiency of utilizing solar energy for distillate production: 16% of the former system and 89% of the latter system. However, much higher production and thermal efficiency also came with a price: electric consumption of VMD-FPC was 0.45 kWh (power consumption per unit distillate 13.25 W L⁻¹), in contrast with only 2.76×10⁻³ kWh of DCMD-FPC (power consumption per unit distillate 0.45 W L⁻¹). These electricity demands have to be provided by installed photovoltaic panels.

Then, the roles of different groups of parameters concerning material properties, operating conditions, position and dimensions were analyzed in details for both the DCMD-FPC and the VMD-FPC systems, comparatively. The discussions on the variations of the parameters all indicated that in the case of direct solar heating with the limited available solar energy, especially when no heat recovery strategy is applied, the VMD-FPC system was restrained by the heat income from solar energy (decided by the aperture area of the collector), while the DCMD-system was even further shackled by the heat conduction from the feed to the distillate (depends on membrane properties and operating temperatures). Besides, the performances of both systems stayed unaffected by the variation of the module surface, which enables a flexible design of the module size based on the productivity and the water provision demand.

Finally, heat recovery and solar concentration were deemed as two possible approaches to enhance the freshwater production of such hybridization. Regarding the former, heat has to be redirected from the low-temperature permeate side to the high-temperature feed circulation in both DCMD and VMD, while the vapor-phase permeate side in VMD enables more possibilities. Furthermore, the production capacity of a small-scale DCMD-FPC system was shown to be incapable of supplying the drinking water demand for dispersed communities under a reasonable heat recovery ratio, while the VMD-FPC system exhibited a more relevant and controllable production. For the latter approach of solar concentration, productivities for both systems could be linearly improved with an increasing solar concentration ratio, displaying good potentials for application. However, 2 ~ 3 times the concentration ratio of the VMD-FPC was required by the DCMD-FPC to produce the same quantity of distillate, which means a much larger footprint and a higher module complexity of the DCMD-FPC module. Therefore, VMD-FPC was deemed more appropriate for further study in the following of this thesis.

The design and integration of a solar concentrator is out of the scope of the current thesis. Hence, the next task is to tailor an innovative design and to provide a feasibility study of heat recovery in the context of integrated VMD-FPC desalination system. Correspondingly, comprehensive performance evaluations and optimizations on water production and energy consumption (pumping, cooling, heat recovery, module design) are expected.

III.4. Conclusions (en français)

Sur le même principe de conception que pour le module intégré couplant le chauffage solaire direct au procédé VMD (système VMD-FPC) vu au chapitre précédent, un système de dessalement intégré de DCMD a été étudié afin de comparer les deux technologies de MD identifiées comme diamétralement opposées en termes de production d'eau et de consommation électrique, et de comparer leur potentiel d'intégration avec un chauffage solaire intégré au module. Pour une comparaison correcte entre le module VMD-FPC original du chapitre II et un module DMCD-FPC intégré, un système de recyclage dynamique similaire a été défini. La modélisation a été revue pour prendre en compte les mécanismes de diffusion spécifique de chaque procédé. De plus, le système de recirculation a été adapté pour le DCMD pour prendre en compte la recirculation du perméat avec un cycle de refroidissement simple côté perméat dans DCMD pour maintenir la différence transmembranaire de température et donc de pression de vapeur.

Les simulations sur une journée pendant 12 heures de fonctionnement montrent que la production d'eau du système DCMD-FPC (0,51 L pour le module de 0,35 m²) est bien inférieure à celle du système VMD-FPC (2,83 L pour le même module de 0,35 m²) pour un même module et des conditions de fonctionnement similaires. Ceci révèle une énorme différence d'efficacité de l'utilisation de l'énergie solaire thermique pour la production de distillats: 16% seulement pour la DCMD-FPC et 89% pour la VMD-FPC. Toutefois, la productivité et l'efficacité thermique ont également un prix : la consommation électrique de VMD-FPC est de 0,45 kWh (la puissance par unité de distillat 13,25 W L⁻¹), et de seulement 2,76×10⁻³ kWh pour la DCMD-FPC (la puissance par unité de distillat 0,45 W L⁻¹). Ces demandes en électricité doivent être fournies par des panneaux photovoltaïques installés.

Ensuite, l'influence de différents groupes de paramètres concernant les propriétés des matériaux constitutifs du module, ses dimensions et sa position ainsi que les conditions de fonctionnement de l'ensemble du système ont été analysés et comparés pour les procédés DCMD-FPC et VMD-FPC. Toutes les études de sensibilité des paramètres montrent que dans le cas du chauffage solaire direct avec l'énergie solaire disponible limitée, surtout sans stratégie de récupération de chaleur, le système VMD-FPC est limité par l'apport thermique solaire (contrôlé par la surface du module), et pourrait donc produire plus dans des conditions d'exposition plus favorables alors que le système DCMD est encore limité par la conduction thermique dans la membrane de l'alimentation vers le distillat (qui dépend surtout des propriétés du matériau membranaire et des températures des fluides). En outre, les performances des deux systèmes ne sont pas affectées par la variation de la surface du module, ce qui permet d'envisager une conception flexible de la taille du module en fonction de la demande d'eau potable et de la taille de la communauté à approvisionner.

Enfin, la récupération de chaleur et la concentration solaire sont identifiées comme deux perspectives possibles pour améliorer la production d'eau d'un tel module hybride. Dans le premier cas, il est nécessaire que la chaleur doit être redirigée du côté de perméat en basse température vers la circulation d'alimentation en haute température dans DCMD et VMD, pour récupérer la chaleur en DCMD et VMD, alors que le fait de récupérer le perméat sous forme vapeur en VMD ouvre davantage de possibilités. En outre, il apparaît que la capacité de production d'un système DCMD-FPC à petite échelle ne permet pas de fournir suffisamment d'eau potable pour une petite communauté avec un taux de récupération de chaleur raisonnable, alors que le système VMD-FPC permet une production plus réaliste et contrôlable facilement

par la pression. Dans le dernier cas de concentration solaire, les productions des deux systèmes pourraient être améliorées linéairement avec un taux de concentration solaire croissant, ce qui ouvre des perspectives d'application et de développement. Cependant, le pour produire le même volume d'eau le système DCMD-FPC nécessite un taux de concentration environ 2 ~ 3 fois plus élevé que pour la VMD-FPC, ce qui pénalise la compacité et accroît la complexité du module. Par conséquent, cette étude permet d'orienter la suite de ces travaux sur le VMD-FPC.

La conception et l'intégration d'un concentrateur solaire sortent du périmètre d'étude de cette thèse. L'objectif de la suite de nos travaux est de préciser une conception novatrice de récupération de chaleur pour un système de dessalement basé sur le module intégré VMD-FPC et d'en étudier la faisabilité. Avant de conclure sur cette faisabilité, il est nécessaire d'évaluer les performances et d'optimiser la conception globale du système (pompage, refroidissement, récupération de chaleur, design du module) sur des critères de production d'eau et de consommation d'énergie.

IV. Optimization and design of a novel integrated vacuum membrane distillation - solar flat plate collector module with heat recovery strategy through heat pumps

This chapter is extracted from a submitted paper.

Q. Ma, A. Ahmadi, C. Cabassud, Optimization and design of a novel integrated vacuum membrane distillation - solar flat plate collector module with heat recovery strategy through heat pumps, *Journal of Membrane Science*. (2019).

IV.1. Introduction (in English)

Chapter II and III have been the subject of in-depth discussions on the direct integration of flat plate solar collectors (FPC) with two diametrically opposed MD systems in terms of production and consumption (VMD and DCMD). As a result, when the same surface area has been set for the solar collector and the membrane, an integrated VMD-FPC module has been pointed out as being more suitable for applications in remote locations for small dispersed communities, because of the higher and controllable permeate flux and the low conductive heat loss associated with this MD configuration.

This chapter therefore presents the optimization and design of an enhanced small-scale solar desalination unit, in which VMD and flat-plate collector (FPC) solar heating are coupled within the same intensified module. In addition, in order to explore the higher potentials of such an integrated VMD-FPC module after the knowledge of the importance of a heat recovery strategy in Chapter II and III, a suitable heat pump is conceived to bridge the heat-demanding feed recirculation to the heat-releasing condensation unit. The heat recovery unit proposed and established based on simulations in this work aims: (i) to offer a practical condensation strategy that exempts the use of additional intensive cooling systems and (ii) to recover the latent heat of the permeate during the condensation.

In the literature, the idea of coupling heat pumps with conventional (non-integrated) MD modules has been advanced by S.I. Andersson et al. [205] as a perspective of their work in 1985. Nevertheless, the feasibility of such an approach and the choice of suited thermal fluids when coupled with MD systems have not been widely studied and elucidated. Recently (2014 and 2016), a heat pump was integrated in a two-loop solar-powered Vacuum Multi-Effect Membrane Distillation (V-MEMD, Memsys) system pilot, to preheat the feed and simultaneously cool down the cooling water [107,110]. This V-MEMD system significantly increased and nearly doubled the water production, indicating the feasibility and value of such a combination in similar MD configurations. Even more recently, a thermoelectric heat pump has been adapted to an SGMD module to simultaneously cool the supply air, condense the permeate vapor and collect the latent heat to redirect it back to the feed side [206]. Two small modules of 0.00849 m² and 0.0151 m² were tested under feed temperatures of 30°C and 40°C, where the results denoted nevertheless a limited performance in water production with an excessive total SEC above 8500 kWh m⁻³ (calculated from the data given in [206]).

In this chapter, firstly, a conceptual heat pump is proposed and conceived within the system of the integrated VMD-FPC module where the absorbed solar energy is recovered by maintaining an energy transfer between the recirculating feed flow (heat pump condenser) and the permeate condensation unit (heat pump evaporator). It should be noted that the integrated heat pump unit is multifunctional. In fact, locating the heat pump evaporator (at low temperature) before the vacuum pump would be a practical strategy for condensing the permeate, avoiding the use of additional intensive cooling systems (which usually is not reported in the literature) and markedly reducing the electrical requirements of the vacuum pump, as raised in Chapter II.

The VMD-FPC module with integrated heat recovery by heat pump is then studied in a suited recirculation system, as proposed in Chapter II and III. Daily distillate production D (L) and Electrical energy consumption E (kWh) are dynamically evaluated for different levels of heat recovery, ranging from no heat recovery to a relatively high heat recovery efficiency. In addition, the present work provides the sensitivity analysis performed by the Delta Moment-Independent (DMI) indicator and fast design-oriented multi-objective optimizations using AMOEAMAP algorithm, with D and E being the two main problem objectives, to globally optimize the most influential parameters among the relevant solar-heating parameters, membrane permeability, operating conditions and module dimensions, and to discuss the key issues for optimal operation of the entire process.

IV.1. Introduction (en français)

Les chapitres II et III ont été consacrés à l'intégration directe de collecteurs solaires plans (FPC) dans deux modules de MD diamétralement opposés en termes de production et de consommation : VMD et DCMD. Ils ont permis de conclure que pour un module intégré, pour lequel par définition le collecteur solaire et la membrane ont la même surface, un système fonctionnant avec un module intégré VMD-FPC permet d'obtenir à la fois un flux de perméat supérieur et contrôlable et une plus faible perte de chaleur par conduction, et est donc plus adapté à l'application visée dans cette thèse : la fourniture d'eau potable à de petites communautés vivant dans des zones isolées.

Ce chapitre IV s'intéresse à approfondir les connaissances sur ce système VMD-FPC dans lequel la distillation membranaire sous vide (VMD) et le chauffage solaire à collecteur plan (FPC) sont intégrés au sein du même module intensifié. Il est plus précisément consacré à l'optimisation et à la conception d'une unité de dessalement solaire améliorée basée sur ce

système pour une faible capacité de production (adaptée à l'application). De plus, afin d'explorer plus largement les potentiels d'un tel module intégré VMD-FPC et du système complet le mettant en œuvre, et après avoir vu au chapitre II et III l'importance d'une récupération de chaleur dans l'efficacité globale du système, il est important de proposer une stratégie réaliste de de pompage et récupération de à chaleur est pour relier la recirculation de l'eau d'alimentation nécessitant un apport conséquent de chaleur à l'unité de condensation émettant de la chaleur. L'unité de récupération de chaleur proposée et mise au point sur la base de simulations dans ce travail a pour objectif : (i) d'élaborer une stratégie de condensation pratique qui permette d'éviter l'utilisation de systèmes de refroidissement intensifs supplémentaires et (ii) de récupérer la chaleur latente du perméat pendant la condensation.

Dans la littérature, l'idée de coupler une pompe à chaleur avec un module MD a été mentionnée dès 1985 par S.I. Andersson et al. [205] à l'issue de leurs travaux, comme une perspective. Néanmoins, la faisabilité de ce concept, le choix de fluides thermiques adaptés et le couplage à des systèmes MD n'ont pas été étudiés ni élucidés. Plus récemment, en 2014 et 2016 une pompe à chaleur a été utilisée dans un pilote de système de distillation membranaire multi-effets sous vide (V-MEMD, Memsys) avec 2 boucles de circulation alimenté par énergie solaire, pour simultanément préchauffer l'eau d'alimentation et refroidir l'eau de refroidissement [107,110]. La mise en oeuvre de la pompe à chaleur avec le V-MEMD module a permis de presque doubler la production d'eau, ce qui est prometteur sur la faisabilité et l'intérêt d'une telle combinaison dans des configurations similaires. Enfin, très récemment, en 2018 une pompe à chaleur thermoélectrique a été adaptée expérimentalement à un module SGMD conventionnel pour refroidir simultanément l'air alimentant le compartiment perméat (sweeping gas), condenser le perméat (obtenu sous forme vapeur) et récupérer la chaleur latente de vaporisation en la redirigeant vers le côté alimentation [206]. Deux très petits modules (de 0,00849 m² et de 0,0151 m²) ont été testés à des températures d'alimentation entre 30 °C et 40 °C. Ceci a mis en évidence une production d'eau limitée avec une SEC totale supérieure à 8500 kWh m⁻³ (valeur calculée à partir des données publiées dans [206]).

Dans ce chapitre, tout d'abord, un concept de pompe à chaleur est proposé et simulé dans le cas du module intégré VMD-FPC, dans lequel l'énergie solaire absorbée est récupérée en assurant un transfert d'énergie entre le flux côté d'alimentation en recirculation (condenseur de la pompe à chaleur) et l'unité de condensation du perméat (évaporateur de la pompe à chaleur). Il est important de noter que l'unité de pompe à chaleur intégrée est multifonctionnelle. En fait, elle

place l'évaporateur de la pompe à chaleur (à basse température) avant la pompe à vide, ce qui pourrait être une stratégie intéressante pour à la fois condenser le perméat, éviter l'utilisation de systèmes de refroidissement intensifs supplémentaires (ce qui n'est pas généralement mentionné dans la littérature) et réduire considérablement la consommation électrique de la pompe à vide, comme indiqué au Chapitre II.

Le module VMD-FPC avec la récupération de chaleur intégrée par pompe à chaleur est ensuite étudié dans un système de recirculation adapté, comme proposé aux chapitres II et III. La production quotidienne de distillat D (L) et la consommation d'énergie électrique E (kWh) sont évaluées de manière dynamique pour différents niveaux de la récupération de chaleur, de l'absence totale de récupération de chaleur à un rendement de récupération de chaleur relativement élevé. De plus, le présent travail fournit une analyse de sensibilité réalisée par l'indicateur DMI (Delta Moment-Independent) et des optimisations multi-objectifs, destinées à orienter la conception du module et le choix des paramètres de fonctionnement du système complet pour optimiser D et E , en prenant en compte notamment les paramètres les plus influents parmi les paramètres de chauffage solaire, la perméabilité de la membrane, les conditions de fonctionnement et les dimensions du module. L'optimisation est réalisée en utilisant l'algorithme AMOEA-MAP adapté à une optimisation multi-objectifs orientée conception rapide.

IV.2. Process description: coupled solar collector - VMD

The flowsheet for the entire system including the VMD-FPC module, heat pump and recirculation system is illustrated in Figure IV.1. One important specificity of the present VMD-FPC module is that it admits the same surface for solar collector and membrane. Seawater is supplied through the feed side and then recycled via the recirculation pump by passing also through a heat pump. The flow rate of the seawater supply is at each time equal to the permeate flow rate, in order to provide a constant recirculation flow at the membrane feed side. If no wetting and no operational failure of the VMD process occurs during the operation, the salt concentration of the feed keeps accumulating. When the highest tolerable concentration (a setting of 300 g L^{-1} was selected in this work [40]) is detected by the concentration meter "c" at the outlet of the module, the whole operation stops and the system is evacuated by the discharge and then refilled through the seawater supply in Figure IV.1.

Chapter IV: Optimization of VMD-FPC with heat pump

The vacuum pump is the key element to maintain the low pressure on the permeate side and to allow for a considerable permeation even at low feed temperatures. The permeate is cooled and condensed in contact with the cold source of the heat pump and then transported to be collected in the distillation tank. The heat pump block in Figure IV.1 allows the energy transfer from the cold source to the hot source by using an intermediate compressor. In this fashion, the latent heat of evaporation is taken from the permeate at the cold source and recovered back to the hot source to heat the recirculation flow. Besides, compared to the placement of the vacuum pump in Chapter II where all the permeate vapor was compressed by the vacuum pump and then condensed (Chapter II), here in this configuration the energy consumption is expected to be much lower due to the smaller amount of vapor to be pumped out by vacuum pump. Summarily, connecting the permeate condensation before the vacuum pump and the heating of the feed side through a heat pump is potentially of great interest in the context of VMD modules, because it allows the simultaneous achievement of the two following goals: (i) ensuring an efficient permeate condensation under vacuum pressure with no extra intensive cooling utilities and lower electricity need for the vacuum pump, (ii) ensuring a relevant degree of heat recovery from permeate condensation.

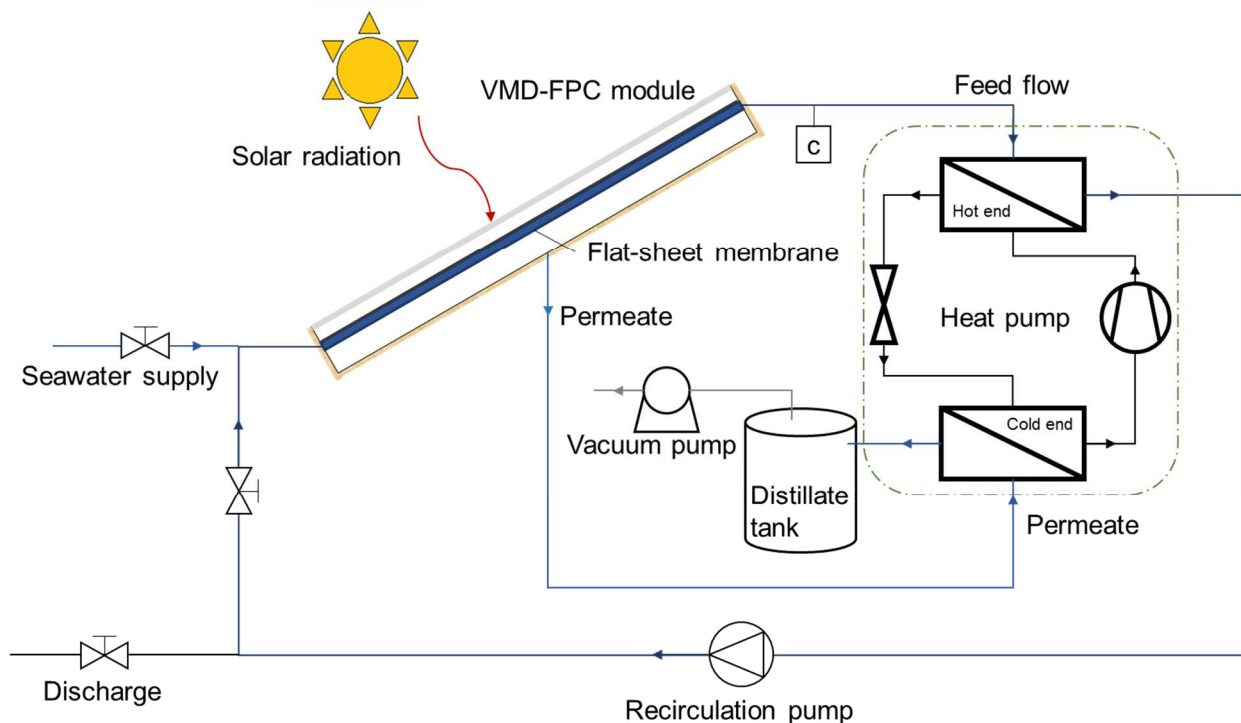


Figure IV.1: Flowsheet for VMD-FPC recycle system with integrated heat recovery through heat pump

IV.3. Design configuration and modeling of VMD-FPC with integrated heat pump

IV.3.1. Coupled solar flat-plate vacuum membrane distillation collector

The configuration of the integrated VMD-FPC module is shown in Figure IV.2, which is the same as Figure II.1, also similar to the configuration in [153,154] for DCMD and AGMD. The present design imposes few modifications to the structure of a normal FPC and also benefits from the high absorption capacity of the absorber-plate in commercially available FPCs. The MD module is inserted into the water circulation space under the absorber-plate (Figure IV.2), sharing the same surface with the solar collector. The glazing glass cover allows solar radiation to penetrate, which is then absorbed by the absorber-plate and heats up the feed side. Identical to a solar collector, the entire module is enclosed by a thermal insulation material.

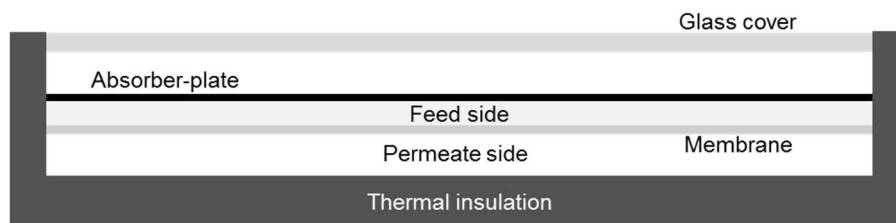


Figure IV.2: Cross-sectional view of integrated FPC-VMD module

Solar radiation model was mainly adapted and developed from Duffie and Beckman [112], and was explained in detail in Chapter II. Its location and time sensitive and cloudiness has not yet been taken into account. Isotropic diffuse model was assumed and the final absorbed solar energy was modeled from the ultimate source, the sun, to the absorber-plate step-by-step. The final utilized solar energy was obtained from the absorbed energy deducted by the thermal loss to the ambient, which is subject to the coupled VMD model.

The membrane pore model was previously developed and validated [22], with the description of permeate flux, as well as both temperature and concentration polarization. The assumptions taken into consideration were (i) no wetting, crystallization or biofouling during all the process, (ii) evaporation occurring at pore inlets where the liquid-vapor interface stands, (iii) only Knudsen diffusion (collisions of vapor molecules with the pore wall) [80] determining mass transfer through the membrane pores, (iv) neglecting heat loss through the membrane due to the vacuum [40], (v) calculation of seawater properties based on its water molar fraction x_w and its activity coefficient γ_w obtained by the PHREEQC software (version 2.13.1, US Geological Survey) [18].

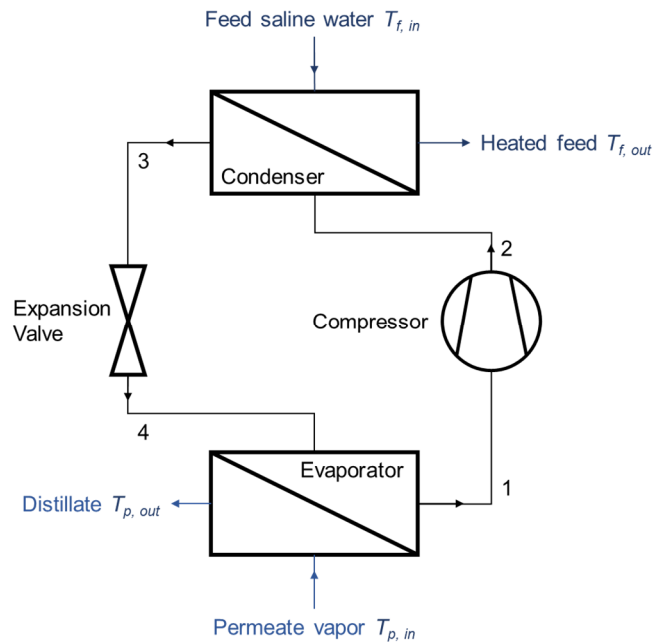
The feed bulk longitudinal model further aggregates the above models by a series of ordinary differential equations to predict the profiles of hydraulic pressure, temperature, flow velocity and salt concentration along the feed flow direction. The solar radiation calculation was coupled to it through the modeling of the utilized solar energy intensity, and the membrane pore model was coupled to it by the local permeate flux.

IV.3.2. Theoretical study of heat recovery from condensation by heat pump

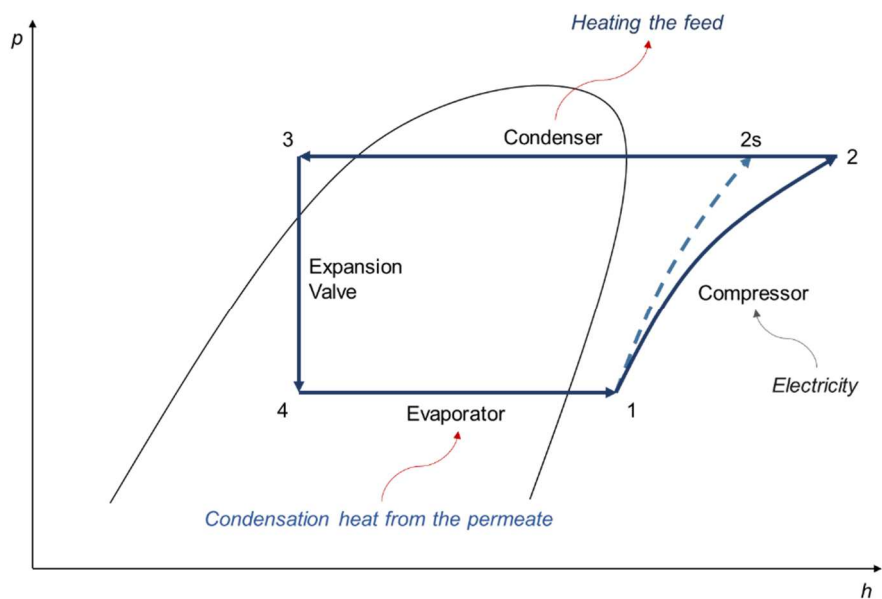
IV.3.2.1. Process description

The structure of the heat pump is shown in Figure IV.3a and the corresponding pressure-enthalpy diagram of the cycle is given in Figure IV.3b. This structure should be seen as a first illustrating attempt for feasibility check, where a single-stage heat pump is used. The coolant is used to condense the permeate vapor at the cold source (Heat pump evaporator in Figure IV.3a) by absorbing the latent heat of water evaporation and to return it to the feed circulation at the hot source (Heat pump condenser in Figure IV.3a). Therefore, the coolant should be capable of working between a low-temperature level (preferably below 0°C) to maximize the condensation of the permeate vapor under vacuum, and a certain temperature level to pass some heat back to the feed recirculation. The two heat exchangers (evaporator and condenser in Figure IV.3a) are the only contact points between the heat pump and the MD system.

As illustrated in Figure IV.3b, the permeate vapor is condensed in the evaporator, passing the heat of water evaporation to the low-temperature and low-pressure coolant which evaporates to Point 1. Then the coolant vapor is taken to relatively higher temperatures and pressures at Point 2 by a compressor and led to the condenser, where the feed saline water flows on the other side of the heat exchanger and can be heated if its temperature is below the dew point of the coolant. On the other hand, the coolant is condensed, then subcooled by the heat transfer to the feed flow (feed saline water in Figure IV.3a). Afterward, it experiences an isenthalpic expansion through the expansion valve (assuming no heat loss), back to Point 4. Finally, the cold coolant reaches the evaporator, where its low temperature ensures again the permeate condensation.



(a)



(b)

Figure IV.3: The heat pump cycle: (a) configuration of heat pump interconnected with MD system; (b) corresponding *pressure-enthalpy* diagram

IV.3.2.2. Process settings and calculation

The vapor permeate reaches the heat pump evaporator at saturation and is condensed, then subcooled down to 0°C ($T_{p,out}$) to maximize the condensation, thanks to the heat exchange with the coolant. A pinch point temperature difference of 2°C for this small-size heat exchanger was assumed between the outlet distillate and inlet coolant (Evaporator, Figure IV.3a). On the other

end of the counter-current evaporator, the coolant was supposed to be superheated 2 °C above its dew point, i.e. admitting $T_1 = 0^\circ\text{C}$. The heat recovery from permeate condensation (\dot{Q}_a) can be determined knowing the vacuum pressure on the permeate side and the temperature of liquid distillate after condensation,

$$\dot{Q}_a = \eta_a \dot{m}_p (h_{w,v,sat} - h_{w,l}) \quad (1)$$

Where, $h_{w,v,sat}$ (J kg^{-1}) is the enthalpy of saturated permeate vapor at the vacuum pressure of the permeate side in the VMD module, $h_{w,l}$ (J kg^{-1}) the enthalpy of the subcooled water after condensation, \dot{m}_p the permeate mass flow rate (kg s^{-1}), and η_a the evaporator efficiency set to 0.95 to ensure an efficient condensation of permeate.

On the other hand, given a reasonable isentropic efficiency η_{is} for a small-scale heat pump in our case [207] and a high working pressure P_2 in the condenser, the coolant temperature (T_2) and coolant enthalpy ($h_{c,2}$) at the outlet of the compressor can be determined.

$$h_{c,2} = \frac{h_{c,2s} - h_{c,1}}{\eta_{is}} + h_{c,1} \quad (2)$$

Where, $h_{c,2s}$ is the isentropic enthalpy of the coolant at P_2 following an ideal compression, and $h_{c,1}$ is the enthalpy of the coolant at point 1 (Figure IV.3).

Similar to the evaporator, a pinch point temperature difference of 2°C was considered between the inlet feed saline water (recirculation flow) and the outlet coolant (Point 3, Figure IV.3). Therefore, knowing the state variables, the coolant enthalpy at Point 3 ($h_{c,3}$) can be obtained. At last, following the isenthalpic expansion at the valve, the coolant enthalpy at point 4 ($h_{c,4}$) equals $h_{c,3}$. The knowledge of $h_{c,4}$ allows for the determination of the coolant flowrate using the heat recovery from permeate condensation (\dot{Q}_a), previously determined in Eq. 1.

$$\dot{m}_c = \dot{Q}_a / (h_{c,1} - h_{c,4}) \quad (3)$$

Finally, the compressor power \dot{W}_{comp} and the heat recovered back to the feed recirculation flow by the condenser \dot{Q}_b are calculated.

$$\dot{W}_{comp} = \dot{m}_c(h_{c,2} - h_{c,1}) \quad (4)$$

$$\dot{Q}_b = \dot{m}_c \eta_b (h_{c,3} - h_{c,2}) \quad (5)$$

Where, η_b the condenser efficiency which directly determines the ratio of condensation heat recovered back to the recirculation flow (Heated feed stream, Figure IV.3a). However, \dot{Q}_b would significantly reduce when the feed temperature is getting really close to the condensation temperature in the condenser, until 0 if the temperature difference in the condenser is equal or even smaller than the pinch temperature of the heat exchanger.

IV.3.2.3. Miscellaneous notes

Oppositely to Chapter II, here the permeate condensation takes place mostly before the vacuum pump, via an effective heat exchange with the evaporator of the heat pump. Along with the assumption of 0.95 on this exchanging efficiency η_a , only a small proportion of 0.05 of the permeate vapor has to be pumped out by the vacuum pump, in contrast with the configuration where all the permeate vapor being pumped out by the vacuum pump. Consequently, the burden of the vacuum pump in this study is much reduced.

Broadly speaking, an effective permeate condensation under vacuum in a VMD system, such as the case in the current study, demands intensive cooling facilities. However, its integration and consumption in the system have seldom been taken into account. Instead, in the current study, the low evaporating temperature of -2°C of the coolant in the heat pump guarantees the effective vapor condensation, whose consumption is included in the compressor work in the heat pump, defined in Eq. 4 above.

IV.3.3. Modeling structure, recirculation and system dynamics

Figure IV.4 provides the structure of models involved in this chapter. In the center of the structure, the model for recirculation and system dynamics is placed as the global combining node. At this level and regarding the process flowsheet in Figure IV.1, the dynamics are included based on time-varying steady-state phases.

As given in Eq. 6, the total mass (m) is assumed to be maintained constant by a continuous compensation (\dot{m}_s) through seawater supply for water permeation ($\dot{m}_p = J_w A_C$, with J_w the

permeate flux and A_C the total area of the module). On the other hand, the concentration accumulation rate in the VMD-FPC module can be described by the incoming rate of salt mass from water supply \dot{m}_s (concentration C_s , density ρ_s), formulated in Eq. 7 with V being the total volume of the module feed side.

Finally, the temperature variation on the feed side is determined by the sum of the recovered heat from the condenser of the heat pump \dot{Q}_b , the utilized solar energy power $G_u A_C$ and the energy carried by the incoming water supply, as well as the outgoing permeate with both sensible and latent heat, as shown in Eq. 8. Therefore, the feed temperature is determined dynamically during the operation, not fixed as an inlet operating parameter.

$$\frac{dm}{dt} = \dot{m}_s - \dot{m}_p = 0 \quad (6)$$

$$\frac{dC}{dt} = \frac{1}{V} \left(\frac{\dot{m}_s C_s}{\rho_s} \right) \quad (7)$$

$$\frac{d(c_p m T_f)}{dt} = \dot{Q}_b + G_u A_C + \dot{m}_s h_s - \dot{m}_p (h_p + \Delta H_v) \quad (8)$$

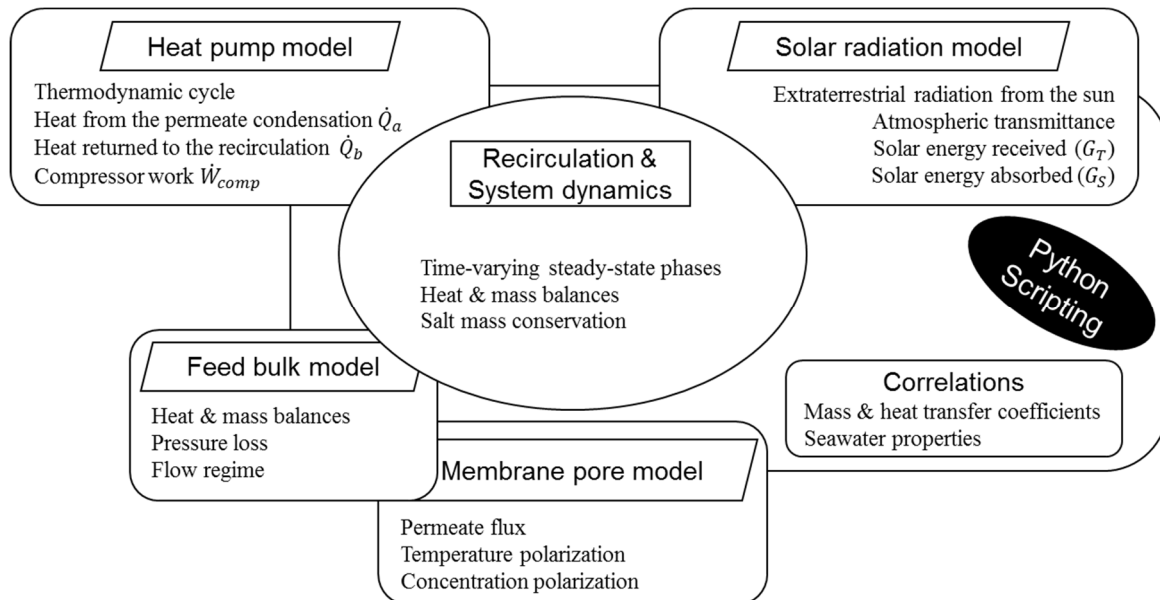


Figure IV.4: Schematic of modeling process of VMD-FPC with heat pump

A comprehensive model for the VMD-FPC module has been built with coupled VMD model and Solar radiation model, both of which have been validated previously in Chapter II. As it is illustrated in Figure IV.4, the above-mentioned VMD-FPC model involved:

- Membrane pore model, admitting Knudsen diffusion, temperature and concentration polarization in order to locally determine temperature and concentration as well as the permeate vapor flux at the membrane surface;
- Feed bulk model, establishing longitudinal properties along the feed side of the module (this includes mass and heat balances and momentum equation);
- Mass and heat transfer coefficients: the convective heat transfer coefficient for the heat transfer from feed bulk to the membrane surface from Nusselt number (Nu) correlations in the rectangular channels for laminar regime [173] and transitional or turbulent regime [81], the mass transfer coefficient for the salt diffusion from feed bulk to the membrane surface from semi-empirical correlations using Sherwood number (Sh) and Schmidt number (Sc) [74];
- Seawater properties: dynamic viscosity μ , density ρ and thermal conductivity λ from the regressions in [18], heat capacity of the seawater is taken from [174], and the diffusion coefficient of the salt in the seawater D_{s-w} from Stokes-Einstein relation with salt being assimilated as NaCl [175];
- Solar radiation model, determining the solar energy utilized (G_u) involving the estimation of solar radiation on the ground based on isotropic sky model where transmission, reflection, and absorption of radiation are included and referred to as functions of incoming radiations and main properties of the solar collector.

Same solution procedure as Chapter II was adopted. First, a system of differential-algebraic equations (DAEs) was resolved by the feed bulk longitudinal profile discretized along the module length and the set of algebraic equations describing the process in membrane pores. Then, Scipy ODE package with the Real-valued Variable-coefficient Ordinary Differential Equation solver (Isoda) [179] was applied to automatically process the system dynamics Eq. 6-8. It should be noted that all models in the thesis were programmed under Python (version 2.7.11).

IV.4. Performance assessment and analysis

IV.4.1. Decision variables, design parameters and main performance indicators

Overall, 15 variables were involved with reasonable value ranges for each one (Table IV.1), as well as several fixed parameters, given in Table IV.2. The decision variables include the slope β° and the azimuth angle γ° of the VMD-FPC collector, the refractive index n_c , the extinction coefficient K (m^{-1}), the thickness δ_c (m) and the emittance ε_c of the glazing cover, the emittance ε_{ap} and the absorptance α_n in normal direction of the absorber-plate, the membrane Knudsen permeability K_{mref} ($\text{s mol}^{1/2} \text{ m}^{-1} \text{ kg}^{-1/2}$), the permeate pressure P_p (Pa), Reynolds number, and the width W (m), the thickness δ_f (m) and the length L (m) of the feed channel. All the ranges of these variables are either limited by practical operating conditions or by realistic properties of the material. The last decision variable, the condenser efficiency in the heat pump (η_b), is particularly important because it directly determines the heat recovery level when heat pump is running. η_b was limited between 0, which means no heat recovery from the condenser of the heat pump to the feed, and 0.8.

Table IV.1: Decision variables for VMD-FPC module with heat pump

Variable	Range	Description
n_c	1.2 ~ 1.8	Refractive index of the cover
K	4 ~ 32	Extinction coefficient of the cover, m^{-1}
δ_c	2 ~ 5	Thickness of the transparent cover, mm
ε_c	0.6 ~ 0.95	Emittance of the cover
ε_{ap}	0.1 ~ 0.95	Emittance of the absorber-plate
α_n	0.8 ~ 0.95	Absorptance in normal direction
β	0.0 ~ 70.0	Slope of the solar collector, $^\circ$
γ	-40.0 ~ 40.0	Azimuth angle of the solar collector, $^\circ$
W	0.1 ~ 1.5	Width of the collector, m
δ_f	0.5 ~ 30	Flow channel thickness, mm
L	0.1 ~ 2.0	Module length, m
K_{mref}	$3.0 \times 10^{-6} \sim 1.85 \times 10^{-5}$	Membrane Knudsen permeability at 20°C , $\text{s mol}^{1/2} \text{ m}^{-1} \text{ kg}^{-1/2}$
Re	500 ~ 10000	Reynolds number at the inlet
P_p	650 ~ 20000	Vacuum pressure on the permeate side, Pa
η_b	0 ~ 0.8	Condenser efficiency in heat pump (When no heat recovery: $\eta_b = 0$)

All simulations were conducted under the condition of a cloudless and sunny day from 8:00 in the morning to 20:00 in the evening (12 hours of daily operation) on 1st August at the location

of Toulouse, to take an example of system operations and to give indications on the experimental tests here in the laboratory. Other fixed parameters are listed in Table IV.2, such as the information on the location and the surroundings, as well as the properties (concentration C_s , temperature T_s) of the supplied seawater and the highest tolerable feed salt concentration (300 g L⁻¹ [40]).

Table IV.2: Parameter settings for VMD-FPC module with heat pump

Parameter	Value	Description
L_{loc}	358.56	Longitude in degrees west, $0^\circ < L < 360^\circ$
φ	43.60	Latitude, north positive, $-90^\circ \leq \varphi \leq 90^\circ$
Al	150.0	Altitude of the location, m
h_{wi}	10	Heat transfer coefficient of the wind, W m ⁻² °C ⁻¹
r_0, r_1, r_k	0.97, 0.99, 1.02	Correction factors for mid-latitude summer [112]
ρ_g	0.2	Diffuse reflectance of the surroundings
T_{amax}	35	Highest ambient temperature, °C
T_{amin}	20	Lowest ambient temperature, °C
C_s	35	Salt concentration of the seawater supply, g L ⁻¹
T_s	25	Temperature of the seawater supply, °C
C_{limit}	300	The highest operating salt concentration, g L ⁻¹
U_{bo}	0.9	Heat loss coefficient of the insulation, W m ⁻² °C ⁻¹
η_a	0.95	Evaporator efficiency in heat pump
η_{is}	0.8	Isentropic efficiency of the compressor in the heat pump

As regards the heat pump, the organic fluid Solkatherm (SES36) was selected as the working fluid as a first attempt of this work, based on the specificity of cooling and heating requirements identified and mentioned in Section 3.2. SES36 is an azeotropic mixture of Pentafluoropropane R365mfc/perfluoropolyether (65 - 35% by mass), well-known in power industry and in organic Rankine cycles. Recently, its application in case of low-temperature ORC systems for waste heat recovery application has been studied [208]. SES36 is not toxic, not flammable, no ozone depletion potential (ODP) and it is more environmentally friendly when compared with commonly used coolants such as R134a or R404a [209]. More importantly, the corresponding pressure difference between the condenser and evaporator of heat pump can be lowered thanks to the thermodynamic properties of SES36, when working between an evaporator temperature of -2°C and a certain condenser temperature.

A low working temperature in the evaporator of the heat pump was set at -2°C (Section 3.2) in order to allow a pinch temperature difference of 2°C and to subcool the condensed permeate down to 0°C (T_1 in Table IV.3). Therefore, the compressor in the heat pump would operate between the coolant saturated pressure at -2°C and the condensing pressure in the condenser of the heat pump. Hence, the condensing pressure and temperature of the coolant preferred to be at lower values, so that the energy consumption of the compressor could be markedly reduced. Consequently, the main operating conditions of the heat pump are given in Table IV.3 that are considered as fixed parameters throughout the following study. All thermodynamic calculations, i.e. enthalpy and entropy calculations as well as phase equilibria regarding SES36 were provided by Python® library CoolProp [210], and the corresponding compressor work can be lowered by around 20% with SES36 when compared to R134a, under the same working temperature.

Table IV.3: Operating parameters of heat pump using SES36 in this study

Symbol	Description	Value
P_4	Evaporator pressure	24 kPa
P_2	Condenser pressure	48 kPa
T_1	Temperature at evaporator outlet	0°C
T_2	Temperature at compressor outlet	16.4°C
T_3	Temperature at condenser outlet	$T_{f,in} + 2^{\circ}\text{C}$
T_4	Temperature at expansion valve outlet	-2°C

The main performance indicators for this VMD-FPC system are the distillate production D in kilogram during the 12-h operation, and the total energy consumption E in kWh, considering the aim of efficient fresh water production in small and distributed scale for low electricity consumption, which further requires installed PV fields if a total autonomous operation is desired.

In the calculation of E , three components are taken into account: the compressor work \dot{W}_{comp} , which has been described by Eq. 4; the power required for the circulation and vacuum pump, \dot{P}_{cp} and \dot{P}_{vp} . \dot{P}_{cp} was determined from the total pressure loss ΔP between the inlet and outlet of the collector, as formulated below in Eq. 9.

$$\dot{P}_{cp} = \frac{F_V \Delta P}{\eta_{cp}} \quad (9)$$

Where, F_V is the volumetric flow rate on the feed side ($\text{m}^3 \text{s}^{-1}$), and η_{cp} the efficiency of the circulation pump.

If the whole system is assumed to be well sealed, \dot{P}_{vp} is then proportional to the amount of permeated water vapor flux that passes by the vacuum pump. By assuming an isothermal compression from the vacuum pressure P_p to atmosphere P_{atm} , Eq. 10 can be derived [180]. Here, the permeate temperature T_p is supposed to be the same as the temperature at the membrane surface on the feed side (T_{fm}) by the assumption of no conductive heat loss through the membrane.

$$\dot{P}_{vp} = \left(\frac{J_w A_c}{M_w \eta_{vp}} \right) R T_p \ln \left(\frac{P_{\text{atm}}}{P_p} \right) \quad (10)$$

Where, J_w is the mass flux of the permeate that passes through the vacuum pump ($\text{kg m}^{-2} \text{s}^{-1}$), M_w the molar mass of the water (kg mol^{-1}), and R the ideal gas constant in $\text{J mol}^{-1} \text{K}^{-1}$. An efficiency η_{vp} of 0.75 is assumed in this study.

IV.4.2. Sensitivity analysis via Delta Moment-Independent (DMI) indicator

The Sensitivity Analysis (SA) aims to comprehend how much the decision variables affect the problem's objectives. Then, the indications on how to ameliorate system performance can be achieved by specifying and analyzing the most influential variables from these results. Instead of a simple one-at-a-time (OAT) analysis in Chapter II and III, a global SA is envisioned in this chapter. Here, the Delta Moment-Independent (DMI) indicator in SALib Python library [211] was selected, i.e. an approach with a global sensitivity index δ based on given data to identify the impact of each parameter at the minimum computational cost [212,213]. It is sampling-free and able to work on an already available set of data, and therefore, compatible with simultaneous coupling with optimization studies. The index δ represents the normalized expected shift in the distribution of the output provoked by fixing a certain input variable, which ranges in $[0, 1]$ and equals 0 when the output is totally independent of the input variable in question [212]. Besides, the DMI package in Python also features a first-order variance-based

sensitivity indicator S1 for each input variable, which represents the expected percentage reduction of the output variance when the variable is fixed [214]. Consequently, S1 is scaled in [0, 1] as well.

IV.4.3. Fast multi-objective optimization on design and operating conditions

A multi-objective problem describes conflicting objectives, where the improvement in one objective results in the deterioration of another. An unconstrained problem can be mathematically stated as,

$$\begin{aligned} \text{Minimize} \quad & f_i(x), \forall i \in \{2, \dots, m\} \\ \text{Subject to} \quad & x \in \mathbb{R}^n \end{aligned} \tag{11}$$

Where, m is the number of objectives, x the vector of decision variables, $f_i(x)$ the objective functions, and \mathbb{R}^n the real space of n decision variables. The concept of domination is defined to discriminate solutions one against another. For two solutions x_1 and x_2 , the solution x_1 is said to dominate x_2 if and only if $f_i(x_1) \leq f_i(x_2)$ for all objective functions and $f_i(x_1) < f_i(x_2)$ for at least one objective function. The Pareto front (PF) comprises all optimal solutions belonging to the set of non-dominated optimal solutions.

In this chapter, by taking $f_1 = (-D)$ and $f_2 = E$ as the objective functions, a bi-objective optimization problem is formed, where as a result, energy consumption (E) is minimized while water production (D) is maximized. The set of 15 decision variables in Table IV.1 is taken into account with their respective ranges, resulting in an intermediate problem dimension. Furthermore, the better choices of some of the decision variables will be discussed based on the optimization results.

For this bi-objective optimization problem, a Pareto front is expected to represent the set of alternative scenarios. However, the dynamic simulations together with interrelated modeling and resolutions, as discussed in Section 3.3, can be time-consuming. Thus, in order to reduce the computational budget as much as possible, the archive-based multi-objective evolutionary algorithm with memory-based adaptive partitioning of search space (AMOEAMAP) was adopted as the fast optimization algorithm [215,216], which aims to provide an efficient and steady convergence over the Pareto front within a limited number of simulation runs. For the

study in this chapter, the computational budget was limited to 3000, which means that overall, 3000 simulations were operated to form the optimal Pareto front.

It should also be noted that the heat recovery level is clearly an essential factor for both objectives in this study, as reported also in the literature [164]. Therefore, in order to better observe its influence on the overall performance, different heat recovery levels determined by fixed $\eta_b = \{0, 0.2, 0.4, 0.6, 0.8\}$ were studied independently, yielding a 14-variable optimization for each case. Varying η_b was also taken into consideration to perform an additional optimization afterwards. For the sake of simplicity, a small reformulation was applied by merging the extinction coefficient K and the thickness δ_c of the glazing cover into a dimensionless product $K\delta_c$, which keeps the number of variables at 14. These two variables are mainly involved in the calculation of the radiation absorbed by the cover, which is determined by their product.

IV.5. Results and discussions

IV.5.1. Sensitivity variation due to heat recovery from permeate condensation

To offer a better view of the global change in sensitivities while operating under different heat recovery regimes, the sensitivities of all decision variables were shown at two opposing regimes: without heat recovery ($\eta_b = 0$) and with maximum heat recovery from permeate condensation ($\eta_b = 0.8$). Figure IV.5a, 5b show the results for no heat recovery and Figure IV.5c, 5d for maximum heat recovery.

With respect to the results provided in Figure IV.5, the two indicators (DMI and S1) more or less describe the same sensitivity trends. However, the S1 indicator clearly shows a larger discrepancy between more sensitive and less sensitive variables than the DMI. Besides, the distribution of all the sensitivities presents more or less the same situation in both objectives D (Figure IV.5a, 5c on the left) and E (Figure IV.5b, 5d on the right). The 3 most influential variables are always found to be the length L , the width W of the module (or the module surface area) and the vacuum pressure P_p of the permeate side, as expected for the VMD process. In the current module, the areas of both the solar absorbing surface and the flat-sheet membrane surface are quantified by $W \times L$. As a result, both the amount of thermal energy source and the water producing area of the distillation membrane are directly determined by these dimensions,

giving the relatively high sensitivities of the objectives. As expected, P_p appears to be another influential variable, based on its predominance in VMD operation, as discussed in Chapter II.

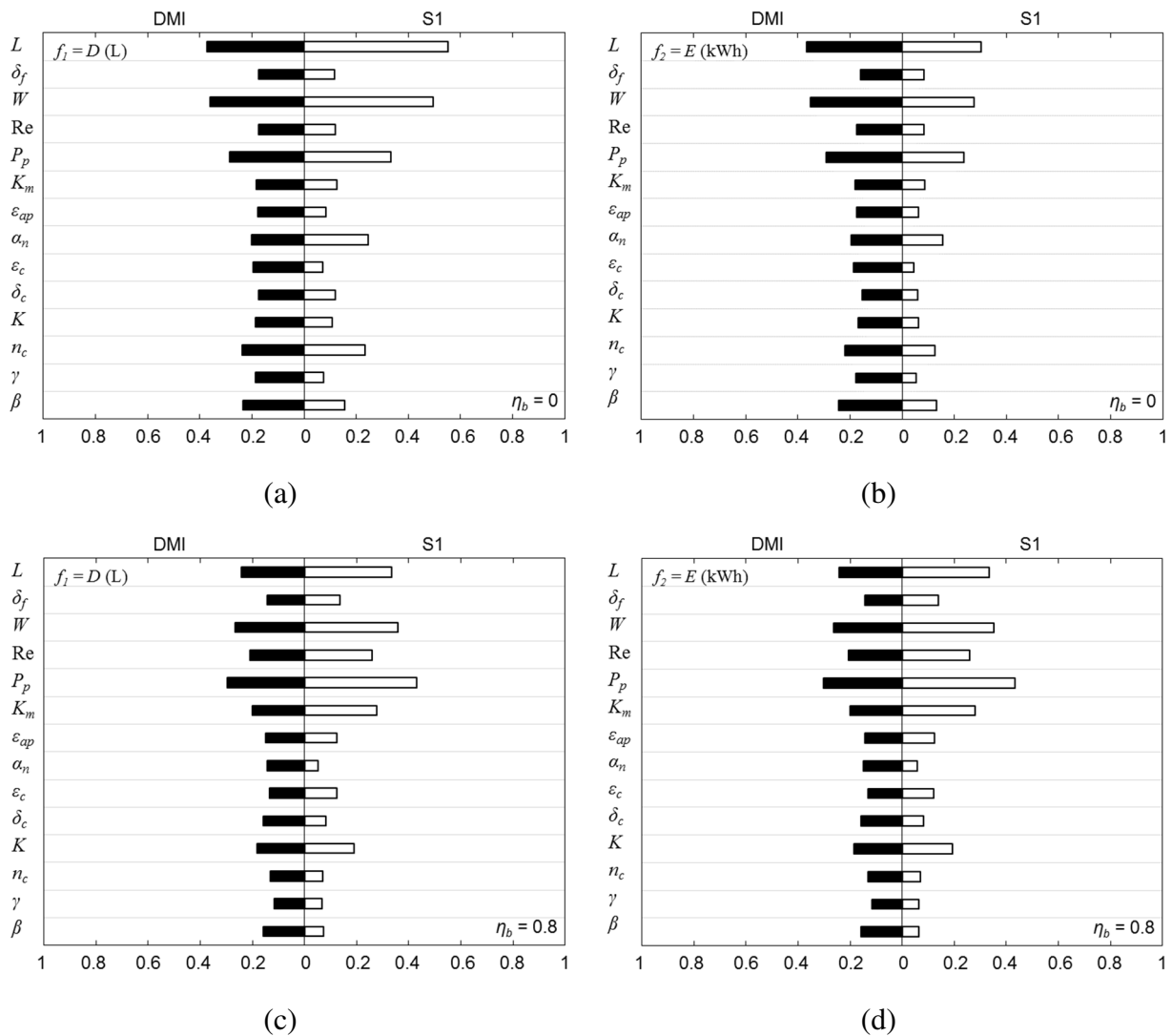


Figure IV.5: DMI and S1 sensitivity indicators with respect to different variables: (a) study of water production D at no heat recovery regime ($\eta_b = 0$); (b) study of energy consumption E at no heat recovery regime ($\eta_b = 0$); (c) study of water production D at maximum heat recovery ($\eta_b = 0.8$); (d) study of energy consumption E at maximum heat recovery ($\eta_b = 0.8$)

Nevertheless, significant differences can be observed between the scenarios with and without condensation heat recovery. Overall, the solar energy-oriented variables, i.e. the bottom 8 variables in all graphics in Figure IV.5, show lower sensitivities for a module operating with heat recovery (Figure IV.5c, 5d) when compared with a system without heat recovery (Figure IV.5a, 5b). Especially for the global solar energy absorptance in the normal direction (α_n) and the inclination of the module (β), less significance was observed in the case where $\eta_b = 0.8$,

because that the amount of solar energy available on the surface of the module was less important when the efficient heat recovery helped relieve the thermal demand. Moreover, in the case of heat recovery from condensation, the sensitivities were more distributed (taking the DMI as the sensitivity indicator, for example) and more particularly for the VMD process variables, namely the Knudsen permeability at the reference temperature (K_{mref}), Reynolds number of the feed flow and vacuum pressure P_p , they gained in weight, compared to a VMD-FPC module without heat recovery.

IV.5.2. Importance of heat recovery level

Performance at different levels of heat recovery is studied in this section by allowing η_b to vary within $[0, 0.9]$. This was achieved practically by taking the condenser efficiency (η_b) of the heat pump as a new variable, and merging the extinction coefficient K and the thickness δ_c of the glazing cover into the dimensionless product $K\delta_c$ to consistently keep 14 variables, as mentioned above. As a result, a new series of sensitivity analyses was performed, based on 3000 newly generated operating points. The sensitivities of D and E were evaluated with 14 decision variables, as shown in Figure IV.6, including η_b as the new operating variable.

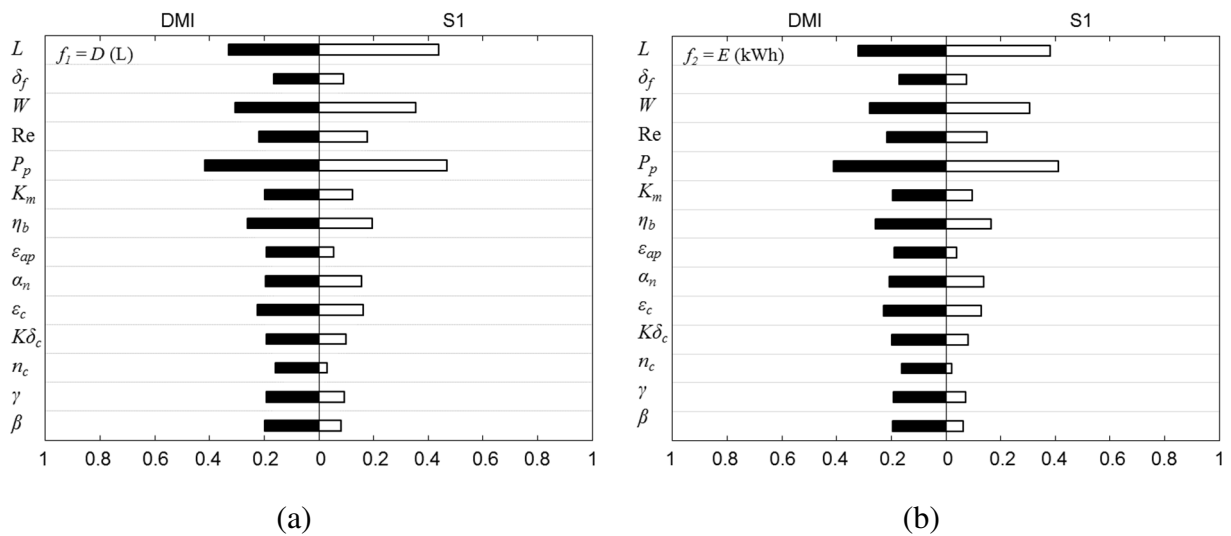


Figure IV.6: DMI and S1 sensitivity indicators with respect to different variables: (a) study of water production D; (b) study of energy consumption E at varying heat recovery level

As can be seen in Figure IV.6, DMI and S1 for all sensitivities show more or less the same shape, but the sensitivities in DMI are more evenly distributed than those in S1. Then, the sensitivities to the variables of the two different objectives (D and E) are similar to each other.

These general features highly resemble the cases in Figure IV.5. The varying η_b did not alter the 3 most important variables in Figure IV.5, i.e. the length L , the width W of the module and the vacuum pressure P_p , while it came as the 4th significant variable for both Figure IV.6a and 6b. However, if considering an existing module with certain dimensions and a certain vacuum level, the efficiency of heat recovery would be clearly of more importance than all the solar absorption-oriented variables and VMD process variables. In other words, the factor of heat recovery would have a strong impact on the performance of a given VMD-FPC module.

IV.5.3. Global optimization and performance improvement using heat pump

According to the problem formulation proposed in this work (Section 4.3), significantly higher water production D and lower energy consumption E were targeted. Taking the heat recovery level as a new variable, as formulated and explained in Section 5.2, the whole system was optimized via the AMOEA-MAP algorithm (Section 4.3) with a budget of calculation of 3000 simulation runs. The ranges of variables have been defined as proposed previously in Table IV.1. As a result, Figure IV.7a shows the non-dominated Pareto front, i.e. the set of globally optimum operating points for a VMD-FPC module with integrated heat recovery by heat pump at varying efficiencies. Additionally, the trend line of the corresponding mean permeate flux J_w in $\text{kg m}^{-2} \text{h}^{-1}$, and the daily average electric power demand \dot{P}_{avg} , which needs to be supplied by a corresponding capacity of PV panels with packs of batteries to tolerate the fluctuation, are calculated and plotted in the Figure IV.7b.

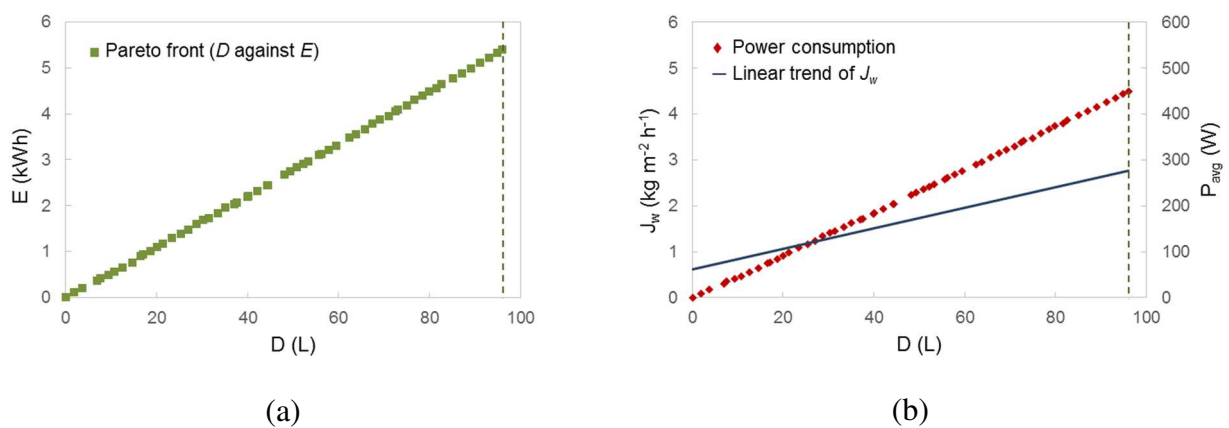


Figure IV.7: Global optimization results for VMD-FPC module with integrated heat recovery via heat pump at varying heat recovery level: (a) Pareto front of D and E ; (b) the corresponding daily average permeate flux and electric power consumption

Logically, a marked increase in the production of water can be achieved by heat recovery, at the expense of an increase in the required electricity. For instance within 12 hours of operation, for a water production (D) of about 3.7 L, the optimal electricity consumption (E) is about 0.2 kWh; while for D up to 96 L, the minimal E is about 5.4 kWh. The corresponding daily average permeate flux varied a bit and could be as high as $2.7 \text{ kg m}^{-2} \text{ h}^{-1}$ along the Pareto front, which was not in proportion to D due to the variation of module dimensions. Contrarily, E and the daily average electric power consumption are almost in linear relation with D in the optimal set shown in Figure IV.7a and 7b, which means the SEEC barely varied, maintained between 52 and 60 kWh m^{-3} regardless of the value of D, even up to nearly 100 L. Therefore, the energy consumption of system operation was effectively lowered compared to conventional MD systems, based on the fact that the thermal energy was already supplied by solar energy. Besides, a maximum module surface area ($2 \times 1.5\text{m}$) was selected by the optimization at the maximum production of 96 L, which corresponds to a daily productivity of $32 \text{ L m}^{-2} \text{ day}^{-1}$.

In the composition of E, it should be noted that the compressor work became the main part of power consumption when operating with an integrated heat pump. At the point where D is about 3.7 L and E equals 0.2 kWh, the consumption by the compressor work was 78.0% of the total E, followed by the vacuum pump consumption for 21.8%, leaving an ignorable circulation pump consumption. Similarly, for the point of the maximum production of 96 L, the total compressor work was 4.22 kWh out of the total E of 5.4 kWh, and the total consumption of the vacuum and circulation pump were respectively 1.17 kWh and 0.011 kWh. Indeed, the evaporator of the heat pump condensed the permeate vapor, as described in Section 3.2, and consequently reduced largely the amount of work required by the vacuum pump. Besides, the recirculation pump remained a minor and even negligible consumption, with the exception of co-occurrence of an extreme module slope β (above 60°) and an extreme feed flow Reynolds number (above 8000), which was never the case in the optimal solutions. Therefore, this invariability of SEEC was due to: (i) the fixed heat pump parameters defined in Table IV.2 and Table IV.3, which led to a compressor work nearly proportional to the permeate production; (ii) the vacuum pump consumption, which was incurred by the uncondensed permeate vapor (0.05 of the total permeate), was in proportion with the permeate production as well.

When comparing the present system (integrated heat pump for permeate condensation and heat recovery) with Chapter II (without heat recovery and without heat pump integration), the production can be substantially enhanced together with a significant improvement in the

specific electricity consumption from 239 to 52 - 60 kWh m⁻³. The latter point can be explained by the location of the permeate condenser before the vacuum pump in the new configuration (Figure IV.1). Thus, the intensive consumption by the vacuum pump in Chapter II (VMD-FPC without heat pump integration) is almost removed and replaced by the compressor consumption in the new configuration as proposed in the present study (VMD-FPC with integrated heat pump).

IV.5.4. Benchmark optimization of VMD-FPC at fixed heat recovery levels

In this section, the optimal performance of the combined system (VMD-FPC with heat pump) was studied at fixed heat recovery levels ($\eta_b = \{0, 0.2, 0.4, 0.6, 0.8\}$) for 3000 simulation runs, respectively. As shown in Figure IV.8, independent optimization studies were conducted per benchmark, and examined separately.

Figure IV.8a shows the optimization with the absence of heat recovery, where the production D is below 32 L and the total consumption E is below 2 kWh. Correspondingly, the daily average permeate flux J_w was limited to be lower than 1 kg m⁻² h⁻¹. The daily average electric power demand and the total electricity consumption E both increase almost linearly with the production D, resulting in an electric power consumption per unit water production of 4.2 - 5.0 W L⁻¹ and an SEEC of 50 - 60 kWh m⁻³, which is nearly the same as the case in Section 5.3.

Then, from Figure IV.8a to 8e, a gradual enhancement of maximum D from 32 L to 96 L accumulated during the 12-hour daily operation can be observed with the increment of η_b , where maximum productions of 40 L, 53 L and 70 L were recorded for fixed η_b at 0.2, 0.4 and 0.6, respectively. Similarly, the highest J_w in each benchmark went up from below 1 kg m⁻² h⁻¹ without heat recovery, to 2.8 kg m⁻² h⁻¹ at $\eta_b = 0.8$. At the same time, the total consumption E and the average electric power from the installed PV system both kept approximately a linear augmentation with D at a constant slope. As a result, the SEEC and the specific electric power consumption was always in the same ranges as in Figure IV.8a discussed above.

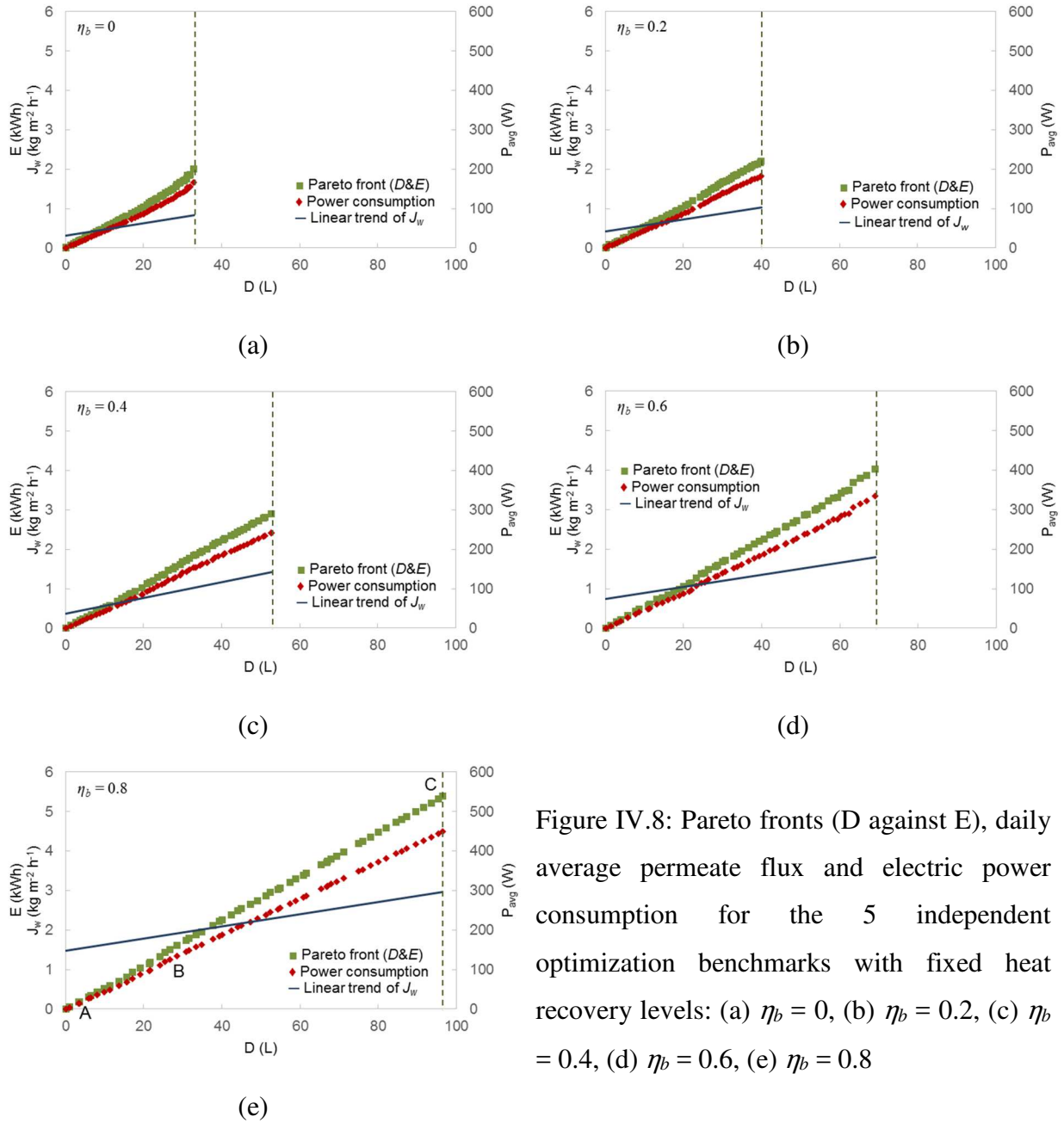


Figure IV.8: Pareto fronts (D against E), daily average permeate flux and electric power consumption for the 5 independent optimization benchmarks with fixed heat recovery levels: (a) $\eta_b = 0$, (b) $\eta_b = 0.2$, (c) $\eta_b = 0.4$, (d) $\eta_b = 0.6$, (e) $\eta_b = 0.8$

Therefore, these observations indicate that we can adjust the production capacity of such a system in a certain range according to our demand, without increasing the specific cost if more water is needed. The adjustment can be realized by altering the heat exchanging intensity between the condenser of the heat pump and the feed recirculation: higher η_b can potentially result in higher productivity, but no obvious change in the unit price of the water produced.

In order to better understand the points on the Pareto front, 3 typical points in Figure IV.8e are chosen to display the detailed variable choices and the performance: Point A, one of the lowest productions on the Pareto front; Point B, an intermediate production (~ 30 L) and consumption

(~ 130 W); Point C, the maximums in both D and E. Corresponding variables and performances are summarized in Table IV.4.

Table IV.4: Performance analysis over the Pareto front in Figure IV.8e (three representative operating points: A, B and C)

<i>Variable</i>		A	B	C
Solar energy	n_c	1.44	1.44	1.44
	K (m ⁻¹)	32	26.4	26.4
	δ_c (mm)	2	2	2
	ε_c	0.845	0.81	0.6
	ε_{ap}	0.695	0.525	0.78
	α_n	0.89	0.89	0.89
	β°	0	0	0
	γ°	0	0	-8
Dimensions	W (m)	0.24	0.52	1.5
	δ_f (mm)	21.2	21.2	12.3
	L (m)	0.735	1.81	1.91
VMD process	K_{mref} (s mol ^{1/2} m ⁻¹ kg ^{-1/2})	1.85×10 ⁻⁵	1.85×10 ⁻⁵	1.85×10 ⁻⁵
	Re	2400	7500	10000
	P_p (Pa)	650	650	650
<i>Performance</i>				
Water Production	Daily production D (L)	3.7	27.7	96.4
	Average permeate flux (kg m ⁻² h ⁻¹)	1.7	2.4	2.8
Electrical Consumption	Total electricity E (kWh)	0.21	1.55	5.38
	Circulation pump (kWh)	4.06×10 ⁻⁶	2.99×10 ⁻⁴	8.93×10 ⁻³
	Vacuum pump (kWh)	0.04	0.33	1.16
	Compressor work (kWh)	0.16	1.21	4.21
	SEEC (kWh m ⁻³)	55.91	55.81	55.83
	Average power demand (W)	17.3	128.8	448.7
Solar energy utilized (kWh)		0.96	5.21	15.26

In terms of the solar energy-oriented variables, the 3 points exhibit similar preferences in general. Moreover, these variables were not among the most influential ones, as shown in Figure IV.5c and 5d. Then in the dimensions, the surface area ($W \times L$) is positively related to the level of water production, while the channel thickness differs among the 3 points. Lastly, among the VMD process variables, the best membrane permeability and the lowest vacuum

pressure level were chosen for all 3 points by the optimization. The former is easy to comprehend, while the latter induced lower feed circulation temperature than the cases with higher vacuum pressure under the same amount of thermal power for evaporation, because the same feed temperature level in relatively high vacuum pressure cases cannot be maintained due to the bigger driving force and bigger permeate flux created by the low vacuum pressure of 650 Pa, which demands higher thermal power provision. Thus, the heat exchanging condition in the condenser of the heat pump would be better in lower vacuum pressure condition, which is favored especially in the case with the highest condenser efficiency when heat recovery played a dominant role. On the other hand, the choice of Reynolds number displays the same trend as the width: higher Re with higher production D . Different production levels were selected for these 3 points: 3.7 L, 27.7 L, and the maximum 96.4 L. Meanwhile, the total consumption E and power demand are directly in proportion to the production, which indicates that bigger installed PV capacity is required for higher demand for water productivity. The composition of the E was the same as discussed in Section 5.3, and the heating solar energy utilized was bigger with larger module surfaces. Therefore according to our calculations of point B in the middle, a daily amount of nearly 28 L, corresponding to the drinking water quantity required for a small community of 10-15 persons, could be autonomously produced on the sunny day of 1st August at Toulouse, assisted by a PV system with a power capacity of about 130 W. Furthermore, the dynamic accumulations of D and E during the operation of point B are presented in Figure IV.9, together with the variation of the solar radiation intensity received on the module surface G_T and the intensity absorbed by the module G_S . Even though the solar condition varied drastically during the operation, the freshwater could be produced at a rather steady pace with an also steadily increasing total consumption. Therefore, the integration of the heat pump was able not only to improve the water productivity, but also to buffer the fluctuation of solar radiation.

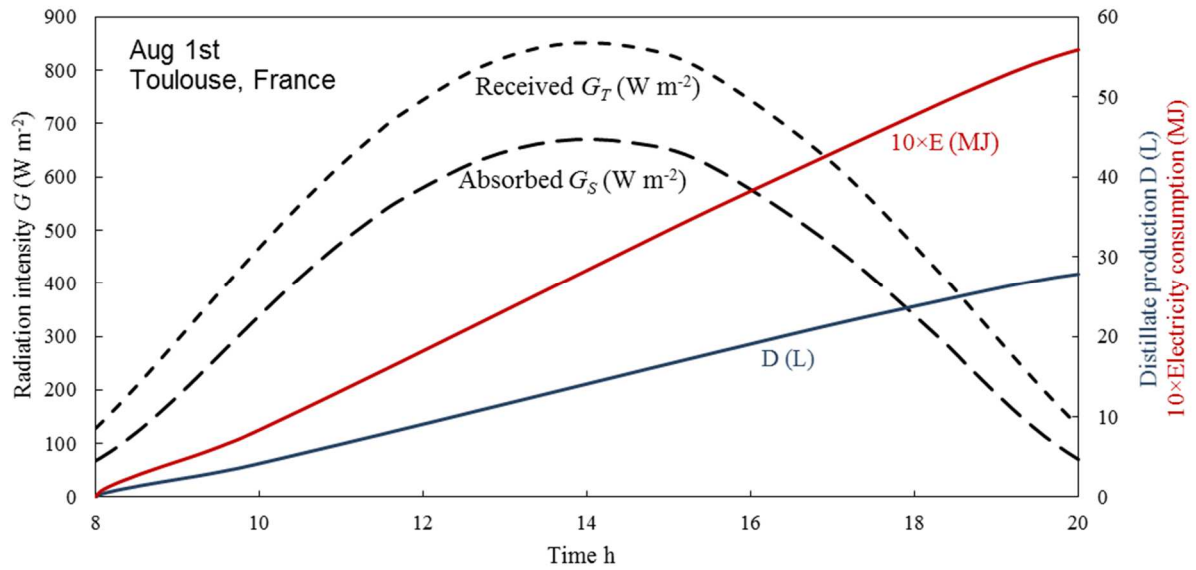


Figure IV.9: Dynamic variations of solar radiation intensities, accumulated distillate production and electricity consumption of Point B in Figure IV.8e

IV.5.5. Pareto-based study of decision variables and key indications on design

Here, the globally optimal decision variables are classified into 3 groups: (i) solar energy-oriented variables, (ii) VMD process variables, and (iii) module dimensions. The range of each decision variable in the optimal Pareto front, i.e. at its optimal values, is summarized, presented and discussed in this section. In addition to the optimal range of variables, the median values were also accounted, to be representative and to give a better idea of a typical value without being distorted by extremely large or small values across the Pareto set.

IV.5.5.1. Solar energy-oriented variables

8 variables belong to this group, namely the slope β° and the azimuth angle γ° of VMD-FPC collector, the refractive index n_c , the extinction coefficient K (m⁻¹), the thickness δ_c (m) and the emittance ε_c of the glazing cover, the emittance ε_{ap} and the absorptance α_n in the normal direction of the absorber-plate. All median values and ranges of these variables are shown in Figure IV.10.

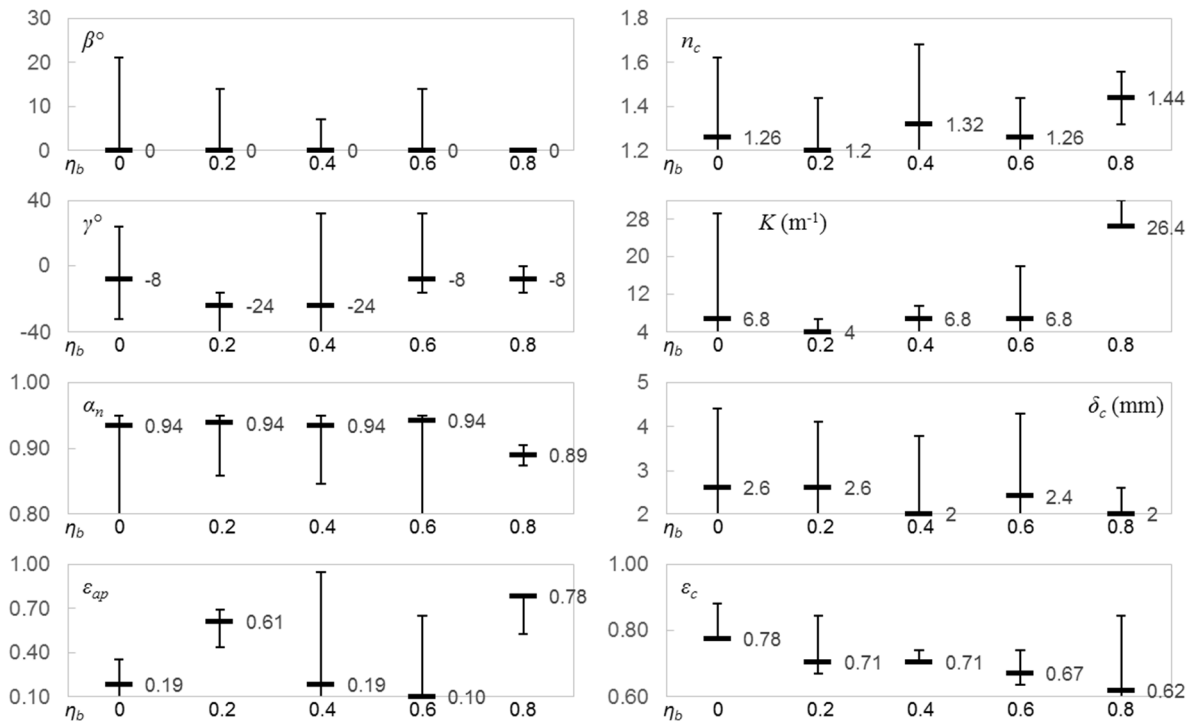


Figure IV.10: Ranges and typical values of optimal solar energy-oriented variables at different η_b

The slope β of the module has an impact on the received solar energy and on the energy consumption of the recirculation pump. For the former, a slightly sloped surface benefits the exposure to solar radiation. While for the latter, the inclination of the module increases the burden of the recirculation pump. The preferred value of β are typically 0 (no slope) no matter the level of heat recovery, but its varying range in the optimal set generally shows a downward trend with higher heat recovery, which implies that when the heat recovery rate is high, the direct solar radiation and absorption becomes less important and the system favors a less inclined surface to reduce the power consumption. On the other hand, the optimal values of the azimuth angle indicated that the collector preferred to be placed a bit to the east (negative value), and not directly to the south. This can be explained by the daily operating time, which was from 8 am to 8 pm with daylight saving in France (1 hour in advance). Hence, the sun was still in the east at 12:00 in local time, instead of at an azimuth angle of zero. Therefore, placing the collector slightly to the east can benefit the reception of solar radiation during the operating time. Normally for an all-day operation from sunrise to sunset, the collectors are placed right to the south ($\gamma = 0^\circ$) to maximize the solar absorption.

Higher values of α_n and lower values of ε_{ap} of the absorber-plate are more preferable to enhance the solar energy absorbed by the module, as also detected by the AMOEA-MAP for most of the five benchmarks with different condenser efficiencies. Abnormalities of a little lower α_n and a higher ε_{ap} were witnessed especially at the highest heat recovery level, which was probably due to the lower dependence of the system performance on the solar energy resource when heat recovery was intensive. Besides, an intermediate value of ε_{ap} of the absorber-plate (0.4 to 0.7) was chosen to be the optimal in the low heat recovery level ($\eta_b = 0.2$), allowing a higher loss coefficient from the top of the collector. This possibly indicates that the feed operating temperatures in this optimal set were not far from the ambient based on its vacuum pressure level (will be seen in Section 5.5.2), thus the top loss was already little, which might need further observations with more simulations.

Generally, lower values of n_c , K , and δ_c of the glass cover are more preferable to optimize the amount of solar energy that penetrates through the cover and gets to the absorber-plate. Nonetheless, the preferences for n_c and K were less demanded when highest heat recovery came into play, especially at $\eta_b = 0.8$, as shown in Figure IV.10. The same interpretation might account for this change, as the amount of solar energy absorbed by the system was lower with a higher level of heat recovery. Regarding the glass emittance ε_c , the tendency of optimal choices decreases slightly with increasing condenser efficiency, indicating that the system preferred the glass cover to store more radiation energy in itself when the heat recovery level was lower.

IV.5.5.2. VMD process variables

The membrane permeability at the reference temperature of 20°C (K_{mref} in $\text{s mol}^{1/2} \text{ m}^{-1} \text{ kg}^{-1/2}$), the permeate vacuum pressure (P_p in Pa), and the Reynolds number are the 3 VMD process variables studied in this chapter. Their optimal ranges and median values are shown in Figure IV.11.

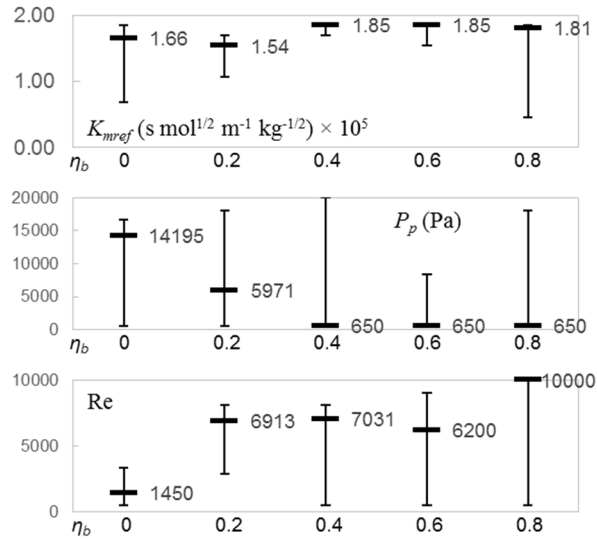


Figure IV.11: Ranges and typical values of optimal VMD process variables at different η_b

Membranes with better permeability were undoubtedly appreciated in all benchmarks, and the optimal value of K_{mref} was further pushed to the highest ($1.85 \times 10^{-5} \text{ s mol}^{1/2} \text{ m}^{-1} \text{ kg}^{-1/2}$) in higher heat recovery levels ($\eta_b \geq 0.4$) when the constraint from solar energy absorption became less significant and the mass transfer quality turned out more important.

As one of the most influential variable as discussed in Section 5.1, the vacuum pressure P_p varied a lot in all benchmarks. However, a gradual change of preference is observable in the figures, from low ($\eta_b = 0$ and 0.2) to high heat recovery levels ($\eta_b = 0.4, 0.6$ and 0.8). In the former cases, the water productivity of the system was more limited by the absorbed solar energy, thus an extreme low vacuum pressure would not be favorable because it only added to E by higher consumption of the vacuum pump and was not capable of largely enhancing D. Consequently, intermediate values were found by the optimization to balance D and E: 14 195 Pa for no heat recovery and 5 971 Pa for $\eta_b = 0.2$, and the latter value is lower due to the less restraining thermal energy income by a little bit of heat recovery. Therefore, lower optimal vacuum pressure can be achieved when heat recovery started to be included. This became even more obvious in the cases of $\eta_b > 0.2$, where the lowest vacuum pressure was often selected in the optimization. Correspondingly, higher productions with higher thermal energy demands were able to be attained with the help of relatively high condenser efficiencies in the heat pump.

Higher Reynolds numbers are beneficial to the heat and mass transfer from the feed bulk to the membrane surface, reducing the thermal and concentration polarizations and strengthening the

permeate flux. With regards to the first benchmark, i.e. the system without heat recovery, the optimum value of Re proved to be 1 450 (laminar regime). Here, lower Re values were preferred because of the connection between the recirculation pump consumption and the flow rate, where an optimal value has been found by balancing energy consumption and water production, which was again limited by solar energy, same as explained in the choice of vacuum pressure. Then, the optimal option of the flow regime of the feed recirculation became totally turbulent and was even pushed up to the maximum of 10 000 at $\eta_b = 0.8$, in order to fully explore the maximum water production despite the elevated consumption by the circulation pump, because it became comparatively ignorable in this benchmark, as presented by the data of the Points A, B and C.

IV.5.5.3. Dimension variables

In Figure IV.12, the optimum dimensions of the feed channel, i.e. the width W (m), the thickness δ_f (m) and the length L (m) are illustrated.

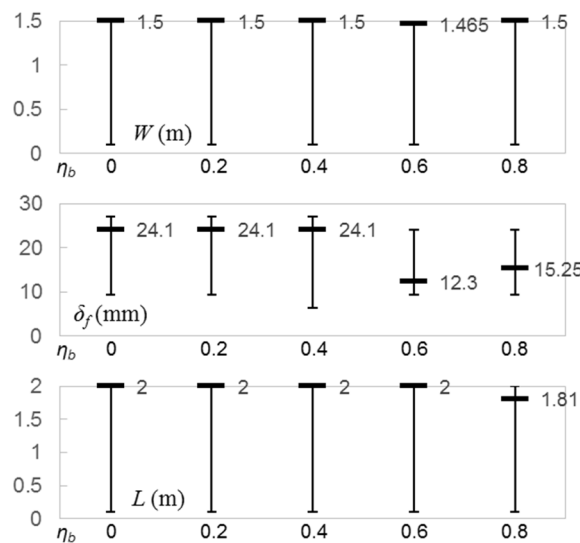


Figure IV.12: Ranges and typical values of dimension variables at different η_b

Among them, W and L possessed great importance to the objectives, as discussed in Section 5.1. Therefore, the collector surface A_C tended to vary between the smallest ($0.1\text{m} \times 0.1\text{m}$) and the largest ($1.5\text{m} \times 2\text{m}$) in all benchmarks, shaping up the Pareto fronts (Figure IV.7 and Figure IV.8) of the total production D and the total energy consumption E after the 12h operation. Despite the dispersion, a larger surface area was apparently more favored, as shown by the median values in the figure, to obtain the highest possible productivity. However, in the design for applications, one may only have to simply fix an appropriate surface dimension according

to the freshwater demand. The electric consumption and the PV capacity to be installed would directly depend on the level of water production based on the linear relation between D and E, as discussed in Section 5.4.

At a certain Re number, the velocity of the feed flow is lower when the characteristic length of the flow channel is bigger, which results in a decrease in the quality of mass transfer due to a stronger temperature and concentration polarization. In that sense, the thickness of the flow channel (δ_f) is a much more determining factor of the characteristic length with respect to the width W , on account that it is much smaller than the other. However, the typical value found by the optimizations was a middle value, not at the lower limit of 0.5mm with the highest feed flow velocity for a given Reynolds number. Indeed, the energy consumption of the recirculation pump increases sharply with the increment in flow velocity, it is therefore necessary to find a balance by adjusting the thickness of the flow channel, which could also have some technical limitations. From no heat recovery to intermediate heat recovery ($\eta_b = 0, 0.2$ and 0.4) where water production was relatively more restrained by incoming solar energy, the balances found by the optimization were closer to the upper boundary of the variable defined in Table IV.1 (30mm), implying that it was more important to limit the pumping consumption than to enhance the flow rate and ameliorate the mass transfer quality. While for higher heat recovery levels ($\eta_b = 0.6$ and 0.8) where the thermal demand for solar energy became less with the help of more efficient heat recovery, lower δ_f values were selected and the balance moved a bit to the opposite direction compared to the other benchmarks.

IV.6. Conclusions (in English)

On the basis of a small-scale integrated vacuum membrane distillation - flat plate collector (VMD-FPC) module previously studied, a simultaneous strategy of heat recovery and permeate condensation by the heat pump was proposed, studied and optimized. It should be noted that the heat pump unit proposed in this work aimed both to recover the latent heat of evaporation and to offer a practical condensation strategy before the vacuum pump, exempting the use of additional intensive cooling systems or the excessive burden on the vacuum pump. The VMD-FPC module with integrated heat pump allowed indeed for a substantial gain in terms of water production with relatively small electricity consumption, which need to be supplied by PV panels for an autonomous operation of the whole system. Under a rather high heat recovery regime, the optimal results for different scales of production revealed that, for a cloudless 12-

hour operation on Aug 1st in Toulouse, France, the water production could largely range from 3.7 L up to 96 L with corresponding electric consumptions equal to 0.21 kWh and 5.38 kWh, respectively. Furthermore, for all simulations, the need for PV power capacity per unit water production was found to be almost constant ranging in 4.2 - 5.0 W L⁻¹.

The process efficiency as well as the significance of design and operating variables, in particular the condenser efficiency in the heat pump, were investigated by involving the Delta Moment-Independent (DMI) indicator for sensitivity analysis and by performing several design-oriented multi-objective optimizations. The results confirmed that, same as concluded for conventional VMD at the scale of a single module (not the whole system), the vacuum pressure and the module surface area both had a great influence on the performance of the integrated module. Besides, compared with the system without heat recovery, the VMD process variables, such as Reynolds number and membrane permeability, gained more impact while the solar energy-oriented variables became less important if heat recovery was included. Finally, the condenser efficiency in the heat pump determined directly the heat recovery level and affected strongly the performance of the integrated module.

Additionally, a detailed study of the Pareto fronts for all 5 benchmarks at different heat recovery levels, i.e. the typical values and ranges of all the decision variables at their optimum, made it possible to provide several indications on the optimal operation of the whole system. Logically, the optimization of a VMD-FPC module without heat recovery leads to an improvement of the solar absorption by adjusting the solar-oriented variables. However, in the case of being equipped with an intensive heat recovery system, the overall performance is less sensitive to these solar-oriented variables. Regarding the VMD variables, high membrane permeability ($> 1.5 \times 10^{-5} \text{ s mol}^{1/2} \text{ m}^{-1} \text{ kg}^{-1/2}$) is always welcome, while a high Reynolds number (up to the maximum 10000), which decides the hydrodynamic condition of the feed compartment of the module, is only to choose for elevated water production scales, i.e. an integrated module with intensive heat recovery level (efficiency of the heat pump condenser = 0.8). Finally, the feed channel thickness should be increased if the heat recovery efficiency is low (efficiency of the heat pump condenser < 0.6), and the surface area of the module determines the scale of production, which needs to be decided according to the actual production demand and the maximum installed PV capacity determined by economic criteria and some logistic constraints for a given application.

Based on the promising results discussed in this chapter and the previous chapters, some first specifications to define a prototype in our laboratory is expected by the LabCom MOST after this thesis, in order to confirm the technical feasibility of such a concept equipment. Chapter V will summarize all the orientations of design and the choices of parameters.

IV.6. Conclusions (en français)

Sur la base d'un module plan intégré VMD-FPC de distillation membranaire précédemment étudié, une stratégie simultanée de récupération de chaleur et de condensation du perméat par la pompe à chaleur a été proposée, étudiée et optimisée. Il est important de noter que l'unité de pompe à chaleur proposée dans ce travail visait à la fois à récupérer la chaleur latente d'évaporation et à proposer une solution de condensation pragmatique avant la pompe à vide, pour éviter l'utilisation de systèmes de refroidissement intensifs supplémentaires ou une consommation électrique importante de la pompe à vide. Sur la base de nos simulations, le système optimisé basé sur un module VMD-FPC avec pompe à chaleur intégrée permet un gain substantiel en termes de production d'eau avec une consommation électrique relativement faible, qui sera fournie par des panneaux photovoltaïques pour un fonctionnement autonome de l'ensemble du système. Pour un régime de récupération de chaleur plutôt élevé et des conditions optimales, D et E varient dans une large gamme. Pour une opération sans nuages de 12 heures le 1er août à Toulouse en France, la production d'eau journalière pourrait varier de 3,7 L à 96 L lorsque la consommation électrique totale varie de 0,21 kWh à 5,38 kWh. En effet, toutes nos simulations montrent que, dans la large gamme des paramètres étudiée, le besoin d'énergie électrique par unité de production d'eau est presque constant, et se situe entre 4,2 et 5,0 W L⁻¹.

L'efficacité du procédé ainsi que l'importance des variables de conception du module et de fonctionnement du système complet, en particulier l'efficacité du condenseur dans la pompe à chaleur, ont été étudiées en utilisant l'indicateur « Delta Moment-Independent » (DMI) pour l'analyse de sensibilité et en réalisant plusieurs optimisations multi-objectifs orientées conception. Les résultats confirment que, pour ce système complexe, on retrouve des conclusions connues pour un module de VMD conventionnel et à l'échelle du seul module (pas du système complet), la pression de vide et la surface du module ont une grande influence sur les performances du module intégré. De plus, quand on ajoute la prise en compte de la récupération de chaleur, par rapport à un système sans récupération de chaleur on observe que les paramètres du procédé de VMD, tels que le nombre de Reynolds et la perméabilité de la membrane, ont une plus grande influence, tandis que les paramètres qualifiant énergie solaire

voient leur influence décroître. Enfin, l'efficacité du condenseur dans la pompe à chaleur détermine directement le niveau de récupération de chaleur et affecte fortement les performances du module intégré.

De plus, une étude détaillée des fronts de Pareto pour les 5 essais à différents niveaux de récupération de chaleur (c'est-à-dire les valeurs et gammes typiques de toutes les variables de décision à leur optimum) fournit plusieurs indications sur l'opération optimale du système complet. Logiquement, un module VMD-FPC sans récupération de chaleur peut être optimisé par une amélioration de l'absorption solaire en ajustant les paramètres impliquant l'énergie solaire thermique. Par contre, dans le cas d'une récupération intensive de la chaleur, les performances globales sont moins sensibles à ces paramètres relatifs à l'énergie solaire thermique. En ce qui concerne les paramètres du procédé de VMD, une perméabilité de membrane élevée ($> 1.5 \times 10^{-5} \text{ s mol}^{1/2} \text{ m}^{-1} \text{ kg}^{-1/2}$) est toujours favorable, tandis que le choix d'un nombre de Reynolds élevé (vers le maximum 10000) pour fixer les conditions hydrodynamiques dans le compartiment d'alimentation du module n'est pertinent que pour les gammes de production d'eau élevées, c'est-à-dire pour un module intégré avec niveau élevé de récupération de chaleur (efficacité du condenseur de la pompe à chaleur = 0.8). Enfin, l'épaisseur du canal d'alimentation doit être augmentée si le rendement de récupération de chaleur est faible (efficacité du condenseur de la pompe à chaleur < 0.6), et la surface du module détermine la gamme de débit de production d'eau et la capacité de panneaux PV, qui doit donc être décidée en fonction de la demande de production réelle, et de la capacité de PV maximale à installer à déterminer sur des critères économiques et de contraintes logistiques pour une application donnée.

Les conclusions de ces travaux et des chapitres précédent sont prometteuses et vont permettre de préciser et de choisir de premiers éléments de définition d'un prototype qui pourra être réalisé par le LabCom MOST à l'issue de la thèse, pour vérifier la faisabilité technique d'un tel concept d'équipement. Le chapitre V va synthétiser toutes les orientations et choix des paramètres à retenir.

V. Practical recommendations on the design of a small MD-FPC system for autonomous and decentralized seawater desalination in remotes areas

V.1. Introduction (in English)

Previous chapters have focused intensively on the understanding of mass and heat transfer in two widely used MD configurations for desalination (VMD and DCMD), as well as on the optimization of an integrated MD - direct solar heating equipment. This final chapter aims to provide detailed recommendations on the design and selection of materials and operating conditions to guide the manufacture of a practical prototype. In other words, the recommendations formulated in this last chapter physically embody the theoretical indications and conclusions made previously.

Detailed specifications on the selected MD-FPC system and the operating system are provided according to: (i) the optimal simulation results on design and operation; (ii) the real-world parameter settings regarding the material properties, ambient conditions and dimensions. Furthermore, corresponding simulations are made to characterize the dynamic operation at a relevant heat recovery level and the overall performance of the integrated module. In addition, considering the mobility of the whole equipment for dispersed communities, an approximate maximal electric power demand of 130W is set by our partner Sunwaterlife to limit the installed PV capacity [217], based on the daily average power consumption. Therefore, only optimal operating conditions corresponding to the same capacity of PV panels are studied in this chapter.

These in-depth evaluations are helpful to further predict the potential and applicability of the equipment in the conditions of both summertime and wintertime, under a pragmatic limitation of electricity provision by a PV system. Daily variations (from sunrise to sunset) of the solar radiation, the permeate flux, the feed temperature and salinity, the power consumption of pumps and compressors are presented and discussed as well. A future prototype in the lab is expected following the guidelines of this chapter.

V.1. Introduction (en français)

Les chapitres précédents ont été consacrés à la compréhension du transfert de matière et de chaleur dans deux configurations MD largement utilisées pour le dessalement (VMD et DCMD), ainsi qu'à l'optimisation d'un système intégrant MD – énergie thermique solaire. Ce dernier chapitre vise à fournir des recommandations détaillées sur la conception, la sélection des matériaux et les conditions de fonctionnement en vue de la réalisation future d'un prototype expérimental. En d'autres termes, les recommandations formulées dans ce dernier chapitre

s'appuient sur physiquement les indications et conclusions théoriques majeures formulées précédemment.

Les spécifications détaillées relatives au système MD-FPC considéré à ses conditions opératoires sont fournies en fonction (i) des résultats optimaux de la simulation concernant la conception préconisée du module et son fonctionnement ; (ii) des paramètres réels tels que les propriétés des matériaux, ses conditions environnementales et ses dimensions. En outre, des simulations sont effectuées pour représenter le fonctionnement dynamique sur une journée de l'ensemble du système à un niveau de récupération de chaleur pertinent ainsi que les performances globales du module intégré. De plus, compte tenu de la mobilité requise du système pour alimenter des communautés isolées, une puissance électrique maximale approximative de 130W est définie par notre partenaire Sunwaterlife, ce qui limite la surface photovoltaïque nécessaire [1], fonction de la consommation moyenne quotidienne d'énergie. Par conséquent, seules les conditions de fonctionnement optimales correspondant à cette capacité de panneaux PV sont étudiées dans ce chapitre.

Ces évaluations approfondies sont utiles pour mieux prévoir le potentiel et la faisabilité de l'équipement dans les conditions estivales et hivernales, dans le cadre d'une limitation pragmatique de l'apport d'électricité par un système photovoltaïque. Les variations quotidiennes (du lever au coucher du soleil) du rayonnement solaire, du flux de perméat, de la température et de la salinité de l'eau d'alimentation, de la consommation d'énergie des pompes et des compresseurs sont également présentées et discutées. Un prototype de laboratoire sera élaboré en s'appuyant sur les recommandations de ce chapitre.

V.2. Choice of integrated MD – direct solar heating module and optimal design of recirculation system

As discussed previously in Chapter III, a hybrid DCMD-FPC module is less favored because of its lower production capacity and lower thermal efficiency when using the sparse solar energy. In addition, DCMD represents considerable limitations in implementing effective heat recovery strategies for the autarky of the solar energy captured, based on its permeate condensation directly inside the cold distillate.

Chapter V: Practical recommendations

On the other hand, VMD process is more competitive than DCMD in terms of productivity and solar utilization efficiency in the integrated module design, as discussed in Chapter III. Moreover, the external vapor condensation of VMD offers the potential of effective latent heat recovery, which has been proven in Chapter IV. Regarding the VMD-FPC module, the compact and integrated design is more suited to small-scale applications, and is able to exempt the whole system from the heat loss in heat exchange, piping and joints. Thus, the process can be intensified as discussed in Chapters I, II and IV. As a result, an integrated VMD-FPC module is therefore recommended and discussed here, following also the indications provided in Chapter IV. The complete flowsheet of the studied VMD-FPC system is shown below in Figure V.1. Explicit discussions on the choices on material properties, operating conditions and dimensions are provided in the next sections.

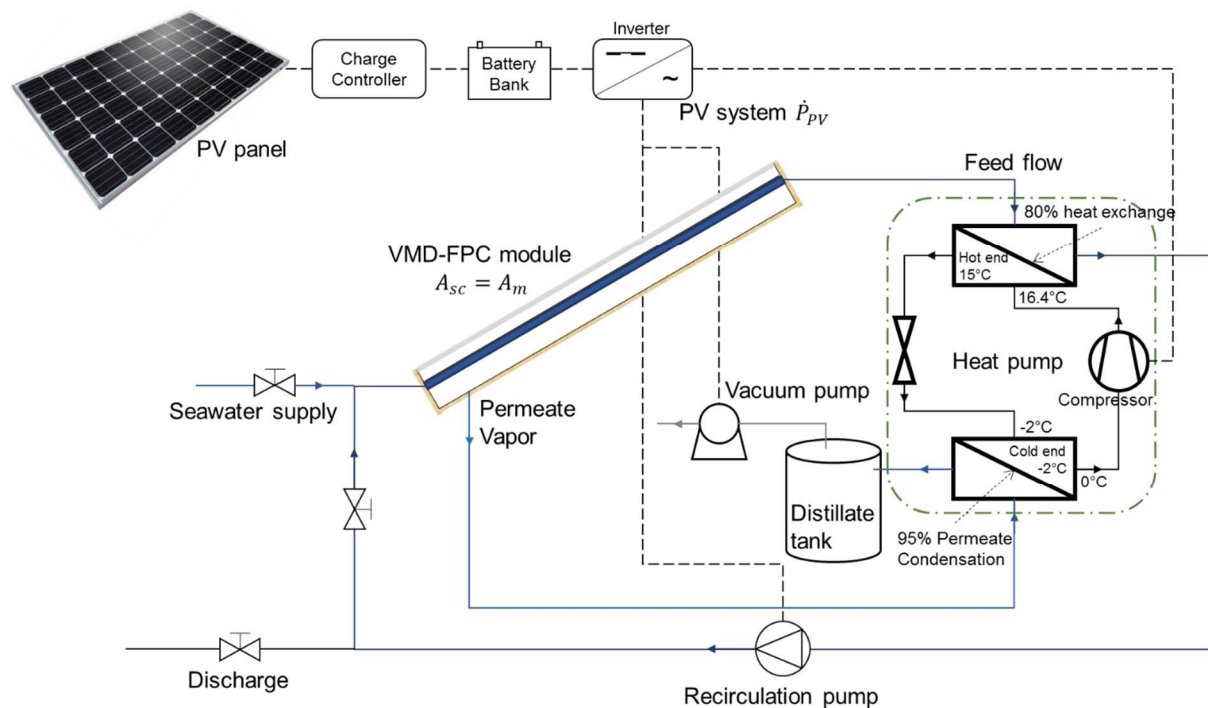


Figure V.1: Flowsheet of the recommended energy-efficient VMD-FPC prototype with integrated heat pump for small-scale desalination

As demonstrated earlier, a significant improvement in both production and energy consumption could be achieved when an intensive heat recovery was introduced (80% heat recovery), compared to the performance of the simple recirculation system with the VMD-FPC module presented in Chapter II (Figure II.1, where the solar collecting surface A_c and the membrane surface A_m are the same). The heat pump used in Figure V.1 allows for an effective condensation

(95%) of the permeate vapor before the vacuum pump while recovering its latent heat of condensation and transferring it to the feed recirculation, the same as in Chapter IV. It should be noted that the permeate condensation takes place before the vacuum pump, thanks to the use of suited coolant (SES36) in the heat pump, which is environmentally friendly. In this fashion, the massive consumption by vacuum pump can be significantly reduced. In addition, the compressor work in the heat pump as well as the ratio between the water production and electricity consumption can be sensibly improved by operating at lower coolant pressures, that is to say at lower feed temperatures. Finally, a photovoltaic (PV) system has to be installed to provide the electric consumption for the continuous operation, normally including a PV panel, a charge controller, a battery bank and a DC-AC inverter. The capacity of the PV system and the surface area of the VMD-FPC module will be discussed and determined afterwards.

V.2.1. VMD-FPC module materials

The first layer of the VMD-FPC module is the glass cover. Concerned properties are the refractive index n_c , the emittance ε_c , the extinction coefficient K and the thickness δ_c . Based on the analysis in Section IV.5.5, low values of all these four parameters are recommended based on that they all contribute to the better solar energy absorption. However, the market availability and the cost of material with improved properties are questionable, except for the thickness δ_c , which can be freely chosen in a certain range. Moreover, as also discussed in Section IV.5.5, these solar energy-oriented parameters are less influential when an intensive heat recovery is introduced. As a result, the cover properties are mainly taken from commercial glasses that adapted to solar installations. The properties of Optiwhite™ by Pilkington [218] are taken into the simulation, which is a kind of low-iron glass with a refractive index n_c of 1.5 and an extinction coefficient K of 5.9 m^{-1} . Besides, the available thickness range of Optiwhite is 2 ~ 19 mm, therefore the thinnest of 2 mm is chosen according to the analysis in Section IV 5.5. Lastly, the emittance ε_c of this kind of glass is not provided online by the producer, thus a normal value of 0.84 is assumed for the simulations in this chapter [219].

Then, the effect of the air or vacuum gap beneath the glass cover has been neglected in the modeling. Therefore, the absorber-plate is the next layer whose properties have been included in the simulation, namely the solar absorptance in normal direction α_n and the emittance ε_{ap} of the absorber-plate. The former determines the amount of the absorbed heat out of the total received solar energy on the absorber-plate, which inclines to be at the highest possible value, as discussed in Section IV 5.5. On the other hand, the preference of the emittance ε_{ap} remains

not very clear, and its influence on the system performance is not strong, according to the sensitivity analysis in Chapter IV. Therefore, an available and highly effective bimetallic (Sn and Ni) coating on the copper substrate with an absorptance as high as 0.98 in the solar radiation range is chosen for the module, together with its emittance of 0.1 taken into simulations [163].

The absorber-plate and the membrane form the two walls of the feed channel, as presented in Figure II.1. The property of the membrane that has been taken into the VMD-FPC modeling and optimization in Chapter II and IV is only the Knudsen permeability at 20°C K_{mref} , while the transmembrane heat conduction has been ignored due to the VMD configuration. Consequently, the choice of the membrane follows the tendency in the optimization, where the highest permeability was approached especially in higher heat recovery levels (Section IV.5.5). The Desal K150 PTFE membrane from Desalination System Inc. is therefore applied, which has a K_{mref} of $1.85 \times 10^{-5} \text{ s mol}^{1/2} \text{ m}^{-1} \text{ kg}^{-1/2}$, being the highest among all membranes adopted in the experimental results in our lab [22].

On the other side of the membrane is the vacuum permeate side, which is enclosed by thermal insulation material together with all of the layers discussed above. A normal insulation material with relatively good thermal property should be adopted in this chapter, and in that sense, polyurethane foam with a low thermal conductivity of $0.018 \text{ W m}^{-1} \text{ }^\circ\text{C}^{-1}$ and a low moisture absorption is selected [220]. Besides, an insulation thickness of 2 cm is assumed for the whole module, resulting in a bottom heat loss coefficient through insulation U_{bo} of $0.9 \text{ W m}^{-2} \text{ }^\circ\text{C}^{-1}$. The heat loss through the edge of the module can be well neglected due to the much smaller area compared to the bottom. Summarily, all the selections of material and the corresponding properties applied to the simulation are listed in Table V.1.

Table V.1: Material property settings in this chapter

Layer	Material or product	Property	Value
Glass cover	Optiwhite™	Refractive index n_c	1.5
		Emittance ε_c	0.84
		Extinction coefficient K	5.9 m^{-1}
		Thickness δ_c	2 mm
Absorber-plate	Thin copper plate with Sn-Ni coating	Absorptance in normal direction α_n	0.98
		Emittance ε_{ap}	0.1
Membrane	Desal K150 (PTFE)	Knudsen permeability at 20°C K_{mref}	$1.85 \times 10^{-5} \text{ s mol}^{1/2} \text{ m}^{-1} \text{ kg}^{-1/2}$
Insulation	Polyurethane foam	Bottom heat loss coefficient U_{bo}	$0.9 \text{ W m}^{-2} \text{ }^\circ\text{C}^{-1}$

V.2.2. Operating conditions

The location of Toulouse is still taken as the place for operations, in order to be realistic for the first trials of the future prototype in the laboratory, and to be consistent with the previous chapters. Hence, the ambient parameters for Aug 1st are set, the same as listed in the “Location” part in Table II.7. In order to fully exploit the daily insolation, an operation from sunrise to sunset is assumed in this chapter, instead of the fixed 12 hours in previous chapters. Regarding the date of Feb 1st, the correction factors for the calculation of solar radiation have to be altered according to Table II.1, and the range of ambient temperature is changed to 0°C ~ 10°C.

Even though Toulouse is not a coastal city, its location data is applied just for demonstration with assumed seawater conditions. A seawater source of 35 g L⁻¹ in salinity is introduced as the exterior seawater supply for the system, and an upper limit of the salinity of 300 g L⁻¹ is set as the trigger of brine discharge, the same as described in previous chapters. The temperature of the supplied seawater is kept at 25°C on Aug 1st as well, while set at 13°C in winter on Feb 1st, according to the data for seawater temperature in Barcelona [221], which is not far from Toulouse.

The heat exchanging efficiency η_b of the condenser in the heat pump is set to the highest 0.8 to push the system up to its best performance, as discussed in the last chapter. Besides, the vacuum pressure P_p and the Reynolds number of the feed recirculation and are also defined according to the observations of the optimal values: $P_p = 650$ Pa and turbulent regime at $Re = 10\ 000$. As discussed in Chapter IV, the application of the heat pump efficiently condenses the permeate vapor before the vacuum pump, which spares the burden of the vacuum pump, thus lower vacuum pressure becomes preferable for better production without adding too much to the VP consumption. Moreover, lower vacuum pressure induces a lower feed working temperature, which is beneficial to the heat recovery of transferring the condensation heat of the thermal fluid in the condenser of the heat pump to the feed circulation. On the other hand, the highest Re in fully turbulent regime is favorable when intensive heat recovery is integrated, based on that the incurred higher consumption of the circulation pump is always ignorable compared to the total consumption even at the maximum of 10 000, according to Table IV.4 in Chapter IV. Therefore, its effect in diminishing the temperature polarization, ameliorating heat and mass transfer, and thus augmenting the productivity is more pursued for better overall performance.

Conclusively, all the concerned parameters are as summarized in Table V.2 below, including the ambient settings and the recommended system operating conditions.

Table V.2: Operating conditions in this chapter

Parameter	Description	Value	
Location (Toulouse)	L_{loc}	Longitude in degrees west, $0^\circ < L < 360^\circ$	358.56°
	φ	Latitude, north positive, $-90^\circ < \varphi < 90^\circ$	43.60°
	Al	Altitude of the location	150.0 m
	h_{wi}	Heat transfer coefficient of the wind	10 W m ⁻² °C ⁻¹
	r_0, r_1, r_k	Correction factors for mid-latitude places	0.97, 0.99, 1.02 (summer) 1.03, 1.01, 1.00 (winter)
	ρ_g	Diffuse reflectance of the surroundings	0.2
	T_{amax}	Highest ambient temperature	35°C (Aug 1); 10°C (Feb 1)
	T_{amin}	Lowest ambient temperature	20°C (Aug 1); 0°C (Feb 1)
Seawater supply	T_s	Temperature of the seawater supply	25°C (Aug 1); 13°C (Feb 1)
	C_s	Salinity of the seawater supply	35 g L ⁻¹
System operating conditions	Duration	Operating time of the day	Sunrise - Sunset
	C_{limit}	The highest operating salt concentration	300 g L ⁻¹
	P_p	Permeate pressure (Vacuum pressure)	650 Pa
	Re	Reynolds number of the feed	10 000
	η_b	Heat exchanging efficiency of the condenser	0.8

V.2.3. Collector positions and module dimensions

Regarding the slope β of the module, the result of the optimization in Chapter IV showed that a surface placed flatwise ($\beta = 0^\circ$) is the best choice, considering the pumping consumption to overcome the vertical height of the module, even if it means a slight decrease in the reception of solar radiation. On the other hand, the azimuth angle γ is also set at 0° (facing due south) for the all-day operation from sunrise to sunset, in order to maximize the total amount of beam radiant energy that falls on the surface of the module.

Regarding the dimensions of the module, an optimal value of 15mm is chosen to be the thickness δ_f of the feed channel when operating under high heat recovery level, as discussed in Section IV.5.5. Apart from the thickness, the other two dimensions of the module, the length L and the width W are of more importance to the system performance as they contribute directly to the total surface area of the membrane and the collector. Considering the mobility of the whole equipment for dispersed communities, a maximum value of 130W of the power

consumption is set to limit the demand of installed PV panels [217], with corresponding packs of batteries to tolerate the fluctuation of solar radiation during the day, as illustrated in Figure V.1. The area of the PV panel can also be approximated based on this value. The most common size of a PV panel is 1.6 m^2 , with a power capacity of around 220W [222]. Therefore, a PV panel of 1 m^2 might be able to yield a capacity of a little bit more than 130W based on the uniformity of solar radiation, which can be deemed suitable for the current application, and will be considered in the following of this chapter.

In order to give a reasonable margin of the power consumption, a total conversion efficiency of about 90% from the PV panel to the output of the inverter is assumed, thus the limit of the average electric power consumption becomes around 117W. Considering the maximum surface area ($W = 1.5\text{m}$, $L = 2\text{m}$) at the intensive heat recovery regime ($\eta_b = 0.8$) together with all other parameters at their optimal value, as indicated in Chapter IV, an average PV power consumption (\dot{P}_{PV}) of 425W and a fresh water production of 110 L can be obtained for the operation from sunrise to sunset on the summer-day. The total surface area can be therefore reduced down to 0.826 m^2 in order to limit the average PV power consumption to around 117W, in the knowledge that the amount of water production is proportional to the surface area of the integrated module, and so does \dot{P}_{PV} due to the constant SEEC discovered in Chapter IV.

Under these considerations, the shape of the module can however vary from a longer module ($W = 0.413\text{m}$, $L = 2\text{m}$) to a wider one ($W = 1.5\text{m}$, $L = 0.551\text{m}$). Hence, the following possible combinations of the width and the length were taken into account to observe the production and the electric demand for the all-day operation on Aug 1st: $0.413 \times 2 \text{ m}^2$, $0.6 \times 1.377 \text{ m}^2$, $0.8 \times 1.033 \text{ m}^2$, $1 \times 0.826 \text{ m}^2$, $1.2 \times 0.688 \text{ m}^2$ and $1.5 \times 0.551 \text{ m}^2$. The simulation results of these difference surface shapes are listed in Table V.3.

Table V.3: Information on production and consumption of different surface shapes

Module surface $W \times L$ (m^2)		0.413×2	0.6×1.377	0.8×1.033	1×0.826	1.2×0.688	1.5×0.551
Water	Daily Production (L)	30.24	30.43	30.61	30.46	30.54	30.64
Production	J_w ($\text{kg m}^{-2} \text{ h}^{-1}$)	2.54	2.55	2.57	2.55	2.56	2.57
Electric	Consumption (kWh)	1.69	1.70	1.71	1.70	1.70	1.71
consumption	\dot{P}_{PV} (W)	116.8	117.5	118.2	117.6	117.9	118.3

From the table above, all these different combinations of the width and length of the module surface seem to yield more or less similar performances. The need for PV system capacity is about 117 ~ 118W, confirming the estimation for the module surface area of 0.826 m². However, slight difference in terms of the productivity, i.e. the average permeate flux J_w , is observed to be at its maximum with the combinations of “0.8×1.033m²” and “1.5×0.551m²”. The former shape is selected to present the system performance. Besides, the production and the power consumption of 118W on Aug 1st can be deemed among the highest throughout the whole year, thus the PV system with a 1 m² panel is also capable of supplying enough electricity in other seasons. In summary, all the optimal settings for the positions and dimensions of the module are listed in Table V.4.

Table V.4: Optimal settings for MD-FPC shape and module dimensions

Parameter	Description	Value	
Positions	β	Slope of the solar collector	0°
	γ	Azimuth angle of the solar collector	0°
Dimensions	L	Length of the MD-FPC	1.033 m
	W	Width of the MD-FPC	0.8 m
	δ_f	Thickness of the feed channel	15 mm
	A_{PV}	Area of PV panel	1 m ²

V.3. Seasonal performance of the VMD–FPC based desalination system

To evaluate the overall performance of the integrated module and the system according to the season, two representative dates, August 1st for summertime and February 1st for wintertime are chosen. Based on the solar model built in Chapter II, the calculated sunrise time on August 1st is at 6:48 in Toulouse local time, while the sunset time is at 21:14. A total operating duration of 14 hours 26 minutes is therefore obtained. On the other hand, the operating duration on February 1st is 9 hours 42 minutes, from 8:17 in the morning to 17:58 in the evening. After the simulations for these two operations, the daily production, the breakdown of the consumption and other information on the operation and production are aggregated in Table V.5.

After the operation, a total permeate of 30.64 L and 13.09 L can be collected on the sunny day of August 1st and February 1st, respectively as indicated in Table V.5. Taking the daytime durations of the two different dates into account, the daily average permeate fluxes are 2.57 and 1.63 kg m⁻² h⁻¹. Health authorities commonly suggest an amount of 2 L of potable water one should drink per day [204]. Therefore in sunny days, the freshwater productions obtained by

this compact desalination system is more than enough all-year-round to supply the drinking demand of a small family. It is worth to mention that, the solar condition in Toulouse is only taken as an example; other locations nearer to the equator could yield even better performances. Besides, the productivity for the summer in terms of the surface area, which equals 37.10 L m^{-2} , is even higher than the optimal value of 32 L m^{-2} in Chapter IV, due to: i) the absorptance α_n of the absorber-plate here (0.98) is higher than the maximum value in Chapter IV (0.95); ii) the operating duration of 14h 26m is longer than the 12-hour operation in Chapter IV.

On the other hand, the total electricity consumptions of the two operations are calculated to be 1.71 and 0.72 kWh, respectively for the summer day and the winter day, including the power demand of the feed recirculation pump, the vacuum pump and the compressor in the heat pump. If divided by the water production, the obtained SEEC on the two dates are nearly the same, being around 55 kWh m^{-3} , though this value of the summer-day is a little bit higher than that of the winter-day (1.3% higher). Then, if they are divided by the operating durations, the daily average electric power demands are 118.3 W and 74.3 W, which are provided by the 1 m^2 PV panel and a set of storage batteries to tolerate the power variation during the day, as introduced in Section V.2.3. Moreover, the majority of the consumption is due to the compressor of the heat pump (around 78%), and the rest is mostly spent by the vacuum pump, as specified in Table V.5. Compared to those consumptions above, the power demand of the circulation pump is completely negligible, the same as stated and discussed in Section IV.5.3.

Table V.5: Daily operation results in a summer-day (Aug 1st) and in a winter-day (Feb 1st) for a 0.826 m^2 VMD-FPC module with 1 m^2 PV panel

Date		Aug 1st	Feb 1st
Operating time	Sunrise time	6:48	8:17
	Sunset time	21:14	17:58
	Duration	14 h 26 m	9 h 42 m
Water Production	Total daily production	30.64 L	13.09 L
	Average permeate flux	$2.57 \text{ kg m}^{-2} \text{ h}^{-1}$	$1.63 \text{ kg m}^{-2} \text{ h}^{-1}$
Electric consumption	Total consumption	1.71 kWh	0.72 kWh
	SEEC	55.74 kWh m^{-3}	55.03 kWh m^{-3}
	Circulation pump consumption	1.73 Wh	1.18 Wh
	Vacuum pump consumption	0.37 kWh	0.16 kWh
	Compressor consumption	1.34 kWh	0.56 kWh
	Average PV power consumption	118.3 W	74.3 W

V.4. Dynamic behaviors of the integrated desalination unit

First, it is worth noting that, the longitudinal profiles of the feed temperature and salinity in the bulk (T_f , C_f) or at the membrane surface (T_{fm} , C_{fm}), as well as permeate flux J_w were observed to be almost constant along the flow direction (differences between the inlet and the outlet were always below 1%), due to the high Reynolds number of 10000, which yields a short residence time of the feed flow. Therefore, the average values of these profiles are deemed representative for the daily variations on Aug 1st and Fed 1st, which will be presented as follows. The corresponding daily accumulated performances are already listed in Table V.5.

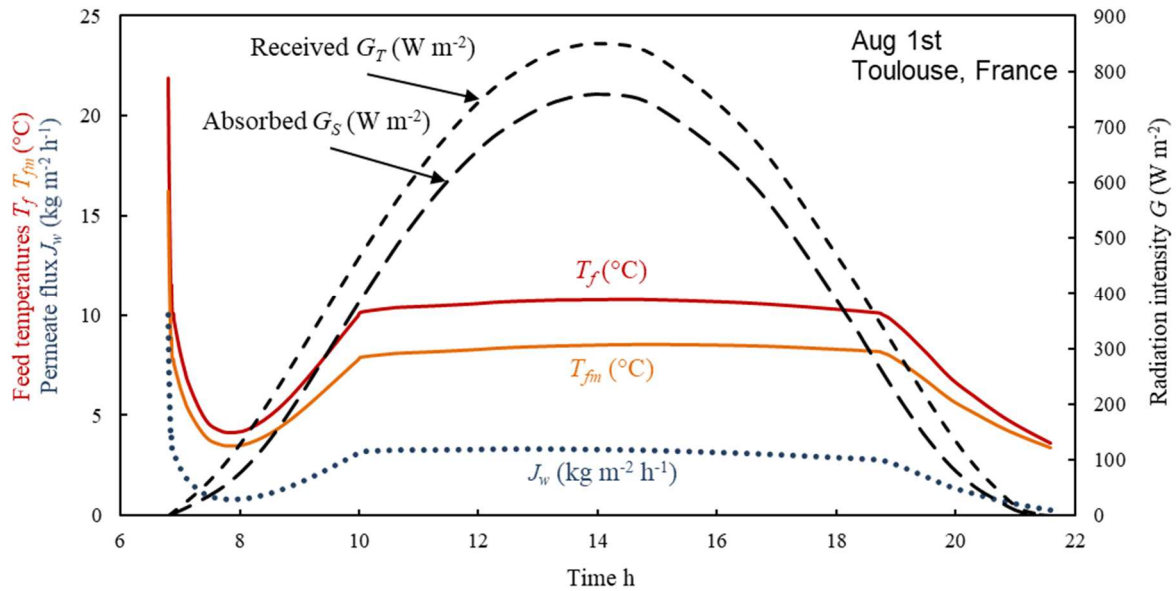
V.4.1. Representative daily variations in summer (August 1st)

Based on the specification in Table V.1 - V.4, Figure V.2 below presents the daily variations of some system operating parameters on Aug 1st. Concerned parameters include: feed temperature in the bulk T_f and at membrane surface T_{fm} , permeate flux J_w , feed salinity in the bulk C_f and at membrane surface C_{fm} , instantaneous power consumption \dot{P} , as well as the solar radiation intensity received on the module G_T and absorbed by the module G_S .

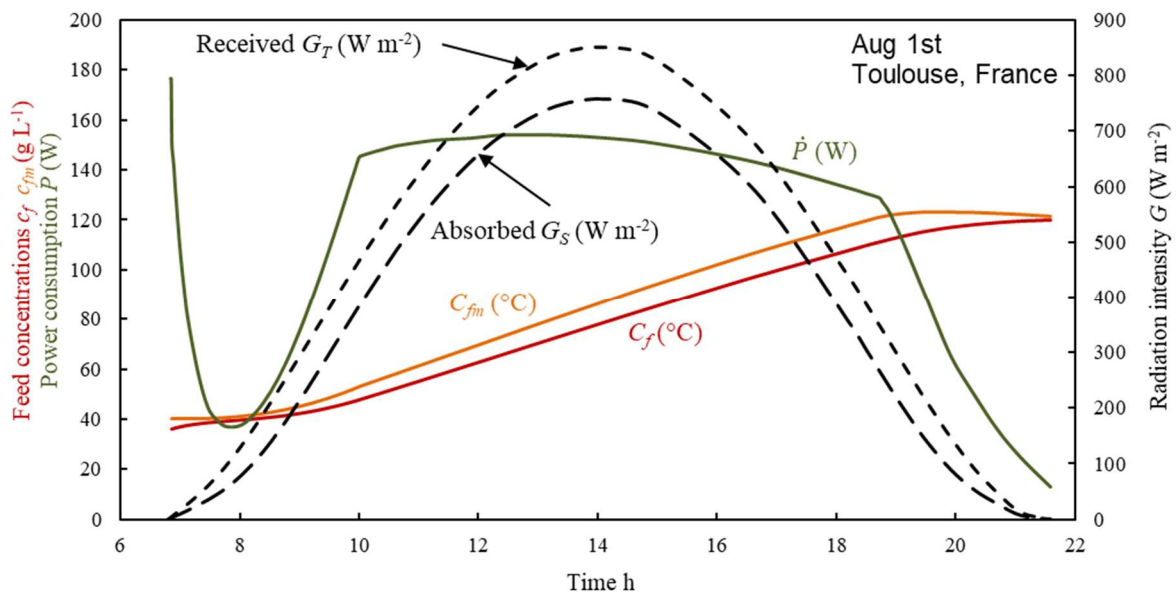
Overall, the variation of solar radiation resembles a sinusoid, assuming a cloudless weather condition. The received solar energy intensity could reach up to more than 850 W m^{-2} at around 14:00 in local time, when a highest intensity of absorbed solar energy by the absorber-plate of the module attained 750 W m^{-2} . Thanks to the integrated design where the feed flow is in direct contact with the absorber-plate, all the absorbed solar energy can be transferred to the feed fluid if neglecting the thermal transfer resistance of the thin copper-based absorber-plate.

Under such a solar radiation condition, the temperatures of the feed, the permeate flux (in Figure V.2a) and the electric power demand (in Figure V.2b) exhibit similar variation trends. A clear feed temperature polarization phenomenon is visible (T_{fm}/T_f around 80% from 10:00 to 19:00), although T_f and T_{fm} always increase and decrease at the same time. The permeate flux J_w shares the same fluctuation, on account that the transmembrane water vapor pressure difference is created by the feed temperature at the membrane T_{fm} and the constant vacuum pressure P_p of the VMD process. Regarding the power demand, it mainly comprises the electric demands of the compressor and the vacuum pump, while the part consumed by the circulation pump is totally ignorable, as shown in Table V.5. The more permeate flux, the more compressor work would be needed to efficiently condense it, and the more vacuum pump work would be needed as well to maintain the vacuum level on the permeate side. Therefore, the level of power

consumption was decided by the permeate flux, which was further determined by the feed temperature as discussed above. Consequently, all these variation trends in the figure resemble each other.



(a)



(b)

Figure V.2: Daily variation of: (a) solar radiation, permeate flux, feed temperature in the bulk and at membrane surface; (b) solar radiation, power consumption, feed salinity in the bulk and at membrane surface on Aug 1st

On the other hand, the variation curves of the salinity are totally different from the others, which indicate a continuously accumulation in salt concentration of the feed recirculation in this batch-operation fashion. In the current operation settings, C_f was not able to reach C_{limit} in one day, thus no brine discharge and seawater refill had to be performed. Similarly to the temperature polarization, a concentration polarization phenomenon was generated by the slightly higher salinity of C_{fm} than C_f (C_{fm} / C_f around 110% from 10:00 to 19:00), as shown in Figure V.2b. Furthermore, the differences between T_f and T_{fm} , and between C_f and C_{fm} were observed to be smaller early in the morning and late in the evening, i.e. the polarization phenomena were less significant when the permeate flux was lower.

A low operating temperature was observed during all day, due to the low vacuum pressure set at 650 Pa in the current example (corresponds to a water saturated temperature of around 0.9°C) and the good thermal insulation of the whole module. In the beginning of the day in Figure V.2a, the seawater temperature of 25°C could not be maintained, because the heat demand by the permeate flux of over 10 kg m⁻² h⁻¹ (generated by the partial vapor pressure difference between 25°C and 0.9°C) could not be continuously fulfilled by solar energy and the recovered heat from the heat pump. This is then confirmed by the quick drop of feed temperature to around 5°C, when the total heat provision began to be able to sustain the lower permeate flux created (around 1 kg m⁻² h⁻¹) by the vapor pressure difference between the lower feed temperature and 0.9°C. Then with the rapid augmentation of solar radiation intensity, the feed temperature and the permeate flux started to ascend due to the rising heat income, which was able to maintain higher transmembrane vapor difference. Later, the feed temperature reached 10°C (with a corresponding permeate flux around 3 kg m⁻² h⁻¹) and stabilized at about 10:00. Here, for the feed recirculation, the utilized solar energy from the direct contact with the absorber-plate, the heat recovered from heat exchanging with the condenser of the heat pump, and the heat loss by the latent heat for water evaporation were more or less poised, keeping the operating temperature level steady until approaching sunset time. More specifically, only a slight increase can be observed in the middle of the day with stronger solar condition, compared to the 10:00 in the morning or 19:00 in the evening. This observation is the result of the assumption in Chapter IV, where the condensation pressure of the thermal fluid SES36 in the heat pump was set to 48 kPa, which corresponds to a rather low saturated temperature of 15°C, in order to limit the compressor work. Therefore, the feed temperature refused to rise substantially because its increase would reduce the efficiency of the heat exchange between the condenser of the heat pump and the feed, which would then push the thermal balance away from the aforementioned

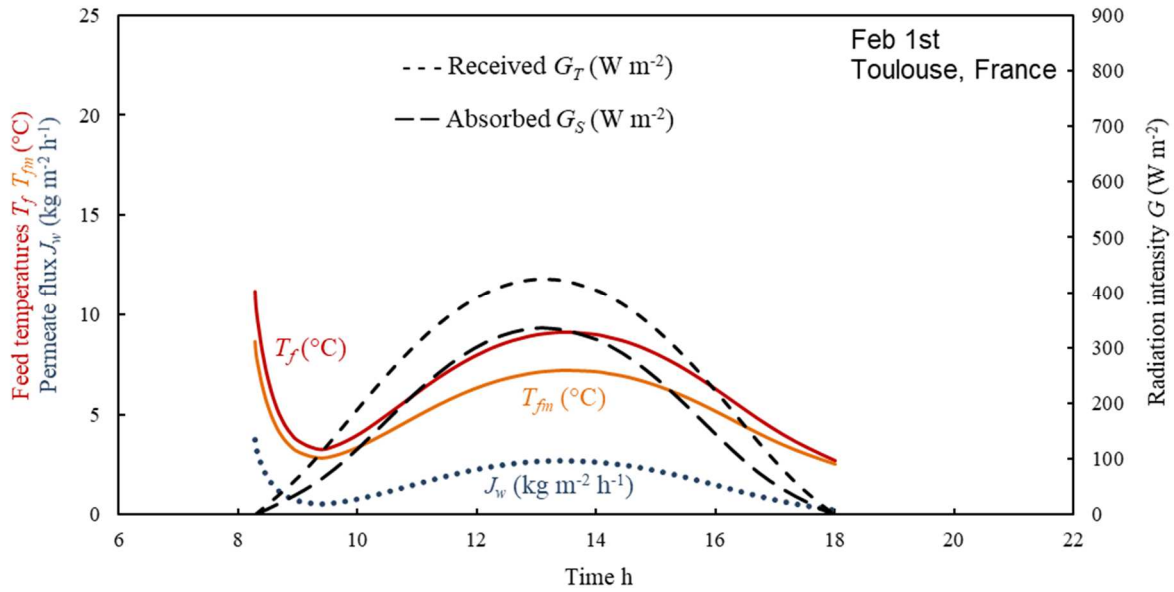
poised point, even when the solar energy was largely improved. This also coincides with the conclusion that the solar energy oriented parameters were much less important when intensive heat recovery is included. After 19:00 when solar radiation was too weak, the poise finally broke due to the lack of solar thermal energy income. All the parameters, except the salinities, descended at a rather fast pace. Therefore, the pressure setting of the thermal fluid in the condenser of the heat pump is capable of, to some extent, controlling the operating feed temperature during a rather long period of the day. Consequently, more simulations and optimizations should be performed on the parameters of the heat pump in the future.

V.4.2. Representative daily variations in winter (February 1st)

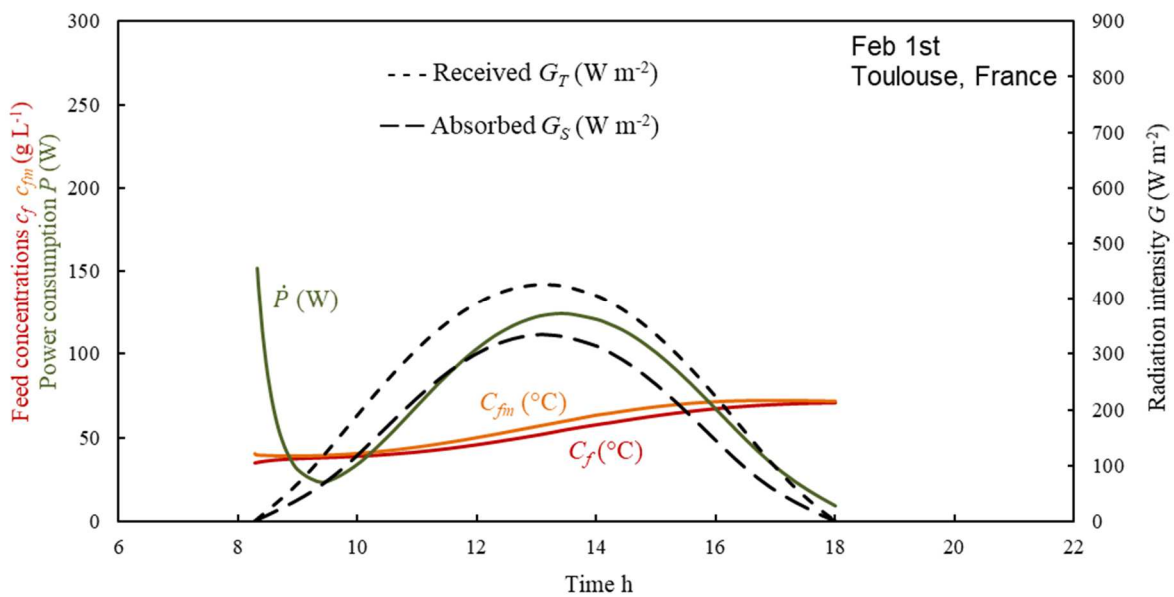
Correspondingly, the daily variations of the same parameters on Feb 1st are illustrated in Figure V.3, with the same coordinate axes as in Figure V.2.

In contrast to the summer day, the solar radiation intensities are less than half of those in Figure V.2, and the daytime is much shorter. Other than that, all the general variation trends during the daytime resemble the situation in summer, where the feed temperatures, the permeate flux and the instantaneous power consumption had a synchronized fluctuation. The same interpretation as in Section V.4.1 can be applied to this observation. Furthermore, these synchronized variations are a bit hysteretic compared to the sinusoidal solar radiations, which indicates that the heat pump also brings in an effect of slowing down the system response to solar energy fluctuation.

Besides, the temperatures also dipped a bit in the beginning of the operation, similar to the operation in summer. However, no obvious poised point (as discussed above for the summer day) can be found for the winter day here, and the feed temperature never reached 10°C again, where the summer operation stabilized. This is easy to understand when combined with the observation of the poise-breaking point in Figure V.2a, where the absorbed solar radiation was around 300 W m⁻². Here in Figure V.3, G_S never rose above 300 W m⁻², therefore the stabilization could not be established. After the operation, the salinities C_f and C_{fm} were much lower than those in Figure V.2b, due to the smaller amount of total permeated fresh water through the membrane. Hence, still no discharge and refill actions in this operation appeared.



(a)



(b)

Figure V.3: Daily variation of: (a) solar radiation, permeate flux, feed temperature in the bulk and at membrane surface; (b) solar radiation, power consumption, feed salinity in the bulk and at membrane surface on Feb 1st

V.5. Conclusions (in English)

This chapter is indeed one more step towards the application of the MD-FPC system. Following all the study in previous chapters, an exemplary equipment with the designed VMD-FPC module and the heat pumping strategy is specified and evaluated in details throughout this

chapter, in order to guide the manufacture and the test of a future prototype and potential applications. Materials for different module parts are carefully selected with the consideration of both the preferred properties (as discussed in Chapter IV) and the availability in the real world. Besides, optimized operating conditions in the last chapter are taken into account for the operation on Aug 1st and Feb 1st in Toulouse, France. The surface area of the module is then chosen to be 0.826m^2 under a practical limitation of electric power provision by the installed PV system, which includes a PV panel of 1m^2 .

Two simulations of all-day (from sunrise to sunset) operation are therefore evaluated. The production obtained in the summer day is more than 30 L, in contrast with the 13 L in winter at the same level of SEEC, which is mostly consumed by the compressor in the heat pump. Such results justify the capability of the recommended equipment to support the drinking need of a small community in remote coastal areas or islands all-year-round with a practical requirement for PV panels. Operations in locations with more abundant solar energy could result in even better performances, which will be examined in the future.

In addition, detailed daily variations of the operating parameters are presented and discussed. Interconnected trends for the feed temperature, the permeate flux and the electric power are found, with a hysteresis compared to the variation of the solar radiation in winter. Furthermore, the heat pump settings seem to be capable of determining a stabilized operating state with a certain amount of solar energy income. Consequently, further investigations on altering heat pump parameters are yet to be conducted.

V.5. Conclusions (en français)

Ce chapitre permet une première preuve de concept et un pas de plus vers le développement d'un système MD-FPC. Après toutes les études des chapitres précédents, un concret de conception de la définition détaillée d'un module VMD-FPC et la stratégie de pompage de chaleur sont spécifiés et évalués en détail tout au long de ce chapitre, en vue de guider la réalisation d'un futur prototype et de ses conditions d'essais. Les matériaux des différentes parties du module ont été définis avec soin en tenant compte à la fois des propriétés idéales (voir le chapitre IV) et de leur disponibilité effective. De plus, les conditions optimales définies dans le dernier chapitre sont prises en compte pour un fonctionnement le 1er août et le 1er février à Toulouse. La surface du module choisie est $0,826\text{ m}^2$ dans le cas d'une limitation

réaliste de l'apport électrique par le système photovoltaïque installé, soit un panneau photovoltaïque de 1 m².

Deux simulations de fonctionnement ont été réalisées sur toute une journée (du lever au coucher du soleil). La production obtenue est supérieure à 30 L le 1er août, et de seulement 13 L en hiver, avec un même niveau de SEEC. L'énergie électrique fournie par PV est principalement consommée par le compresseur de la pompe à chaleur. Les résultats démontrent que la capacité de l'équipement recommandé à subvenir aux besoins d'une petite communauté vivant dans des zones côtières ou des îles isolées tout au long de l'année, avec une requise modérée de cellules photovoltaïques. Une utilisation de cet équipement dans des endroits où les radiations solaires sont plus fortes ou plus étendues dans la journée pourrait permettre d'améliorer les performances, ce qui sera examiné dans le futur.

De plus, les variations quotidiennes des paramètres de fonctionnement sont présentées et discutées. On observe des interactions des effets de la température d'alimentation, le flux de perméat et la puissance électrique, avec une hystérésis par rapport à la variation du rayonnement solaire en hiver. De plus, les réglages de la pompe à chaleur semblent permettre de déterminer un état de fonctionnement stabilisé avec l'aide d'un certain apport d'énergie solaire. Par conséquent, des recherches supplémentaires sur l'adaptation des paramètres de la pompe à chaleur doivent encore être menées.

General conclusions and perspectives

General conclusions and perspectives

The present work has contributed to the understanding and optimal design of an integrated Membrane Distillation – direct solar heating (MD-solar) for seawater desalination within the same module, targeting self-sufficiency of drinking water for small communities in remote coastal areas or isolated islands. As highlighted throughout this thesis, solar-driven desalination is a promising alternative for freshwater supply in these remote areas where centralized supply of heat and power is often inaccessible. The lack of commercially available and robust desalination systems, suitable for dispersed use in small communities, as well as the relatively high operational cost, further deters widespread application of the desalination technology in the above-mentioned places.

As part of the LabCom MOST project [8] aiming to contribute to research on desalination membrane processes and the coupling of solar energy and MD, the design and optimization of an intensified and integrated MD-solar module for decentralized desalination at domestic scale has been investigated to promote a stable freshwater supply system meeting the demand of a small family. MD was chosen as the desalination technology because of its advantages in terms of module compactness and adaptability to small-scale applications, as opposed to the conventional thermal distillation (Multi-Stage Flash, MSF; Multi-Effect Distillation, MED), and because of its high water recovery rate under simple operating conditions without pressurization compared to Reverse Osmosis (RO). In addition, renewable low-grade solar energy, naturally replenished at no extra cost, has been used as a heating source instead of depleting fossil fuels, thanks to the mild operating temperatures in MD and its flexibility in dealing with fluctuating heat inputs.

Initially, a direct integration of Vacuum MD (VMD) and Flat-Plate solar Collector (FPC) in the same intensified module was proposed and studied to demonstrate the contribution of VMD and the integrated design of MD-solar module to the efficiency of desalination, when operating with a limited amount of solar energy absorbed. The study was carried out throughout explicit descriptions of simultaneous mass and heat transfer within the integrated module, at the scale of the membrane (membrane pore model) and the module (feed bulk longitudinal model), as well as dynamic solar energy calculations involving the approximation of solar radiation on the ground based on an isotropic sky, where the transmission, reflection, and absorption of solar radiation were integrated and referred to as functions of incoming radiations and main properties of the solar collector. The designed VMD-FPC hybrid module admitted the same surface area for the membrane module and the solar collector, which consisted of a glass cover,

an absorber-plate, a hydrophobic microporous membrane, and feed and vapor compartments on opposite sides of the membrane, under different recycling and control strategies. The relatively high and controllable permeate flux and the thermal efficiency of VMD, as well as the simplicity and availability of FPC on the market have made them good candidates for such a combination.

This first VMD-FPC module proved to be operational at its basic design and could provide a daily water production (12 hours operation) of 8 kg m^{-2} per module area, where the Gained Output Ratio (GOR) exceeded 0.71 at a vacuum pressure between 4500 and 7500 Pa. In-depth performance evaluations and feasibility tests on this first design also revealed that without the addition of auxiliary heat and when no heat recovery strategy is used for energy efficiency purposes, the solar heating and heat transfer have had a greater influence on water production and have become the main drivers of the process, regardless of the quality of mass transfer. When comparing a temperature-controlled batch regime (to attain higher feed temperatures) and a continuous VMD operation for the recirculating feed, it was observed that a continuous operation was preferred with the feed temperature and the permeate flux remaining at a low sustainable level throughout a sparse solar heating, rather than an intermittent operation of VMD. As a result, the low working temperatures were surprisingly favored, even though the average transient permeate flux remained low.

On the other hand, the first series of simulations revealed that the water production can be markedly improved by recovering the heat usually lost from permeate condensation, namely the heat recovery strategy as developed in this work. However, the additional power requirement for the integration of the heat recovery strategy needs to be truly evaluated as it directly depends on the operating temperatures and specific features of a given MD-solar module. Moreover, the location of the permeate condenser had a marked influence on the electrical power required by the vacuum pump in the case of VMD, since the condensation of permeate before the vacuum pump could reduce the volume of vapor and consequently the work of vacuum pump.

Before investigating further the optimal design of the MD-solar system and on the use of a suited heat recovery system in the case of an integrated MD-solar module, the proposed VMD-FPC module was compared with a similar design using the well-known Direct Contact MD (DCMD) because of the substantial difference between VMD and DMCD in terms of permeate

General conclusions and perspectives

flux and required energy. The comparative study was carried out for the same dimensions and setting similar characteristics and operating conditions, in order to identify the main factors contributing to the improvement of the two systems and to discuss their different perspectives of hybridization within a MD-solar desalination unit.

A significant difference in the efficiency of solar energy utilization was observed throughout the two approaches setting the same surface area of the integrated module, 16% for DCMD-FPC and 89% for VMD-FPC, the latter being able to allow a more substantial and controllable permeate flux. At this level, the heat recovery and the solar concentration by multiplying the intensity of the incident radiation were also discussed as two possible paths of improvement for either of the two MD-solar systems. Given the difference in the nature of heat exchange on the permeate side in these MD configurations, i.e. the sensible heat for DCMD-FPC and the latent heat for VMD-FPC, the latter has been identified as being more suitable for coupling to a heat recovery system. On the other hand, solar concentration had a direct positive influence on desalination via the VMD-FPC and DCMD-FPC modules. Actually, their performance improved proportionally, almost linearly, with the increase in solar concentration, but with different improvement ratios (below 4 for the DCMD-FPC and 8 for the VMD-FPC, on average), the improvement ratio being the ratio between the water production and the concentration factor.

Because of its flexible and higher permeate flux, its stronger response to an intensified solar collector and improved heat transfer using for instance the solar concentration, its associated lower conduction heat loss, and its easier adaptation in a heat recovery system, the integrated VMD-FPC module, as proposed in this thesis, has been selected for further developments and readjustments, and has been the subject of additional sensitivity analyses and multi-criteria optimizations.

First, a heat pump was connected to the two thermal sources of the desalination system, namely the heat-demanding feed recirculation system and the heat-releasing permeate condenser. The VMD-FPC with integrated heat pump has recovered the latent heat of condensation and brought it back to the feed side of the module in the recirculation system, while at the same time providing a practical condensation strategy that exempts excessive vacuum pump consumption and use of additional intensive cooling power. The organic Solkatherm (SES36) was chosen as working fluid for the heat pump. Thanks to the thermodynamic properties of the SES36, the

corresponding pressure difference between the condenser and the evaporator of the heat pump can be decreased, which considerably reduces the compressing work of the heat pump by 20%.

Second, the design and operating conditions of the VMD-FPC system with integrated heat recovery through heat pump were optimized and the overall performance was examined under different heat recovery regimes, ranging from zero heat recovery (VMD-FPC stand-alone with no heat recovered from heat pump condenser) up to maximum heat recovery achievable from permeate condensation (referred to as a heat pump condenser efficiency of 80%). The VMD-FPC module with integrated heat pump has indeed allowed a substantial gain in terms of water production with a relatively low power consumption, which had to be supplied by photovoltaic (PV) panels for an autonomous water supply system. Multi-objective optimization has identified optimal design and operating conditions for varying production scales, ranging from 3.7 L to 96 L, with corresponding power consumption equal to 0.21 kWh and 5.38 kWh, respectively, for a cloudless 12-hour operation on Aug 1st in Toulouse, France. In addition, for all simulations, it was found that the PV capacity requirement per unit of water production was almost constant, ranging from 4.2 to 5.0 W L⁻¹.

These results have proven not only the ability of such an intensified desalination system to provide fresh water for small communities, but also its flexibility at different scales of production with a near constant specific power consumption of less than 5 W L⁻¹ to be supplied by PV panels. Moreover, the power consumption was much lower than that of the initial VMD-FPC including the recirculation system without heat pump, where the dominant consumption was related to the work of the compressor in the heat pump instead of the work of the vacuum pump.

Global observations and statistical analyses showed also a profound discordance of variable sensitivities when comparing the VMD-FPC module with and without heat recovery. Under a relevant heat recovery regime, the overall performance of the system is less sensitive to solar-oriented variables. In fact, in such a situation, the permeability of the membrane and the flow regime become as important as the vacuum pressure and module dimensions (length and width) to enhance the quality of mass transfer and the production of freshwater. This is why, in the case of heat recovery, higher membrane permeability ($> 1.5 \times 10^{-5} \text{ s mol}^{1/2} \text{ m}^{-1} \text{ kg}^{-1/2}$) and turbulent feed flow (high Re) have been recommended for optimal operation. Meanwhile, the mass transfer-oriented parameters were less influential for an integrated VMD-FPC module

General conclusions and perspectives

without heat recovery, since in this situation the overall performance was drastically limited by the limited amount of solar energy that could be captured and used. Interestingly, the module area (length and width) not only determined the scale of production, but also acted as one of the main production drivers. They have been identified as being as sensitive as the vacuum pressure in a VMD-FPD module for the recirculation system with and without heat recovery, and have been able to flexibly adjust water production according to the real demand of freshwater and the practical limitation of PV power supply.

Based on the Pareto-optimal results previously explored and illustrated, practical recommendations were finally provided on the design, choice of materials and operating conditions for a small-scale MD-solar hybrid desalination device to guide a future prototype. Under a practical limitation of 130W on the supply of PV power, a VMD-FPC module with an area of 0.83m^2 has been adopted. On the same site in Toulouse, a 30 L freshwater production was obtained for the whole day operation on August 1st, while the value fell to 13 L in winter on February 1st, which was still sufficient to meet the daily drinking needs (2 L per person) of a small family. The large variation in production implies the need for a future study of performance under fluctuating solar conditions and the improvement of the robustness of the system. The models provided and used in this thesis were predictive and could be readapted to different geometries of solar collectors, properties of material on membrane and solar system. The solar radiation model depends on time and location, however it has been configured to represent the city of Toulouse, France, to guide the construction of the experimental prototype in the laboratory. Therefore, the system performance must also be studied for true remote geographical locations, often characterized by better solar conditions with a longer day and stronger radiation intensity.

In addition to the integrated MD-solar module for desalination of seawater, the heat pump was studied in a simple loop with SES36 as working fluid to ensure heat recovery at a reduced working cost of the compressor in the heat pump. Nevertheless, the examination of the heat pump parameters and the in-depth evaluations of the choice of coolant, the optimal pressure levels and the study of more complex heat pump cycles were excluded from this work. In this way, the optimal design of an enhanced heat pump system, combined with an MD-solar hybrid desalination system, can be explored further in future studies.

The combination or design of other improved modules and geometries, including for example the use of hollow fibers for the membrane and the cylindrical or parabolic trough for the solar thermal collector, is also a promising perspective, as the significant influence of solar concentration has been confirmed on production and overall performance, and since the importance of mass transfer quality has been particularly highlighted in energy-efficient systems using improved heat recovery strategies.

An experimental prototype in the lab is actually expected, following the main guidelines of this work, which is in fact the main perspective of this study. The prototype will soon be manufactured and tested to confirm the technical feasibility of such an MD-solar integrated desalination module for small communities in remote locations.

Nomenclature

A	surface area, m^2
Al	local altitude, km
B	overall mass transfer coefficient in pores, s m^{-1}
C	concentration, g L^{-1}
c_p	heat capacity of the seawater, $\text{J kg}^{-1} \text{ }^\circ\text{C}^{-1}$
D	distillate production, L / diffusion coefficient, $\text{m}^2 \text{ s}^{-1}$
d	diameter, m / angular position of the sun at solar noon, $^\circ$
E	electric consumption, kWh
f	Darcy friction factor
F_{c-s}	view factor of the surface to the sky
F_{c-g}	view factor of the surface to the ground
F_V	volumetric flow rate, $\text{m}^3 \text{ s}^{-1}$
G	solar irradiance, the intensity of radiation received per unit area, W m^{-2}
h	convective heat transfer coefficient, $\text{W m}^{-2} \text{ }^\circ\text{C}^{-1}$ / enthalpy, J kg^{-1}
J	permeate flux, $\text{kg m}^{-2} \text{ h}^{-1}$
K	extinction coefficient of the glass, m^{-1}
K_m	membrane Knudsen permeability coefficient, $\text{s mol}^{1/2} \text{ m}^{-1} \text{ kg}^{-1/2}$
k_m	mass transfer coefficient, m s^{-1}
k_t	thermal conductivity, $\text{W m}^{-1} \text{ }^\circ\text{C}^{-1}$
L	length of the feed channel, m / longitude, $^\circ$
l	mean free path, m
M	mass molar mass, kg mol^{-1}
m	mass, kg
\dot{m}	mass flow rate, kg s^{-1}
N	number of glass cover
n	refractive index / n th day of the year
P^0	vapor pressure of pure water, Pa
P	pressure, Pa
\dot{P}	power, W
Q	heat flux, W m^{-2}
\dot{Q}	heat flow rate, W

Nomenclature

r	radius, m / reflectance
s	entropy, J kg ⁻¹ °C ⁻¹
T	temperature, °C
t	time, h
U	heat loss coefficient, W m ⁻² °C ⁻¹
V	volume, m ³
v	flow velocity, m s ⁻¹
W	module width, m
\dot{W}	work rate, W
w	salt mass fraction
x	molar fraction
ΔH	latent heat, J kg ⁻¹

Greek letters

α	solar absorptance
β	slope of the surface, °
γ	azimuth angle of the surface, ° / activity coefficient
δ	thickness, m
ε	emittance / porosity of the membrane
η	efficiency
θ	incidence angle
λ	thermal conductivity, W m ⁻¹ °C ⁻¹
μ	dynamic viscosity, Pa s
ρ	density, kg m ⁻³
ρ_g	diffuse reflectance of the surroundings
σ	collision diameter of molecule, m
τ	atmospheric transmittance / tortuosity of the membrane pore
τ_a	transmittance of the cover when only absorption losses considered
τ_r	transmittance of the cover when only reflection losses considered
φ	latitude, °
ω	hour angle, °

Subscripts

a	ambient / evaporator side of heat pump
-----	--

<i>amax</i>	ambient maximum
<i>amin</i>	ambient minimum
<i>ap</i>	absorber-plate
<i>atm</i>	atmosphere
<i>avg</i>	average
<i>b</i>	beam / condenser side of heat pump
<i>bo</i>	bottom
<i>C</i>	collector
<i>c</i>	coolant / cover
<i>comp</i>	compressor
<i>cp</i>	circulation pump
<i>D</i>	molecular diffusion
<i>d</i>	diffuse / distillate
<i>e</i>	equivalent
<i>f</i>	feed bulk
<i>g</i>	ground-reflected / gas
<i>h</i>	hydraulic
<i>i</i>	insulation
<i>in</i>	inlet
<i>is</i>	isentropic
<i>K</i>	Knudsen diffusion
<i>l</i>	liquid
<i>loc</i>	local
<i>m</i>	membrane surface / mass
<i>me</i>	mechanical
<i>n</i>	normal direction
<i>o</i>	extraterrestrial
<i>out</i>	outlet
<i>p</i>	permeate / productivity
<i>ref</i>	reference
<i>S</i>	absorbed
<i>s</i>	seawater supply / solid
<i>sat</i>	saturated
<i>sr</i>	sunrise

Nomenclature

<i>ss</i>	sunset
<i>s-w</i>	salt in water
<i>T</i>	received on tilted surface
<i>t</i>	top / thermal
<i>u</i>	utilized
<i>V</i>	viscous flow
<i>v</i>	vapor
<i>vp</i>	vacuum pump
<i>vap</i>	vaporization
<i>w</i>	pure water
<i>wi</i>	wind
<i>z</i>	zenith
	parallel
⊥	perpendicular

Constants

G_{SC}	solar constant, 1367 W m^{-2}
g	gravitational acceleration, 9.81 m s^{-2}
R	ideal gas constant, $8.314 \text{ J mol}^{-1} \text{ K}^{-1}$
k_B	Boltzmann constant, $1.38 \times 10^{-23} \text{ m}^2 \text{ kg s}^{-2} \text{ K}^{-1}$

Abbreviations

AGMD	Air gap membrane distillation
AMOE-MAP	Archive-based multi-objective evolutionary algorithm with memory-based adaptive partitioning of search space
CFD	Computational fluid dynamics
CP	Circulation pump
CPC	Compound parabolic collector
CSP	Concentrating solar power
DAE	Differential-algebraic equation
DCMD	Direct contact membrane distillation
DMI	Delta moment-independent
ETC	Evacuated-tube collector
FPC	Flat-plate collector

GOR	Gained output ratio
HR	Heat recovery
HRR	Heat recovery ratio
LFR	Linear Fresnel reflectors
MD	Membrane distillation
MED	Multi-effect distillation
MGMD	Material gap membrane distillation
MOO	Multi-objective optimization
MSF	Multi-stage flash
ODE	Ordinary differential equation
ODP	Ozone depletion potential
ORC	Organic rankine cycle
PDC	Parabolic dish collector
PGMD	Permeate gap membrane distillation
PP	Polypropylene
PTC	Parabolic trough collector
PTFE	Polytetrafluoroethylene
PV	Photovoltaic
PV/T	Photovoltaic/thermal
PVDF	Polyvinylidene fluoride
RO	Reverse osmosis
RR	Recovery rate
SA	Sensitivity analysis
SC	Solar collector
SEC	Specific energy consumption
SEEC	Specific electric energy consumption
SGMD	Sweeping gas membrane distillation
SGSP	Salinity-gradient solar pond
STEC	Specific thermal energy consumption
V	Valve
VGMD	Vacuum gap membrane distillation
VMD	Vacuum membrane distillation
V-MEMD	Vacuum multi-effect membrane distillation
VP	Vacuum pump

Nomenclature

Dimensionless numbers

Kn Knudsen number

Nu Nusselt number

Pr Prandtl number

Re Reynolds number

Sc Schmidt number

Sh Sherwood number

Index of figures

Figure 1: System configurations coupling MD and SC (adapted from Méricq et al. [27])	5
Figure I.1: Schematic of the MD process.....	10
Figure I.2: Basic configurations of membrane distillation: (a) DCMD; (b) VMD; (c) AGMD; (d) SGMD.....	14
Figure I.3: Configurations of MD modules: (a) plate and frame; (b) tubular; (c) spiral wound (from [55]).....	17
Figure I.4: Scheme of Scarab AGMD module with two adjacent cassettes (shown in yellow) with their corresponding membranes and condensing walls (from [57]).....	18
Figure I.5: The arrangement of thermal resistances in MD process	20
Figure I.6: The arrangement of mass transfer resistances in MD process	23
Figure I.7: Configuration of a normal FPC (from [115]).....	29
Figure I.8: Configurations of ETCs (from top to bottom): water-in-glass type and heat-pipe type	30
Figure I.9: Different layers of an SGSP	31
Figure I.10: Line-focusing concentrating solar collectors (from left to right): CPC, PTC, and LFR.....	32
Figure I.11: Point-focusing concentrating solar collectors (from left to right): PDC and solar tower.....	32
Figure I.12: Schematic diagram of the solar thermal DCMD process in [69]	35
Figure I.13: Schematics of solar driven MD: (a) One-loop compact systems; (b) Two-loop large systems	36
Figure I.14: Flowsheet of the solar-heated MD system in [140]	37
Figure I.15: Flowsheet of the large “SMADES” MD system in Aquaba, Jordan (from [99]) ..	39
Figure I.16: The schema of the hybrid solar distillator in [105]	42
Figure I.17: Schematic of the directly integrated DCMD module in [153]	43
Figure I.18: Schema of high-efficient solar-thermal membrane distillation module in [155] .	43
Figure I.19: Hollow fiber membranes integrated inside the absorber of a CPC (from [156]).	44
Figure I.20: Configuration of the VMD-ETC module in [158]	45
Figure I.21: The direct radiation absorption on the surface of a composite membrane in [161]	46

Index of figures

Figure II.1: Cross-sectional view of the proposed integrated VMD-FPC module.....	57
Figure II.2: Schematic of the modeling process of VMD-FPC module.....	58
Figure II.3: Zenith angle, slope, azimuth angle, and solar azimuth angle for a tilted surface [1 12]	59
Figure II.4: Incidence and refraction angles in the interface of two media.....	63
Figure II.5: Schematic of VMD modeling	64
Figure II.6: Configurations for the recycling batch system	70
Figure II.7: Control strategy for the recycling batch system.....	72
Figure II.8: Comparison between the theoretical modeling of solar radiation on a fixed absorber with the data provided by the Photovoltaic Geographical Information System 5 (PVGIS 5) .	76
Figure II.9: Comparison between experimental and predicted permeate flux from VMD model	77
Figure II.10: Daily variation of solar radiation, feed temperature, feed concentration and permeate flux when operating under controlled temperature (Toulouse, Aug 1st; $\beta = 25^\circ$; $K_m =$ $3.7 \times 10^{-6} \text{ s mol}^{1/2} \text{ m}^{-1} \text{ kg}^{-1/2}$; $P_p = 5000 \text{ Pa}$; $\text{Re} (40^\circ\text{C}) = 600$)	79
Figure II.11: Influence of operating temperature levels on the module performance of (a) water productivity D_p ; (b) GOR; (c) SEEC.....	81
Figure II.12: Daily variation of solar radiation, feed temperature, feed concentration and permeate flux when operating under continuous pumping regime (Toulouse, Aug 1st; $\beta = 25^\circ$; $K_m = 3.7 \times 10^{-6} \text{ s mol}^{1/2} \text{ m}^{-1} \text{ kg}^{-1/2}$; $P_p = 5000 \text{ Pa}$; $\text{Re} (40^\circ\text{C}) = 600$).....	83
Figure II.13: System performance at varying glazing cover properties: (a) refractive index n_c , (b) extinction coefficient K , (c) thickness δ_c	84
Figure II.14: System performance at varying solar absorptances in normal direction (α_n)	86
Figure II.15: System performance at varying collector slopes β	86
Figure II.16: System performance at varying membrane permeability coefficients (K_{mref}).....	87
Figure II.17: System performance at varying vacuum pressures (P_p).....	88
Figure II.18: System performance at varying Reynolds numbers.....	89
Figure II.19: System performance at varying heat recovery ratios	90
Figure III.1: Configuration for an integrated DCMD-FPC module	97
Figure III.2: Flowsheet of recirculation system for DCMD-FPC module	103
Figure III.3: Schematic of interconnected modeling structure: MD model, solar radiation model and system dynamics.....	107

Figure III.4: Daily variation of solar irradiance, feed and permeate temperature, feed concentration and permeate flux of (a) DCMD-FPC system; (b) VMD-FPC system	111
Figure III.5: Daily distillate productivity and specific electrical energy consumption for DCMD-FPC and VMD-FPC systems at varying glass cover properties: (a) refractive index n_c ; (b) product of extinction coefficient K and thickness δ_c	114
Figure III.6: Daily distillate productivity and specific electrical energy consumption for DCMD-FPC and VMD-FPC systems at varying absorptance α_n in normal direction of absorber-plate	115
Figure III.7: Daily distillate productivity and specific electrical energy consumption for DCMD-FPC and VMD-FPC systems at varying membrane properties: (a) porosity ε , (b) tortuosity τ , (c) thickness δ_m , (d) pore size r	117
Figure III.8: Daily distillate productivity and specific electrical energy consumption for the DCMD-FPC system at varying thermal conductivities k_p of membrane polymer	118
Figure III.9: Daily distillate productivity and specific electrical energy consumption at varying Reynolds numbers: (a) feed side for both DCMD-FPC and VMD-FPC modules; (b) permeate side for DCMD-FPC module only	120
Figure III.10: Daily distillate productivity and specific electrical energy consumption at varying: (a) cooling circulation flow rate, (b) cooling heat exchange capacity $U_c A_c$	122
Figure III.11: Daily distillate productivity and specific electrical energy consumption at varying slope β	123
Figure III.12: Daily distillate productivity and specific electrical energy consumption at varying module dimensions for DCMD-FPC and VMD-FPC systems: (a) length L , (b) width W , (c) thickness of feed channel δ_f ($W \times L = 0.5 \times 0.7 \text{ m}^2$), (d) thickness of permeate channel δ_p ($W \times L = 0.5 \times 0.7 \text{ m}^2$)	125
Figure III.13: Daily distillate productivity D_p for DCMD-FPC and VMD-FPC systems at varying heat recovery ratios (HRR)	128
Figure III.14: Daily distillate productivity D_p for DCMD-FPC and VMD-FPC systems at varying concentration ratios (CR)	129
Figure IV.1: Flowsheet for VMD-FPC recycle system with integrated heat recovery through heat pump	140
Figure IV.2: Cross-sectional view of integrated FPC-VMD module.....	141
Figure IV.3: The heat pump cycle: (a) configuration of heat pump interconnected with MD system; (b) corresponding <i>pressure-enthalpy</i> diagram	143

Index of figures

Figure IV.4: Schematic of modeling process of VMD-FPC with heat pump	146
Figure IV.5: DMI and S1 sensitivity indicators with respect to different variables: (a) study of water production D at no heat recovery regime ($\eta_b = 0$); (b) study of energy consumption E at no heat recovery regime ($\eta_b = 0$); (c) study of water production D at maximum heat recovery ($\eta_b = 0.8$); (d) study of energy consumption E at maximum heat recovery ($\eta_b = 0.8$).....	154
Figure IV.6: DMI and S1 sensitivity indicators with respect to different variables: (a) study of water production D; (b) study of energy consumption E at varying heat recovery level.....	155
Figure IV.7: Global optimization results for VMD-FPC module with integrated heat recovery via heat pump at varying heat recovery level: (a) Pareto front of D and E; (b) the corresponding daily average permeate flux and electric power consumption	156
Figure IV.8: Pareto fronts (D against E), daily average permeate flux and electric power consumption for the 5 independent optimization benchmarks with fixed heat recovery levels: (a) $\eta_b = 0$, (b) $\eta_b = 0.2$, (c) $\eta_b = 0.4$, (d) $\eta_b = 0.6$, (e) $\eta_b = 0.8$	159
Figure IV.9: Dynamic variations of solar radiation intensities, accumulated distillate production and electricity consumption of Point B in Figure IV.8e	162
Figure IV.10: Ranges and typical values of optimal solar energy-oriented variables at different η_b	163
Figure IV.11: Ranges and typical values of optimal VMD process variables at different η_b	165
Figure IV.12: Ranges and typical values of dimension variables at different η_b	166
Figure V.1: Flowsheet of the recommended energy-efficient VMD-FPC prototype with integrated heat pump for small-scale desalination	174
Figure V.2: Daily variation of: (a) solar radiation, permeate flux, feed temperature in the bulk and at membrane surface; (b) solar radiation, power consumption, feed salinity in the bulk and at membrane surface on Aug 1st	183
Figure V.3: Daily variation of: (a) solar radiation, permeate flux, feed temperature in the bulk and at membrane surface; (b) solar radiation, power consumption, feed salinity in the bulk and at membrane surface on Feb 1st	186

Index of tables

Table I.1: Advantages and disadvantages of different MD configurations [15,53]	16
Table I.2: Some correlations for the calculation of heat transfer coefficients	22
Table I.3: Characteristics of different solar thermal collectors [118,123,125,126]	33
Table I.4: Data from the literature on the coupling of solar collectors and MD systems	39
Table I.5: Potential Advantages and limitations of the direct integration of MD and SC	41
Table II.1: Correction factors for climate types [168].....	60
Table II.2: Coefficients a, b, c in Eq. 22 for the calculation of viscosity [18]	66
Table II.3: Coefficients a, b, c, d, e in Eq. 23 for the calculation of density [18]	66
Table II.4: Coefficients a, b, c in Eq. 24 for the calculation of thermal conductivity [18]	67
Table II.5: Coefficients in Eq. 25 for the calculation of heat capacity [174].....	67
Table II.6: Dynamics of the recycling batch system.....	73
Table II.7: Parameters of the integrated VMD-solar module.....	78
Table III.1: Parameter settings of integrated module and system operation for both DCMD-FPC and VMD-FPC	108
Table IV.1: Decision variables for VMD-FPC module with heat pump	148
Table IV.2: Parameter settings for VMD-FPC module with heat pump.....	149
Table IV.3: Operating parameters of heat pump using SES36 in this study.....	150
Table IV.4: Performance analysis over the Pareto front in Figure IV.8e (three representative operating points: A, B and C).....	160
Table V.1: Material property settings in this chapter	176
Table V.2: Operating conditions in this chapter	178
Table V.3: Information on production and consumption of different surface shapes.....	179
Table V.4: Optimal settings for MD-FPC shape and module dimensions.....	180
Table V.5: Daily operation results in a summer-day (Aug 1st) and in a winter-day (Feb 1st) for a 0.826m ² VMD-FPC module with 1m ² PV panel.....	181

References

- [1] Where is Earth's water? USGS Water-Science School, (n.d.). <https://water.usgs.gov/edu/earthwherewater.html> (accessed September 18, 2018).
- [2] M.M. Mekonnen, A.Y. Hoekstra, Four billion people facing severe water scarcity, *Science Advances*. 2 (2016) e1500323. doi:10.1126/sciadv.1500323.
- [3] P. Burek, Y. Satoh, G. Fischer, M.T. Kahil, A. Scherzer, S. Tramberend, L.F. Nava, Y. Wada, S. Eisner, M. Flörke, N. Hanasaki, P. Magnuszewski, B. Cosgrove, D. Wiberg, *Water Futures and Solution - Fast Track Initiative (Final Report)*, (2016). <http://pure.iiasa.ac.at/id/eprint/13008/> (accessed September 18, 2018).
- [4] A. Islam, H. Sakakibara, R. Karim, M. Sekine, Potable water scarcity: options and issues in the coastal areas of Bangladesh, *J Water Health*. 11 (2013) 532–542. doi:10.2166/wh.2013.215.
- [5] E. Weber, Water in the Pacific islands: case studies from Fiji and Kiribati, *Water: A Source of Conflict or Cooperation*. (2007) 269–309.
- [6] J. Liu, H. Yang, S.N. Gosling, M. Kummu, M. Flörke, S. Pfister, N. Hanasaki, Y. Wada, X. Zhang, C. Zheng, J. Alcamo, T. Oki, Water scarcity assessments in the past, present, and future, *Earth's Future*. 5 (2017) 545–559. doi:10.1002/2016EF000518.
- [7] A. Ahmadi, L. Tiruta-Barna, E. Benetto, F. Capitanescu, A. Marvuglia, On the importance of integrating alternative renewable energy resources and their life cycle networks in the eco-design of conventional drinking water plants, *Journal of Cleaner Production*. 135 (2016) 872–883. doi:10.1016/j.jclepro.2016.06.201.
- [8] labruyer, LabCom MOST, un nouveau challenge pour le LISBP et SunwaterLife, (2017). <http://www.lisbp.fr/fr/actualites/nos-actus-passees/actualites-2017/labcom-most.html> (accessed February 15, 2019).
- [9] A.D. Khawaji, I.K. Kutubkhanah, J.-M. Wie, Advances in seawater desalination technologies, *Desalination*. 221 (2008) 47–69. doi:10.1016/j.desal.2007.01.067.
- [10] V.G. Gude, Desalination and water reuse to address global water scarcity, *Rev Environ Sci Biotechnol*. 16 (2017) 591–609. doi:10.1007/s11157-017-9449-7.
- [11] E. Guillén-Burrieza, J. Blanco, G. Zaragoza, D.-C. Alarcón, P. Palenzuela, M. Ibarra, W. Gernjak, Experimental analysis of an air gap membrane distillation solar desalination pilot system, *Journal of Membrane Science*. 379 (2011) 386–396. doi:10.1016/j.memsci.2011.06.009.

References

- [12] L.F. Greenlee, D.F. Lawler, B.D. Freeman, B. Marrot, P. Moulin, Reverse osmosis desalination: Water sources, technology, and today's challenges, *Water Research*. 43 (2009) 2317–2348. doi:10.1016/j.watres.2009.03.010.
- [13] D. González, J. Amigo, F. Suárez, Membrane distillation: Perspectives for sustainable and improved desalination, *Renewable and Sustainable Energy Reviews*. 80 (2017) 238–259. doi:10.1016/j.rser.2017.05.078.
- [14] C. Cabassud, H.R. Balmann, 14. Dessalement d'eau de mer, in: A. Euzen, C. Jeandel, R. Mosseri (Eds.), *L'eau à Découvert*, CNRS Éditions, Paris, 2017: pp. 228–229. <http://books.openedition.org/editions-cnrs/10006> (accessed February 19, 2019).
- [15] E. Drioli, A. Ali, F. Macedonio, Membrane distillation: Recent developments and perspectives, *Desalination*. 356 (2015) 56–84. doi:10.1016/j.desal.2014.10.028.
- [16] N. Couffin, Elimination de composés organohalogénés volatils à l'état de traces dans l'eau par distillation membranaire sous vide, thesis, Toulouse, INSA, 2000. <http://www.theses.fr/2000ISAT0007> (accessed February 15, 2019).
- [17] D. Wirth, Etude de la distillation membranaire sous vide pour le dessalement d'eau de mer : de l'analyse des mécanismes de transfert à l'optimisation énergétique du procédé, thesis, Toulouse, INSA, 2002. <http://www.theses.fr/2002ISAT0040> (accessed February 15, 2019).
- [18] J.-P. Mericq, Approche intégrée du dessalement d'eau de mer: Distillation membranaire sous vide pour la réduction des rejets salins et possibilités de couplage avec l'énergie solaire, 2009. <http://eprint.insa-toulouse.fr/archive/00000341/> (accessed February 12, 2016).
- [19] T.D. Dao, Procédés membranaires pour l'élimination des métaux lourds: application de la distillation membranaire à l'élimination de l'Arsenic contenu dans les eaux, Toulouse, INSA, 2013. <http://www.theses.fr/2013ISAT0040> (accessed February 12, 2016).
- [20] P. Jacob, *Detection and Understanding of Wetting Mechanisms in Vacuum Membrane Distillation Applied to Desalination of Seawater*, 2018.
- [21] K.W. Lawson, D.R. Lloyd, Membrane distillation, *Journal of Membrane Science*. 124 (1997) 1–25. doi:10.1016/S0376-7388(96)00236-0.
- [22] J.-P. Mericq, S. Laborie, C. Cabassud, Vacuum membrane distillation for an integrated seawater desalination process, *Desalination and Water Treatment*. 9 (2009) 287–296. doi:10.5004/dwt.2009.862.
- [23] A.C. Sun, W. Kosar, Y. Zhang, X. Feng, Vacuum membrane distillation for desalination of water using hollow fiber membranes, *Journal of Membrane Science*. 455 (2014) 131–142. doi:10.1016/j.memsci.2013.12.055.

- [24] R. Miladi, N. Frikha, S. Gabsi, Exergy analysis of a solar-powered vacuum membrane distillation unit using two models, *Energy*. (n.d.). doi:10.1016/j.energy.2016.11.133.
- [25] J. Cai, F. Guo, Study of mass transfer coefficient in membrane desalination, *Desalination*. 407 (2017) 46–51. doi:10.1016/j.desal.2016.12.013.
- [26] T.U.K. Nutakki, Integration of Membrane Distillation and Solar Thermal Systems for Co-production of Purified Water and Heat, 2015. <http://www.diva-portal.org/smash/record.jsf?pid=diva2:878008> (accessed March 3, 2016).
- [27] J.-P. Mericq, S. Laborie, C. Cabassud, Evaluation of systems coupling vacuum membrane distillation and solar energy for seawater desalination, *Chemical Engineering Journal*. 166 (2011) 596–606. doi:10.1016/j.cej.2010.11.030.
- [28] K.R. Ranjan, S.C. Kaushik, Thermodynamic and economic feasibility of solar ponds for various thermal applications: A comprehensive review, *Renewable and Sustainable Energy Reviews*. 32 (2014) 123–139. doi:10.1016/j.rser.2014.01.020.
- [29] A. Gabelman, S.-T. Hwang, Hollow fiber membrane contactors, *Journal of Membrane Science*. 159 (1999) 61–106. doi:10.1016/S0376-7388(99)00040-X.
- [30] B.W. Reed, M.J. Semmens, E.L. Cussler, Chapter 10 Membrane contactors, in: R.D. Noble, S.A. Stern (Eds.), *Membrane Science and Technology*, Elsevier, 1995: pp. 467–498. doi:10.1016/S0927-5193(06)80012-4.
- [31] M.S. El-Bourawi, Z. Ding, R. Ma, M. Khayet, A framework for better understanding membrane distillation separation process, *Journal of Membrane Science*. 285 (2006) 4–29. doi:10.1016/j.memsci.2006.08.002.
- [32] M.K. Souhaimi, T. Matsuura, *Membrane distillation: principles and applications*, Elsevier, 2011.
- [33] L. Martínez-Díez, M.. Vázquez-González, Temperature and concentration polarization in membrane distillation of aqueous salt solutions, *Journal of Membrane Science*. 156 (1999) 265–273. doi:10.1016/S0376-7388(98)00349-4.
- [34] D. Wirth, C. Cabassud, Water desalination using membrane distillation: comparison between inside/out and outside/in permeation, *Desalination*. 147 (2002) 139–145. doi:10.1016/S0011-9164(02)00601-X.
- [35] P. Jacob, S. Laborie, C. Cabassud, Visualizing and evaluating wetting in membrane distillation: New methodology and indicators based on Detection of Dissolved Tracer Intrusion (DDTI), *Desalination*. 443 (2018) 307–322. doi:10.1016/j.desal.2018.06.006.
- [36] B. Bodell, Silicone rubber vapor diffusion in saline water distillation, United States Patent Serial. (1963).

References

- [37] M.E. Findley, Vaporization through Porous Membranes, *Ind. Eng. Chem. Proc. Des. Dev.* 6 (1967) 226–230. doi:10.1021/i260022a013.
- [38] K. Smolders, A. Franken, Terminology for membrane distillation, *Desalination*. 72 (1989) 249–262.
- [39] N. Thomas, M.O. Mavukkandy, S. Loutatidou, H.A. Arafat, Membrane distillation research & implementation: Lessons from the past five decades, *Separation and Purification Technology*. 189 (2017) 108–127. doi:10.1016/j.seppur.2017.07.069.
- [40] J.-P. Mericq, S. Laborie, C. Cabassud, Vacuum membrane distillation of seawater reverse osmosis brines, *Water Research*. 44 (2010) 5260–5273. doi:10.1016/j.watres.2010.06.052.
- [41] G. Raluy, L. Serra, J. Uche, Life cycle assessment of MSF, MED and RO desalination technologies, *Energy*. 31 (2006) 2361–2372. doi:10.1016/j.energy.2006.02.005.
- [42] A. Deshmukh, C. Boo, V. Karanikola, S. Lin, A.P. Straub, T. Tong, D.M. Warsinger, M. Elimelech, Membrane Distillation at the Water-Energy Nexus: Limits, Opportunities, and Challenges, *Energy Environ. Sci.* (2018). doi:10.1039/C8EE00291F.
- [43] C. Fritzmann, J. Löwenberg, T. Wintgens, T. Melin, State-of-the-art of reverse osmosis desalination, *Desalination*. 216 (2007) 1–76. doi:10.1016/j.desal.2006.12.009.
- [44] S. Al-Obaidani, E. Curcio, F. Macedonio, G. Di Profio, H. Al-Hinai, E. Drioli, Potential of membrane distillation in seawater desalination: Thermal efficiency, sensitivity study and cost estimation, *Journal of Membrane Science*. 323 (2008) 85–98. doi:10.1016/j.memsci.2008.06.006.
- [45] R. Long, X. Lai, Z. Liu, W. Liu, Direct contact membrane distillation system for waste heat recovery: Modelling and multi-objective optimization, *Energy*. 148 (2018) 1060–1068. doi:10.1016/j.energy.2018.02.027.
- [46] M. Khayet, Membranes and theoretical modeling of membrane distillation: A review, *Advances in Colloid and Interface Science*. 164 (2011) 56–88. doi:10.1016/j.cis.2010.09.005.
- [47] A. Alkudhiri, N. Darwish, N. Hilal, Membrane distillation: A comprehensive review, *Desalination*. 287 (2012) 2–18. doi:10.1016/j.desal.2011.08.027.
- [48] K. Zhao, W. Heinzl, M. Wenzel, S. Büttner, F. Bollen, G. Lange, S. Heinzl, N. Sarda, Experimental study of the memsys vacuum-multi-effect-membrane-distillation (V-MEMD) module, *Desalination*. 323 (2013) 150–160. doi:10.1016/j.desal.2012.12.003.
- [49] A.A. Kiss, O.M.K. Read, An industrial perspective on membrane distillation processes, *Journal of Chemical Technology & Biotechnology*. 0 (2018). doi:10.1002/jctb.5674.

- [50] A. Cipollina, M.G. Di Sparti, A. Tamburini, G. Micale, Development of a Membrane Distillation module for solar energy seawater desalination, *Chemical Engineering Research and Design*. 90 (2012) 2101–2121. doi:10.1016/j.cherd.2012.05.021.
- [51] J. Swaminathan, H.W. Chung, D.M. Warsinger, F.A. AlMarzooqi, H.A. Arafat, J.H. Lienhard V, Energy efficiency of permeate gap and novel conductive gap membrane distillation, *Journal of Membrane Science*. 502 (2016) 171–178. doi:10.1016/j.memsci.2015.12.017.
- [52] L. Francis, N. Ghaffour, A.A. Alsaadi, G.L. Amy, Material gap membrane distillation: A new design for water vapor flux enhancement, *Journal of Membrane Science*. 448 (2013) 240–247. doi:10.1016/j.memsci.2013.08.013.
- [53] M.A.E.-R. Abu-Zeid, Y. Zhang, H. Dong, L. Zhang, H.-L. Chen, L. Hou, A comprehensive review of vacuum membrane distillation technique, *Desalination*. 356 (2015) 1–14. doi:10.1016/j.desal.2014.10.033.
- [54] S.O. Olatunji, L.M. Camacho, Heat and Mass Transfer in Modeling Membrane Distillation Configurations: A Review., *Front. Energy Res*. 6 (2018). doi:10.3389/fenrg.2018.00130.
- [55] J. Schwinge, P.R. Neal, D.E. Wiley, D.F. Fletcher, A.G. Fane, Spiral wound modules and spacers: Review and analysis, *Journal of Membrane Science*. 242 (2004) 129–153. doi:10.1016/j.memsci.2003.09.031.
- [56] L.M. Camacho, L. Dumée, J. Zhang, J. Li, M. Duke, J. Gomez, S. Gray, Advances in membrane distillation for water desalination and purification applications, *Water*. 5 (2013) 94–196.
- [57] G. Zaragoza, A. Ruiz-Aguirre, E. Guillén-Burrieza, Efficiency in the use of solar thermal energy of small membrane desalination systems for decentralized water production, *Applied Energy*. 130 (2014) 491–499. doi:10.1016/j.apenergy.2014.02.024.
- [58] D. Woldemariam, A. Martin, M. Santarelli, Exergy Analysis of Air-Gap Membrane Distillation Systems for Water Purification Applications, *Applied Sciences*. 7 (2017) 301.
- [59] B.L. Pangarkar, S.K. Deshmukh, V.S. Sapkal, R.S. Sapkal, Review of membrane distillation process for water purification, *Desalination and Water Treatment*. 57 (2014) 2959–2981. doi:10.1080/19443994.2014.985728.
- [60] E. Curcio, E. Drioli, Membrane Distillation and Related Operations—A Review, *Separation & Purification Reviews*. 34 (2005) 35–86. doi:10.1081/SPM-200054951.

References

- [61] J. Wang, L. Zheng, Z. Wu, Y. Zhang, X. Zhang, Fabrication of hydrophobic flat sheet and hollow fiber membranes from PVDF and PVDF-CTFE for membrane distillation, *Journal of Membrane Science*. 497 (2016) 183–193. doi:10.1016/j.memsci.2015.09.024.
- [62] P. Yazgan-Birgi, M.I. Hassan Ali, H.A. Arafat, Comparative performance assessment of flat sheet and hollow fiber DCMD processes using CFD modeling, *Separation and Purification Technology*. 212 (2019) 709–722. doi:10.1016/j.seppur.2018.11.085.
- [63] E. Drioli, A. Ali, F. Macedonio, Membrane Operations for Process Intensification in Desalination, *Applied Sciences*. 7 (2017) 100. doi:10.3390/app7010100.
- [64] D. Winter, J. Koschikowski, M. Wiegand, Desalination using membrane distillation: Experimental studies on full scale spiral wound modules, *Journal of Membrane Science*. 375 (2011) 104–112. doi:10.1016/j.memsci.2011.03.030.
- [65] A. Ruiz-Aguirre, D.-C. Alarcón-Padilla, G. Zaragoza, Productivity analysis of two spiral-wound membrane distillation prototypes coupled with solar energy, *Desalination and Water Treatment*. 55 (2015) 2777–2785. doi:10.1080/19443994.2014.946711.
- [66] A. Ruiz-Aguirre, J.A. Andrés-Mañas, J.M. Fernández-Sevilla, G. Zaragoza, Experimental characterization and optimization of multi-channel spiral wound air gap membrane distillation modules for seawater desalination, *Separation and Purification Technology*. (2018). doi:10.1016/j.seppur.2018.05.044.
- [67] G. Ramon, Y. Agnon, C. Dosoretz, Heat transfer in vacuum membrane distillation: Effect of velocity slip, *Journal of Membrane Science*. 331 (2009) 117–125. doi:10.1016/j.memsci.2009.01.022.
- [68] Baghel Rakesh, Upadhyaya Sushant, Singh Kailash, Chaurasia Satyendra P., Gupta Akhilendra B., Dohare Rajeev Kumar, A review on membrane applications and transport mechanisms in vacuum membrane distillation, *Revce*. 34 (2018) 73. doi:10.1515/revce-2016-0050.
- [69] H.C. Duong, L. Xia, Z. Ma, P. Cooper, W. Ela, L.D. Nghiem, Assessing the performance of solar thermal driven membrane distillation for seawater desalination by computer simulation, *Journal of Membrane Science*. 542 (2017) 133–142. doi:10.1016/j.memsci.2017.08.007.
- [70] M. Gryta, M. Tomaszewska, Heat transport in the membrane distillation process, *Journal of Membrane Science*. 144 (1998) 211–222. doi:10.1016/S0376-7388(98)00050-7.
- [71] J. Phattaranawik, R. Jiratananon, A. Fane, Heat transport and membrane distillation coefficients in direct contact membrane distillation, *Journal of Membrane Science*. 212 (2003) 177–193. doi:10.1016/S0376-7388(02)00498-2.

- [72] M. del C. García-Payo, M.A. Izquierdo-Gil, Thermal resistance technique for measuring the thermal conductivity of thin microporous membranes, *Journal of Physics D: Applied Physics*. 37 (2004) 3008.
- [73] I. Hitsov, T. Maere, K. De Sitter, C. Dotremont, I. Nopens, Modelling approaches in membrane distillation: A critical review, *Separation and Purification Technology*. 142 (2015) 48–64. doi:10.1016/j.seppur.2014.12.026.
- [74] T.L. Bergman, F.P. Incropera, *Fundamentals of heat and mass transfer*, John Wiley & Sons, 2011.
- [75] S. Srisurichan, R. Jiratananon, A.G. Fane, Mass transfer mechanisms and transport resistances in direct contact membrane distillation process, *Journal of Membrane Science*. 277 (2006) 186–194. doi:10.1016/j.memsci.2005.10.028.
- [76] M.A. Izquierdo-Gil, C. Fernández-Pineda, M.G. Lorenz, Flow rate influence on direct contact membrane distillation experiments: Different empirical correlations for Nusselt number, *Journal of Membrane Science*. 321 (2008) 356–363. doi:10.1016/j.memsci.2008.05.018.
- [77] M. Gryta, M. Tomaszewska, A.W. Morawski, Membrane distillation with laminar flow, *Separation and Purification Technology*. 11 (1997) 93–101. doi:10.1016/S1383-5866(97)00002-6.
- [78] M. Tomaszewska, M. Gryta, A.W. Morawski, A study of separation by the direct-contact membrane distillation process, *Separations Technology*. 4 (1994) 244–248. doi:10.1016/0956-9618(94)80028-6.
- [79] S. Bandini, C. Gostoli, G.C. Sarti, Separation efficiency in vacuum membrane distillation, *Journal of Membrane Science*. 73 (1992) 217–229. doi:10.1016/0376-7388(92)80131-3.
- [80] J.I. Mengual, M. Khayet, M.P. Godino, Heat and mass transfer in vacuum membrane distillation, *International Journal of Heat and Mass Transfer*. 47 (2004) 865–875. doi:10.1016/j.ijheatmasstransfer.2002.09.001.
- [81] V. Gnielinski, New equations for heat and mass-transfer in turbulent pipe and channel flow, *International Chemical Engineering*. 16 (1976) 359–368.
- [82] J. Phattaranawik, R. Jiratananon, A. Fane, Effect of pore size distribution and air flux on mass transport in direct contact membrane distillation, *Journal of Membrane Science*. 215 (2003) 75–85. doi:10.1016/S0376-7388(02)00603-8.
- [83] A. Luo, N. Lior, Critical review of membrane distillation performance criteria, *Desalination and Water Treatment*. (2016) 1–48. doi:10.1080/19443994.2016.1152637.

References

- [84] R.W. Schofield, A.G. Fane, C.J.D. Fell, Heat and mass transfer in membrane distillation, *Journal of Membrane Science*. 33 (1987) 299–313. doi:10.1016/S0376-7388(00)80287-2.
- [85] J. Zhang, J.-D. Li, M. Duke, M. Hoang, Z. Xie, A. Groth, C. Tun, S. Gray, Modelling of vacuum membrane distillation, *Journal of Membrane Science*. 434 (2013) 1–9. doi:10.1016/j.memsci.2013.01.048.
- [86] E.A. Bruges, B. Latta, A.K. Ray, New correlations and tables of the coefficient of viscosity of water and steam up to 1000 bar and 1000°C, *International Journal of Heat and Mass Transfer*. 9 (1966) 465–480. doi:10.1016/0017-9310(66)90102-5.
- [87] S. Kim, S. Kim, Z. Ahmed, D.K. Cha, J. Cho, Flux model for the membrane distillation process to treat wastewater: effect of solids concentration, *Journal of Membrane Science*. (2018). doi:10.1016/j.memsci.2018.09.018.
- [88] Q. Ma, A. Ahmadi, C. Cabassud, Direct integration of a vacuum membrane distillation module within a solar collector for small-scale units adapted to seawater desalination in remote places: Design, modeling & evaluation of a flat-plate equipment, *Journal of Membrane Science*. 564 (2018) 617–633. doi:10.1016/j.memsci.2018.07.067.
- [89] M.M.A. Shirazi, A. Kargari, A.F. Ismail, T. Matsuura, Computational Fluid Dynamic (CFD) opportunities applied to the membrane distillation process: State-of-the-art and perspectives, *Desalination*. 377 (2016) 73–90. doi:10.1016/j.desal.2015.09.010.
- [90] GECO, (n.d.). <https://www.iea.org/geco/> (accessed November 2, 2018).
- [91] E. Bellos, Z. Said, C. Tzivanidis, The use of nanofluids in solar concentrating technologies: A comprehensive review, *Journal of Cleaner Production*. 196 (2018) 84–99. doi:10.1016/j.jclepro.2018.06.048.
- [92] H. Lund, Renewable energy strategies for sustainable development, *Energy*. 32 (2007) 912–919. doi:10.1016/j.energy.2006.10.017.
- [93] M. Mussard, Solar energy under cold climatic conditions: A review, *Renewable and Sustainable Energy Reviews*. 74 (2017) 733–745. doi:10.1016/j.rser.2017.03.009.
- [94] A.N. Celik, T. Muneer, P. Clarke, A review of installed solar photovoltaic and thermal collector capacities in relation to solar potential for the EU-15, *Renewable Energy*. 34 (2009) 849–856. doi:10.1016/j.renene.2008.05.025.
- [95] S.A. Kalogirou, Solar thermal collectors and applications, *Progress in Energy and Combustion Science*. 30 (2004) 231–295. doi:10.1016/j.peccs.2004.02.001.
- [96] K. Sopian, K.S. Yigit, H.T. Liu, S. Kakaç, T.N. Veziroglu, Performance analysis of photovoltaic thermal air heaters, *Energy Conversion and Management*. 37 (1996) 1657–1670. doi:10.1016/0196-8904(96)00010-6.

- [97] M.R. Qtaishat, F. Banat, Desalination by solar powered membrane distillation systems, *Desalination*. 308 (2013) 186–197. doi:10.1016/j.desal.2012.01.021.
- [98] F. Banat, N. Jwaied, M. Rommel, J. Koschikowski, M. Wiegghaus, Desalination by a “compact SMADES” autonomous solarpowered membrane distillation unit, *Desalination*. 217 (2007) 29–37. doi:10.1016/j.desal.2006.11.028.
- [99] F. Banat, N. Jwaied, M. Rommel, J. Koschikowski, M. Wiegghaus, Performance evaluation of the “large SMADES” autonomous desalination solar-driven membrane distillation plant in Aqaba, Jordan, *Desalination*. 217 (2007) 17–28. doi:10.1016/j.desal.2006.11.027.
- [100] H.E.S. Fath, S.M. Elsherbiny, A.A. Hassan, M. Rommel, M. Wiegghaus, J. Koschikowski, M. Vatansever, PV and thermally driven small-scale, stand-alone solar desalination systems with very low maintenance needs, *Desalination*. 225 (2008) 58–69. doi:10.1016/j.desal.2006.11.029.
- [101] R.B. Saffarini, E.K. Summers, H.A. Arafat, J.H. Lienhard V, Economic evaluation of stand-alone solar powered membrane distillation systems, *Desalination*. 299 (2012) 55–62. doi:10.1016/j.desal.2012.05.017.
- [102] R.G. Raluy, R. Schwantes, V.J. Subiela, B. Peñate, G. Melián, J.R. Betancort, Operational experience of a solar membrane distillation demonstration plant in Pozo Izquierdo-Gran Canaria Island (Spain), *Desalination*. 290 (2012) 1–13. doi:10.1016/j.desal.2012.01.003.
- [103] S. Ben Abdallah, N. Frikha, S. Gabsi, Design of an autonomous solar desalination plant using vacuum membrane distillation, the MEDINA project, *Chemical Engineering Research and Design*. 91 (2013) 2782–2788. doi:10.1016/j.cherd.2013.06.012.
- [104] J.R.B. Rodríguez, V.M. Gabet, G.M. Monroy, A.B. Puerta, I.F. Barrio, Distilled and drinkable water quality produced by solar membrane distillation technology, *Desalination and Water Treatment*. 51 (2013) 1265–1271. doi:10.1080/19443994.2012.693683.
- [105] K. Murase, K. Chikamatsu, T. Kyuno, Evaluation of a solar membrane distillator hybridized with a photovoltaic cell, *Desalination and Water Treatment*. 51 (2013) 686–694. doi:10.1080/19443994.2012.693625.
- [106] N. Frikha, R. Matlaya, B. Chaouachi, S. Gabsi, Simulation of an autonomous solar vacuum membrane distillation for seawater desalination, *Desalination and Water Treatment*. 52 (2014) 1725–1734. doi:10.1080/19443994.2013.809638.

References

- [107] A. Chafidz, S. Al-Zahrani, M.N. Al-Otaibi, C.F. Hoong, T.F. Lai, M. Prabu, Portable and integrated solar-driven desalination system using membrane distillation for arid remote areas in Saudi Arabia, *Desalination*. 345 (2014) 36–49. doi:10.1016/j.desal.2014.04.017.
- [108] E.U. Khan, A.R. Martin, Optimization of hybrid renewable energy polygeneration system with membrane distillation for rural households in Bangladesh, *Energy*. 93, Part 1 (2015) 1116–1127. doi:10.1016/j.energy.2015.09.109.
- [109] S.T. Bouguecha, S.E. Aly, M.H. Al-Beiruty, M.M. Hamdi, A. Boubakri, Solar driven DCMD: Performance evaluation and thermal energy efficiency, *Chemical Engineering Research and Design*. 100 (2015) 331–340. doi:10.1016/j.cherd.2015.05.044.
- [110] A. Chafidz, E.D. Kerme, I. Wazeer, Y. Khalid, A. Ajbar, S.M. Al-Zahrani, Design and fabrication of a portable and hybrid solar-powered membrane distillation system, *Journal of Cleaner Production*. 133 (2016) 631–647. doi:10.1016/j.jclepro.2016.05.127.
- [111] S.E. Moore, S.D. Mirchandani, V. Karanikola, T.M. Nenoff, R.G. Arnold, A. Eduardo Sáez, Process modeling for economic optimization of a solar driven sweeping gas membrane distillation desalination system, *Desalination*. 437 (2018) 108–120. doi:10.1016/j.desal.2018.03.005.
- [112] J.A. Duffie, W.A. Beckman, *Solar engineering of thermal processes*, Wiley New York, 2013.
- [113] Z. Wang, W. Yang, F. Qiu, X. Zhang, X. Zhao, Solar water heating: From theory, application, marketing and research, *Renewable and Sustainable Energy Reviews*. 41 (2015) 68–84. doi:10.1016/j.rser.2014.08.026.
- [114] Y.R. Sekhar, K. Sharma, M.B. Rao, Evaluation of heat loss coefficients in solar flat plate collectors, *ARNP Journal of Engineering and Applied Sciences*. 4 (2009) 15–19.
- [115] W.S. Sarsam, S.N. Kazi, A. Badarudin, A review of studies on using nanofluids in flat-plate solar collectors, *Solar Energy*. 122 (2015) 1245–1265. doi:10.1016/j.solener.2015.10.032.
- [116] I. Budihardjo, G.L. Morrison, M. Behnia, Natural circulation flow through water-in-glass evacuated tube solar collectors, *Solar Energy*. 81 (2007) 1460–1472. doi:10.1016/j.solener.2007.03.002.
- [117] T.-T. Chow, Z. Dong, L.-S. Chan, K.-F. Fong, Y. Bai, Performance evaluation of evacuated tube solar domestic hot water systems in Hong Kong, *Energy and Buildings*. 43 (2011) 3467–3474. doi:10.1016/j.enbuild.2011.09.009.
- [118] J. Leblanc, A. Akbarzadeh, J. Andrews, H. Lu, P. Golding, Heat extraction methods from salinity-gradient solar ponds and introduction of a novel system of heat extraction for

- improved efficiency, *Solar Energy*. 85 (2011) 3103–3142. doi:10.1016/j.solener.2010.06.005.
- [119] R.B. Mansour, C.T. Nguyen, N. Galanis, Transient heat and mass transfer and long-term stability of a salt-gradient solar pond, *Mechanics Research Communications*. 33 (2006) 233–249. doi:10.1016/j.mechrescom.2005.06.005.
- [120] K. Manzoor, S.J. Khan, Y. Jamal, M.A. Shahzad, Heat extraction and brine management from salinity gradient solar pond and membrane distillation, *Chemical Engineering Research and Design*. 118 (2017) 226–237. doi:10.1016/j.cherd.2016.12.017.
- [121] H. Xie, J. Wei, Z. Wang, G. Yang, Q. Ma, Design and performance research on eliminating multiple reflections of solar radiation within compound parabolic concentrator (CPC) in hybrid CPV/T system, *Solar Energy*. 129 (2016) 126–146. doi:10.1016/j.solener.2016.01.037.
- [122] G. Morin, J. Dersch, W. Platzer, M. Eck, A. Häberle, Comparison of Linear Fresnel and Parabolic Trough Collector power plants, *Solar Energy*. 86 (2012) 1–12. doi:10.1016/j.solener.2011.06.020.
- [123] M.T. Islam, N. Huda, A.B. Abdullah, R. Saidur, A comprehensive review of state-of-the-art concentrating solar power (CSP) technologies: Current status and research trends, *Renewable and Sustainable Energy Reviews*. 91 (2018) 987–1018. doi:10.1016/j.rser.2018.04.097.
- [124] G. Zhu, T. Wendelin, M.J. Wagner, C. Kutscher, History, current state, and future of linear Fresnel concentrating solar collectors, *Solar Energy*. 103 (2014) 639–652. doi:10.1016/j.solener.2013.05.021.
- [125] M. Hazami, N. Naili, I. Attar, A. Farhat, Solar water heating systems feasibility for domestic requests in Tunisia: Thermal potential and economic analysis, *Energy Conversion and Management*. 76 (2013) 599–608. doi:10.1016/j.enconman.2013.07.079.
- [126] Y. Kim, G. Han, T. Seo, An evaluation on thermal performance of CPC solar collector, *International Communications in Heat and Mass Transfer*. 35 (2008) 446–457. doi:10.1016/j.icheatmasstransfer.2007.09.007.
- [127] M.I. Soomro, W.-S. Kim, Parabolic-trough plant integrated with direct-contact membrane distillation system: Concept, simulation, performance, and economic evaluation, *Solar Energy*. 173 (2018) 348–361. doi:10.1016/j.solener.2018.07.086.
- [128] M.I. Soomro, W.-S. Kim, Performance and economic evaluation of linear Fresnel reflector plant integrated direct contact membrane distillation system, *Renewable Energy*. 129 (2018) 561–569. doi:10.1016/j.renene.2018.06.010.

References

- [129] M.I. Soomro, W.-S. Kim, Performance and economic investigations of solar power tower plant integrated with direct contact membrane distillation system, *Energy Conversion and Management*. 174 (2018) 626–638. doi:10.1016/j.enconman.2018.08.056.
- [130] E. Guillén-Burrieza, D.-C. Alarcón-Padilla, P. Palenzuela, G. Zaragoza, Techno-economic assessment of a pilot-scale plant for solar desalination based on existing plate and frame MD technology, *Desalination*. 374 (2015) 70–80. doi:10.1016/j.desal.2015.07.014.
- [131] P.A. Hogan, Sudjito, A.G. Fane, G.L. Morrison, Desalination by solar heated membrane distillation, *Desalination*. 81 (1991) 81–90. doi:10.1016/0011-9164(91)85047-X.
- [132] Welcome | TRNSYS: Transient System Simulation Tool, (n.d.). <http://www.trnsys.com/> (accessed January 20, 2019).
- [133] Z. Ding, L. Liu, M.S. El-Bourawi, R. Ma, Analysis of a solar-powered membrane distillation system, *Desalination*. 172 (2005) 27–40. doi:10.1016/j.desal.2004.06.195.
- [134] H. Chang, G.-B. Wang, Y.-H. Chen, C.-C. Li, C.-L. Chang, Modeling and optimization of a solar driven membrane distillation desalination system, *Renewable Energy*. 35 (2010) 2714–2722. doi:10.1016/j.renene.2010.04.020.
- [135] Aspen Technology, (n.d.). <https://www.aspentech.com/en/products/pages/aspen-custom-modeler> (accessed January 20, 2019).
- [136] H. Chang, S.-G. Lyu, C.-M. Tsai, Y.-H. Chen, T.-W. Cheng, Y.-H. Chou, Experimental and simulation study of a solar thermal driven membrane distillation desalination process, *Desalination*. 286 (2012) 400–411. doi:10.1016/j.desal.2011.11.057.
- [137] Y.-H. Chen, Y.-W. Li, H. Chang, Optimal design and control of solar driven air gap membrane distillation desalination systems, *Applied Energy*. 100 (2012) 193–204. doi:10.1016/j.apenergy.2012.03.003.
- [138] Y.-D. Kim, K. Thu, N. Ghaffour, K. Choon Ng, Performance investigation of a solar-assisted direct contact membrane distillation system, *Journal of Membrane Science*. 427 (2013) 345–364. doi:10.1016/j.memsci.2012.10.008.
- [139] J.-G. Lee, W.-S. Kim, J.-S. Choi, N. Ghaffour, Y.-D. Kim, Dynamic solar-powered multi-stage direct contact membrane distillation system: Concept design, modeling and simulation, *Desalination*. 435 (2018) 278–292. doi:10.1016/j.desal.2017.04.008.
- [140] X. Wang, L. Zhang, H. Yang, H. Chen, Feasibility research of potable water production via solar-heated hollow fiber membrane distillation system, *Desalination*. 247 (2009) 403–411. doi:10.1016/j.desal.2008.10.008.

- [141] Y. Wang, Z. Xu, N. Lior, H. Zeng, An experimental study of solar thermal vacuum membrane distillation desalination, *Desalination and Water Treatment*. 53 (2015) 887–897. doi:10.1080/19443994.2014.927187.
- [142] A.E. Kabeel, M. Abdelgaied, E.M.S. El-Said, Study of a solar-driven membrane distillation system: Evaporative cooling effect on performance enhancement, *Renewable Energy*. 106 (2017) 192–200. doi:10.1016/j.renene.2017.01.030.
- [143] E. Guillén-Burrieza, G. Zaragoza, S. Miralles-Cuevas, J. Blanco, Experimental evaluation of two pilot-scale membrane distillation modules used for solar desalination, *Journal of Membrane Science*. 409–410 (2012) 264–275. doi:10.1016/j.memsci.2012.03.063.
- [144] R. Schwantes, A. Cipollina, F. Gross, J. Koschikowski, D. Pfeifle, M. Rolletschek, V. Subiela, Membrane distillation: Solar and waste heat driven demonstration plants for desalination, *Desalination*. 323 (2013) 93–106. doi:10.1016/j.desal.2013.04.011.
- [145] H.-J. Joo, H.-Y. Kwak, Freshwater production characteristics of vacuum membrane distillation module for seawater desalination using a solar thermal system by seawater feed conditions, *Desalination and Water Treatment*. (2016) 1–9. doi:10.1080/19443994.2016.1152639.
- [146] J. Koschikowski, M. Wieghaus, M. Rommel, Solar thermal-driven desalination plants based on membrane distillation, *Desalination*. 156 (2003) 295–304. doi:10.1016/S0011-9164(03)00360-6.
- [147] A.M. Alklaibi, N. Lior, Membrane-distillation desalination: Status and potential, *Desalination*. 171 (2005) 111–131. doi:10.1016/j.desal.2004.03.024.
- [148] M. Asim, N.T.U. Kumar, A.R. Martin, Feasibility analysis of solar combi-system for simultaneous production of pure drinking water via membrane distillation and domestic hot water for single-family villa: pilot plant setup in Dubai, *Desalination and Water Treatment*. 57 (2016) 21674–21684. doi:10.1080/19443994.2015.1125806.
- [149] F. Suárez, J.A. Ruskowitz, S.W. Tyler, A.E. Childress, Renewable water: Direct contact membrane distillation coupled with solar ponds, *Applied Energy*. 158 (2015) 532–539. doi:10.1016/j.apenergy.2015.08.110.
- [150] W.G. Shim, K. He, S. Gray, I.S. Moon, Solar energy assisted direct contact membrane distillation (DCMD) process for seawater desalination, *Separation and Purification Technology*. 143 (2015) 94–104. doi:10.1016/j.seppur.2015.01.028.

References

- [151] F. Suárez, R. Urtubia, Tackling the water-energy nexus: an assessment of membrane distillation driven by salt-gradient solar ponds, *Clean Techn Environ Policy*. 18 (2016) 1697–1712. doi:10.1007/s10098-016-1210-3.
- [152] K. Murase, Y. Yamagishi, K. Tano, Development of a hybrid solar distillator of a basin type distillator and a membrane distillator, *Desalination and Water Treatment*. 9 (2009) 96–104. doi:10.5004/dwt.2009.757.
- [153] T.-C. Chen, C.-D. Ho, Immediate assisted solar direct contact membrane distillation in saline water desalination, *Journal of Membrane Science*. 358 (2010) 122–130. doi:10.1016/j.memsci.2010.04.037.
- [154] C.-D. Ho, C.A. Ng, P.-H. Wang, C.-H. Cheng, Theoretical and experimental studies of immediate assisted solar air gap membrane distillation systems, *Desalination and Water Treatment*. 57 (2016) 3846–3860. doi:10.1080/19443994.2014.989274.
- [155] G. Xue, Q. Chen, S. Lin, J. Duan, P. Yang, K. Liu, J. Li, J. Zhou, Highly Efficient Water Harvesting with Optimized Solar Thermal Membrane Distillation Device, *Global Challenges*. 0 (2018) 1800001. doi:10.1002/gch2.201800001.
- [156] S.B. Abdallah, N. Frikha, S. Gabsi, Study of the performances of different configurations of seawater desalination with a solar membrane distillation, *Desalination and Water Treatment*. 52 (2014) 2362–2371. doi:10.1080/19443994.2013.792746.
- [157] S. Abdallah, N. Frikha, S. Gabsi, Numerical Investigations of Coupling a Vacuum Membrane Desalination System with a Salt Gradient Solar Pond, *J Fundam Renewable Energy Appl*. 6 (2016) 2.
- [158] Q. Li, L.-J. Beier, J. Tan, C. Brown, B. Lian, W. Zhong, Y. Wang, C. Ji, P. Dai, T. Li, P. Le Clech, H. Tyagi, X. Liu, G. Leslie, R.A. Taylor, An integrated, solar-driven membrane distillation system for water purification and energy generation, *Applied Energy*. 237 (2019) 534–548. doi:10.1016/j.apenergy.2018.12.069.
- [159] E.K. Summers, J.H. Lienhard V, A novel solar-driven air gap membrane distillation system, *Desalination and Water Treatment*. 51 (2013) 1344–1351. doi:10.1080/19443994.2012.705096.
- [160] E.K. Summers, J.H. Lienhard V, Experimental study of thermal performance in air gap membrane distillation systems, including the direct solar heating of membranes, *Desalination*. 330 (2013) 100–111. doi:10.1016/j.desal.2013.09.023.
- [161] Politano Antonio, Argurio Pietro, Di Profio Gianluca, Sanna Vanna, Cupolillo Anna, Chakraborty Sudip, Arafat Hassan A., Curcio Efrem, Photothermal Membrane Distillation

- for Seawater Desalination, *Advanced Materials*. 29 (2016) 1603504. doi:10.1002/adma.201603504.
- [162] X. Wu, Q. Jiang, D. Ghim, S. Singamaneni, Y.-S. Jun, Localized Heating by a Photothermal Polydopamine Coating Facilitates a Novel Membrane Distillation Process, *Journal of Materials Chemistry A*. (2018). doi:10.1039/C8TA05738A.
- [163] R. Kirilov, P. Stefchev, Z. Alexieva, H. Dikov, A High Effective Selective Absorbing Coating for Solar Thermal Collectors, *Solid State Phenomena*. (2010). doi:10.4028/www.scientific.net/SSP.159.97.
- [164] M. Khayet, Solar desalination by membrane distillation: Dispersion in energy consumption analysis and water production costs (a review), *Desalination*. 308 (2013) 89–101. doi:10.1016/j.desal.2012.07.010.
- [165] A. Criscuoli, M.C. Carnevale, E. Drioli, Evaluation of energy requirements in membrane distillation, *Chemical Engineering and Processing: Process Intensification*. 47 (2008) 1098–1105. doi:10.1016/j.cep.2007.03.006.
- [166] M. Iqbal, *An introduction to solar radiation*, Elsevier, 2012.
- [167] P.I. Cooper, The absorption of radiation in solar stills, *Solar Energy*. 12 (1969) 333–346. doi:10.1016/0038-092X(69)90047-4.
- [168] H.C. Hottel, A simple model for estimating the transmittance of direct solar radiation through clear atmospheres, *Solar Energy*. 18 (1976) 129–134. doi:10.1016/0038-092X(76)90045-1.
- [169] B.Y.H. Liu, R.C. Jordan, The interrelationship and characteristic distribution of direct, diffuse and total solar radiation, *Solar Energy*. 4 (1960) 1–19. doi:10.1016/0038-092X(60)90062-1.
- [170] B.Y. Liu, R.C. Jordan, The long-term average performance of flat-plate solar-energy collectors: with design data for the US, its outlying possessions and Canada, *Solar Energy*. 7 (1963) 53–74.
- [171] J.R. Howell, M.P. Menguc, R. Siegel, *Thermal radiation heat transfer*, CRC press, 2010.
- [172] M.J. Brandemuehl, W.A. Beckman, Transmission of diffuse radiation through CPC and flat plate collector glazings, *Solar Energy*. 24 (1980) 511–513. doi:10.1016/0038-092X(80)90320-5.
- [173] E.N. Sieder, G.E. Tate, Heat transfer and pressure drop of liquids in tubes, *Industrial & Engineering Chemistry*. 28 (1936) 1429–1435.

References

- [174] D.T. Jamieson, J.S. Tudhope, R. Morris, G. Cartwright, Physical properties of sea water solutions: heat capacity, *Desalination*. 7 (1969) 23–30. doi:10.1016/S0011-9164(00)80271-4.
- [175] L. Yuan-Hui, S. Gregory, Diffusion of ions in sea water and in deep-sea sediments, *Geochimica et Cosmochimica Acta*. 38 (1974) 703–714. doi:10.1016/0016-7037(74)90145-8.
- [176] S. Klein, Calculation of flat-plate collector loss coefficients, *Solar Energy*. 17 (1975) 79–80.
- [177] L. Li, K.K. Sirkar, Studies in Vacuum Membrane Distillation with Flat Membranes, *Journal of Membrane Science*. (n.d.). doi:10.1016/j.memsci.2016.09.028.
- [178] J.-G. Lee, W.-S. Kim, Numerical study on multi-stage vacuum membrane distillation with economic evaluation, *Desalination*. 339 (2014) 54–67. doi:10.1016/j.desal.2014.02.003.
- [179] `scipy.integrate.ode` — SciPy v0.18.1 Reference Guide, (n.d.). <https://docs.scipy.org/doc/scipy-0.18.1/reference/generated/scipy.integrate.ode.html> (accessed December 14, 2017).
- [180] W.L. McCabe, J.C. Smith, P. Harriott, Unit operations of chemical engineering, McGraw-Hill New York, 1993.
- [181] J. Swaminathan, H.W. Chung, D.M. Warsinger, J.H. Lienhard V, Energy efficiency of membrane distillation up to high salinity: Evaluating critical system size and optimal membrane thickness, *Applied Energy*. 211 (2018) 715–734. doi:10.1016/j.apenergy.2017.11.043.
- [182] J. Swaminathan, H.W. Chung, D.M. Warsinger, J.H. Lienhard V, Membrane distillation model based on heat exchanger theory and configuration comparison, *Applied Energy*. 184 (2016) 491–505. doi:10.1016/j.apenergy.2016.09.090.
- [183] Y. Zhang, Y. Peng, S. Ji, J. Qi, S. Wang, Numerical modeling and economic evaluation of two multi-effect vacuum membrane distillation (ME-VMD) processes, *Desalination*. 419 (2017) 39–48. doi:10.1016/j.desal.2017.05.032.
- [184] JRC's Directorate C, Energy, Transport and Climate - PVGIS - European Commission, (n.d.). <http://re.jrc.ec.europa.eu/pvgis/index.htm> (accessed October 31, 2017).
- [185] T.D. Dao, J.-P. Mericq, S. Laborie, C. Cabassud, A new method for permeability measurement of hydrophobic membranes in Vacuum Membrane Distillation process, *Water Research*. 47 (2013) 2096–2104. doi:10.1016/j.watres.2013.01.040.

- [186] R.H. French, J.M. Rodríguez-Parada, M.K. Yang, R.A. Derryberry, N.T. Pfeifferberger, Optical properties of polymeric materials for concentrator photovoltaic systems, *Solar Energy Materials and Solar Cells*. 95 (2011) 2077–2086. doi:10.1016/j.solmat.2011.02.025.
- [187] C. Cabassud, D. Wirth, Membrane distillation for water desalination: How to chose an appropriate membrane?, *Desalination*. 157 (2003) 307–314. doi:10.1016/S0011-9164(03)00410-7.
- [188] P. Boutikos, E.S. Mohamed, E. Mathioulakis, V. Belessiotis, A theoretical approach of a vacuum multi-effect membrane distillation system, *Desalination*. 422 (2017) 25–41. doi:10.1016/j.desal.2017.08.007.
- [189] H.C. Duong, P. Cooper, B. Nelemans, T.Y. Cath, L.D. Nghiem, Optimising thermal efficiency of direct contact membrane distillation by brine recycling for small-scale seawater desalination, *Desalination*. 374 (2015) 1–9. doi:10.1016/j.desal.2015.07.009.
- [190] E.K. Summers, H.A. Arafat, J.H. Lienhard V, Energy efficiency comparison of single-stage membrane distillation (MD) desalination cycles in different configurations, *Desalination*. 290 (2012) 54–66. doi:10.1016/j.desal.2012.01.004.
- [191] C. Huayan, W. Chunrui, J. Yue, W. Xuan, L. Xiaolong, Comparison of three membrane distillation configurations and seawater desalination by vacuum membrane distillation, *Desalination and Water Treatment*. 28 (2011) 321–327. doi:10.5004/dwt.2011.1605.
- [192] H. Fan, Y. Peng, Application of PVDF membranes in desalination and comparison of the VMD and DCMD processes, *Chemical Engineering Science*. 79 (2012) 94–102. doi:10.1016/j.ces.2012.05.052.
- [193] J. Koo, J. Han, J. Sohn, S. Lee, T.-M. Hwang, Experimental comparison of direct contact membrane distillation (DCMD) with vacuum membrane distillation (VMD), *Desalination and Water Treatment*. 51 (2013) 6299–6309. doi:10.1080/19443994.2013.780817.
- [194] G. Guan, X. Yang, R. Wang, R. Field, A.G. Fane, Evaluation of hollow fiber-based direct contact and vacuum membrane distillation systems using aspen process simulation, *Journal of Membrane Science*. 464 (2014) 127–139. doi:10.1016/j.memsci.2014.03.054.
- [195] L. Eykens, T. Reyns, K. De Sitter, C. Dotremont, L. Pinoy, B. Van der Bruggen, How to select a membrane distillation configuration? Process conditions and membrane influence unraveled, *Desalination*. 399 (2016) 105–115. doi:10.1016/j.desal.2016.08.019.
- [196] A. Bahmanyar, M. Asghari, N. Khoobi, Numerical simulation and theoretical study on simultaneously effects of operating parameters in direct contact membrane distillation,

References

- Chemical Engineering and Processing: Process Intensification. 61 (2012) 42–50. doi:10.1016/j.cep.2012.06.012.
- [197] Heat exchanger sizing and rating (ht.hx) — Heat Transfer 0.1 documentation, (n.d.). <https://ht.readthedocs.io/en/latest/ht.hx.html> (accessed October 18, 2018).
- [198] R.K. Shah, A.L. London, Laminar flow forced convection in ducts: a source book for compact heat exchanger analytical data, Academic press, 2014.
- [199] scipy.optimize.fsolve — SciPy v0.14.0 Reference Guide, (n.d.). <https://docs.scipy.org/doc/scipy-0.14.0/reference/generated/scipy.optimize.fsolve.html> (accessed October 18, 2018).
- [200] Heat Exchanger Heat Transfer Coefficients, (n.d.). https://www.engineeringtoolbox.com/heat-transfer-coefficients-exchangers-d_450.html (accessed February 7, 2019).
- [201] P. Datt, Latent Heat of Vaporization/Condensation, in: V.P. Singh, P. Singh, U.K. Haritashya (Eds.), Encyclopedia of Snow, Ice and Glaciers, Springer Netherlands, Dordrecht, 2011: pp. 703–703. doi:10.1007/978-90-481-2642-2_327.
- [202] P. Wang, T.-S. Chung, Recent advances in membrane distillation processes: Membrane development, configuration design and application exploring, Journal of Membrane Science. 474 (2015) 39–56. doi:10.1016/j.memsci.2014.09.016.
- [203] J.-G. Lee, S. Jeong, A.S. Alsaadi, N. Ghaffour, Influence of high range of mass transfer coefficient and convection heat transfer on direct contact membrane distillation performance, Desalination. 426 (2018) 127–134. doi:10.1016/j.desal.2017.10.034.
- [204] How Much Water Should You Drink Per Day?, Healthline. (2018). <https://www.healthline.com/nutrition/how-much-water-should-you-drink-per-day> (accessed January 10, 2019).
- [205] S.-I. Andersson, N. Kjellander, B. Rodesjö, Design and field tests of a new membrane distillation desalination process, Desalination. 56 (1985) 345–354. doi:10.1016/0011-9164(85)85037-2.
- [206] Y.Z. Tan, L. Han, N.G.P. Chew, W.H. Chow, R. Wang, J.W. Chew, Membrane distillation hybridized with a thermoelectric heat pump for energy-efficient water treatment and space cooling, Applied Energy. 231 (2018) 1079–1088. doi:10.1016/j.apenergy.2018.09.196.
- [207] J. Schiffmann, D. Favrat, Design, experimental investigation and multi-objective optimization of a small-scale radial compressor for heat pump applications, Energy. 35 (2010) 436–450. doi:10.1016/j.energy.2009.10.010.

- [208] A. Desideri, S. Gusev, M. van den Broek, V. Lemort, S. Quoilin, Experimental comparison of organic fluids for low temperature ORC (organic Rankine cycle) systems for waste heat recovery applications, *Energy*. 97 (2016) 460–469. doi:10.1016/j.energy.2015.12.012.
- [209] R. Andrzejczyk, T. Muszyński, The performance of H₂O, R134a, SES36, ethanol, and HFE7100 two-phase closed thermosyphons for varying operating parameters and geometry, *Archives of Thermodynamics*. 38 (2017) 3–21. doi:10.1515/aoter-2017-0013.
- [210] Welcome to CoolProp — CoolProp 6.1.0 documentation, (n.d.). <http://www.coolprop.org/> (accessed June 8, 2018).
- [211] J. Herman, W. Usher, SALib: an open-source Python library for sensitivity analysis, *The Journal of Open Source Software*. 2 (2017).
- [212] E. Borgonovo, A new uncertainty importance measure, *Reliability Engineering & System Safety*. 92 (2007) 771–784. doi:10.1016/j.ress.2006.04.015.
- [213] E. Plischke, E. Borgonovo, C.L. Smith, Global sensitivity measures from given data, *European Journal of Operational Research*. 226 (2013) 536–550. doi:10.1016/j.ejor.2012.11.047.
- [214] A. Saltelli, Sensitivity analysis for importance assessment, *Risk Analysis*. 22 (2002) 579–590.
- [215] A. Ahmadi, L. Tiruta-Barna, F. Capitanescu, E. Benetto, A. Marvuglia, An archive-based multi-objective evolutionary algorithm with adaptive search space partitioning to deal with expensive optimization problems: Application to process eco-design, *Computers & Chemical Engineering*. 87 (2016) 95–110. doi:10.1016/j.compchemeng.2015.12.008.
- [216] A. Ahmadi, Memory-based adaptive partitioning (MAP) of search space for the enhancement of convergence in Pareto-based multi-objective evolutionary algorithms, *Applied Soft Computing*. 41 (2016) 400–417. doi:10.1016/j.asoc.2016.01.029.
- [217] Mobile and autonomous water purification system - AQUALINK, Sunwaterlife - Water Purification Systems. (n.d.). <http://www.sunwaterlife.com/en/products/mobile-and-autonomous-water-purification-system-aqualink/> (accessed January 28, 2019).
- [218] Pilkington Optiwhite™, (n.d.). <http://www.pilkington.com/uk/products/product-categories/special-applications/pilkington-optiwhite> (accessed January 25, 2019).
- [219] H.J. McQueen, M.M. Shapiro, D. Feldman, Selection of materials for flat plate solar collectors, *JMES*. 2 (1980) 65–82. doi:10.1007/BF02833399.

References

- [220] B. z. Azmi, M. y. Sulaiman, M.A. Wahab, M. a. Alghoul, Review of materials for solar thermal collectors, *Anti-Corrosion Meth & Material*. 52 (2005) 199–206. doi:10.1108/00035590510603210.
- [221] C.G.S.T.-A.-C. Ltd, Mediterranean | Sea Temperatures, (n.d.). <http://www.seatemperature.org/mediterranean-sea> (accessed February 14, 2019).
- [222] Solar panels, Energy Saving Trust. (n.d.). <https://www.energysavingtrust.org.uk/renewable-energy/electricity/solar-panels> (accessed February 15, 2019).

